

AD-A100 524

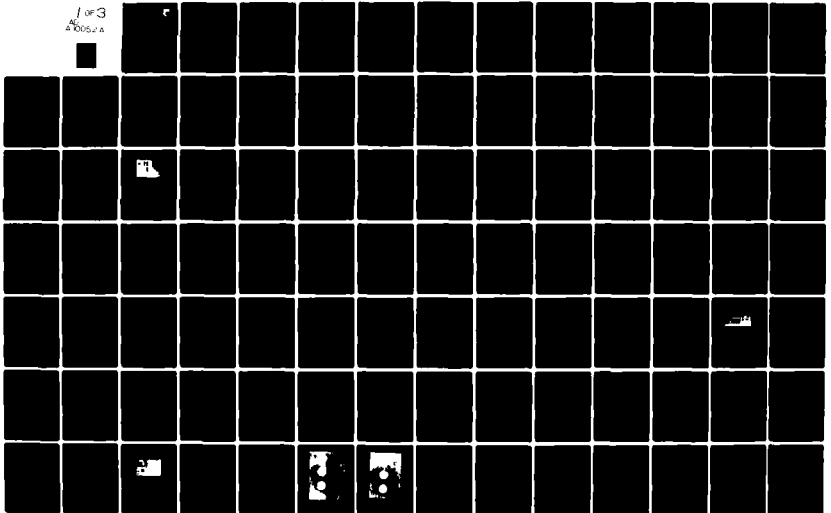
MICHIGAN STATE UNIV EAST LANSING DIV OF ENGINEERING --ETC F/6 13/5  
AN EXPERIMENTAL STUDY OF LARGE COMPRESSIVE LOADS UPON RESIDUAL --ETC(U)  
FEB 81 G CLOUD, R SULAIMANA F33615-78-C-5123

UNCLASSIFIED

AFWAL-TR-80-4206

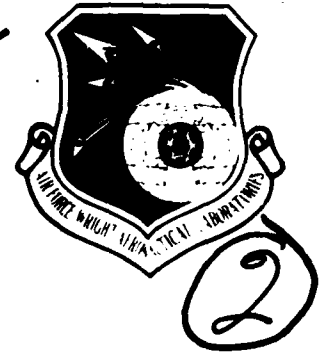
NL

1 of 3  
400524



**LEVEL II**

AFWAL-TR-80-4206

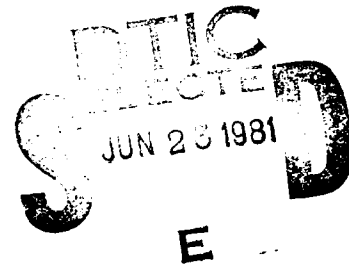


**AD A100524**

AN EXPERIMENTAL STUDY OF LARGE COMPRESSIVE LOADS UPON RESIDUAL STRAIN FIELDS  
AND THE INTERACTION BETWEEN SURFACE STRAIN FIELDS CREATED BY COLDWORKING  
FASTENER HOLES

Gary Cloud  
Rajab Sulaimana

Division of Engineering Research  
Michigan State University  
East Lansing, Michigan 48824



February 1981  
TECHNICAL REPORT AFWAL-TR-80-4206  
Final Report for Period June 1978 to February 1980

**UN FILE COPY** Approved for public release; distribution unlimited

MATERIALS LABORATORY  
AIR FORCE WRIGHT AERONAUTICAL LABORATORIES  
AIR FORCE SYSTEMS COMMAND  
WRIGHT-PATTERSON AIR FORCE BASE, OHIO 45433

81 6 23 019

NOTICE

When Government drawings, specifications, or other data are used for any purpose other than in connection with a definitely related Government procurement operation, the United States Government thereby incurs no responsibility nor any obligation whatsoever; and the fact that the government may have formulated, furnished, or in any way supplied the said drawings, specifications, or other data, is not to be regarded by implication or other wise as in any manner licensing the holder or any other person or corporation, or conveying any rights or permission to manufacture use, or sell any patented invention that may in any way be related thereto.

This report has been reviewed by the Office of Public Affairs (ASD/PA) and is releasable to the National Technical Information Service (NTIS). At NTIS, it will be available to the general public, including foreign nations.

This technical report has been reviewed and is approved for publication.

*Robert C. Donath.*

ROBERT C. DONATH  
Project Engineer

*Walter H. Reimann*

WALTER H. REIMANN, Acting Chief  
Metals Behavior Branch  
Metals and Ceramics Division

"If your address has changed, if you wish to be removed from our mailing list, or if the addressee is no longer employed by your organization please notify AFWAL/MLLN W-PAFB, OH 45433 to help us maintain a current mailing list."

Copies of this report should not be returned unless return is required by security considerations, contractual obligations, or notice on a specific document.

REPORT DOCUMENTATION PAGE		READ INSTRUCTIONS BEFORE COMPLETING FORM
1. REPORT NUMBER AFWAL TR-80-4206	2. GOVT ACCESSION NO. AD-A100	3. RECIPIENT'S CATALOG NUMBER 524
4. TITLE (and Subtitle) AN EXPERIMENTAL STUDY OF LARGE COMPRESSIVE LOADS UPON RESIDUAL STRAIN FIELDS AND THE INTERACTION BETWEEN SURFACE STRAIN FIELDS CREATED BY COLDWORKING FASTENER HOLES.		5. TYPE OF REPORT & PERIOD COVERED Final for Period June 1978 - Feb 1980
7. AUTHOR(s) Gary Cloud and Rajab Sulaimana		6. PERFORMING ORG. REPORT NUMBER
9. PERFORMING ORGANIZATION NAME AND ADDRESS Division of Engineering Research Michigan State University East Lansing, MI 48824		8. CONTRACT OR GRANT NUMBER(s) F33615-78-C-5123
11. CONTROLLING OFFICE NAME AND ADDRESS Materials Laboratory (AFWAL/MLLN) Air Force Wright Aeronautical Laboratories Air Force Systems Command Wright-Patterson Air Force Base, Ohio 45433		10. PROGRAM ELEMENT, PROJECT, TASK AREA & WORK UNIT NUMBERS 2418403-05
14. MONITORING AGENCY NAME & ADDRESS (if different from Controlling Office)		12. REPORT DATE February 1981
		13. NUMBER OF PAGES 219
		15. SECURITY CLASS. (of this report) Unclassified
		15a. DECLASSIFICATION/DOWNGRADING SCHEDULE
16. DISTRIBUTION STATEMENT (of this Report) Approved for public release; distribution unlimited.		
17. DISTRIBUTION STATEMENT (of the abstract entered in Block 20, if different from Report)		
18. SUPPLEMENTARY NOTES		
19. KEY WORDS (Continue on reverse side if necessary and identify by block number) Fasteners      Moire Coldwork      Strain Plasticity      Holes		
20. ABSTRACT (Continue on reverse side if necessary and identify by block number) This research investigated three related problems, namely: (1) the evaluation of the residual strain redistribution around an initially coldworked fastener hole in a semi-infinite plate subjected to large in-plane compressive loads; (2) the determination of the effects of a near edge on a row of coldworked holes parallel to such an edge, and the possible creation of a strain climate at the straight edge which could lead to stress corrosion problems; and, (3) the interactions of surface strain fields between rivet holes which are being coldworked. The strain distributions were obtained by a moire technique, with		

the aid of coherent optical processing and digital data reduction. Many useful conclusions about the residual strain fields near coldworked holes were established. Specific important deductions include:

- a. In-plane compressive loads tend to decrease residual hoop strain parallel to the axis of applied load and to increase residual hoop strain transverse to the load axis.
- b. The effects of cycling of the in-plane loads were complex, but in general increased residual hoop strain around the fastener hole boundary.
- c. In-plane loads have little effect on radial strains.
- d. Coldworking a fastener hole or a row of holes introduces undesirable tensile strain climate at a plate edge, whereas peak compressive residual radial strains are shifted away from important areas near fastener holes.
- e. A minimum effective coldwork fastener hole separation is about 2 hole diameters for a radial interference level of 6 mils. Below this limit, the effect of coldworking the holes diminishes the residual compressive strain field.
- f. The interaction of coldwork-induced strain fields with one another and with free boundaries is quite complex. Unexpected reductions and increases of residual strains are common with practical situations involving several holes and plate edges.
- g. Coldworking a group of holes is a dynamic process; the order of hole treatment is important.

FOREWORD

This report was prepared by the Department of Metallurgy, Mechanics and Material Science, Michigan State University, East Lansing, Michigan 48824, under Contract No. F33615-78-C-5123, "Coldworked Hole Stress Analysis." The contract, which was initiated under Project No. 2418, Task 24180305, was administered under the direction of the Air Force Materials Laboratory, Metals Behavior Branch (AFWAL/MLIN), by Dr. Robert C. Donath, Project Engineer.

The research reported herein was submitted by Dr. Gary Cloud who was the Principal Investigator, and covers work conducted during the period 1 June 1978 to 15 February 1980.

Accession For	
NTIS	<input checked="" type="checkbox"/>
DIA	<input type="checkbox"/>
USCIB	<input type="checkbox"/>
J. Res. Dev.	<input type="checkbox"/>
By	
Distribution	
Availability Codes	
Dist	Avail and/or Special
A	

## TABLE OF CONTENTS

SECTION	Page
I. INTRODUCTION . . . . .	1
1.1 Purpose and Motivation . . . . .	3
1.2 Organization . . . . .	3
II. DEVELOPMENT OF COLDWORKING-RESIDUAL STRAINS IN AND AROUND COLDWORKED HOLES . . . . .	5
2.1 Development of Coldworking . . . . .	5
2.2 Experimental Coldworking Procedure . . . . .	8
2.3 Residual Strains In and Around Coldworked Holes . . . . .	14
2.3.1 Introduction . . . . .	14
2.3.2 Analytical Approaches to the Problem . . . . .	14
2.3.3 Discussion of Theoretical Studies . . . . .	23
2.4 Overview of Experimental Studies . . . . .	24
III. MATERIALS AND SPECIMEN PREPARATION . . . . .	25
3.1 Material Specification and Specimen Preparation . . . . .	25
3.2 Moiré Submaster Grating Production . . . . .	33
3.3 Grating Frequency Measurement of Submasters . . . . .	38
3.4 Specimen Gratings . . . . .	41
3.4.1 Photoresists . . . . .	41
3.4.2 Photoresist Applications . . . . .	42
3.5 Printing and Development of Specimen Gratings . . . . .	44
3.6 Deposited Copper Film Gratings . . . . .	47
IV. GRATING PHOTOGRAPHY AND OPTICAL DATA PROCESSING . . . . .	48
4.1 Specimen Grating Photography . . . . .	48
4.2 Grating Recording System . . . . .	49
4.3 Optical Data Processing - Fundamental Concepts . . . . .	54
4.4 Spatial Filtering for Moiré Analysis . . . . .	64

SECTION	Page
4.5 Creation of Moiré Fringe Photographs. . .	68
4.6 Moire Data Reduction. . . . .	74
4.6.1 The Geometrical Approach. . . . .	74
4.6.2 The Displacement-Derivative Approach. . . . .	77
4.7 Digitization of Moiré Fringes - Radial and Tangential Strains. . . . .	80
 V. EFFECTS OF LARGE COMPRESSIVE IN-PLANE LOADS ON RESIDUAL STRAIN FIELD. . . . .	82
5.1 Introduction. . . . .	82
5.2 Overview. . . . .	82
5.3 Experimental Procedure. . . . .	83
5.4 Results and Discussion. . . . .	89
5.4.1 Axial Hoop Strain Distribution. . .	89
5.4.2 Transverse Hoop Strain Distri- bution. . . . .	104
5.4.3 Radial Strain Distribution. . . . .	116
 VI. HOLE INTERACTION STUDY. . . . .	125
6.1 Introduction. . . . .	125
6.2 Experimental Procedure. . . . .	126
6.3 Results and Discussion. . . . .	127
6.3.1 Radial Strain Distribution. . . . .	127
6.3.2 Hoop Strain Distribution. . . . .	140
 VII. EDGE EFFECT STUDY . . . . .	149
7.1 Overview. . . . .	149
7.2 Material and Experimental Procedures. . .	151
7.3 Experimental Results and Discussion . . .	153
7.3.1 Hoop Strain Distribution. . . . .	153
7.3.2 Radial Compressive Strain Distribution. . . . .	167
 VIII. CONCLUSIONS. . . . .	179
8.1 Introduction. . . . .	179
8.2 Experimental Apparatus. . . . .	179
8.3 Summary of Results. . . . .	180
8.4 Future Research . . . . .	185
 REFERENCES . . . . .	186
 APPENDIX . . . . .	190

LIST OF TABLES

TABLE	PAGE
3.1 Typical Diametral Measurements at Three Angular Locations $0^\circ$ , $45^\circ$ , $90^\circ$ from the Horizontal Line (SP2) . . . . .	28
3.2 Typical Determination of Radial Interference (in) from Repeated Diametral Measurements (SPP) . . . . .	32

## LIST OF FIGURES

FIGURE	PAGE
2.2.1 Schematic of coldworking using mandrel and sleeve (King process) . . . . .	9
2.2.2 Schematic of the coldworking procedure . . . . .	.11
2.2.3 The Instron coldworking set-up . . . . .	.13
2.3.1 Geometry and coordinate system used in Coldworked Hole Theories . . . . .	.16
3.1.1 Dimensions and fiducial mark system of the in-plane compressive overload specimen: dimensions in inches . . . . .	.26
3.1.2 Dimensions and fiducial mark system of the "plate edge effect specimens": dimensions in inches. . . . .	.29
3.1.3 Dimensions and fiducial mark system of the "hole interaction" and "plate edge effect" specimen; dimensions inches. . . . .	.30
3.2.1 Optical system for contact copying submaster . . . . .	.35
3.2.2 System for grating submaster production. . . . .	.36
3.3.1 Optical creation of Fourier transform of input signal in the form of a transparency . . . . .	.40
3.5.1 Optical system for printing grating on specimen . . . . .	.45
4.2.1 Schematic of Apparatus for grating photography. . . . .	.50
4.2.2 Equipment for grating photography. . . . .	.51
4.3.1 Arrangement of components of optical spatial filtering system . . . . .	.55
4.3.2 Diffraction of light by two superimposed sine gratings having slightly different spatial frequencies. . . . .	.57

FIGURE	PAGE
4.3.3 Formation of two-beam interference fringe pattern by light diffracted through 2 sine gratings having slightly different spatial frequencies. . . . .	59
4.3.4 Diffraction of wide collimated beam by two sine gratings to form whole-field interference pattern. . . . .	60
4.3.5 Diffraction of narrow beam by two bar and space gratings to form ray groups containing higher diffraction orders. . . . .	61
4.3.6 Schematic used for coherent optical processing. . . . .	63
4.3.7 Example of optical spatial filtering to create bar grating from a grid of dots or crossed lines. . . . .	65
4.4.1 Optical system for spatial filtering in Fourier transform plane and creation of inverse transform of filtered image . . . . .	67
4.5.1 Data processing system . . . . .	69
4.5.2 Baseline Moiré fringe photograph of specimen SPC. . . . .	72
4.5.3 Moiré fringe photograph of specimen SPC after coldworking holes, 1,2 and 4 . . . . .	73
4.6.1 Moiré fringe geometry. . . . .	76
4.7.1 Digitizer components . . . . .	81
5.1 Apparatus for overload compressive test application. . . . .	85
5.2 Moiré fringe photograph of specimen SP2 after 15,000 lbf load application. . . . .	86
5.3 Moiré fringe photograph of specimen SP2 after 20,000 lbf load application. . . . .	87
5.4 Moiré fringe photograph of specimen SP2 after 25,000 lbf load application. . . . .	88
5.5 Effect of in-plane compression on residual axial maximum hoop strain at a point on hole boundary . . . . .	90

FIGURE	PAGE
5.6	Residual axial hoop strain distribution along several axes at different radial interferences 5.6 mils radial interference. . . . . 91
5.7	Residual maximum axial strain distributions at various points on a radial line for zero mils radial interference . . . 92
5.8	Residual maximum axial strain distributions at various points on a radial line for 5.6 mils radial interference . . . 93
5.9	Measured residual axial hoop strain distributions along several axes at different radial distances for 6.5 mils radial interference . . . . . 94
5.10	Residual axial hoop strain distributions along several axes for 7.2 mils radial interference (load 15,000 lbf) . . . . . 95
5.11	Residual axial hoop strain distributions along several axes for 7.2 mils radial interference (load 32,560 lbf) . . . . . 96
5.12	Residual axial hoop strain distributions along several axes at different radial distances for 7.2 mils radial interference (load 37,120 lbf). . . . . 97
5.13	Measured residual axial hoop strain distributions along several axes near a non-coldworked hole (load 18,600 lbf). . . . . 98
5.14	Measured residual axial hoop strain distributions along several axes near a non-coldworked hole (load 23,360 lbs). . . . . 99
5.15	Measured residual axial hoop strain distributions along several axes at different radial distances for 6.5 mils radial interference (load 28,104 lbf) . . . . . 100
5.16	Measured residual axial hoop strain distributions along several axes near a non-coldworked hole (load 32,560 lbf). . . . . 101
5.17	Measured residual axial hoop strain distributions along several axes near a non-coldworked hole (load 37,120 lbf). . . . . 102

FIGURE	PAGE
5.18	Effect of in-plane compression on residual transverse maximum hoop strain distributions at a point on hole boundary (specimen SP2). . . 105
5.19	Effect of in-plane compression on residual transverse maximum hoop strain distributions at a point on hole boundary (Specimen C10). . . 106
5.20	Measured residual transverse hoop strain distributions along several axes at different radial distances for 6.5 mils radial interference (load 5,000 lbf). . . . . 107
5.21	Measured residual transverse hoop strain distributions along several axes at different radial distances for 6.5 mils radial interference (load 10,000 lbf) . . . . . 108
5.22	Measured residual transverse hoop strain distributions along several axes at different radial distances for 6.5 mils radial interference (load 15,000 lbf) . . . . . 109
5.23	Measured residual transverse hoop strain distributions along several axes at different radial distances for 6.5 mils radial interference (load 20,000 lbf) . . . . . 110
5.24	Measured residual transverse hoop strain distributions along several axes at different radial distances for 6.5 mils radial interference (load 25,000 lbf) . . . . . 111
5.25	Measured residual transverse hoop strain distributions along several axes at different radial distances for 6.5 mils radial interference (load 30,000 lbf) . . . . . 112
5.26	Residual transverse hoop strain distributions along several axes for 7.2 mils radial interference (load 18,600 lbf) . . . . . 113
5.27	Residual transverse hoop strain distributions along several axes for 7.2 mils radial interference (load 32,560 lbf) . . . . . 114
5.28	Residual transverse hoop strain distributions along several axes for 7.2 mils radial interference (load 37,120 lbf) . . . . . 115

FIGURE	PAGE
5.29	Effect of in-plane compression on residual axial maximum compressive strain distributions at a point on hole boundary . . . . .117
5.30	Compressive (radial) surface strain distribution near a coldworked hole for 6.5 mils radial interference . . . . .118
5.31	Compressive (radial) surface strain distribution near a coldworked hole for 6.5 mils radial interference (load 15,000 lbf) . . . .119
5.32	Compressive (radial) surface strain distribution near a coldworked hole for 6.5 mils radial interference (load 20,000 lbf) . . . .120
5.33	Compressive (radial) surface strain distribution near a coldworked hole for 6.5 mils radial interference (load 25,000 lbf) . . . .121
5.34	Comparison of experimental results with theoretical predictions of Nadai (41), Hsu and Forman (2), and Adler and Dupree(29).123
6.1	Specimen SPB Moiré fringe pattern . . . . .128
6.2	Moiré fringe pattern for specimen SPB after coldworking hole #1 . . . . .129
6.3	Specimen SPB after coldworking all holes in order 1,2,3,4. . . . .130
6.4	Moiré fringe pattern of holes 2-4 in specimen SPC after coldworking in order 1,2,4. . . .131
6.5	Fringe photograph of holes 1-3 in specimen SPC after coldworking in order 1,2,4,3. . . . .132
6.6	Measured residual compressive strain distribution along an axis .1 inches from the centerline between holes 3 and 4. . . . .133
6.7	Measured residual compressive strain distributions along an axis .13 inches from the centerline between holes 1 and 2. . . . .134
6.8	Measured residual compressive strain distribution along an axis .2 inches from the centerline between holes 3 and 4. . . . .135

FIGURE	PAGE
6.9 Measured residual compressive strain distributions along an axis .06 inches from the centerline between holes 2 and 3. . . . .	.136
6.10 Measured residual compressive strain distributions along an axis .13 inches from the centerline between holes 2 and 3. . . . .	.137
6.11 Measured residual compressive strain distributions along an axis .06 inches from the centerline between holes 3 and 4. . . . .	.138
6.12 Residual hoop strain distribution along several axes after the coldworking of hole #1 for 9 mils radial interference. . . . .	.141
6.13 Residual hoop strain along several axes on the "eastern" side of hole #4 for 6 mils radial interference. . . . .	.142
6.14 Measured residual hoop strain distributions along several axes between holes 3 and 4 for 6 mils radial interference . . . . .	.143
6.15 Measured residual hoop strain distributions along several axes between holes 2 and 3 for 6 mils radial interference . . . . .	.144
6.16 Measured residual hoop strain distributions along several axes between holes 1 and 2 for 6 mils radial interference . . . . .	.145
6.17 Moiré fringe photograph of specimen SPC after coldworking all holes (1,2,4,3). . . . .	.146
6.18 Measured residual hoop strain distributions along several axes between holes 2 and 3 for 6 mils radial interference . . . . .	.147
7.1 SPP after hole coldworking; grating parallel to axis N-S. . . . .	.154
7.2 SPT after hole coldworking . . . . .	.155
7.3 SPP Moiré fringe photography for compressive strain evaluation near plate edge; grating parallel to axis W-E . . . . .	.156

FIGURE	PAGE
7.4 Residual hoop strain distribution along an axis tangent to the hole boundary for 8.9 mils radial interference. . . . .	157
7.5 Measured residual hoop strain distributions along several axes near a plate edge at different radial distances for 8.9 mils interference (Specimen SPP). . . . .	158
7.6 Measured residual hoop strain distributions along several axes near a plate edge at different radial distances for 8.9 mils interference (Specimen SPT). . . . .	159
7.7 Residual hoop strain distribution along an axis 0.24 in. from a plate edge for 8.9 mils radial interference. . . . .	160
7.8 Residual hoop strain distribution along an axis tangent to the hole boundary for 8.9 mils radial interference. . . . .	161
7.9 Measured residual hoop strain distributions along several axes near a plate edge at different radial distances for 8.9 mils interference (Specimen SPE). . . . .	162
7.10 Residual hoop strain along plate edge for 8.9 mils radial interference. . . . .	164
7.11 Peak residual hoop strain along radial line from hole boundary to plate edge . . .	165
7.12 Measured residual hoop strain distributions along specimen edge for various coldwork situations. . . . .	166
7.13 Moiré fringe photograph used in the evaluation of radial compressive strains near a plate edge (specimen SPC) . . . . .	168
7.14 Residual radial strain from hole boundary to plate edge . . . . .	169
7.15 Residual compressive (radial) strain between the plate edge and hole #1 after coldworking the hole #1 only for 6 mils radial interference . . . . .	170

FIGURE	PAGE
7.16 Residual compressive (radial) strain between the plate edge and hole #1 after coldworking at 6 mils radial interference. . .	171
7.17 Residual compressive strain distributions after coldworking. . . . .	172
7.18 Residual compressive strain from hole boundary to plate edge for multi-hole pattern specimen . . . . .	173
7.19 Residual compressive strain distributions after coldworking holes 1,2 and 4. . . . .	174
7.20 Residual compressive strain distributions for holes 2 and 4 after coldworking all holes.	175
7.21 Residual compressive strain distributions after coldworking all holes. . . . .	176

## SECTION I

### INTRODUCTION

Studies of fatigue crack initiation and growth indicate that the distribution of residual strains (stresses) produced by the drawing of an oversized mandrel through a joint fastener hole in a machine assembly markedly improves the fatigue life of the structure (30). This procedure is particularly useful in the aerospace industry where one of the major problems common to today's aircraft is that of structural fatigue beginning at joints. To counter this problem, two of the techniques that have evolved are the fatigue improvement fastener systems--(1) the IFF (interference fit fastener system) and (2) the C/W (cold-working fastener system).

Structures in which flaw-induced fracture may be responsible for failure are easy to find. Among these are tanks, pressure vessels and turbines. In a turbine, for instance, bolt holes in high speed rotating parts, such as the engine fan and compressor disks, act as stress raisers. The local stresses and strains around the hole are higher than the nominal values in the bulk of the material. Flaws, which are always induced by the hole

generation processes, form a focus in a high-stress region for the beginning of crack growth and eventual failure.

Most engineering structures are primarily load-transmitting devices in which high ductility allows yielding in small regions of stress concentration under static or cyclically changing stresses. Thus, ductility and strength are the important considerations in material selection in these situations as an alternative approach to the problem of structural fatigue (36). The material strength is utilized in carrying the imposed loads, whereas stress concentrations are blunted by plastic flow so that crack initiation and failure of the machine part is prevented. This design approach, however, is relatively uneconomical (40).

The manufacturing process of drawing an oversized mandrel through the fastener hole is considered to be one of the most economical and effective (45). The essential principle is the same for the two classes of the fatigue improvement fastener systems. That is, the material around the fastener hole is coldworked and the surfaces adjacent to the hole are left in a state of residual compression.

In order to utilize prestressing effectively, one must understand the relationship between interference induced stress and the subsequent redistribution of stress by applied external loads.

Analytical tools are helpful in understanding interference-induced stress in a few simple cases, but in

practical applications, experimental techniques are needed to gain the required insight.

### 1.1 Purpose and Motivation

The objective of this investigation is to use empirical tools to further our understanding of fatigue-rated cold-work fastener systems, particularly in situations which pose intractable analytical problems.

Three useful application problems are studied, viz.:

- (i) The effects of large compressive in-plane loads on the residual strain field surrounding a coldworked fastener hole.
- (ii) The interaction between the surface strain fields which are created by coldworking a row of holes which are parallel to and near the straight edge of a semi-infinite plate (row of rivet holes).
- (iii) The effects of the straight edge of the semi-infinite plate on the surface strain field and establishing whether coldworking a hole creates a strain climate that could lead to stress corrosion on the straight edge.

### 1.2 Organization

The next section deals with the development of cold-working and residual strains in and around coldworked holes.

Section 2 also contains some of the experimental procedures pertaining to coldworking procedure and an overview of the analytical and experimental approaches to the problem.

Section 3 presents material specifications and specimen preparations procedures.

Section 4 discusses grating photography and optical data processing.

The fifth section tackles the first phase of the project, dealing with the effects of large in-plane compressive loads on the residual strain field.

Sections 6 and 7 deal with the results of the interaction of the surface strain fields for a row of rivets, and the edge effect on the residual strain climate for the multi-hole pattern in an infinite plate.

Section 8 presents the conclusions.

## SECTION II

### DEVELOPMENT OF COLDWORKING RESIDUAL STRAINS IN AND AROUND COLDWORKED HOLES

#### 2.1 Development of Coldworking

The fatigue-strengthening effects of coldworking were accidentally discovered by the Buick Motor Division of General Motors in 1929 (35) where it was noticed that valve springs which had been grit-blasted to remove scale possessed superior fatigue properties.

Today this technique, commonly known as shot-peening, is widely used with gears, connecting rods and springs of all kinds. Forces imparted by the shot-peening operation leave the surface material with a residual compressive pre-stress, whereas the material in the subsurface goes into a state of residual tension pre-stress.

Shot-peening is by no means the only method of imparting residual stresses to a material. In general there are three ways of producing residual pre-stresses,

- (i) chemically,
- (ii) by heat treatment and
- (iii) by mechanical treatment

Chemical methods alter the material composition of the surface layers. Carburizing and nitriding are two of the common processes used in surface hardening of materials.

An example of the second method is flame hardening. Unlike the chemical method, this process does not alter the chemical composition of the material. Rather, its metallurgical structure is changed.

Coldworking, rolling, peening and coining are mechanical treatments for creating residual stresses in a material. These residual stresses (strains) can be thought of as unevenly distributed mean stresses (strains), and they can be viewed as static values upon which alternating loads are to be superimposed.

It was briefly mentioned in Chapter I that the two fatigue enhancement methods for holes are: (1) the IFF, (or Interference Fit Fastener system) and, (2) the C/W, or coldworking system. The IFF is older than the C/W. An example of the IFF is the Taper-Lock bolt. The C/W system seems to be slowly replacing the Taper-Lock bolt because the Taper-Lock is highly sensitive to fastener hole preparation and fastener installation anomalies. Some of these anomalies are installation of a fastener with a fastener-to hole interference level below minimum specifications; and-hole surface conditions--rough finish, scratches, rifling, ovality and bell mouthing. In addition, the

preparation of tapered holes requires great care and skill, and hole and installation factors must be confirmed by extensive and frequent inspection (45).

There are basically four different types of C/W fasteners, viz.:

- (i) the seamless sleeve
- (ii) the split sleeve
- (iii) the EXL Lockbolt and
- (iv) the "Op-One"

In the seamless sleeve method of coldworking holes, a pilot hole is first drilled and then reamed to size. A mandrel and sleeve are then inserted into the hole from either side in the case of the split sleeve method and from the head side in the seamless technique. With the help of a puller nose piece, the mandrel is installed into a puller and the mandrel is pulled through the sleeve and hole.

In the split sleeve technique, the split sleeve is removed from the pilot hole. Final reaming of the hole is made and, after countersinking it, the fastener and nut are installed. Neither removal of the sleeve nor final reaming and countersinking operations are necessary in the seamless sleeve method. (This will be discussed in detail in section 2.2).

Patents for the seamless and split sleeve methods are held by J.O. King, Inc. and Boeing Aircraft, respectively.

Op-One, a process based on a patent held by Lockheed-Georgia Company, is intended as a means of automating the J.O. King seamless sleeve method. A distinctive feature of this process is that part of the mandrel serves as a fastener when the mandrel pull stem is broken away from the fastener portion.

The EXL Lockbolt, patented by Huck Manufacturing Company, is similar to the "Op-One" in that the mandrel portion serves as a fastener when the stem breaks off. Pilot drilling is followed by drilling the hole to size. The "EXL" is then inserted into the hole, a puller is attached and the mandrel pulled through. The pull stem portion of the mandrel is broken off and discarded.

## 2.2 Experimental Coldworking Procedure

The coldworking procedure and apparatus studied in this research is the seamless sleeve method marketed by J.O. King, Inc., 711 Trabert Avenue, N.W., Atlanta, Georgia, 30318. This system was chosen because of its apparent advantages over the other procedures in hole preparation and fastener installation. Figure 2.2.1 shows a schematic of this coldworking process.

The mandrels used are part numbers JK6540-06-188 to 192. These oversized mandrels cause plastic flow at the edge of the hole when they are pulled through, and leave behind residual compressive stresses that aid in the fatigue life improvement of the structure.

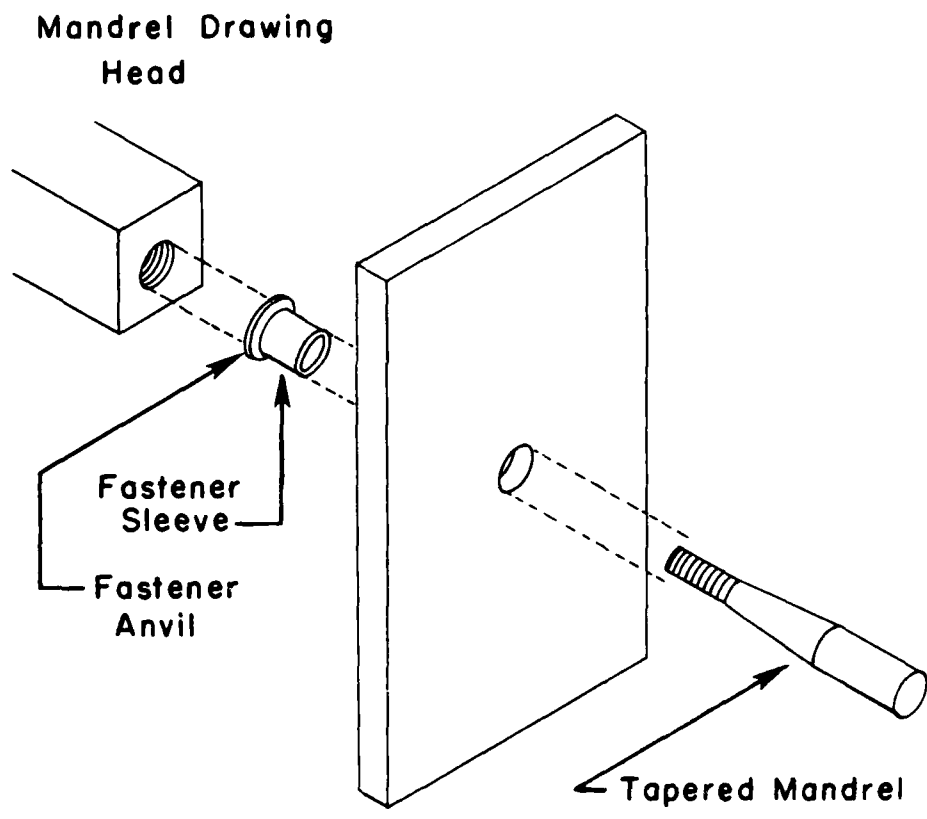


Figure 2.2.1 Schematic of Coldworking Using Mandrel and Sleeve (King Process).

In the experiments, diametral measurements of the tapered mandrels were made before mandrelizing. Likewise, the thickness of the sleeves that were to be inserted into the hole were measured. This was generally accomplished by first measuring their inside and outside diameters with a ball gage and a micrometer. The difference was obtained and used in the computation of radial interference of the hole.

The radial interference was computed as:

$$\frac{\text{Mandrel diam}}{2} + \text{Sleeve Thickness} - \text{Hole Radius.}$$

Uncertainties encountered in the determination of radial interference come from three sources. First, the quantity sought is the small difference between the measured values of large quantities. Second, when the mandrel is pulled through the specimen, a degree of elastic spring-back occurs. Third, the sleeves come with their own anti-corrosion coating and lubricant on the outside and inside. Since the lubricant coating has uneven thickness, the sleeve thickness is not constant.

Two set-ups were employed in this coldworking procedure. The first is shown in Figure 2.2.2. Only one specimen was coldworked on this set-up, where pulling force is provided by a hydraulic ram in a small table top testing frame. The rest of the specimen were mandrelized in an Instron testing machine.



In the first set-up, a sleeve that was carefully cut to match the thickness of the specimen was first inserted into the hole with its collar on the unpolished side of the specimen. The specimen was then laid on the base with the grating side upwards and a mandrel inserted into the hole, small end first. The ram of a double acting 2-ton capacity hydraulic jack was then clamped to the threaded end of the mandrel underneath the bench. The hydraulic jack was then pressurized to pull the mandrel through, thus coldworking the specimen.

The sleeve for this particular specimen was not lubricant coated, so molybdenum disulfide grease (Molycote) was applied to the stem of the mandrel to prevent seizing and galling of the hole sides.

The other set-up used was an Instron testing machine, Figure 2.2.3. A Sanborn Twin Viso - Cardette recorder was used to monitor the mandrel pulling force via strain gages attached to a tension rod linking the mandrel to the machine's crosshead. This force was recorded as a function of the mandrel displacement during the coldworking operation. The mandrel drawing rate was set at 0.5 cm/min.

In this investigation several coldworking levels were used. The values chosen depended on the mandrel sizes available.

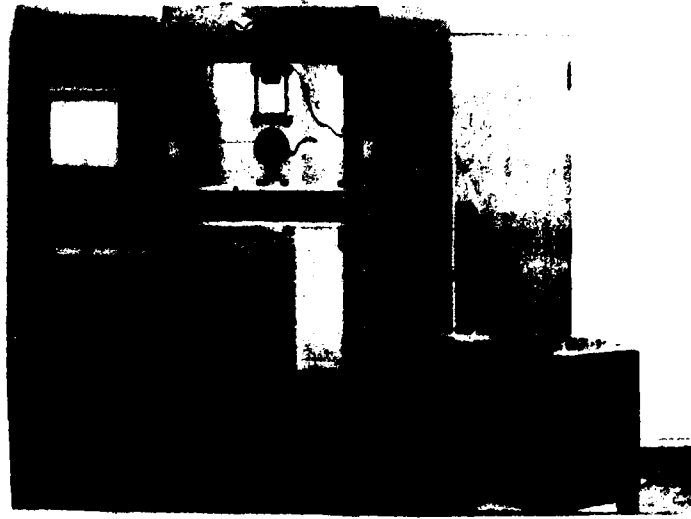


Figure 2.2.3 The Instron Coldworking Set-up.

## 2.3 Residual Strains In and Around Coldworked Holes

### 2.3.1 Introduction

Although strength and stiffness are customarily computed based on the elastic properties of the member, it is a well-known fact that at some highly stressed areas, for example, around fasteners in aircraft structural components, the stresses do exceed the theoretical elastic limits of the materials without necessarily causing structural damage (5). One of the major problems facing the structural designer is to obtain the most efficient strength-to-weight ratio around these highly critical areas. The problem is highly complex and does not lend itself to straightforward analytical solutions.

This is not to say that analytical efforts to understand the problem are lacking. Rather, theoretical solutions have been advanced by various authors. These will be discussed in the next section.

### 2.3.2 Analytical Approaches to the Problem

This section presents an overview of the analytical work which has been published in the general area of cold-working holes. None of these theories apply directly to the problem under investigation here since the present problem is highly nonlinear and because of its complex geometrical boundary conditions.

Probably the simplest of all analytical theories is the case where the mathematical assumptions boil down to treating the problem as being linear. Deductions for the finite specimen are then based on linear elasticity. In some cases, the specimen is treated as an infinite sheet, treating the problem of the hole in the finite-width specimen as a small hole in an infinite plate with a state of plane stress existing everywhere in the sheet on loading the specimen (40).

Some theories assume that the material unloads elastically with no reverse yielding when the mandrel is drawn all through. Still other theories neglect work-hardening effects during the coldworking of the specimen (2).

Figure 2.3.1 presents a simple specimen model which is of some importance in practice. The fundamental equations of elasticity in the given coordinate system take the following form:

$$\sigma_{\theta} - \sigma_r - r d\sigma_r/dr = 0 \quad (2.1)$$

which is the differential equation of the equilibrium state for an element of volume in the wall of the tube. Here

$\sigma_{\theta}$  is the circumferential stress,

$r$  is the distance from the axis of the cylinder,  
and

$\sigma_r$  is the radial stress.

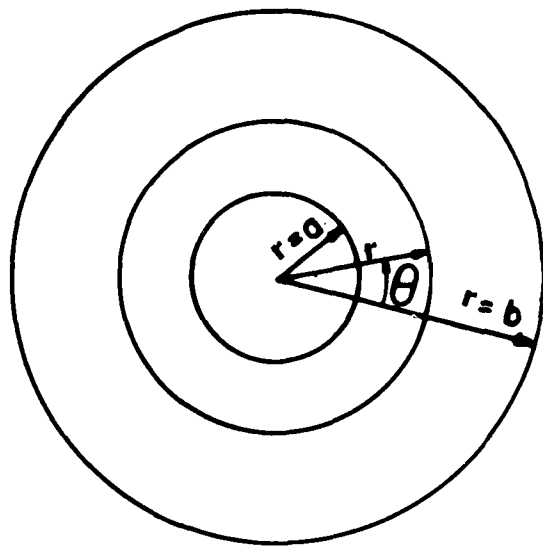


Figure 2.3.1 Geometry and Coordinate System Used in Coldworked Hole Theories.

Equation (2.1) is applicable to all states of the material be it elastic or plastic.

The assumption of an infinite specimen would then imply that "b" is infinitely large and thus  $a \ll b$ .

Because of the loading nature of the hole, assuming uniform radial mandrelizing the problem simplifies to being symmetric about the longitudinal axis. Thus the strains are given by (38):

$$\epsilon_r = \frac{\partial u}{\partial r} \quad (2.2)$$

$$\epsilon_\theta = \frac{u}{r} \quad (2.3)$$

where  $u$  is the radial displacement of an element originally located by  $r, \theta$ . The radial displacement  $u$  satisfies the compatibility equation.

$$\epsilon_r = \frac{d(r\epsilon_\theta)}{dr} \quad (2.4)$$

For an elastic radial displacement, Little (21) shows that the stress, strain and the displacement fields are given by:

$$\sigma_r = C \left\{ \frac{-1}{r^2} + \frac{1}{b^2} \right\} \quad (2.5)$$

$$\sigma_\theta = C \left\{ \frac{1}{r^2} + \frac{1}{b^2} \right\} \quad (2.6)$$

$$\epsilon_r = \frac{C}{E} \left\{ -\frac{1+\nu}{r^2} + \frac{1-\nu}{b^2} \right\} \quad (2.7)$$

$$\epsilon_\theta = \frac{C}{E} \left\{ \frac{1+\nu}{r^2} + \frac{1-\nu}{b^2} \right\} \quad (2.8)$$

$$u = \frac{C}{E} \left\{ \frac{1+\nu}{r} + \frac{(1-\nu)r}{b^2} \right\} \quad (2.9)$$

where

$$C = \left[ \frac{Eu_a}{\frac{1+\nu}{a} + \frac{(1-\nu)a}{b^2}} \right]$$

a = hole radius

b = radius of the stress free external surface

E = Young's modulus

$U_a$  = the radial displacement at  $r=a$

$\nu$  = Poisson's ratio

Plasticity considerations must be made when the radial displacement exceeds  $U'_a$ , where

$$U'_a = \frac{\sigma_y}{E \left( \frac{1}{b^4} + \frac{3}{a^4} \right)^{\frac{1}{2}}} \left( \frac{1+\nu}{a} + \frac{(1-\nu)a}{b^2} \right) \quad (2.10)$$

where  $\sigma_y$  is the yield stress of the material as determined in a standard tensile test.

Swainger considered this problem with the assumption that the large plate with a circular hole was in a state of plane stress (43). Furthermore he assumed uniform radial pressure loading on the hole and yielding of the plate material according to the energy of distortion theory--the Mises-Hencky criterion:

$$2\sigma_y^2 = (\sigma_\theta - \sigma_r)^2 + (\sigma_\theta - \sigma_z)^2 + (\sigma_z - \sigma_r)^2 \quad (2.11)$$

where  $\sigma_\theta$  is the hoop stress or circumferential stress

$\sigma_z$  = the longitudinal stress and

$\sigma_r$  = the radial stress

The details of his method of approach and all the assumptions that he made can be found in reference (43).

Extension of these ideas, which form the transition from elasticity to plasticity, is based on different theories of plastic flow. For our purpose here, it suffices to consider only two of these: viz., the maximum shear and the energy of distortion theories.

According to Tresca, or maximum shearing stress theory, yielding will begin when the maximum shearing stress is

$$\tau_{\max} = \frac{1}{2} (\sigma_{\max} - \sigma_{\min}) = \frac{1}{2} \sigma_y \quad (2.12)$$

where

$\sigma_{\max}$  = maximum principal stress,

$\sigma_{\min}$  = minimum principal stress, and

$\sigma_y$  = the yield stress of the material as determined in a standard tensile test= twice the flow stress.

According to (2.12) plastic flow occurs whenever the difference between the largest and smallest principal stresses is equal to the flow stress,  $\frac{1}{2}\sigma_y$ .

In the specimens under consideration here, the longitudinal stress is zero, the radial stress  $\sigma_r$  is always negative and the hoop stress or circumferential stress is always positive. This is true during mandrelizing only. Afterwards  $\sigma_\theta$  is negative although  $\epsilon_\theta$  is positive. Thus  $\sigma_\theta$  is the largest principal stress and  $\sigma_r$  is the smallest. The condition of yielding during coldworking can be expressed as (2.12) or simply

$$\sigma_\theta - \sigma_r = \sigma_y \quad (2.13)$$

According to the Mises-Hencky or energy of distortion theory, the condition of yielding is

$$2 \sigma_y^2 = (\sigma_\theta - \sigma_r)^2 + (\sigma_\theta - \sigma_z)^2 + (\sigma_z - \sigma_r)^2 \quad (2.14)$$

But because the longitudinal stress  $\sigma_z = 0$ , Eq. (2.14) reduces to

$$2 \sigma_y^2 = (\sigma_\theta - \sigma_r)^2 + \sigma_\theta^2 + \sigma_r^2 \quad (2.15)$$

Nadai (41) utilized a linearized approximation form of this energy of distortion theory (Mises-Hencky criteria) to solve the plate problem. His other assumptions were

- (1) uniform pressure at the edge of the hole and
- (2) a perfectly plastic material response. He calculated the stress and displacement fields to be:

$$\sigma_r = \frac{\sigma_y}{\sqrt{3}} \left( -1 + 2 \ln \frac{r}{r_p} \right) \quad (2.16)$$

$$\sigma_\theta = \frac{\sigma_y}{\sqrt{3}} \left( 1 + 2 \ln \frac{r}{r_p} \right) \quad (2.17)$$

$$U = \frac{\left( \frac{3}{2} \right)^3 U_a' \frac{r}{r_p}}{\left\{ \frac{3}{2} + \ln \frac{r}{r_p} \right\}^3} \quad (2.18)$$

where  $r_p$  = the interface between the elastic and plastic regions.

In 1948, however, S. Taylor (42) developed essentially the same equations as Nadai's for the case of a thin plastic sheet.

Likewise Hsu and Forman (2) in 1975 making use of the Mises-Hencky yield criterion and assuming uniform pressure at the hole and a Ramberg-Osgood characterization of the stress-strain curve obtained basically the Nadai formulae. They considered an infinite sheet with a circular hole subjected to internal pressure, P. Their solution was based on  $J_2$  deformation theory together with a modified Ramberg-Osgood law, viz.:

$$\begin{aligned} \epsilon &= \sigma/E \quad \text{for } |\sigma| \leq \sigma_y \text{ and} \\ \epsilon &= \left( \frac{\sigma}{E} \right) \frac{\sigma^{n-1}}{\sigma_y^{n-1}} \quad \text{for } |\sigma| \geq \sigma_y \end{aligned} \quad (2.19)$$

where E,  $\sigma_y$  and n are the Young's modulus, the yield stress and the parameter defining the shape of the uniaxial stress-strain curve and is equal to or less than 17.

Carter and Hanagud (46) in 1974 attempted the solution of this problem based on the Tresca yield condition and elastic-plastic material behavior. Based on these conditions they proceeded to seek a relationship between the displacement and the elastic-plastic boundary and arrived at the result:

$$U_a = U'_a + \frac{\sigma_y}{2E} \left( 3 - \nu \right) \frac{a}{2} \left( \frac{r_p}{2} - 1 \right) - 2(1 - \nu) a \ln \left( \frac{r_p}{a} \right) \quad (2.20)$$

Besides the analytical work mentioned here, numerical and finite element methods have been attempted.

Adler and Dupree (29) developed a finite-element model idealization to determine the stress states for a cold-worked fastener hole. They used a Ramberg-Osgood relation:

$$\bar{\epsilon}_p = \left( \frac{\bar{\sigma}}{K} \right)^n \quad (2.21)$$

in their development of the constitutive behavior of the material. Here  $\bar{\epsilon}_p$  is the equivalent plastic strain for an equivalent stress state  $\bar{\sigma}$ , a state of stress that comes from employing the Von Mises yield criterion Eq. (2.12) for the case of plane stress and is defined as

$$\bar{\sigma} = \sqrt{\sigma_x^2 + \sigma_y^2 + 3\tau_{xy}^2} \quad (2.22)$$

Parameters K and n took the experimentally determined values of 87.5 and 54 ksi respectively.

Even though their finite element analysis attempted to model a 0.25 in. (6.35 mm) thick 7075-T6 aluminum specimen similar to the ones employed in this study, the loading conditions differed. Their program was based on uniaxial tension loading after coldworking, whereas, for this study compressive loads were considered with coldworking levels slightly higher than those used by Adler and Dupree. Nevertheless, their results are shown in Figure 5.34 to permit a comparison of the results later.

The interaction between surface strain fields at the edge of a plate and the effect of that edge on the strain field have no analytical or numerical solution in the literature.

### 2.3.3 Discussion of Theoretical Studies

None of the analytical work mentioned above predicts the strains very well. Furthermore, the general underlying assumptions for all these theories, that the plate is infinite in extent with a state of plane stress, is not satisfactory, especially in the case where the fastener hole is located close to a plate edge.

It is also noted that there is some degree of variation in the results obtained by the earlier investigators

due to differing assumptions concerning the constitutive material representation and the assumed mode of yielding.

Nevertheless for modeling practical coldworking operations the analytical work is useful, providing reasonable predictions in areas removed from the hole boundary.

#### 2.4 Overview of Experimental Studies

The experimental work that has been performed in this area is relatively recent.

Adler and Dupree (29) in 1974 evaluated the stress and strain distributions around an initially coldworked hole in a plate and the subsequent redistribution of the stresses and strains when the plate was subjected to a uniform tensile loading.

Sharpe (44) and Chandawanich and Sharpe (40) investigated the change of residual strain during crack initiation, the stress intensity factor for the crack emanating from a circular hole and the strain ahead of a crack tip. Cloud (24) 1978, measured surface strain distributions in the vicinity of holes in  $\frac{1}{4}$  in (6.35 mm) thick aluminum alloy plate which had been coldworked to various degrees by the J.O. King commercial process. He focussed his attention mainly on radial strains, and measuring hoop strains at two coldworking levels.

## SECTION III

### MATERIALS AND SPECIMEN PREPARATION

#### 3.1 Material Specification and Specimen Preparation

The material used in this investigation is structural material from a sheet of 7075-T6 aluminum alloy  $\frac{1}{4}$  inch (6.35 mm) thick made by Aluminum Company of America (ALCOA).

There were three types of specimen. Part One of the experiments was a study of the effects of large in-plane compressive loads upon the residual strain field surrounding a coldworked fastener hole. Two specimens, measuring 4.5 in. (11.43 cm) long and 2.5 in. (6.35 cm) wide, were fabricated according to the design shown in Figure 3.1.1. The length dimension was larger than the width so that the moiré grid printed on its surface would not be damaged during load applications. The hole design diameter was 0.261 inches (6.63 mm).

Various methods of hole preparation, including drilling with honing and drilling with reaming, were tried out in the beginning of the investigation. The best procedure involved drilling the specimen hole undersize and then boring to size with an adjustable boring tool. Hole size

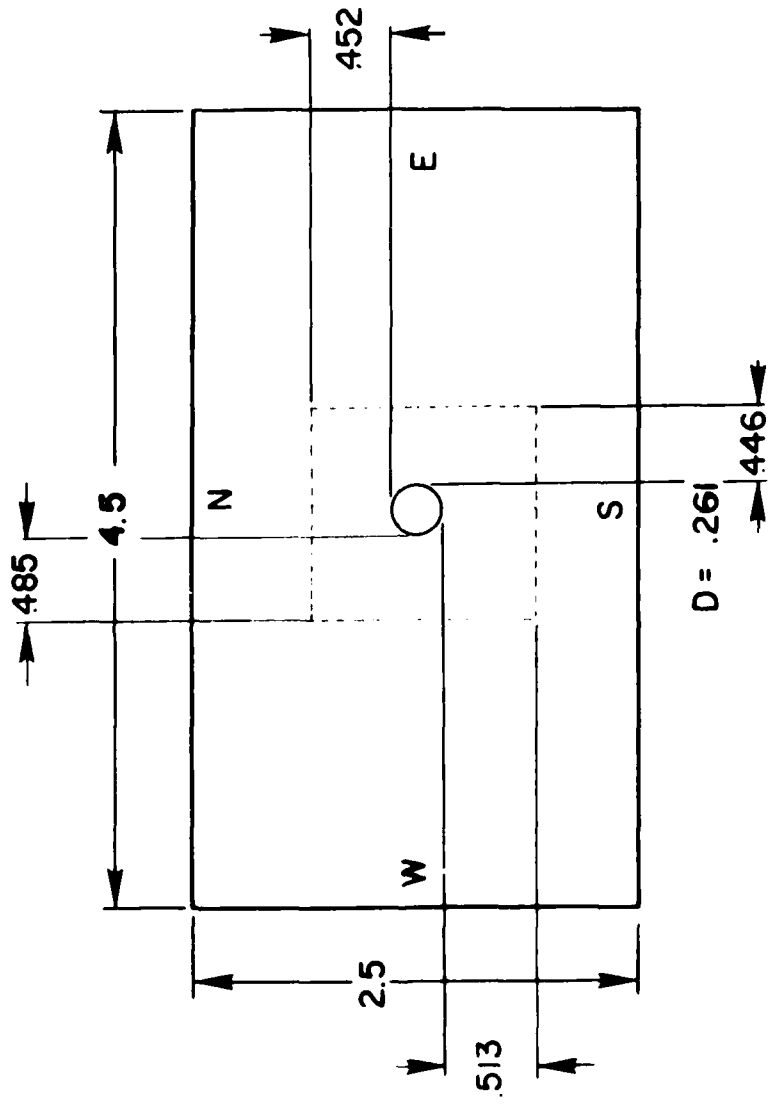


Figure 3.1.1.1 Dimensions and Fiducial Mark System of the In-Plane Compressive Overload Specimen; Dimensions in Inches.

checking was done with an adjustable ball gage and micrometer and a microscope.

Table 3.1 shows the hole diameter measurements. The figures in the table indicate that this measurement deviated from the nominal diameter by  $+ 0.0006$  in ( $+0.015$ mm)  $- 0.0002$  in ( $-0.005$ mm)

A microscope equipped with an x-y stage was used to verify the diametral and fiducial measurements of the specimens. Difficulties in locating the edge of the hole in this fashion led to differences in the measured values.

Second and third specimens were designed to determine the effects of an edge upon the surface strain distribution and/or the interactions between the surface strain fields which are created by coldworking two or more fastener holes which are near each other. The configuration and dimensioning of such specimens (including a multi-hole pattern) are shown in Figure 3.1.2 and 3.1.3. In these specimens, attention was focused upon the edge distance/diameter or e/d ratio. Here "e" is defined as the distance between the edge of the plate and the hole center. An e/d ratio of 2.0 is used in the design of aircraft structures as a working minimum, and it is believed that lower ratios degrade fatigue life (24). The e/d ratios used were chosen to be on either side of the threshold value of e/d = 2.0, viz., e/d = 1.8, e/d = 2.25, and at the threshold value of e/d = 2.0.

TABLE 3.1 TYPICAL DIAMETRAL MEASUREMENTS AT THREE ANGULAR LOCATIONS 0°, 45° AND 90° FROM THE HORIZONTAL LINE (SP2)

TRIAL	HOLE DIAMETER		
	0°	45°	90°
1	0.2615	0.2615	0.2610
2	0.2616	0.2606	0.2611
3	0.2620	0.2611	0.2610
4	0.2608	0.2612	0.2605
5	0.2610	0.2619	0.2611
6	0.2618	0.2610	0.2610
7	0.2619	0.2622	0.2612
8	0.2617	0.2619	0.2610
9	0.2615	0.2620	0.2609
10	0.2620	0.2610	0.2610

Average Hole Diameter = 0.2613 (6.637 mm)

(Measurements by microscope)

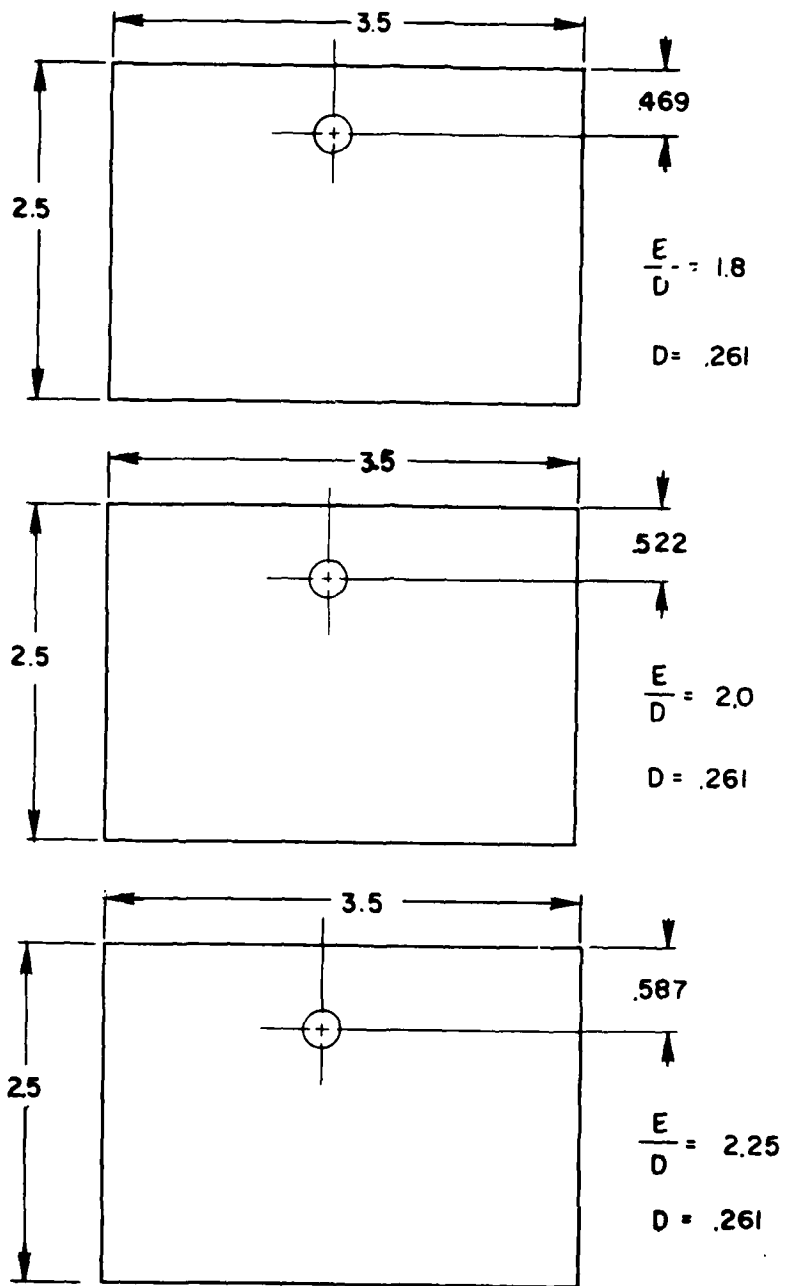
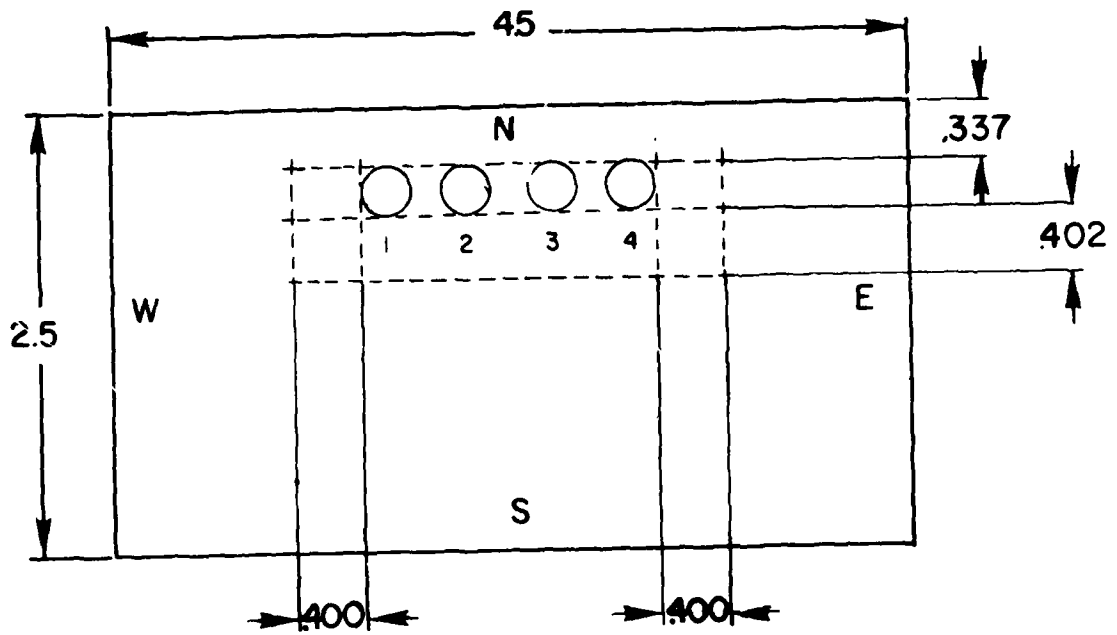


Plate Edge Effect Specimens

Figure 3.1.2 Dimensions and Fiducial Mark System of the "Plate Edge Effect Specimens;" Dimensions in Inches.



Hole Separation  
 = 1.75 D  
 D = Hole Diameter

Figure 3.1.3 Dimensions and Fiducial Mark System of the "Hole Interaction" and "Plate Edge Effect" Specimen; Dimensions in Inches.

The preparation of the holes followed essentially that described for the in-plane load study. The main goal was to obtain holes which were not tapered and whose sides were square and straight so as to permit easy determination of the amount of coldworking that was to be subsequently imposed. Table 3.2 shows a representative sample of the diametral measurements for this part.

Reference marks were scribed on all the specimens. These fiducial marks took various forms as the experiment progressed and as more experience was attained. The first method adopted was the machinists' technique of gaging and scribing with a vernier height gage placed on a smooth flat surface. To avoid disturbing the strain distributions the scribed marks were made extremely light. These marks tended to disappear in the final photographic prints of the specimens.

For the majority of the specimens, a number of "natural" fiducial points, such as edges far removed from the influence of the mandrelizing process, were identified with "prestyle" lettering to aid as fiducial marks. In addition, line rulings on master gratings printed on the specimen were included and located as part of the fiducial marks system. Since it was always possible to locate at least one of these markings, these several forms of fiducial marks tended to facilitate data collection. In some cases, the redundant markings provided a good way of double-checking

TABLE 3.2 TYPICAL DETERMINATION OF RADIAL INTERFERENCE  
(in.) FROM REPEATED DIAMETRAL MEASUREMENTS (SPP)

Trials	Mandrel Diameter (in)	Sleeve Diameters		Hole Diameter
		Inside Diameter	Outside Diameter	
1	0.2590	0.2385	0.2546	0.2615
2	0.2585	0.2375	0.2539	0.2616
3	0.2595	0.2385	0.2540	0.2617
4	0.2590	0.2375	0.2550	0.2615
5	0.2594	0.2376	0.2540	0.2615
6	0.2580	0.2372	0.2551	0.2612
7	0.2582	0.2380	0.2549	0.2616
8	0.2590	0.2379	0.2550	0.2605
9	0.2583	0.2381	0.2545	0.2616
10	0.2587	0.2375	0.2542	0.2619

Average sleeve thickness = 8.3 mils (0.211 mm)

Average outside diameter of sleeve = 0.2552 in. (6.48 mm)

Average inside diameter of sleeve = 0.2378 in. (6.04 mm)

Mandrel average diameter = 0.2587 in. (6.57 mm)

Radial Interference = 6.2 mils (.158 mm)

(Measurements by microscope)

specimen measurements from the enlarged photographic prints of moiré fringe patterns.

When the diametral and fiducial measurements were completed, the specimens were lapped on a Lap Master model 12C machine manufactured by the Crane Packing Company of Illinois. Before machine lapping was introduced the specimens were successively lapped with a 350 or 240 emery cloth followed by a 400 and 600 grit metallurgical preparation paper dipped in mineral spirits to serve as a lapping fluid. These operations were done on a flat surface. The flat lapped surface of each specimen was then polished. The final polishing was performed on spinning metallurgical polishing wheels with 1 and then .3 microns alumina particles suspended in oil as the abrasive. Acetone was then sprayed over the surface to degrease it. The specimen was then ready for printing of a moiré grating on the polished surface.

### 3.2 Moiré Submaster Grating Production

The production of submaster copies of high frequency gratings has been explored and discussed by several authors including Luxmoore and Herman (18), Holister (37) and Cloud (24).

The 1000 lpi (39.4 lines/mm) master gratings used for the production of the various submasters were purchased from Photolastic Inc., Malvern, PA, and from Graticules

Limited, Sovereign Way, Towbridge, Kent, U.K. The set-up for reproduction is shown in Figure 3.2.1. The figure indicates that the light source was a Mercury arc lamp placed approximately 11 in. (27.94 mm) from a green Kodak Watten filter #74. A plane mirror folded the light beam through an angle of  $90^0$ . Between the mirror and the master plus photosensitive plate assembly was placed a collimating lens having 39.37 in. (1 meter) focal length. Both Kodak HRP and Kodak 649F plates were tried for submaster production. Exposure time of .5 sec. to 1 sec. gave the best results with development times of approximately 3.30 min. in D-8. Fixing was done in Kodak Rapid Fixer solution for about 5 minutes.

To establish correct grating mismatches, it was found necessary to produce a set of submasters other than the 1:1 contact copies described above. Four different grating groups were made. The first category comprised those submasters clustered around 1000 lpi (39.4 lines/mm). The remaining three groups were clustered around 960, 980, and 1500 lpi (37.8, 38.6, 59.1 lines/mm). In each category, spatial frequency deviations ranged from  $\pm 2$  to  $\pm 8$  lpi (.1 to .3 lines/mm).

Figure 3.2.2 shows the submaster grating production set-up. A Schneider Xenar 1:4.5 350 mm focal length lens at f/11 was used, and a Besler enlarger light head served as a source with a circular diffuser placed between the light source and master. Although the resolving power of

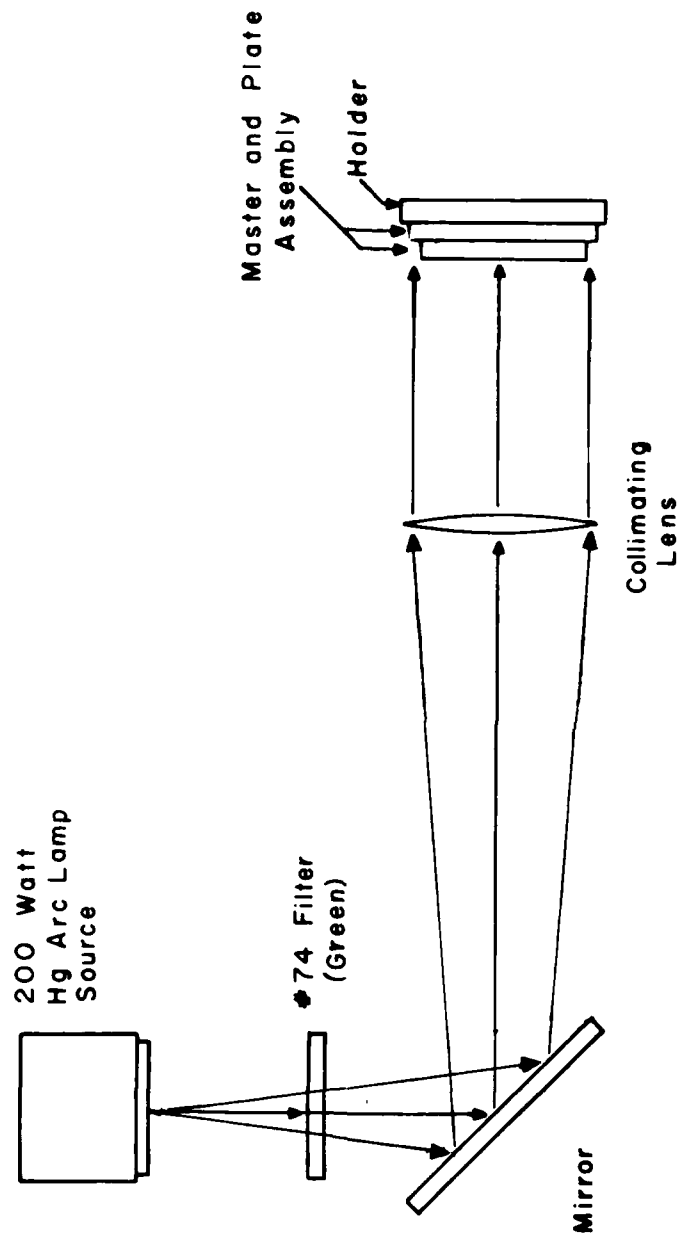


Figure 3.2.1 Optical System for Contact Copying Submaster.

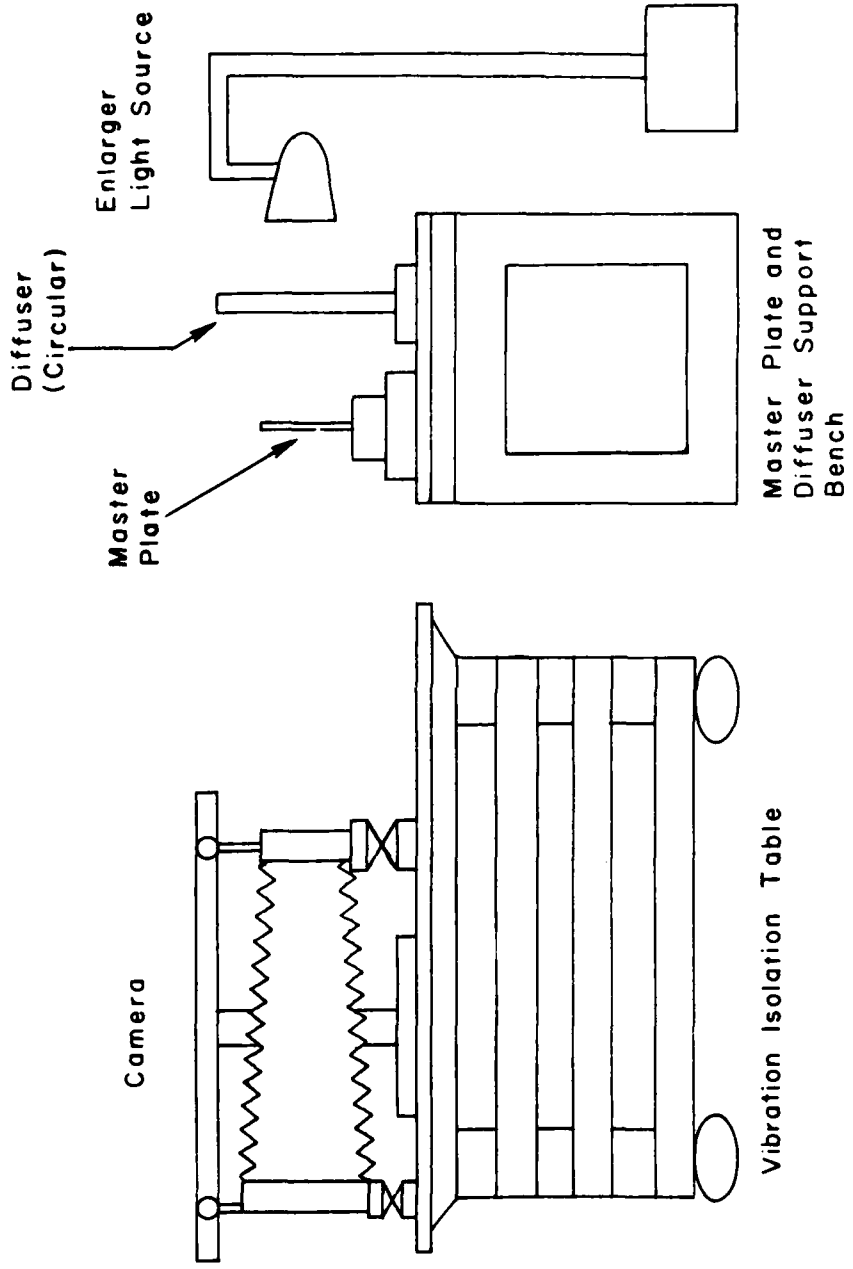


Figure 3.2.2 System for Grating Submaster Production.

the whole system was barely adequate, working submasters were obtained.

Most of the photo copying was done on Kodak HRP (High Resolution Plates) exposed for 57 sec. and developed for 2 minutes in D-8 and fixed for 3 minutes in Kodak Rapid Fixer. Kodak type 649F spectroscopic plate was also used, but it did not seem to work as well for this purpose as the Kodak HRP plates.

For high density copying, precise focusing of the image is crucial. A 50X microscope made by Bausch and Lomb was used as an aid in focusing.

The grating pitch values mentioned above are a multiple of the fundamental spatial frequency of the specimen grating images as determined by the 1000 (lpi) (39.4 lines/mm) grating divided by the base magnification used. In addition to this base pitch, negative and positive frequency mismatches are introduced by changing the base magnification slightly. The procedure for focusing at the correct magnification is as follows. After the rough determination of camera-to-master separation, an image of the master was brought to a focus in the back of the camera on ground glass. At this point a rough check on the desired submaster frequency was made. The image was focused "permanently" in a plane which remained fixed with respect to the lens. The ground glass was then removed and, by use of the microscope, the precise location of the ariel image was established.

With the microscope in place, a blank undeveloped photo-plate having scratches in its emulsion was put in the back of the camera. By moving the camera plate holder back and forth, the scratches on the plate were brought into the same focal plane as the master image.

Best results were obtained at an aperture of  $f/11$ . Vignetting and cosine light fall-off were troublesome. The quality of the submaster was always checked during processing by observing its diffraction characteristics under a pen pocket light or by holding it up to bright room fluorescent light. In a number of cases the quality of the finished submasters was checked by observing the grating lines under a microscope.

It was important that the table supporting the camera had to be as vibration free as possible. Air bags were used to isolate the cast iron bench from mechanical disturbances.

### 3.3 Grating Frequency Measurement of Submasters

Strain determination by use of the manufactured submasters requires knowledge of the spatial frequency of master and submaster. Initially the spatial frequency of a submaster was determined by means of dial gage indicators and a microscope. Repeated measurements by this method tended to vary widely. Since an error of even  $\pm 2$  grating

lines/1000 lpi could result in strain measurement error, the method was discontinued.

Next, the diffraction characteristics of the sub-master were used in the determination of their spatial frequencies. Figure 3.3.1 shows the basic optical system. The first lens collimates the beam and the second lens acts as a transform lens. An array of images of the source appear in the focal plane of the field lens. Each of the image sources is comprised of all the rays that emerge from the pair of grating in a specific direction. This will be explained in detail in Section 4.3 These images on the screen are in the form of a dot pattern called "ray groups" or diffraction orders--thus are obtained the 0,  $\pm 1$ ,  $\pm 2$ , . . . diffraction orders. Separation between successive images is approximately  $\frac{\lambda F}{d}$  where

$\lambda$  is the wavelength of the monochromatic light used,

F is the focal length of the decollimating lens, and,

d is the basic pitch of the gratings.

The laser employed was a He-ne HN7 Laser by Jodon Engineering of Ann Arbor, MI. With some modifications the distance between the diffraction orders was calculated from the formula:

$$d = \frac{D \lambda}{x} \quad (3.1)$$

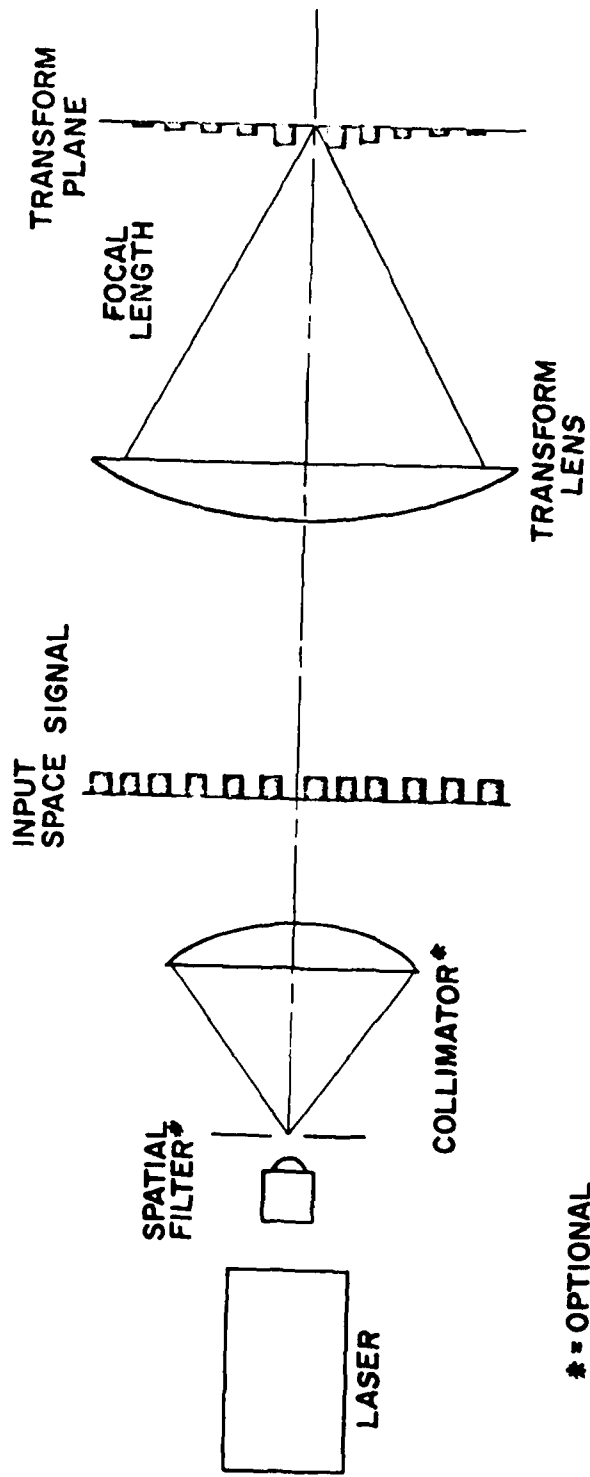


Figure 3.3.1 Optical Creation of Fourier Transform of Input Signal in the Form of a Transparency.

where

- D is the distance between the submaster and the paper screen,
- $\lambda$  is the wavelength of the monochromatic laser light - 6328A =  $2491.3 \times 10^{-8}$  cm.,
- d is the pitch of the submaster grating, and
- x is the separation distance between the diffraction orders.

This method proved to be very successful.

### 3.4 Specimen Gratings

#### 3.4.1 Photoresists

Photoresists and their applications have been explored by Luxmoore and Herman (18), Holister (37), and Cloud (24). Here the discussion is limited to the way they were adapted and modified to suit the current problem under investigation. The photoresist (or acid-resist) employed in this study was AZ-1350B (AZO Plate) purchased from Shipley Co., Inc., Newton, Mass. It is a polymeric emulsion sensitive to ultraviolet light that leaves a pattern of clear and resist-protected areas on the specimen surface after development. There are two types--negative resists which produce a nonsoluble exposed pattern, and positive resists which cannot be dissolved by the developer until after exposure; the latter was used in this experiment. The AZ-1350 type was chosen because of its high resolving power; the manufacturer claims that line widths of  $2 \times 10^{-8}$  in. ( $.508 \times 10^{-6}$  mm) have

been reproduced with this resist. The manufacturer's data specify that maximum resolution (line/in) exceeds 2500, (98.4 lines/mm). Drying time recommended is 1 hr. at 40°C, exposure duration to radiation for maximum line density is set at 4 min., and development times are around 2 min. The resist comes with a thinning solution and a resist remover.

### 3.4.2 Photoresist Application

The lapped, polished and degreased surface of the specimen, including the sides of the hole, was cleaned thoroughly with cotton swabs dipped in methyl ketone or acetone. The specimen was allowed to dry for approximately 15 min.

There are a number of ways of applying the resist to the metal surface, among them spraying, dipping, wiping, spinning, painting, and roller coating. Whatever method is employed, the ultimate goal is to obtain an even, thin coating of the photo resist with no build-up around the edge, the critical area under study.

In the early stages of the experiment, an artist's airbrush was used. Its use tended to be tricky since a good coating depended on many variables including the spray geometry, the distance of the spraying nozzle to the surface, the number of passes for a given specimen, the average time taken per pass across the specimen and the viscosity of the photoresist. It was necessary that the gun be held

at least 14 in. (35.6 cm) from the specimen surface, with 3 or 4 strokes across the entire surface taken slowly at constant speed. Sometimes by merely dipping a fluffed Q-tip into a photoresist solution and applying it first one way across the surface, and then, with another dry Q-tip, spreading the deposited photoresist at an angle  $90^{\circ}$  to the first pass proved functional, though the results tended to be not quite as good. It was later found that a combination of some of the above techniques produced the most desirable coating. Since high resolution demands a thin uniform coating, spraying and then spinning proved to be the best way.

Bubbling of photoresist on the surface was an indicator of excessive viscosity which called for thinning--1 part thinner to 5 parts resist seemed to work well. If coating thickness was deemed too thick, exposure and development times needed to be increased accordingly.

It is recommended that the resist thickness should not exceed the line width to be printed (18). In some cases, however, thicker coatings were deliberately introduced, since on exposure to the mercury lamp, thinner coatings tended to leave a bare area near the hole ranging from approximately .001 - 0.008 in. (.025 - 0.2 mm) wide all around. Thicker coatings could be built up by applying several thin coatings successively and allowing a suitable drying time between applications.

Securing a perfect coating was not automatic. At times eight or even ten trials were required. Removal of the bad coating was done with acetone. In fact, coating characteristics tended to increasingly get better with several trials. After the specimen was properly sprayed, it was baked at 90<sup>0</sup> C for approximately 25 min.

### 3.5 Printing and Development of Specimen Gratings

The coated and baked specimen was allowed to cool, and then it was taken for printing a moiré grating into the photoresist by a contact printing procedure. A grating submaster was clamped to the specimen and the assembly exposed to ultraviolet light radiation from a 200 watt Mercury lamp placed 21 in. (53.34 cm) from that submaster-specimen assembly as shown in Figure 3.5.1. Clamping of the submaster to the specimen, emulsion to emulsion, was accomplished by using ordinary spring type clothes pins. It was important to clamp the assembly in perfect alignment. Lenticular effects in the submaster were ignored, and no index-matching solution was used between the submasters and the photoresist.

Exposures tended to center around 3-5 min. To determine exposure duration, a narrow exposure test area on the side of the specimen far removed from the important study area was used with checking intervals of 3, 3½, 4, 4½ and 5 min.

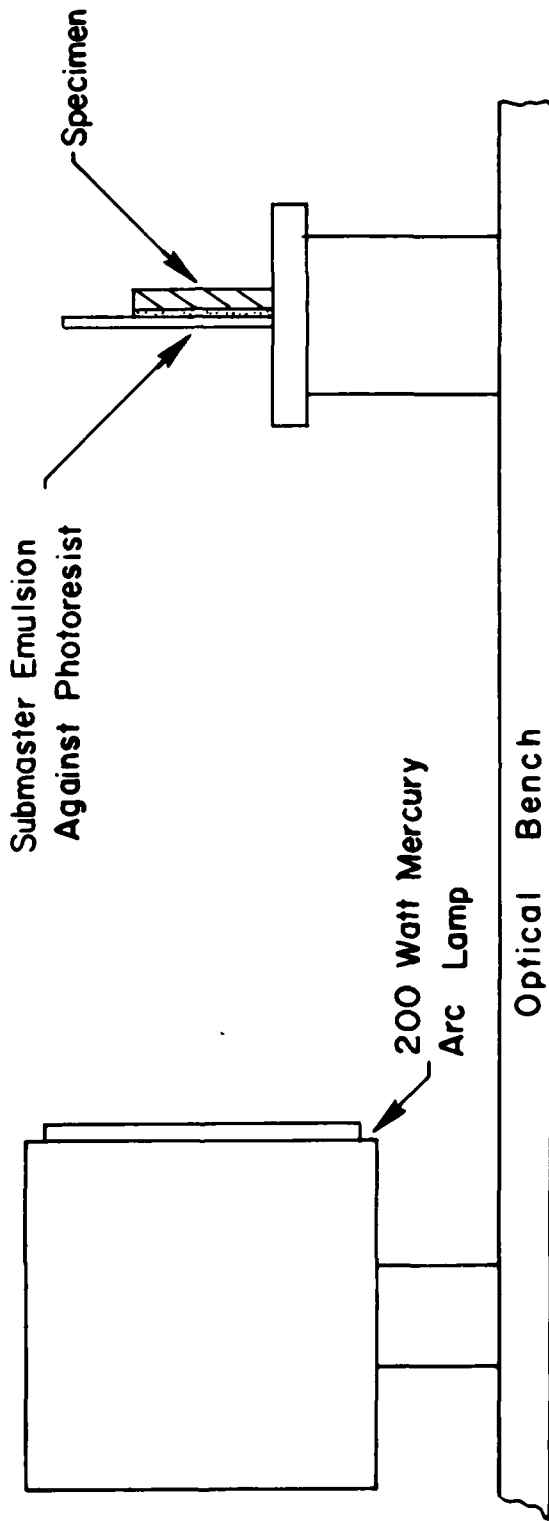


Figure 3.5.1 Optical System for Printing Grating on Specimen.

Development of the exposed specimen photoresist followed with an AZ developer provided for AZ 1350B photoresist. Development times centered around 45 seconds. Longer development times tended to produce the same ill-effect as those observed when specimen photoresist was over-exposed.

The recommended strength of the developer was obtained by diluting the concentrated developer in the ratio 1:1 with distilled water; ordinary tap water was used. Immediately after development, the specimens were rinsed under running tap water for a few minutes and then were allowed to dry in open air.

Half of the specimens in this investigation were exposed twice to obtain a dot pattern for strain measurement in two perpendicular directions. The dot pattern was produced by rotating the submaster  $90^{\circ}$  with respect to the specimen and exposing a second time; the duration of the second exposure was a little more than one-half of a single exposure.

One more point deserves special emphasis. It was imperative that the specimen and submaster gratings were in contact with each other during exposure to avoid unwanted mismatch. To double check this, the developed specimen grating and the 1000 lpi (39 lines/mm) submaster were superimposed and rotated in the direction of decreasing fringe

spacing. Complete disappearance of the fringes implied that the specimen grating had indeed a similar grating of 1000 lpi as intended. For mismatched gratings, no disappearance of the fringes could be expected.

### 3.6 Deposited Copper Film Gratings

This technique was developed as a result of lack of image contrast and sharpness in the photographs of the specimen grating.

The exposed and developed specimen was placed in a High Vacuum Evaporator made by Denton Vacuum, Inc., Cherry Hill, N.J. 08003, and a film of copper metal was deposited over the entire surface. One specimen (SP1) was treated with acetone after the deposition to wash off the photoresist lines, leaving behind a copper grating. This copper grating could be heated with a Bunsen burner flame to further enhance its visibility and contrast. The grating in copper film could also be utilized without washing the photoresist off with acetone. Such gratings also tended to be vulnerable to dirt - mere handling of the specimen tended to leave oily marks which did not fare well in the subsequent photography of the specimen grating.

## SECTION IV

### GRATING PHOTOGRAPHY AND OPTICAL DATA PROCESSING

#### 4.1 Specimen Grating Photography

The complete state of strain throughout an extended field can be determined from moiré fringe photographs obtained through superposition of a submaster grating with deformed and undeformed specimen (baseline) grating replicas. Such a superposition yields baseline moiré fringes and data (at strain) fringe patterns.

A direct superposition of a submaster (or an analyzer grating) with the specimen grating is not possible here because the sleeve protrudes slightly above the surface and because there are out-of-plane displacements--a rumpling of the surface. Superposition was done optically, a technique that has an advantage in that moiré sensitivity can be increased by the introduction of a pitch mismatch to increase the capability to interpolate between fringes.

Optical superposition can be performed in real time in which the specimen grating is imaged by a lens onto the master grating or its image. In this investigation such a technique was not adopted because of its difficulty. Rather, the specimen grating was photographed on glass photoplates

in two states, the undeformed state (baseline) and the deformed state (data). The plates from each state were then superimposed with the submaster plate in turn to produce the moiré fringe photographs. Examination of these photographs reveal any changes between the corresponding two states of the specimen.

#### 4.2 Grating Recording System

A sketch of the apparatus for photographing the specimen grating is shown as Figure 4.2.1, and Figure 4.2.2 shows the equipment used.

An 8 x 10 Linhof Technical camera is used in the optical system with an f4.5 Schneider-Optik lens of 300 mm (11.8") focal length. The specimen was imaged with a basic magnification of 2. Later this was slightly changed to introduce a pitch mismatch. For best results the aperture was set at f/11. The distance from the lens to the mismatch image focal plane was estimated at around 35 in. (88.9 cm). For illumination two 500 watt flood lamps were placed 12 in. (30.48 cm) from the specimen at an angle of incidence of about  $30^{\circ}$ . One lamp gave a sharp, well-contrasted image, due to shadow effects resulting from one-sided illumination. The disadvantage of using only one lamp was lopsided illumination, one side being much brighter than the other. Such problems can be compensated to a degree in the Fourier optical analysis stage.

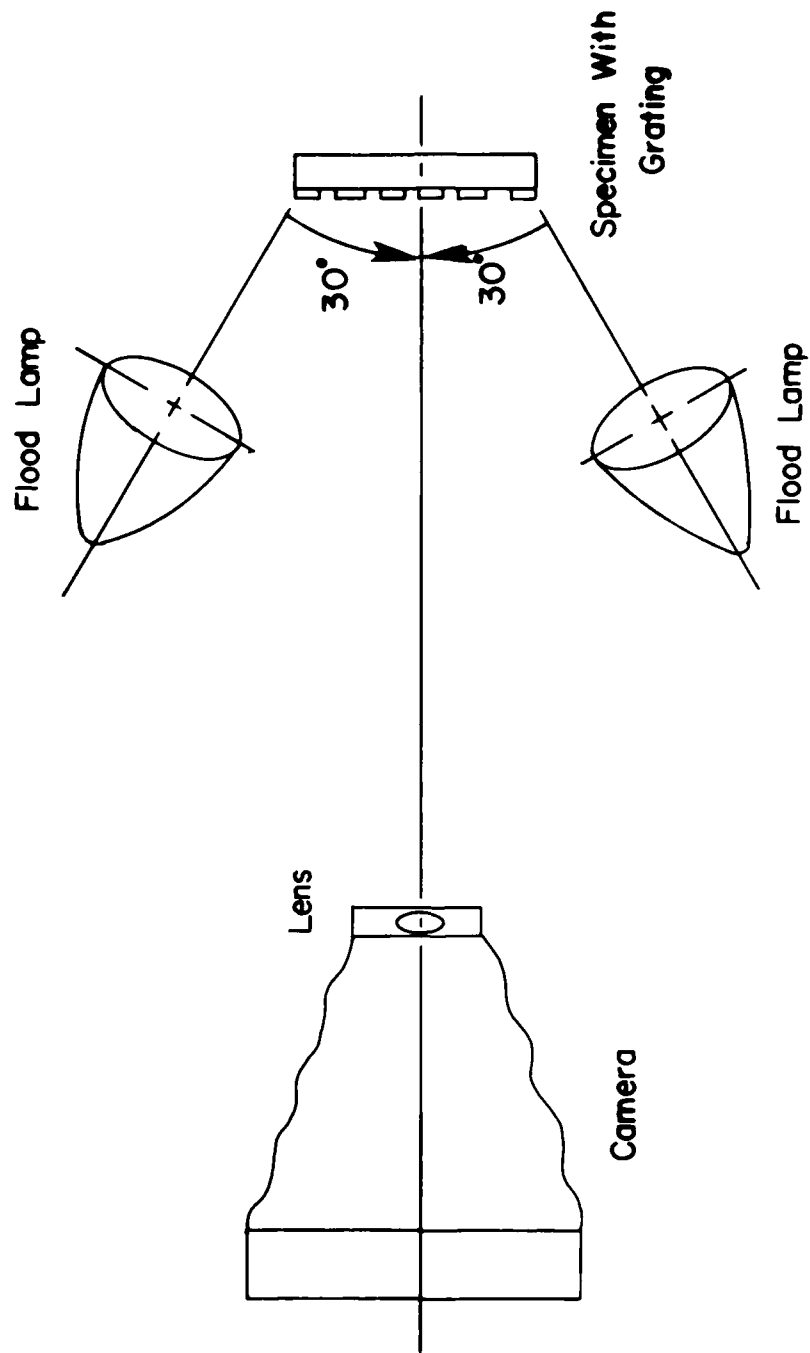


Figure 4.2.1.1 Schematic of Apparatus for Grating Photography.

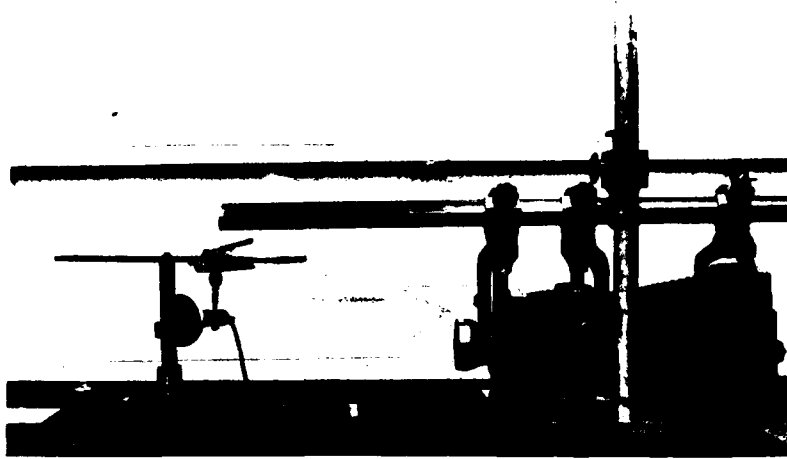


Figure 4.2.2 Equipment for Grating Photography.

Even though  $30^{\circ}$  proved to be the optimum illumination incidence angle for some specimens, other specimens, especially those designed for study of the effects of a plate edge upon the surface strain field required an individual trial and error determination of the best angle of incident light. The multi-hole specimen configurations gave the most problems in almost all phases of the experiment because of the closeness of the array of holes to the plate edge boundary.

Depending on the type of specimen and film selected, the exposure times also had to be arrived at by trial and error. An ordinary light meter was available but this was not adequate for this high resolution requirement.

As the experimentation progressed, it was discovered that the lens in a reversed position (back to front) gave the best sharpness and improved image definition.

The basic magnification was 2.0. Fine tuning from this value to obtain a mismatch led to a need to refocus. Sample developed specimen plates taken to the optical Fourier analyzer could reveal too much mismatch, which meant there were too many fringes to be resolved. Sensitivity enhancement by the moiré fringe mismatch technique had exceeded the capabilities of the fringe photographic system available.

Corrective procedures implied utilizing a 1000 lpi grating submaster in the back of the camera (the focal plane). Real time fringes could be observed whenever the specimen

grating image plane coincided with the submaster's. If moiré interference was not obvious or not pronounced, re-focusing was accomplished by slightly moving the camera lens until maximum fringe spacing was obtained. It was now left to the discretion of the experimenter to choose the best pitch mismatch by slightly altering this magnification with the lens. Building vibrations and air drafts in the laboratory could result in not seeing the fringes at all, even with the stiff camera set-up.

Precise timing of exposures was obtained with dark-room "Time-0-Lite" timers connected to the flood lamps and set for the correct exposure durations.

In general, AGFA type 10E56 plates proved the best. Kodak High Resolution plates and backed Kodak Spectroscopic 649-F plates were used on some occasions. AGFA-Gavaert (4" x 5") type 10E57 and 10E56 and also Kodak High Resolution holographic plates type 131-02 (4" x 5" x .04") (10.2 cm x 12.7 cm x .1 cm) were used as the image recording photoplates. With the former, exposures tended to center around 4 sec. whereas the latter required 2-3 sec. AGFA 10E56 gave the best sharpness and least graininess. All emulsions had good resolution and accuttance characteristics, however. Development of the plates in D-8 did not work well. D-19 developer was tried and development times ranged from  $6\frac{1}{2}$  - 8 min. with an optimum at around 7 min. depending on exposure times. The best developer in the end turned out to be Kodak HRP (high resolution plate developer, 1:2 parts water dilution) with

development times around 3 min. Finally, the plates were fixed in Kodak Rapid Fixer for  $5\frac{1}{2}$  - 7 min. and then allowed to sit in a bath of running water for about  $\frac{1}{2}$  hour. The plates were then ready for coherent optical processing.

#### 4.3 Optical Data Processing - Fundamental Concepts

The basic data processing system is shown in Figure 4.3.1. Between the object plane  $P_1$  and the laser is placed a collimating lens  $L_1$ . The lens,  $L_2$  decollimates and focuses the beam at the spectrum plane  $P_2$  (a first image plane). A camera and filter are placed at  $L_2$  and the final image is focused on the plane  $P_3$ .

The reason for using  $L_2$  is to bring the diffraction pattern of the object (the superimposed assembly of sub-master and undeformed/deformed specimen photoplate) in from infinity. The imaging lens  $L_3$  focuses the image at the plane  $P_3$ . The spatial frequency spectrum of the object is spread across the transform (spectrum) plane  $P_2$ , that is, it produces on  $P_2$  a two-dimensional Fourier transform of the object. Thereafter  $L_3$  (the inverse transform lens) projects the diffraction pattern of the light distributed over  $P_2$  onto the image plane. In other words, it diffracts the diffracted beam which means that it generates an (inverted) inverse transform. Thus the inverse transform of the Fourier data appears on  $P_3$ . The moiré fringes appear in plane  $P_3$ .

Fundamental to this moiré fringe generation process are three concepts, namely, two beam interference, the

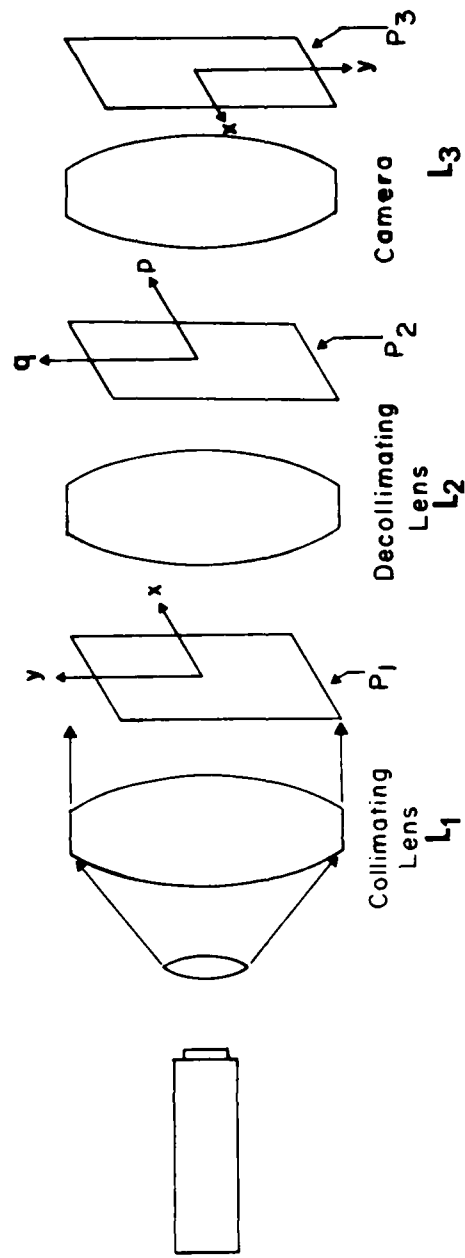


Figure 4.3.1 Arrangement of Components of Optical Spatial Filtering System.

diffraction of light by an amplitude grating, and finally the lens as a Fourier transformer.

When a coherent monochromatic laser beam is made to transilluminate a grating, part of the light suffers a deviation from its original path--the optical axis. The deviation in this case will depend on a number of factors, viz.: the wavelength of the monochromatic light, the grating frequency and the angle of incidence. The simplest example is that of a sine grating. The light transmittance,  $T$  of the grating is given by

$$T = T_0 \left( 1 - K \sin \frac{2\pi x}{\rho} \right) \quad (4.1)$$

$$= T_0 \left( 1 - K \sin 2\pi f \right) \text{ and} \quad (4.2)$$

the deviation of the diffracted beam is given by:

$$\theta = \sin^{-1} \frac{\lambda}{\rho} \quad (4.3)$$

where  $\rho$  = grating period,  $x$  = distance in the grating plane,  $f$  = grating spatial frequency, and  $\lambda$  is the wavelength of light.

This idea can be extended to a two-grating assembly instead of one. The component beam deviations of each of the two grating transparencies will be as shown in Figure 4.3.2. Altogether, there will be five different ray groups that emerge. The outer ray groups, orders  $\pm 2$ , are not of much interest in moire work, having come from a single ray diffracted at each one of the two gratings. Of considerable

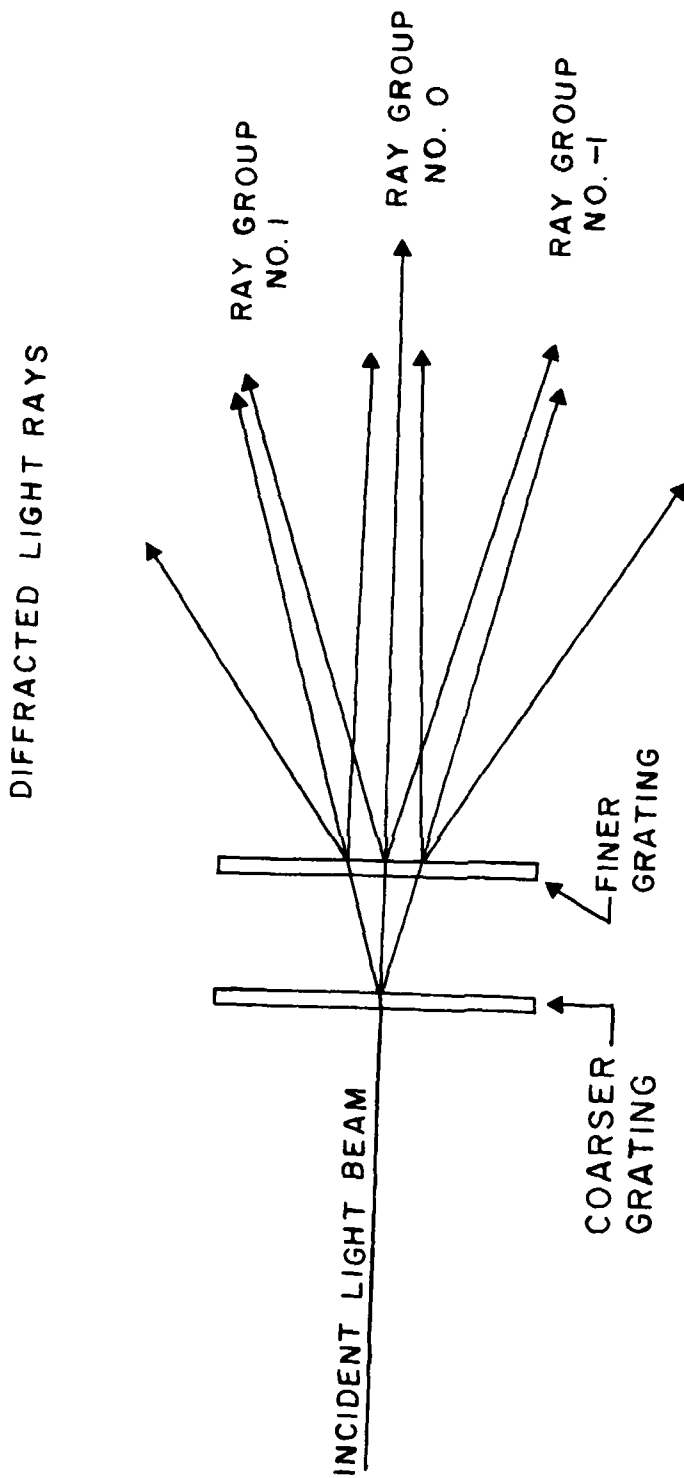


Figure 4.3.2 Diffraction of Light by Two Superimposed Sine Gratings Having Slightly Different Spatial Frequencies (Ref. 24).

interest are the  $\pm 1$  order ray groups. The two rays in these groups have suffered deviations at one of the two gratings in turn, and in the limiting case the two rays become parallel as the spatial frequency difference between them approaches zero. The decollimating lens  $L_2$  focuses these two rays, thereby causing them to overlap at the plane  $P_2$ . Because the two laser beams (rays) are coherent and, in general, not parallel, an interference pattern will be observed in the area in which they intersect. The dark and light zones which would be seen on a screen placed in the region of interference are known as interference fringes. This interference fringe pattern is a function of the pitch and orientational differences of the submaster and specimen gratings. Figure 4.3.3 and Figure 4.3.4. illustrate the diffraction of a narrow and a wide beam by two sine gratings with small mismatch levels.

The moiré fringe photographs for strain analysis in this investigation were obtained by using a superimposed assembly of submaster and data photoplates as the input signal in place of the sine gratings used for illustration above. Employed in this investigation are bar and space rulings. Such gratings can be thought of as a rectangular wave periodic structure or as a superposition of many such sine gratings of varying frequencies. The diffraction of a narrow beam of light by such a bar and space grating is shown in Figure 4.3.5, which illustrates the Fraunhofer (far-field)

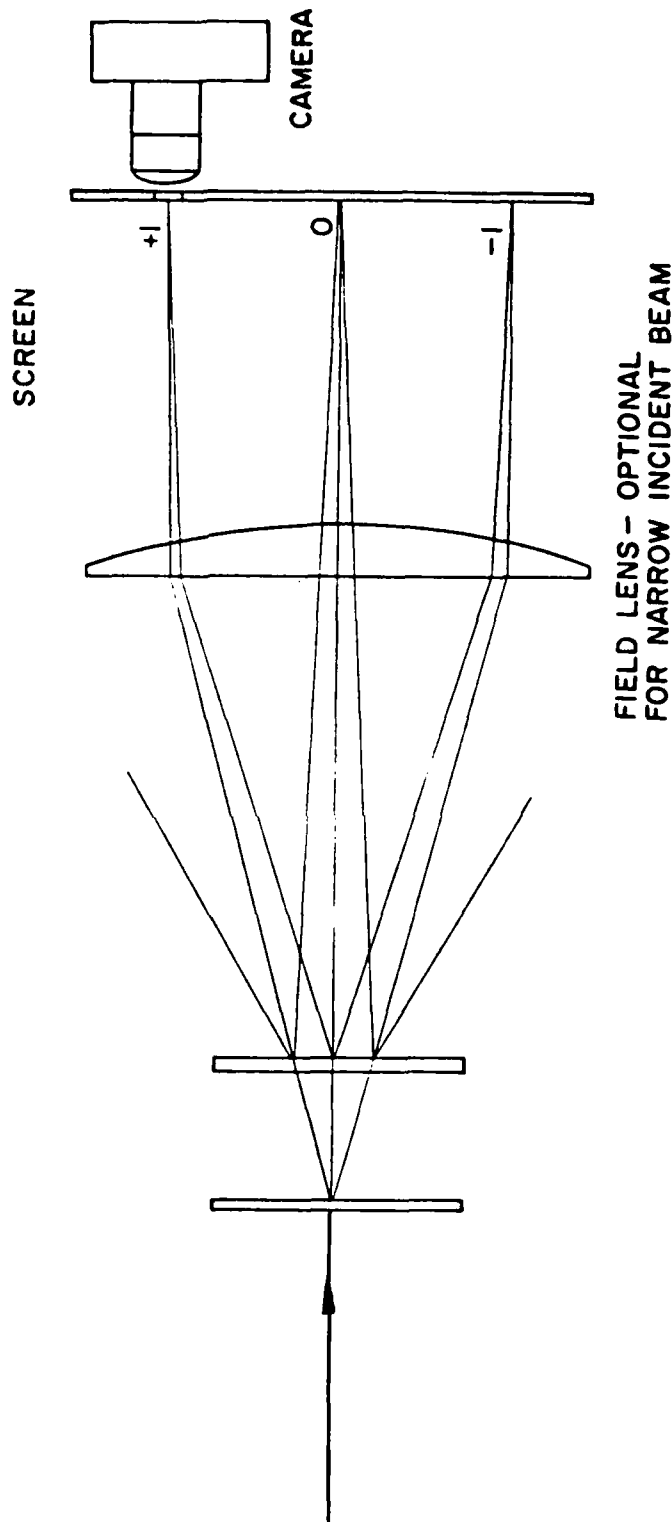


Figure 4.3.3 Formation of Two-Beam Interference Fringe Pattern by Light Diffracted Through 2 Sine Gratings Having Slightly Different Spatial Frequencies (Ref. 24).

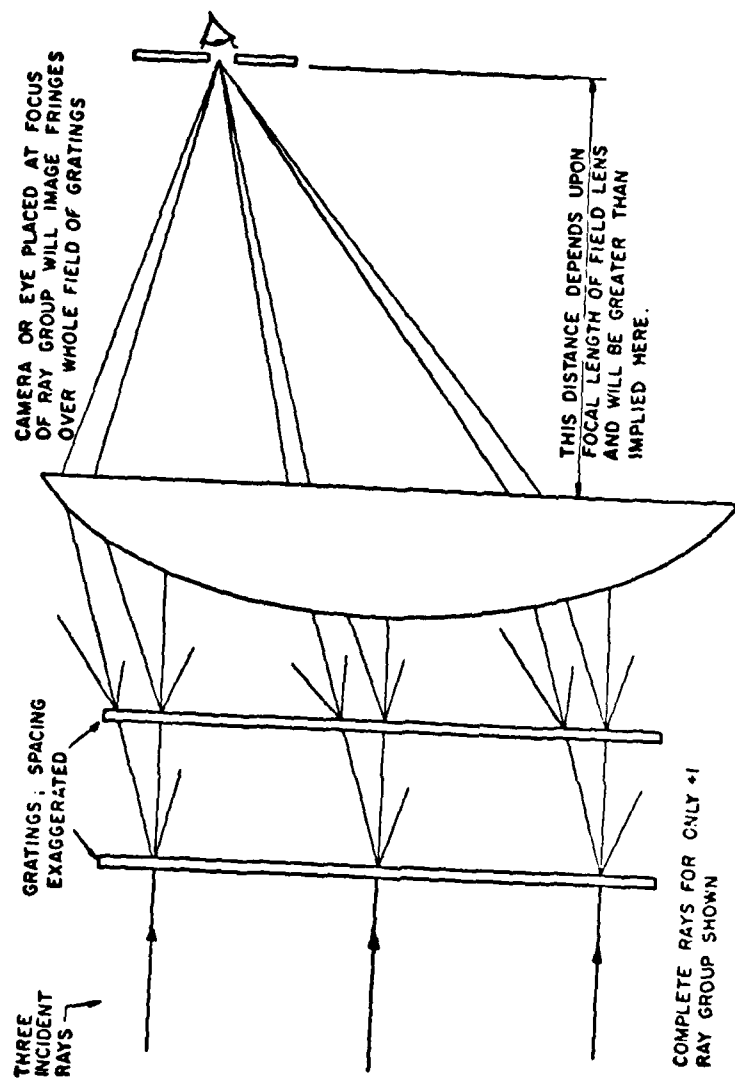


Figure 4.3.4 Diffraction of Wide Collimated Beam by Two Sine Gratings to Form Whole-Field Interference Pattern (Ref. 24).

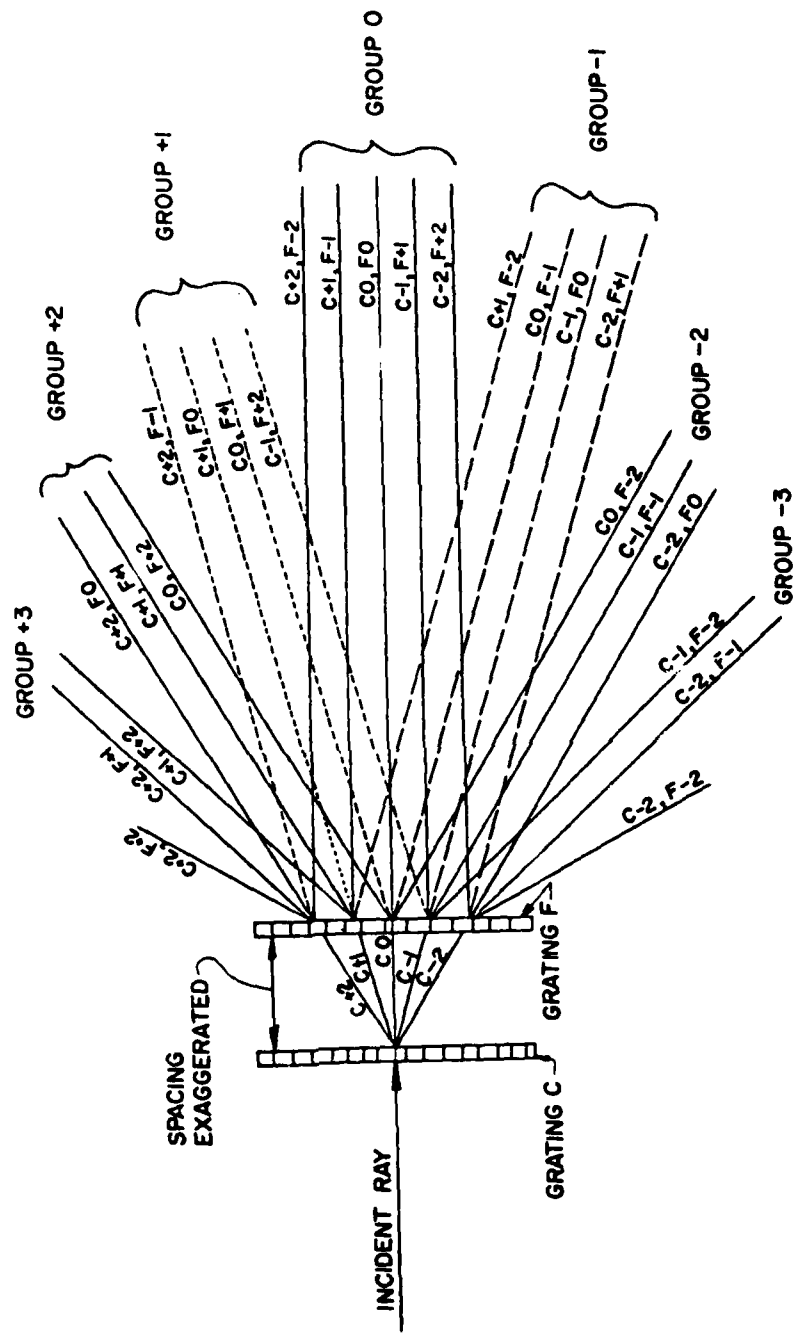


Figure 4.3.5 Diffraction of Narrow Beam by Two Bar and Space Gratings to Form Ray Groups Containing Higher Diffraction Orders (Ref. 24).

diffraction pattern. It is convenient to confine discussion to Fraunhofer diffraction for simplicity.

The mathematical details of the Fraunhofer diffraction pattern of the input signal distribution are amply explained by Thompson (26) and Chiang (28). This explanation is based on their work.

This Fraunhofer pattern in this complex field is a Fourier transform of the input signal. For a two dimensional grid input, i.e. grating lines in two orthogonal directions, a two-dimensional array of dots corresponding to a two-dimensional Fourier transform is produced. If a constant input signal is imaged at the input, then the resulting transform will consist only of a dot--a d.c. signal output. For a signal with multiple frequency components ranging from low to high the distribution spectrum will be such that all the low frequency components will show near the optical axis, whereas the higher frequency components will be distributed away from it.

Consider Figure 4.3.6 shown below. The amplitude transmittance of the grating is designated as  $f(x,y)$ . The Fourier transform of  $f(x,y)$  occurs in plane  $P_2$  with coordinate axes  $p, q$  and is represented as  $F(p,q)$ . The final image amplitude lies in the plane  $P_3(\xi, \eta)$  and is represented as  $Z(\xi, \eta)$ . Note that the  $(\xi, \eta)$  plane is in reflected geometry to account for the sign change that occurs during the retransformation by the camera lens  $L_2$ .

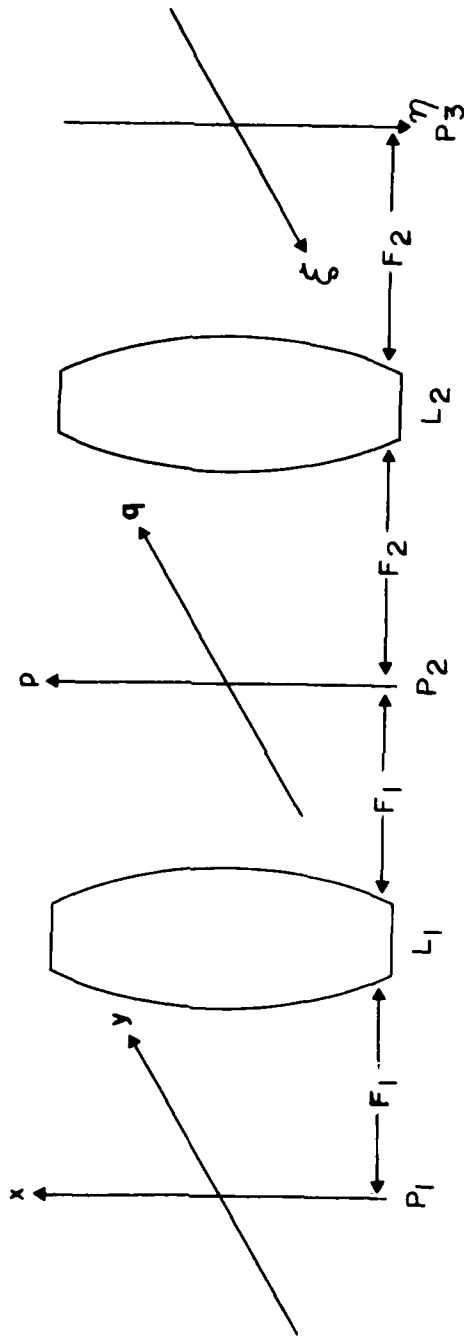


Figure 4.3.6 Schematic Diagram of Coherent Optical Processing.

Where spatial filtering is desired, it is done at the plane  $P_2$ . The diffraction spectrum of the complex amplitude of the light flux at the plane  $P_1$  ( $f(x,y)$ ) is expressed by the Fourier transform

$$F(p,q) = \iint_{-\infty}^{\infty} f(x,y) e^{i(px + qy)} dx dy \quad (4.4)$$

The Fourier transforms, and therefore the spatial distributions of their diffraction spectra will be produced corresponding to various spatial frequency contents in the signals (26). This principle allows us to eliminate any unwanted signal in the final picture by preventing its diffraction spectrum from entering the inverse transform lens (the camera lens). The process is called spatial filtering. Figure 4.3.7 illustrates these ideas for a grid input signal (24).

#### 4.4 Spatial Filtering for Moire Analysis

As suggested above, spatial filtering is an optical procedure that takes advantage of the diffraction properties of light, and consists of blocking portions of the Fraunhofer (far-field) diffraction pattern of superimposed sub-master and specimen grating photo-plates or images.

There are various forms of filters which can be used in the transform plane. Among them are phase filters which are used to control the phase, and complex filters

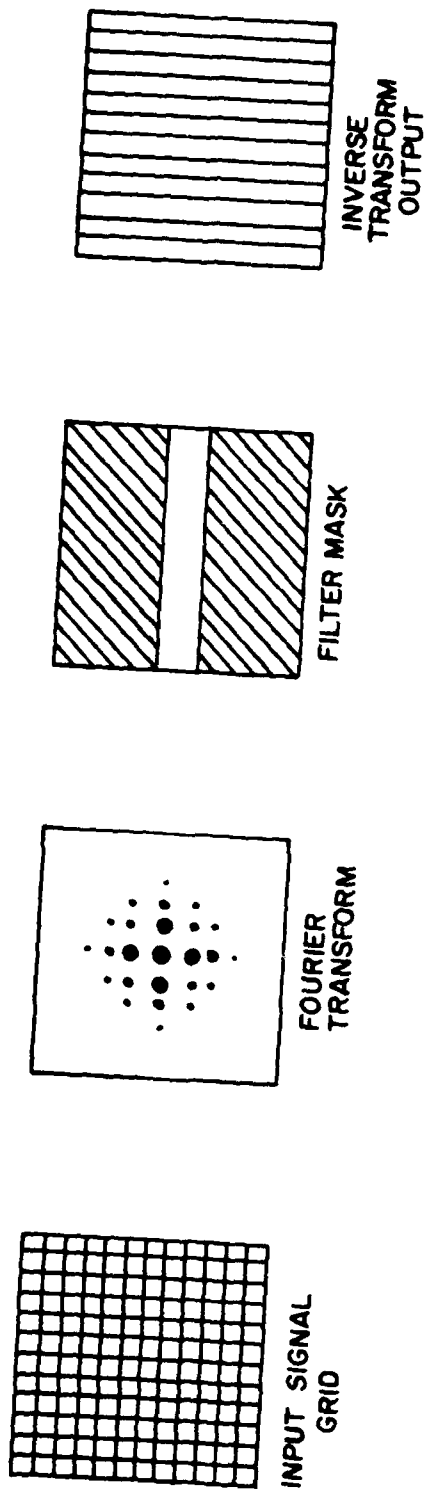


Figure 4.3.7 Example of Optical Spatial Filtering to Create Bar Grating from a Grid of Dots or Crossed Lines (Ref. 24).

which change both the amplitude and phase. Amplitude filters are used to control the amplitude transmittance in the transform plane without changing the phase of the signal components.

Figure 4.4.1 shows an optical system for spatial filtering in the plane  $P_2$  (24). For moiré analysis, the filtering is accomplished by eliminating all but one of the dots from the transform. For a filter, one can use a hole slightly larger than the diameter of the dot (diffraction order chosen) in a dark mask. When placed in the transform plane, it allows only the particular diffraction order through. When the filtered light strikes the camera lens, this order forms the desired inverse Fourier transform--a modified image of the input transparency.

Some of the orders which produced good moiré fringe patterns had high background noise. Since the noise and moiré fringe order signal had the same spatial frequencies, the noise could not be removed. Had that not been the case, the diffraction spectrum of the noise and that of the moiré fringe would occupy different positions at the transform plane  $P_2$ . As mentioned previously, some of the specimens had a crossed grating printed on them so as to facilitate the complete determination of the state of strain at a point. From such specimens the U-field and V-field displacements were obtained separately by filtering.

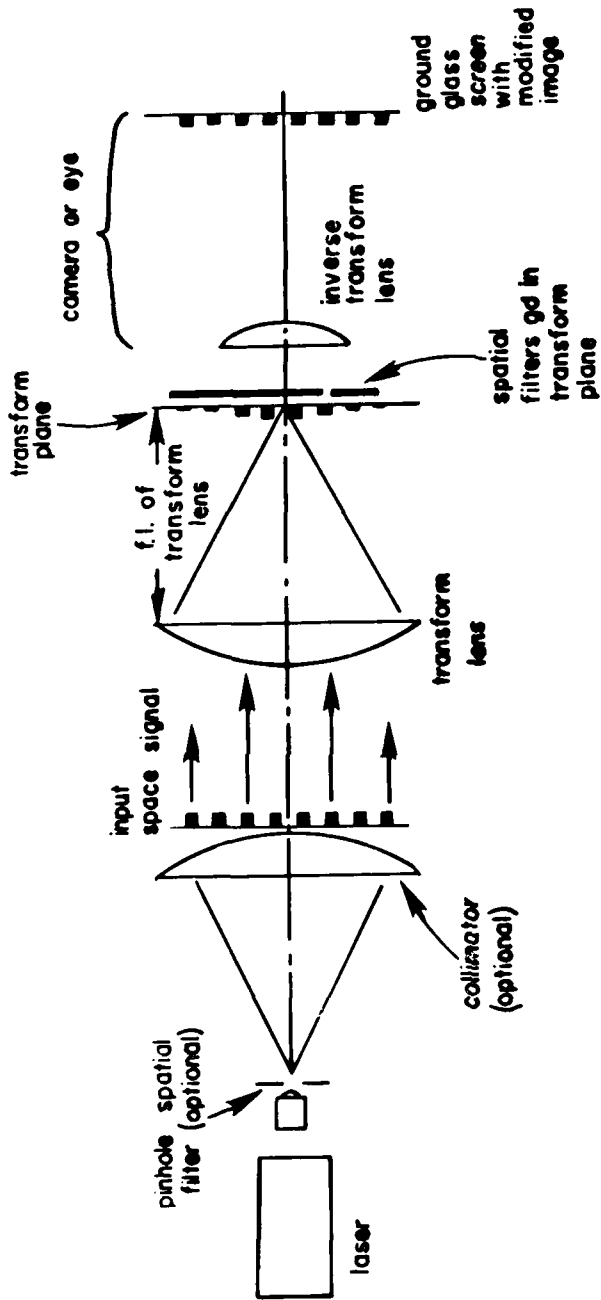


Figure 4.4.1 Optical System for Spatial Filtering in Fourier Transform  
 Pl. 2 and Creation of Inverse Transform of Filtered Image  
 (Ref. 24)

In general, where symmetry of the strain field is lacking, the u and v isothetics (lines connecting points of equal components of displacement) may interfere to create other fringe families, and a complex moiré pattern may result. To eliminate this problem, the specimen gratings were made of a rectangular dot array, and the master or submaster grating used was unidirectional. The moiré fringes of each family are obtained separately by rotation of the master grating through an angle of  $90^\circ$ . The center dot in the Fourier transform plane designated as the (0,0) order is the D.C. output signal, and any one order along the central horizontal array of orders contains only the u-field fringes; and any one order along the central vertical array of orders contains only v-field fringes. Therefore, if a black paper mask with a hole is placed at the transform plane to let through the optical system one order along the central horizontal (or vertical) array the u- (or v-) field fringes will be obtained, again making sure that the order allowed to pass has the least entanglement with the spectrum of noise.

#### 4.5 Creation of Moiré Fringe Photographs

The apparatus used to obtain the fringe photographs in this investigation is shown in Figure 4.5.1.

An effective monochromatic and coherent point source of light was provided by a Helium-Neon 10 milliwatt laser made by Jodon Corporation of Ann Arbor, Michigan. The laser

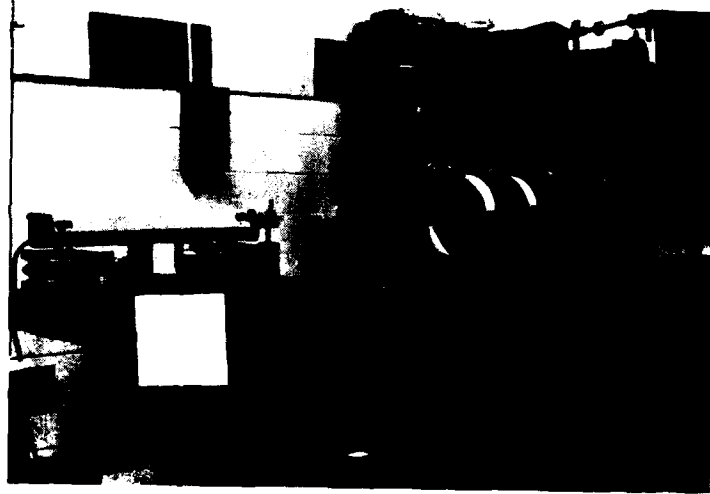


Figure 4.5.1 Data Processing System.

beam passed through a Jodon model LPS100 pinhole spatial filter which converted it to a clean diverging beam.

The lens  $L_1$  was located at roughly its focal length from the spatial filter to collimate the beam. The near-parallel beam of light transluminated the sub-master and specimen assembly at the plane  $P_1$ . The spatial filter—a round black paper with a  $3/16$  in. (4.76 mm) hole was contained in a filter mount of the camera lens. The Nikon F camera was fitted with a Coligon zoom lens with a focal length range of 95 mm - 205 mm. Even though zoom lenses have the disadvantage of decreased image quality and speed, and though this disadvantage gets worse with greater zooming ranges, this type of arrangement seemed to work better here than "normal lens" or wide-field lens. The camera mount consisted of a cylindrical cast iron base roughly 5 in. (12.7 cm) long with a standing 4 in. (10.16 cm) post serving as the support attachment. The whole camera-stand assembly could be moved across the bench sideways to locate the optimum fringe diffraction order.

Pinhole spatial filter and laser separation distance was 2.75 in. (6.98 cm) and the distance between the collimating and decollimating lenses approximately 18 in. (45.72 cm). The two lenses were 15 in. (38.10 cm) in diameter and had focal lengths of 39 in. (1 meter).

The procedure of obtaining the fringe photographs began with locating the position of the ray groups with a white cardboard. With the aid of a mounted diaphragm filter, the orders were examined one by one and the one with the least noise identified. During the examination, it was important to be sure that the far field (no strain) fringes were vertical. If slanted, relative inclinations of the plates were altered by rotating one with respect to the other slightly until maximum fringe spacing was obtained, which automatically implied fringe uprightness.

The camera and filter assembly was set in position already loaded with Kodak Plus-X Pan (PX 135-136) black and white film. Most of the pictures were taken with a zoom setting of 205 mm and exposure times in the range of  $\frac{1}{4}$  - sec.

The development of the 35 mm negatives of the fringe patterns was done in D-76 developer, an all-purpose developer that produces negatives of normal contrast and moderate to low grain. Average development times were 7 min. Then the films were processed in Kodak Indicator Stop bath for 30 sec. and Kodak Rapid Fixer for  $4\frac{1}{2}$  min. After the films were washed for 20-30 min. they were dried and printed on 8 x 10 in. (20.34 x 25.4 cm) Kodalith paper for fringe analysis.

Samples of the moiré fringe patterns are shown in Figure 4.5.2 and Figure 4.5.3.

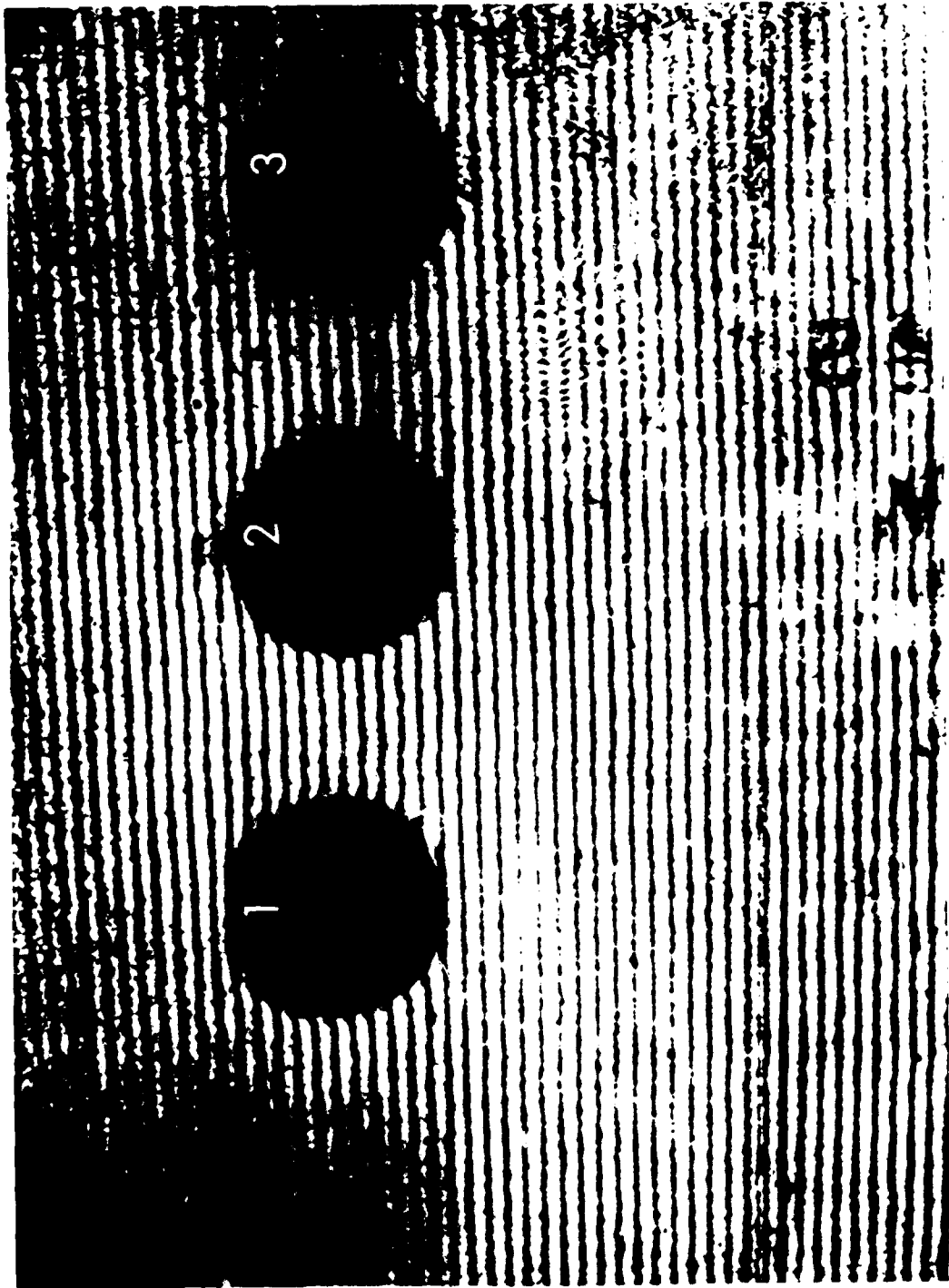


Figure 4.5.2 Baseline Moire Fringe Photograph of Specimen SPC.

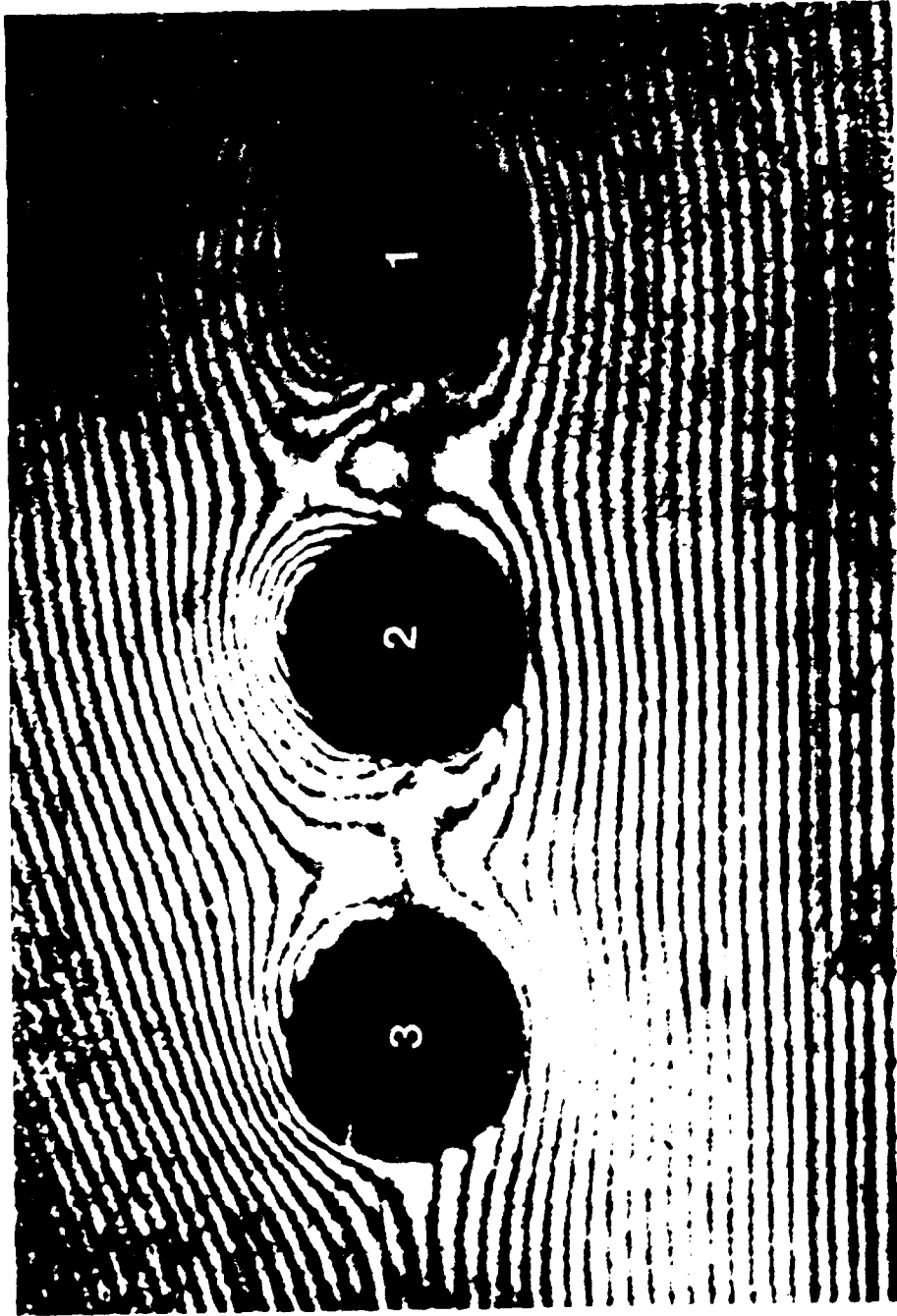


Figure 4.5.3 Moiré Fringe Photograph of Specimen SPC after Coldworking Holes 1, 2, and 4.

#### 4.6 Moiré Data Reduction

The moiré method of strain measurement utilizes the fringes observed when two grids are superimposed and slightly displaced. The method is relatively old, dating back to 1874 when Lord Rayleigh first put it to practical use (11). In the measurements of surface strain fields, two approaches for the interpretation of moiré fringe patterns are useful, viz.:

- (a) geometrical approach,
- (b) displacement-derivative approach.

The former approach was recognized by Tollenard, in 1945 (53). But it was not until 1952 that Kaczer (10) put Tollenard's ideas into practice.

Weller and Shepard (13) in 1948 suggested the second approach. Extensive development of this method is attributed to Dantu, who employed it in the measurement of elastic and plastic strains (10).

In this investigation the displacement-derivative method was employed. However, a brief description of the geometrical approach will also be illustrated as it gives a good insight into the general theory of the moiré method of determination of strain.

##### 4.6.1 The Geometrical Approach

Moiré fringes are produced whenever two superposed gratings, the master and specimen grating (assumed equal in

pitch, say  $p$ ,) are either rotated one with respect to the other or when the specimen grating pitch  $p$  is changed to  $p'$  due to deformation. In general, both these sources of fringe formation occur simultaneously at a point.

Figure 4.6.1 depicts the geometry of the moire fringes in terms of fringe separation. The following is a relationship between the rotation angle  $\theta$  of the specimen grating with respect to the master orientation, fringe separation distance  $\delta$  and the master grating pitch  $p$ . Thus we have:

$$\frac{AB}{\sin \theta} = \frac{AC}{\sin 90^\circ} \quad , \quad \frac{AC}{\sin (\psi - \theta)} = \frac{AC}{\sin 90^\circ}$$

$$\frac{p}{\sin \theta} = \frac{\delta}{\sin (\psi - \theta)} \quad , \text{now using the addition formula,}$$

$$\sin (\psi - \theta) = \sin \psi \cos \theta - \cos \psi \sin \theta$$

and solving for  $\theta$  we get:

$$\tan \theta = \frac{\sin \psi}{\delta/p + \cos \psi}$$

In terms of the angle of orientation  $\theta$ , the law of sines yields:  $\frac{p}{\sin (\pi - \psi)} = \frac{p'}{\sin (\psi - \theta)}$

Solving for  $p'$  as a function of the other parameters, the following relationship is obtained:

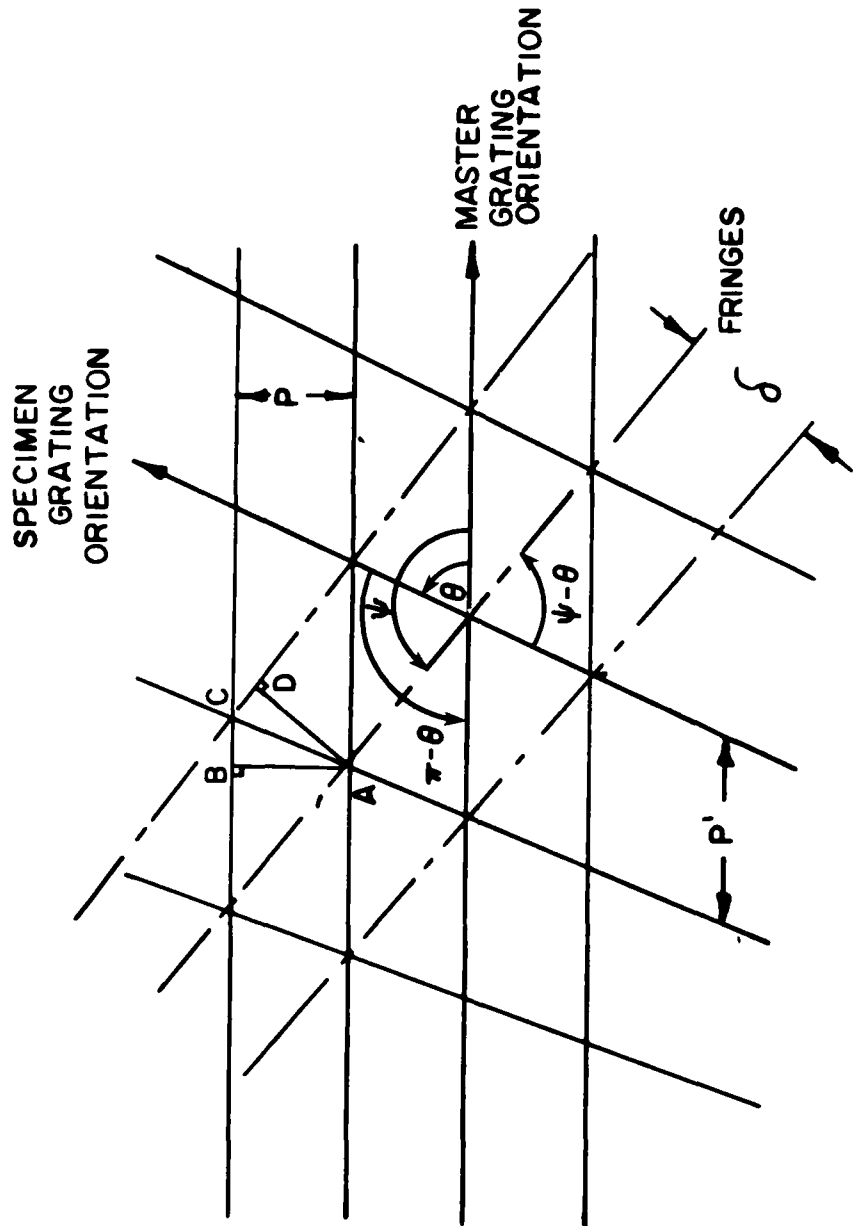


Figure 4.6.1 Moiré Fringe Geometry

$$p' = \frac{\delta}{\sqrt{1 + \left(\frac{\delta}{p}\right)^2 + 2\left(\frac{\delta}{p}\right)\cos\psi}} \quad (4.5)$$

where  $\psi$  is the fringe inclination angle and  $p$  and  $\delta$  are the pitch of the master and the fringe separation respectively as before.

For negligible rotations, the specimen grating pitch takes the form  $p' = \frac{p\delta}{p \pm \delta}$ . This expression is then substituted into the definition of normal strain, in this case for the direction perpendicular to the lines of the master grating.

#### 4.6.2. The Displacement - Derivative Approach

The displacement derivative approach to moiré-fringe analysis of strain is basically a graphical differentiation process. Moiré fringes represent the loci of points of constant displacement in a direction normal to the grid lines.

The mechanics of this process involve first plotting the curve of fringe spacing versus fringe order, the zero order being chosen arbitrarily. The order of a fringe is given by the parameter  $m$ .

Denoting the horizontal displacement as  $u$ , we obtain the relation:  $u = mp$  where  $m$  is the fringe order and  $p$  is the master pitch.

For the determination of vertical displacements,  $v$ , the grating is oriented perpendicular to the vertical axis and the strain determination procedure is repeated.

From the above displacement field the strains are obtained from the definition of strain; that is:

$$\epsilon_x = \frac{\partial u}{\partial x} = \frac{\partial(mp)}{\partial x} = p \frac{\partial m}{\partial x} \quad (4.6)$$

$$\epsilon_y = \frac{\partial(mp)}{\partial y} = p \frac{\partial m}{\partial y} \quad (4.7)$$

$$\text{and } \gamma_{xy} = \frac{\partial u}{\partial y} + \frac{\partial v}{\partial x} = p \left\{ \frac{\partial m}{\partial y} + \frac{\partial m}{\partial x} \right\} \quad (4.8)$$

where  $p$  the master grating pitch is constant.

The accuracy with which the strain can be calculated depends on the effective gauge length which is given by the spatial distances between fringes. The smaller the pitch of the submaster employed, the more precise the results obtained, a factor which is especially crucial in areas of the highest strain gradients.

Submasters come in densities of 10-50,000 lpi (.4- 2000 lines/mm respectively). For most structural materials one might expect the measurement of maximum strain in the elastic range of the member to require at least 5000 lpi (200 lines/mm) submaster with normal moiré procedures (1). Unfortunately even this submaster would not give reliable results in areas of very high strain gradients. In

order to surmount this obstacle a "mismatch technique" was utilized. In this method, different specimen and analyzer grids are chosen. The pitch difference between the specimen and analyzer was obtained by a photographic technique.

If we suppose for a moment that the pitch or frequency of the specimen grid exceeds that of the master analyzer by a multiple  $(1+r)$ ,  $0 < r < 1$ , a fringe pattern of straight parallel lines called the baseline data (or fictitious strain data) is obtained on superimposing the two grids. This fictitious strain must be subtracted from the data obtained by superimposing the deformed specimen grating grid plate with that of the analyzer. Thus, the true strain is given by:

$$\epsilon_{\text{true}} = \epsilon_x - \epsilon_i = p \left[ \frac{1}{f_m} - \frac{1}{f_i} \right]$$

where:

$\epsilon_i$  is the baseline data =  $\frac{p}{f_i}$

$\epsilon_x$  is the strain obtained in the deformed case

$f_i$  is the fringe spacing for initial pitch mismatch,

and

$p$  is the master (original) pitch,

$f_m$  is the data fringe spacing.

In this investigation the reduction of moiré fringe data was done numerically. The accuracy of the reduction procedure is crucial since in the final analysis differentiation of the displacements is required.

#### 4.7 Digitization of Moiré Fringes - Radial and Tangential Strains

Digitization of the photographs was performed using the University's Computer Laboratory microprocessor controlled digitizer. Figure 4.7.1 illustrates its physical components.

The photograph to be digitized was placed firmly under a protective cover and digitization of points one by one was done by placing a cross-hair over the point or any one of the fiducial marks and identifying labels. One advantage of this set-up was that scaling to specimen dimensions was done automatically. The required scaling factors were based on two digitized points and the corresponding specimen coordinates for each. The further away the fiducial points were from each other, the more accurate was the digitization procedure. For radial strains (i.e.,  $\epsilon_x$ ) digitization of one axis on each baseline and data photograph was all that was needed. For the tangential strains several axes perpendicular to the y axis had to be drawn and digitized.

The appendix contains a computer program and sub-routines based on analysis programs originally prepared at the Air Force Materials Lab-Computer Activities Branch. These routines were adapted for use in the computation of the residual hoop and compressive strains. The function of these programs has been described by Cloud (24). It was necessary to modify the original routines for use with the computational facility at Michigan State University.

AD-A100 524

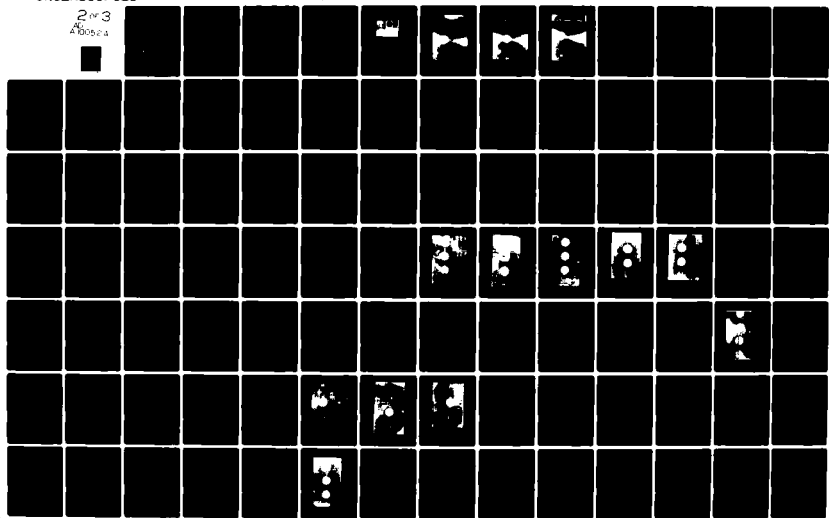
MICHIGAN STATE UNIV EAST LANSING DIV OF ENGINEERING --ETC F/6 13/5  
AN EXPERIMENTAL STUDY OF LARGE COMPRESSIVE LOADS UPON RESIDUAL --ETC(U)  
FEB 81 6 CLOUD, R. SULAIMANA F33615-78-C-5123

UNCLASSIFIED

AFWAL-TR-80-4206

NL

213  
460024



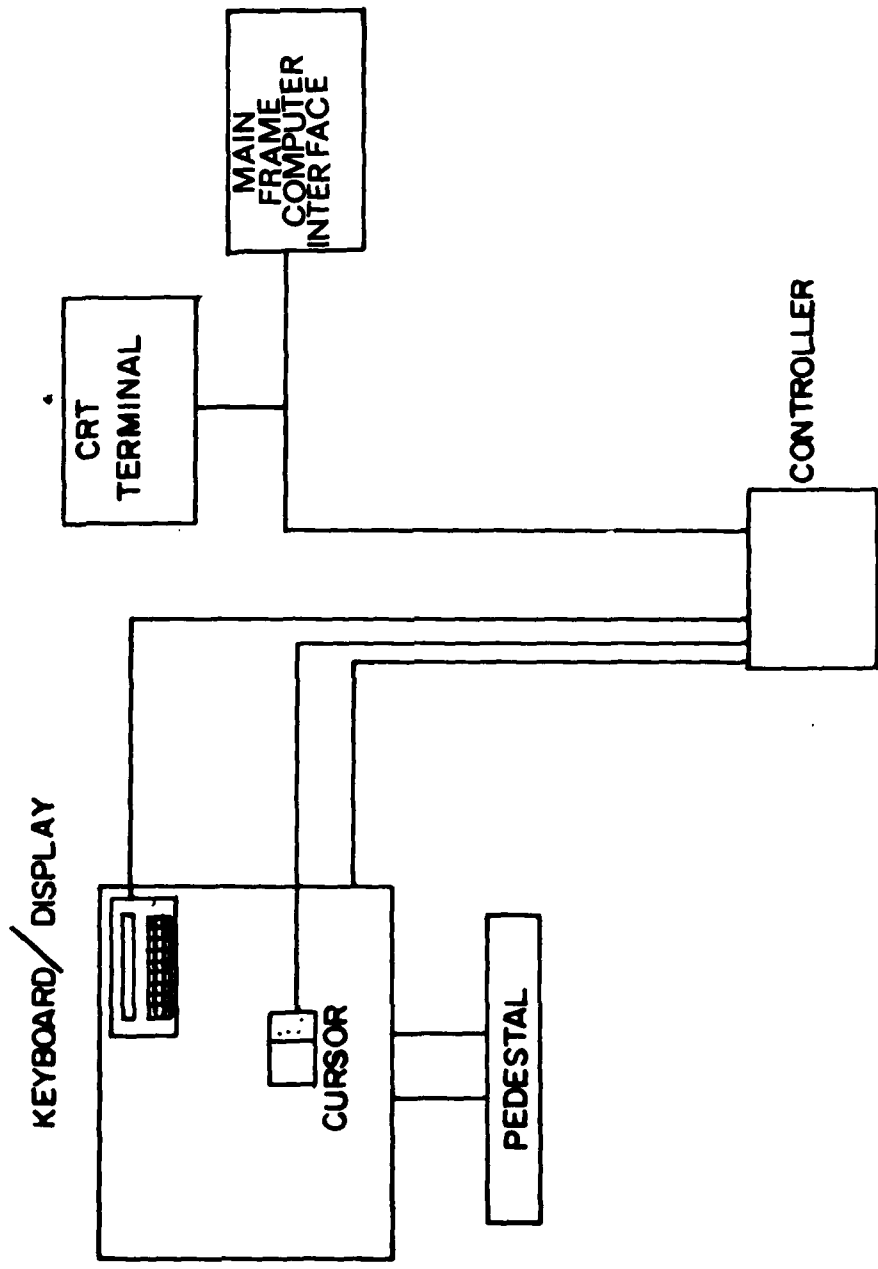


Figure 4.7.1 Digitizer Components.

## SECTION V

### EFFECTS OF LARGE COMPRESSIVE IN-PLANE LOADS ON RESIDUAL STRAIN FIELD

#### 5.1 Introduction

Work was begun on this topic at Wright-Patterson Air Force Base by Cloud (24). Three specimens designated C9, C10, and C11 were tested for the effect of in-plane load and cycling of that load on the residual strain near a coldworked fastener hole. At a design stress level of 24 ksi; (165 MPa) for aircraft skins, specimens C9 and C10 (C11 was used as a control specimen) were cycled for 50 cycles to study the cycling's effect on the imposed residual strain field. The 50 cycles represents to a limited degree aircraft wing loading during landing.

In this study, Cloud's results are verified and extended with the testing of two specimens designated SP1 and SP2. These specimens were tested to investigate further the effects of large in-plane compressive loads upon the residual strain field surrounding a coldworked fastener hole.

Axial hoop, transverse hoop, and radial residual strain fields were evaluated. The results are presented in section 5.4.1, 5.4.2, and 5.4.3 respectively. The radial

residual strain results are compared to the results of Adler and Dupree (29) and Hsu-Forman (2) for the coldworked state only.

## 5.2 Overview

The reasons for overstraining and thus prestressing machine or structural elements depend to a large extent on the nature of the applied loads--that is, whether the load is steady (static) or cyclic (fatigue). This overstraining of the structural material may result in the reduction of high peak stresses and stress gradients when the applied loads are static in nature. In some cases this operation will accomplish the reduction of the maximum stress in the assembly at the expense of raising the average stress level--a price which can be tolerated (7). Ultra-high pressure devices and heat exchanger tubes are two application examples among many to be found in industry.

In structural design, the overstraining or cold-working of a fastener hole results in improvement of the fatigue life of the structure. In this case, cyclic tensile stresses are lowered by the deliberate introduction of residual compressive stresses. Without them, the tensile stress at the edge of the hole would rise to approximately 3 times the applied nominal stress (35). Although some details about the effect of residual compressive stresses are understood, there is still a major unanswered question about the

modification of this residual stress distribution by an application of compressive loads on the structure. For an example, consider an aircraft landing when the undersides of the wings go into a state of compression.

### 5.3 Experimental Procedure

The specimen design used to explore this problem was illustrated in Figure 2.2.1 and that for specimens C9, C10, and C11 by Cloud can be obtained from his earlier technical report (24). Later on in the investigation it was deemed necessary to print the grid on the specimen in two directions so as to facilitate the measurement of strain distributions along both axes, x and y.

Loading of the specimens SP1 and SP2 was performed on a Tinius Olsen machine (Figure 5.1) in load increments of 5000 lbf ( $22.24 \times 10^3$  N). The specimens were loaded to failure, which turned out to be roughly  $32.5 \times 10^3$  lbf ( $144.57 \times 10^3$  N). This was equivalent to a nominal remote compressive overload stress of around  $52 \times 10^3$  lbf/in<sup>2</sup> (358 MPa). Cloud's specimens C9 and C10 endured the same type of loading as SP2 except for a 50 cycle cycling at a nominal stress of 24 ksi (165 MPa). Specimen C11 experienced the same type of loading history but with no initial hole prestress.

Figure 5.2, 5.3 and 5.4 show typical fringe photographs for situations where the strain distribution showed significant departure from the coldworked state.

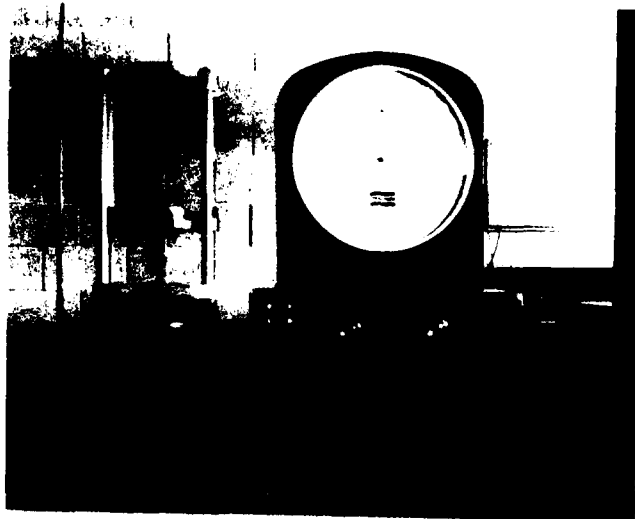


Figure 5.1 Apparatus for Overload Compressive Test Application.

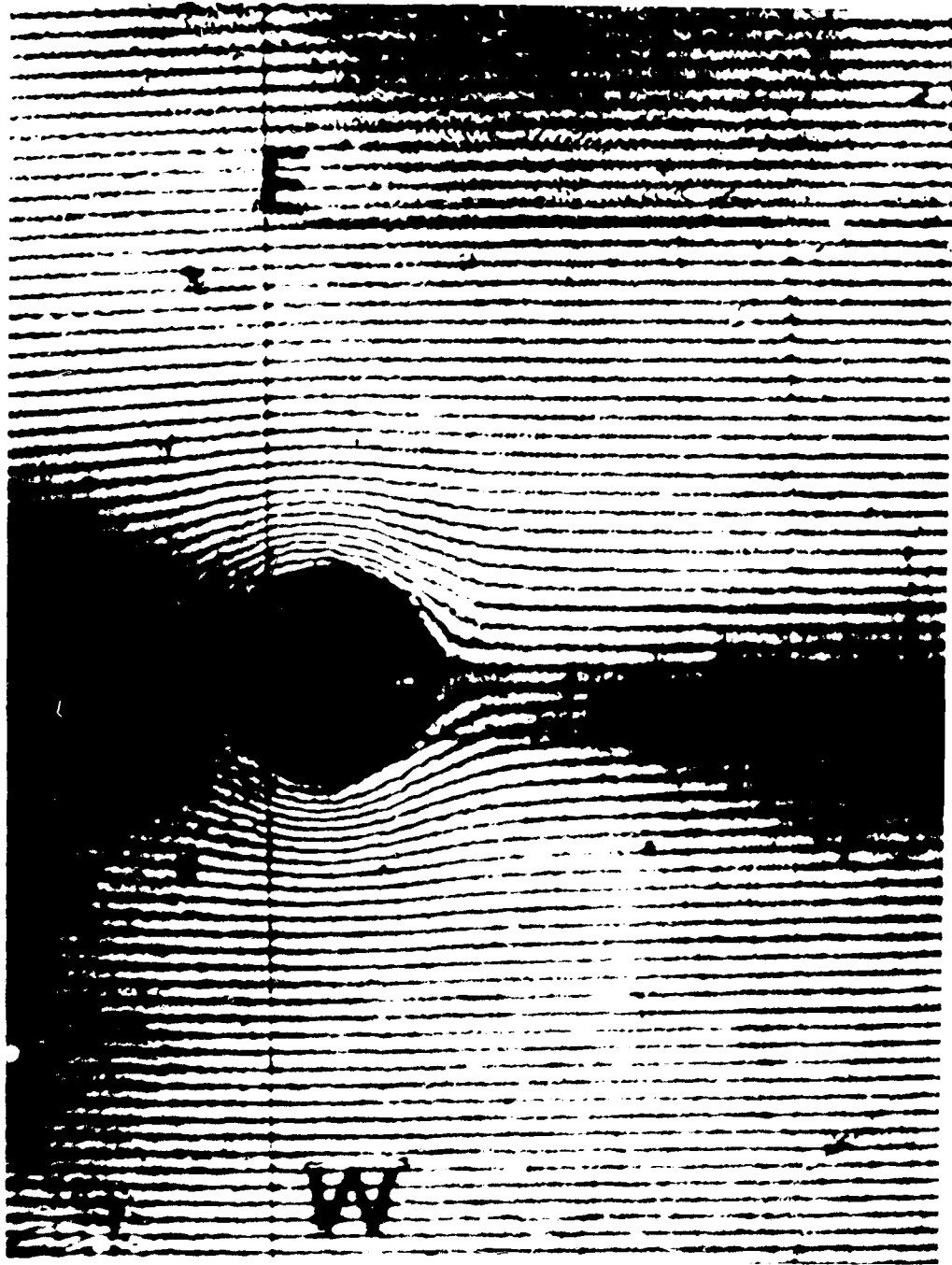


Figure 5.2 Moiré Fringe Photograph of Specimen SP 2 after 15,000 lb<sub>f</sub> Load Application.

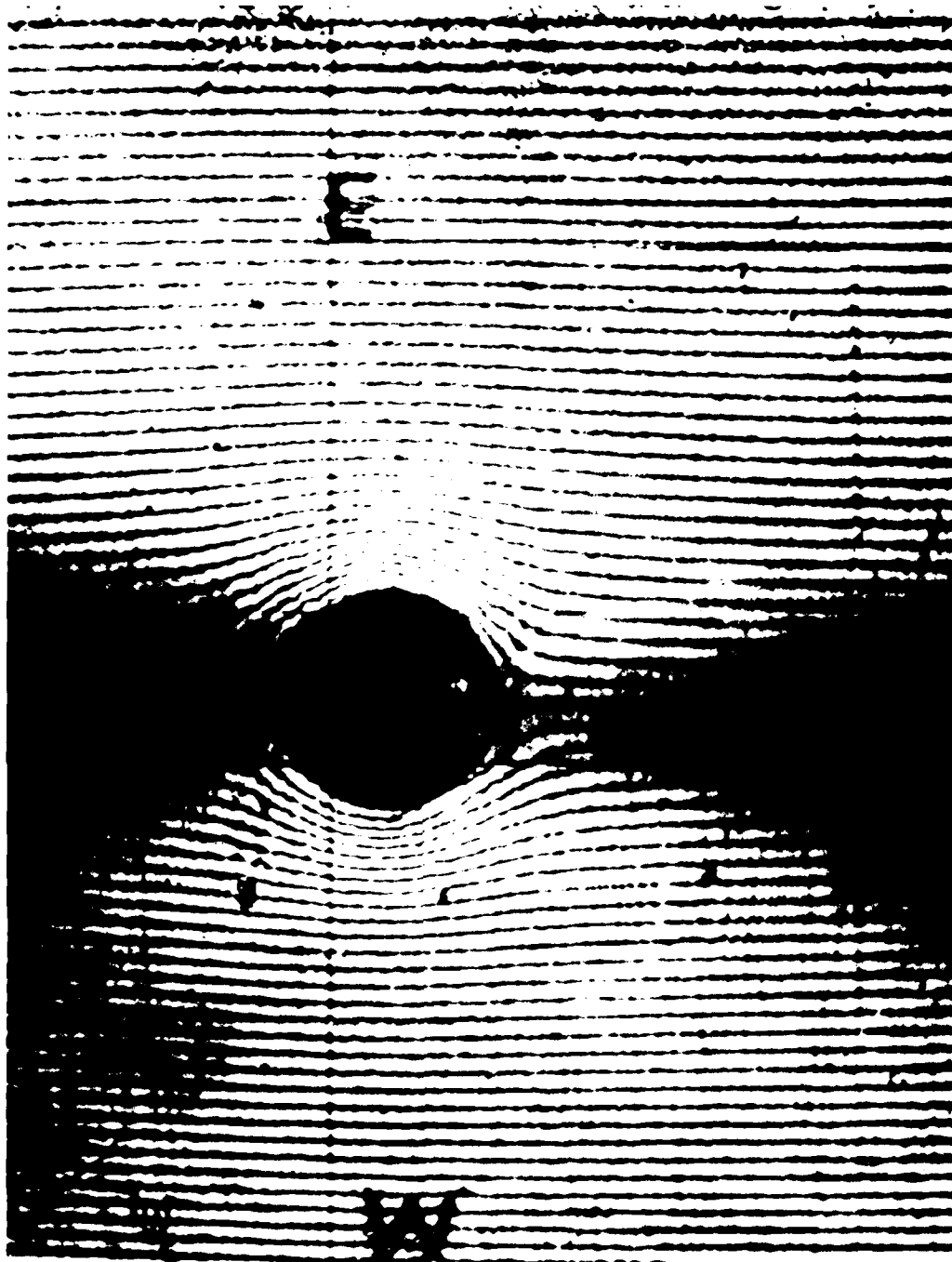


Figure 5.3 Moiré Fringe Photograph of Specimen SP 2 after 20,000 lb<sub>f</sub> Load Application.

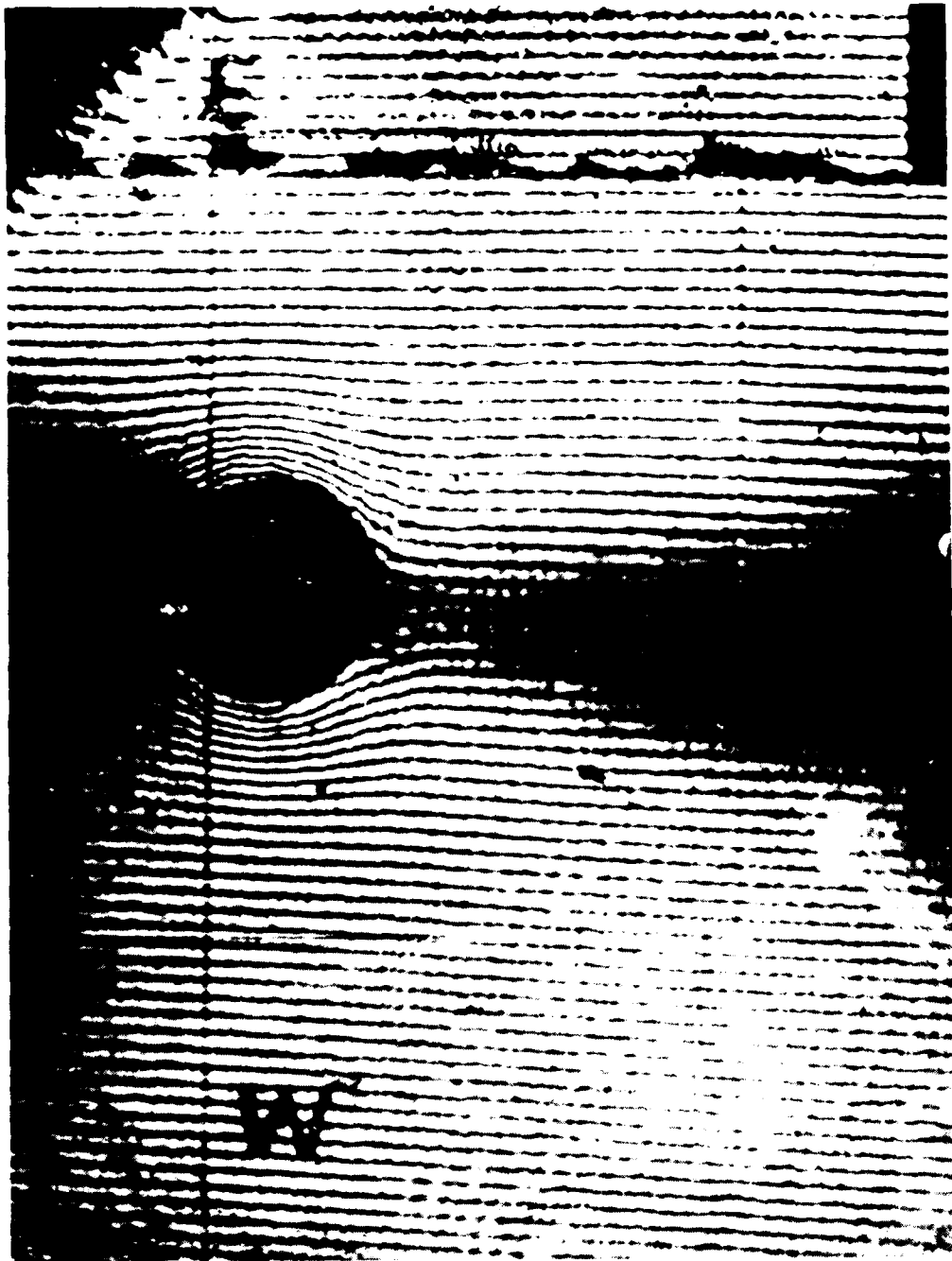


Figure 5.4 Moiré Fringe Photograph of Specimen SP 2 after 25,000 lb<sub>f</sub> Load Application.

## 5.4 Results and Discussion

### 5.4.1 Axial Hoop Strain Distribution

The results from Cloud's experiments, namely specimens C9 and C10, do not quite agree (Figure 5.5 and 5.6). For C10 the results do not depart appreciably from plasticity theory (36) except for the initial material response for the second part of the continuing remote in-plane compressive overload stress application. As might be expected from theoretical predictions of the dependence of mean residual strains on cyclic plastic strains, the residual strain climate tended to become smaller as cycling progressed (36). The results of specimen C9 reveal the same material characteristic response as that of C10 for radial distances of roughly 0.100 in. (2.54 mm) from the fastener hole. For distances less than 0.040 in. (1.02 mm) from the hole edge the results for C9 and C10 agree very well. Also, the overall material response before and after the cyclically imposed load for both specimens is in good agreement; that is, that increasing remote loading has a residual strain relaxation effect.

Results from Cloud's specimen C11, which served as a control specimen (Figure 5.7, a summary plot), indicate that residual hoop strains start showing up only in the region of the stress raiser, the fastener hole, at near buckling and buckling specimen failure loads.

Figures 5.8 through 5.17 are the detailed results of the axial hoop strain evaluation versus distance from

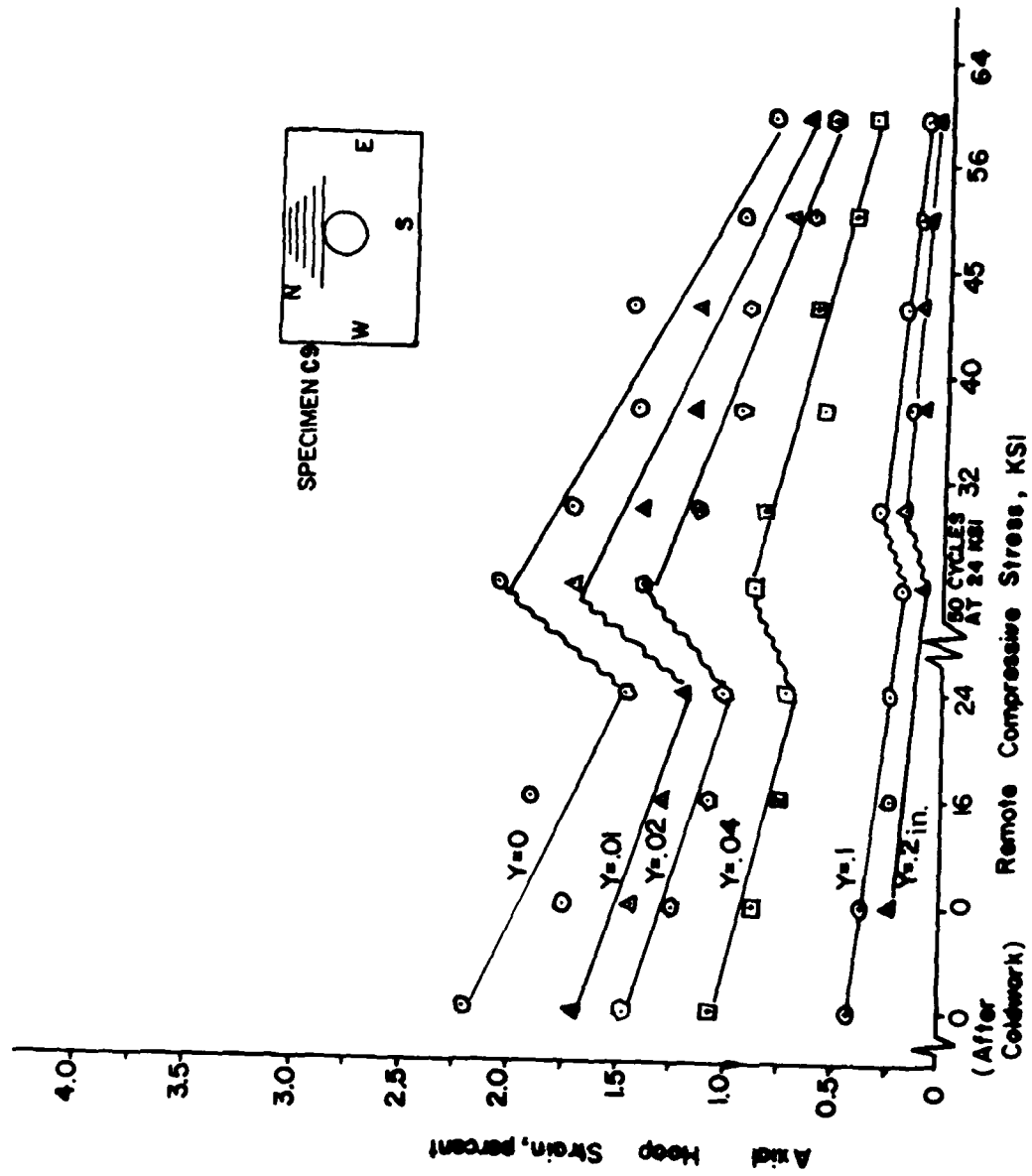


Figure 5.5 Effect of In-Plane Compression on Residual Axial Maximum Hoop Strain Distributions at a Point on Hole Boundary.

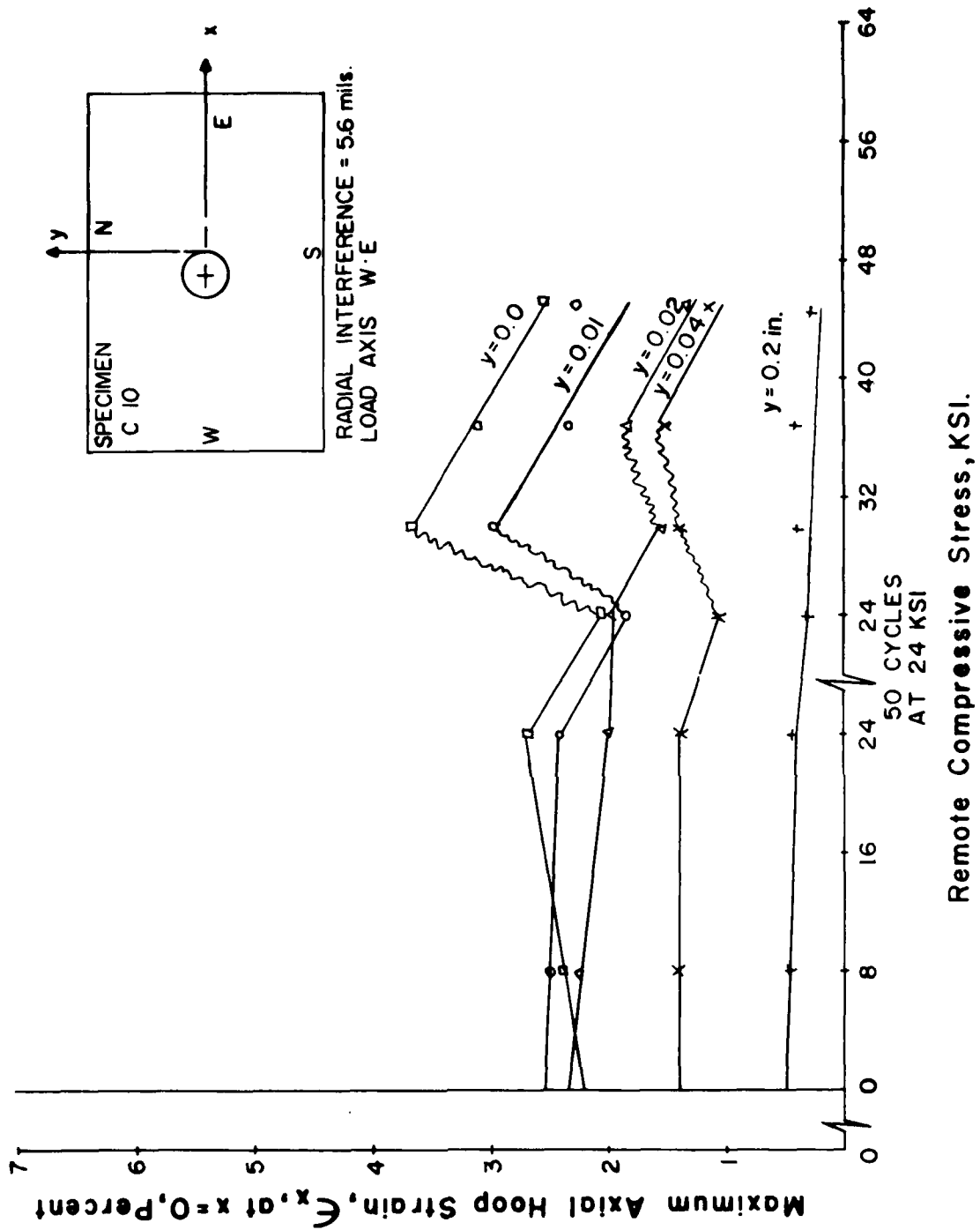


Figure 5.6 Residual Axial Hoop Strain Distributions Along Several Axes at Different Radial Distances for 5.6 mils Radial Interference.

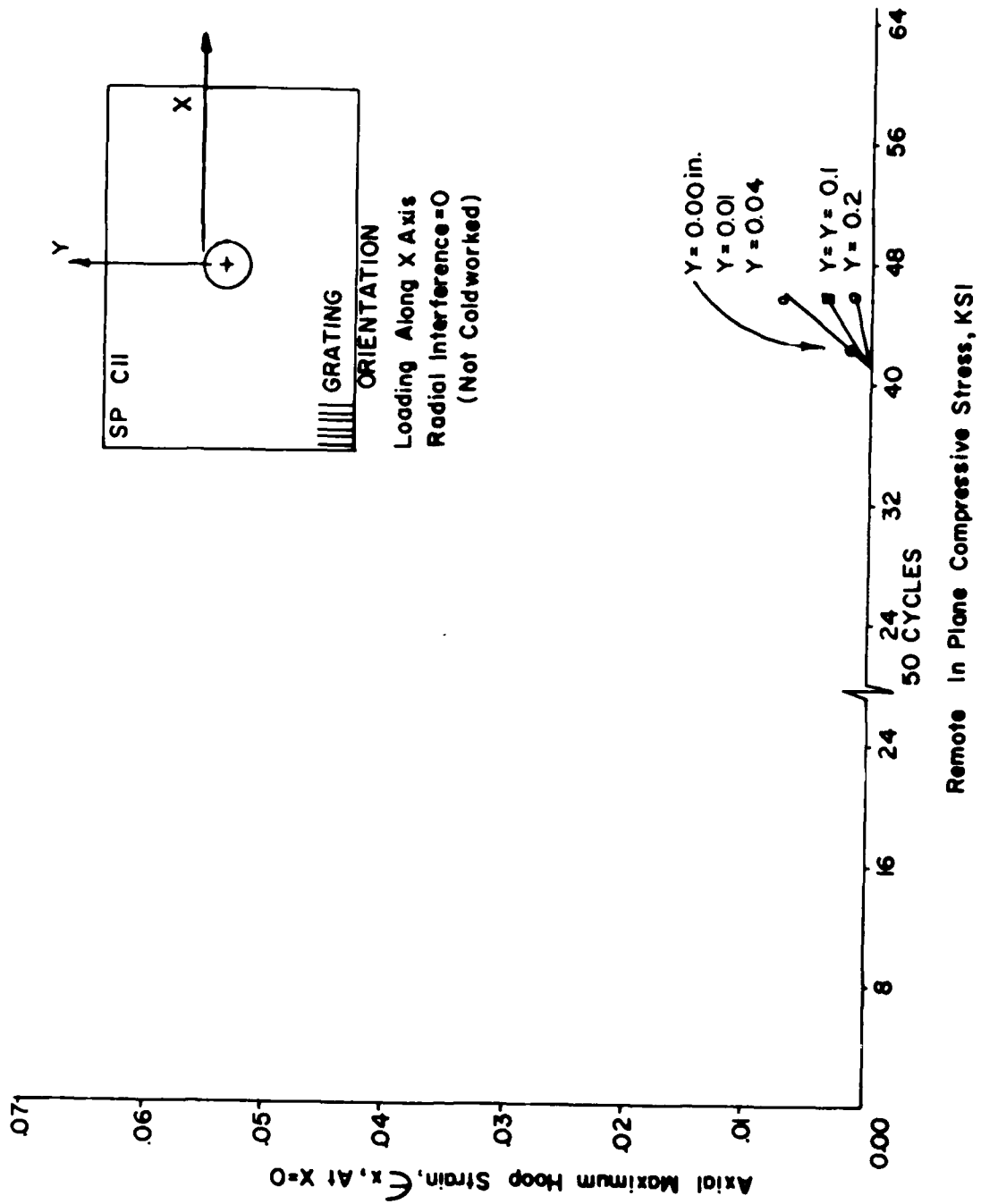


Figure 5.7 Residual Maximum Axial Strain Distributions at Various Points on a Radial Line for Zero mils Radial Interference.

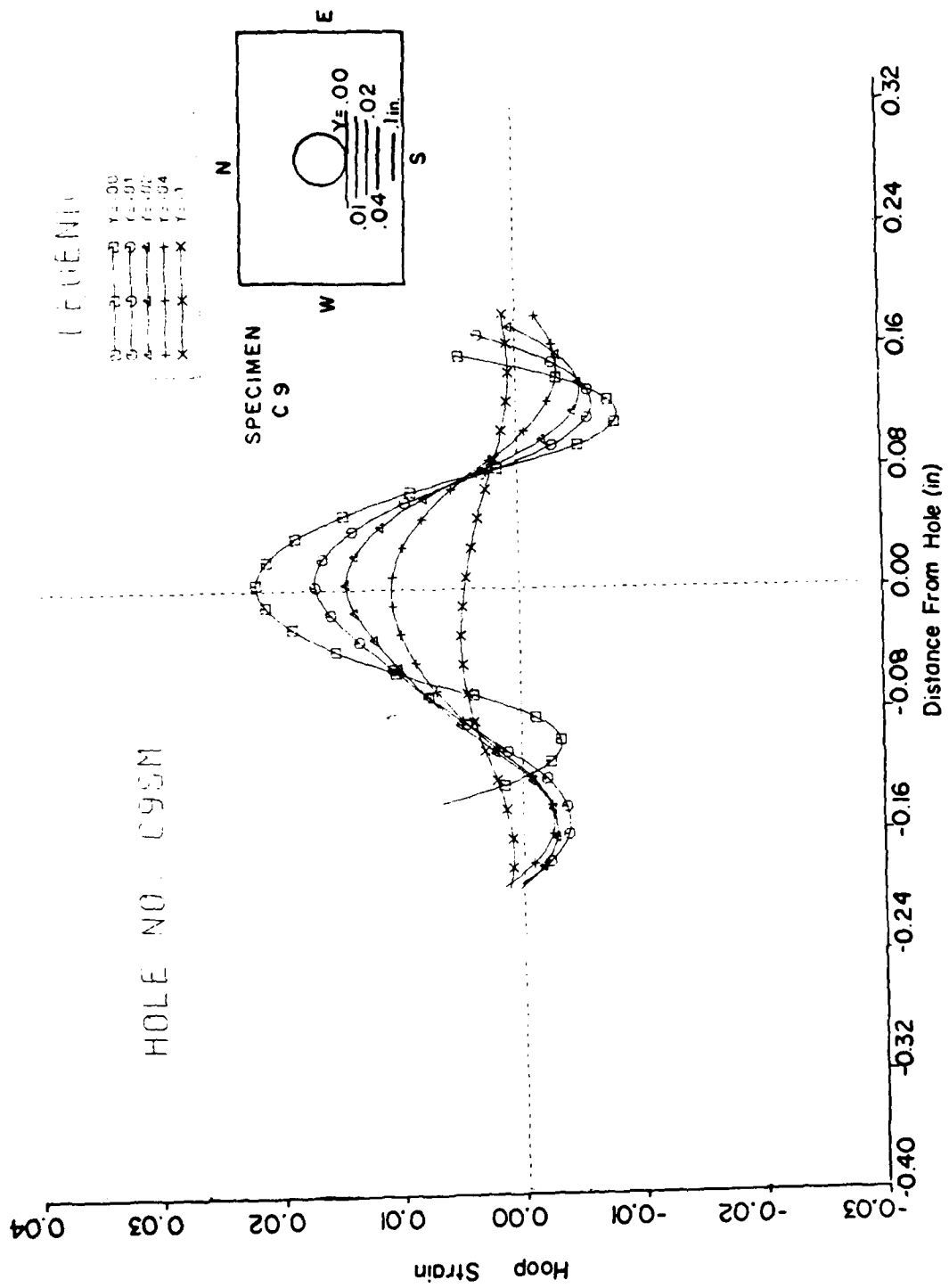


Figure 5.8 Residual Maximum Axial Strain Distributions at Various Points on a Radial Line for 5.6 mils Radial Interference.

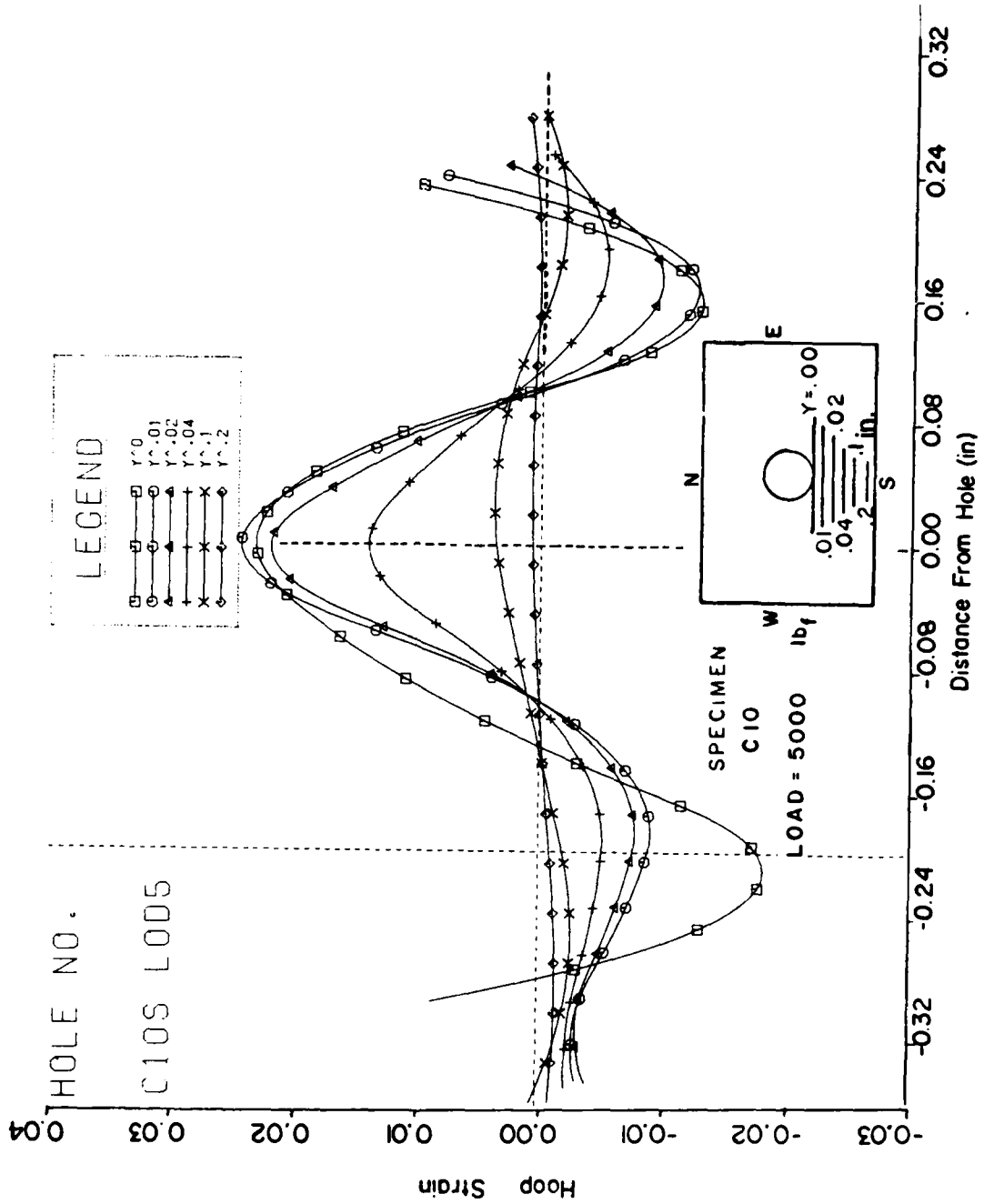


Figure 5.9 Measured Residual Axial Hoop Strain Distribution Along Several Axes at Different Radial Distances for 6.5 mils Radial Interference.

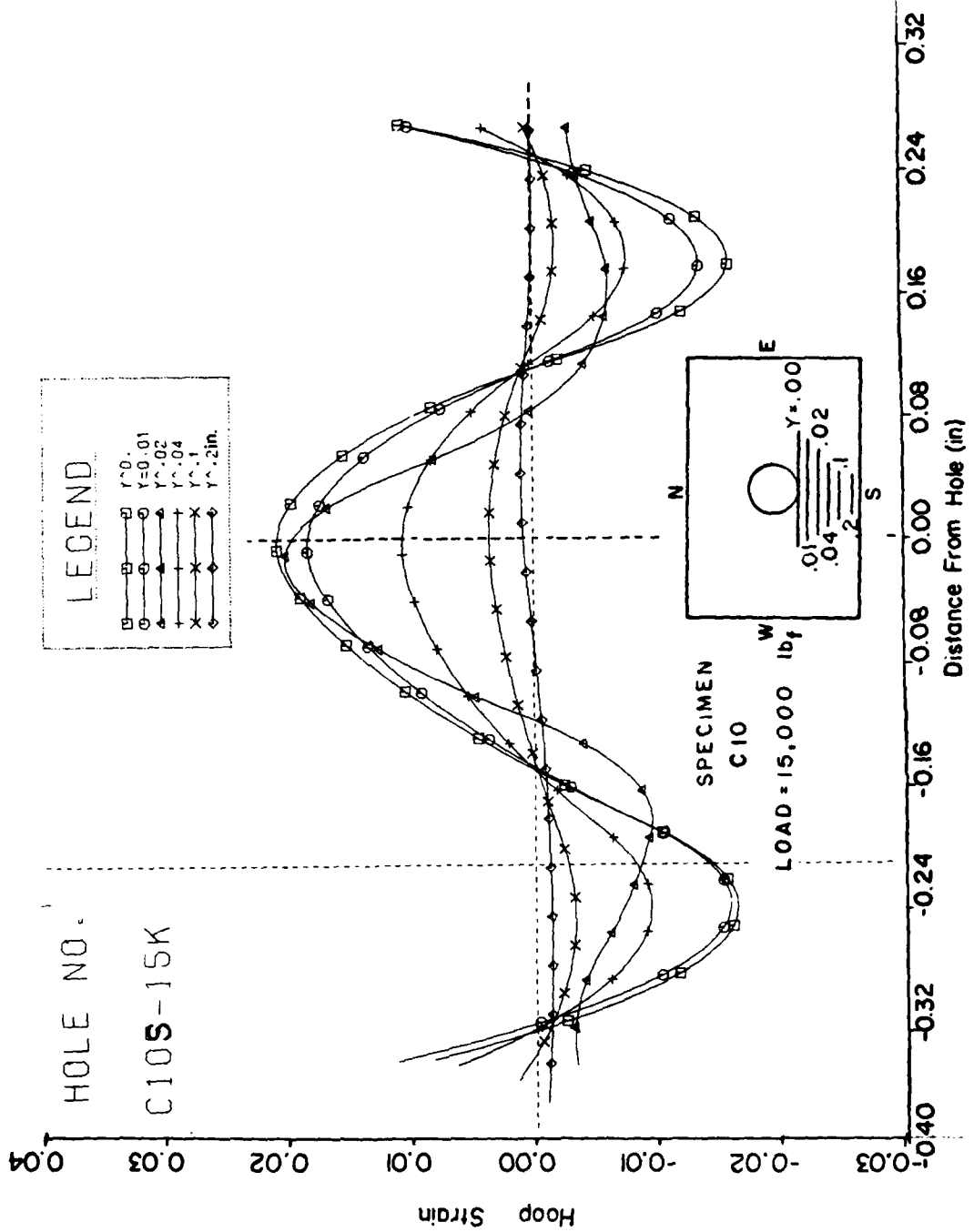


Figure 5.10 Residual Axial Hoop Strain Distributions Along Several Axes for 7.2 mils Radial Interference (Load 15,000 lb<sub>f</sub>).

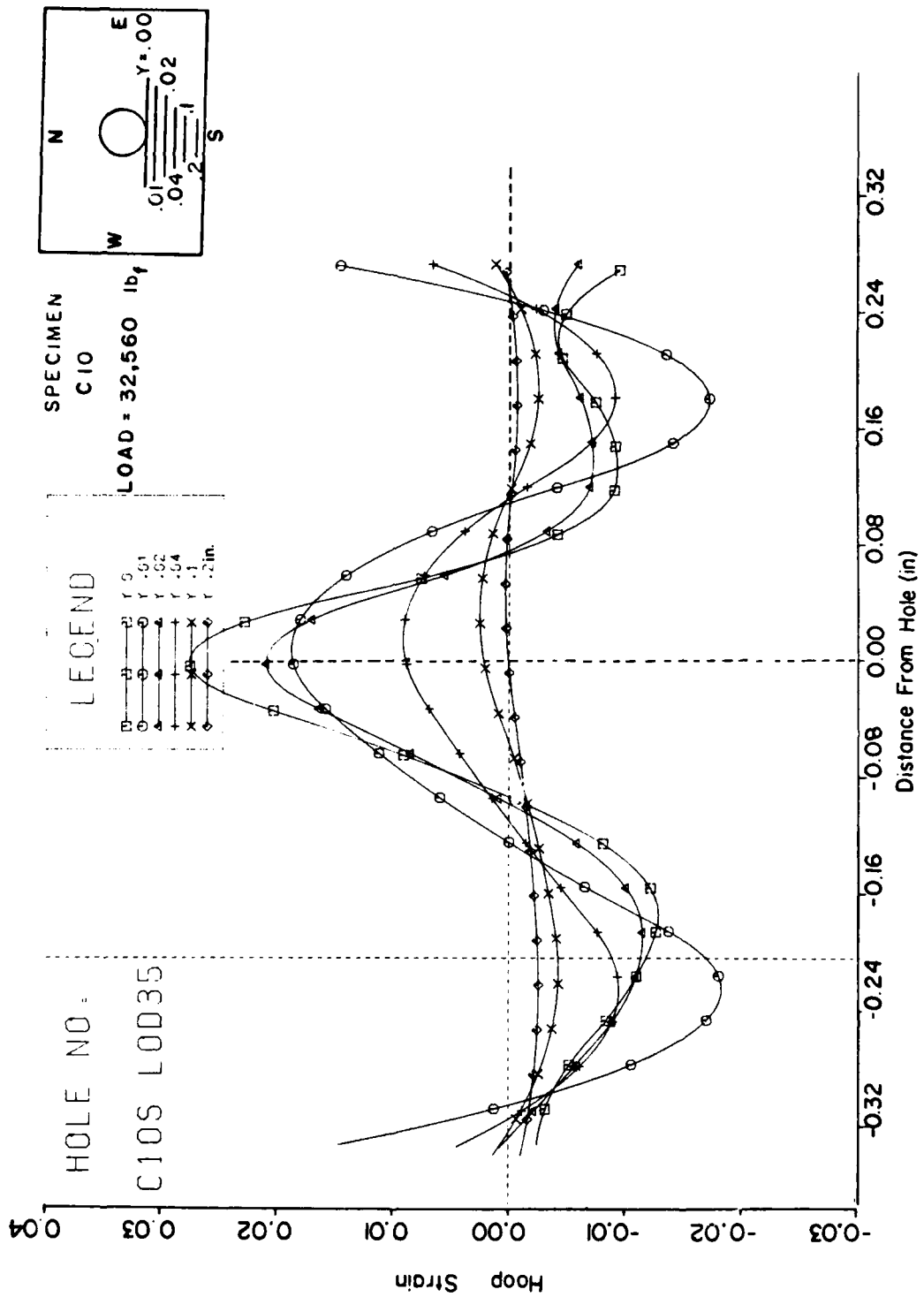


Figure 5.11 Residual Axial Hoop Strain Distributions Along Several Axes for 7.2 mils Radial Interference (32,560 lb<sub>f</sub>).

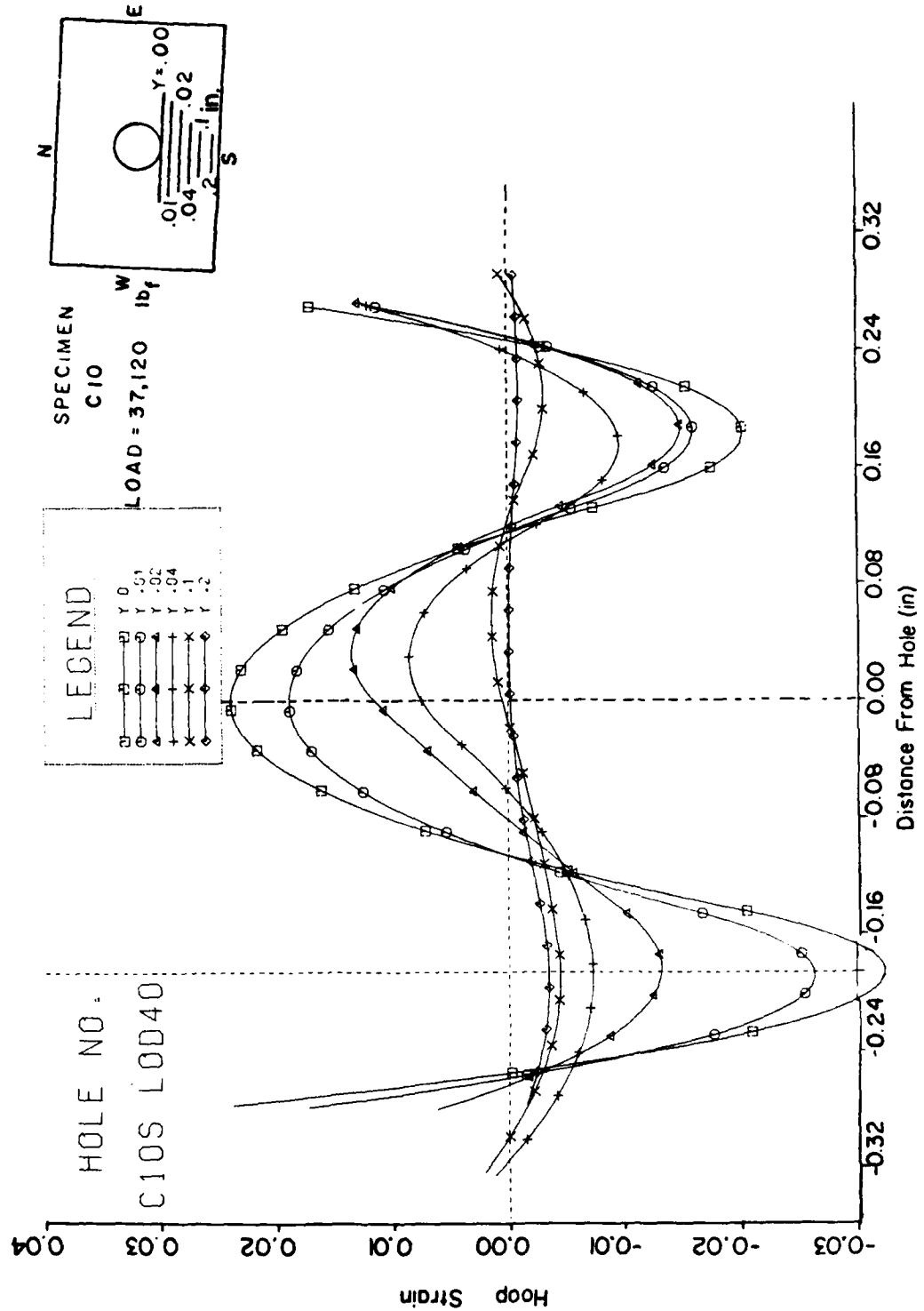


Figure 5.12 Residual Axial Hoop Strain Distributions Along Several Axes at Different Radial Distances for 7.2 mils Radial Interference (Load 37,120 lb<sub>f</sub>).

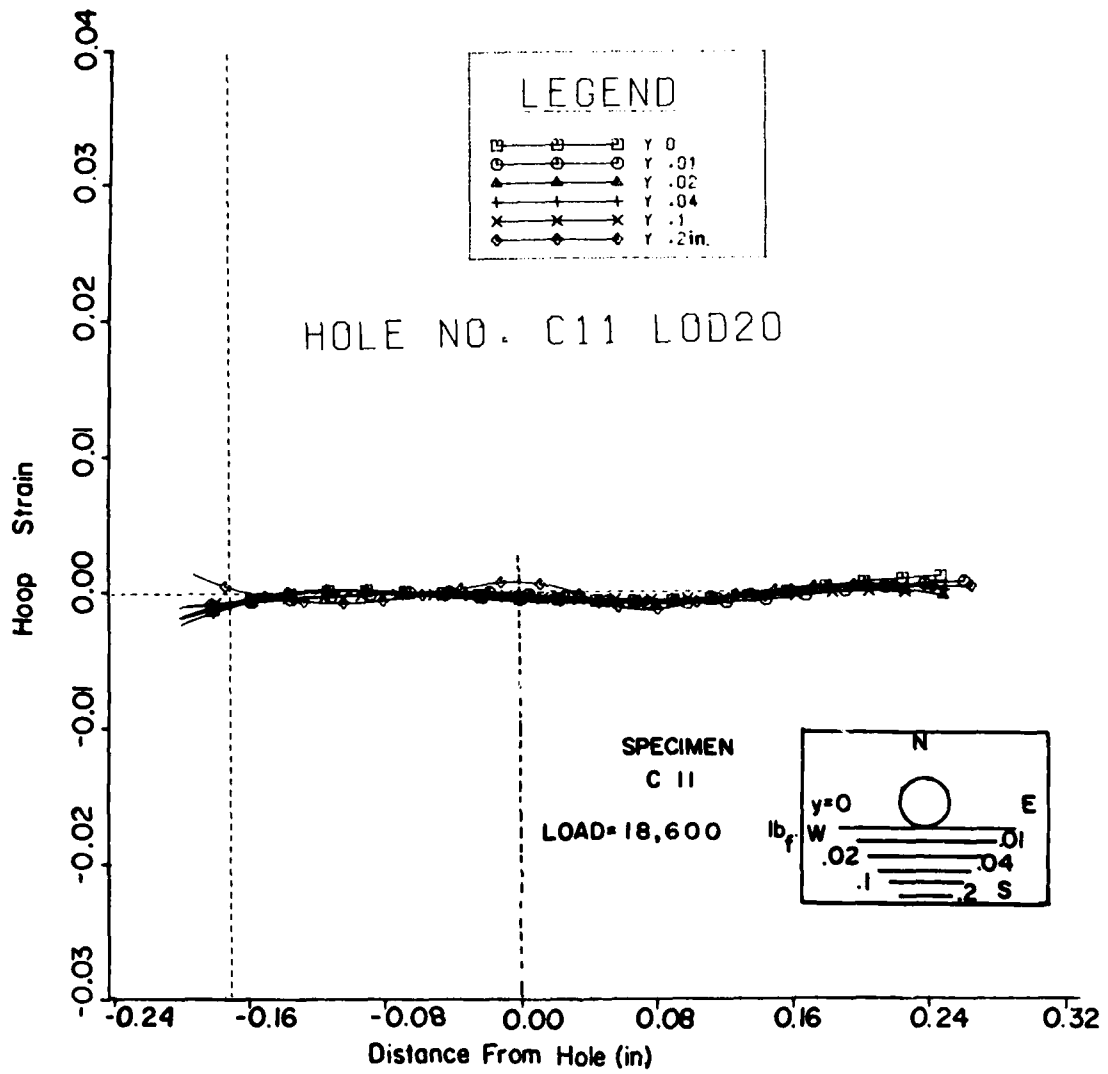


Figure 5.13 Measured Residual Axial Hoop Strain Distributions Along Several Axes Near a Non-Coldworked Hole (Load 18,600 lb<sub>f</sub>).

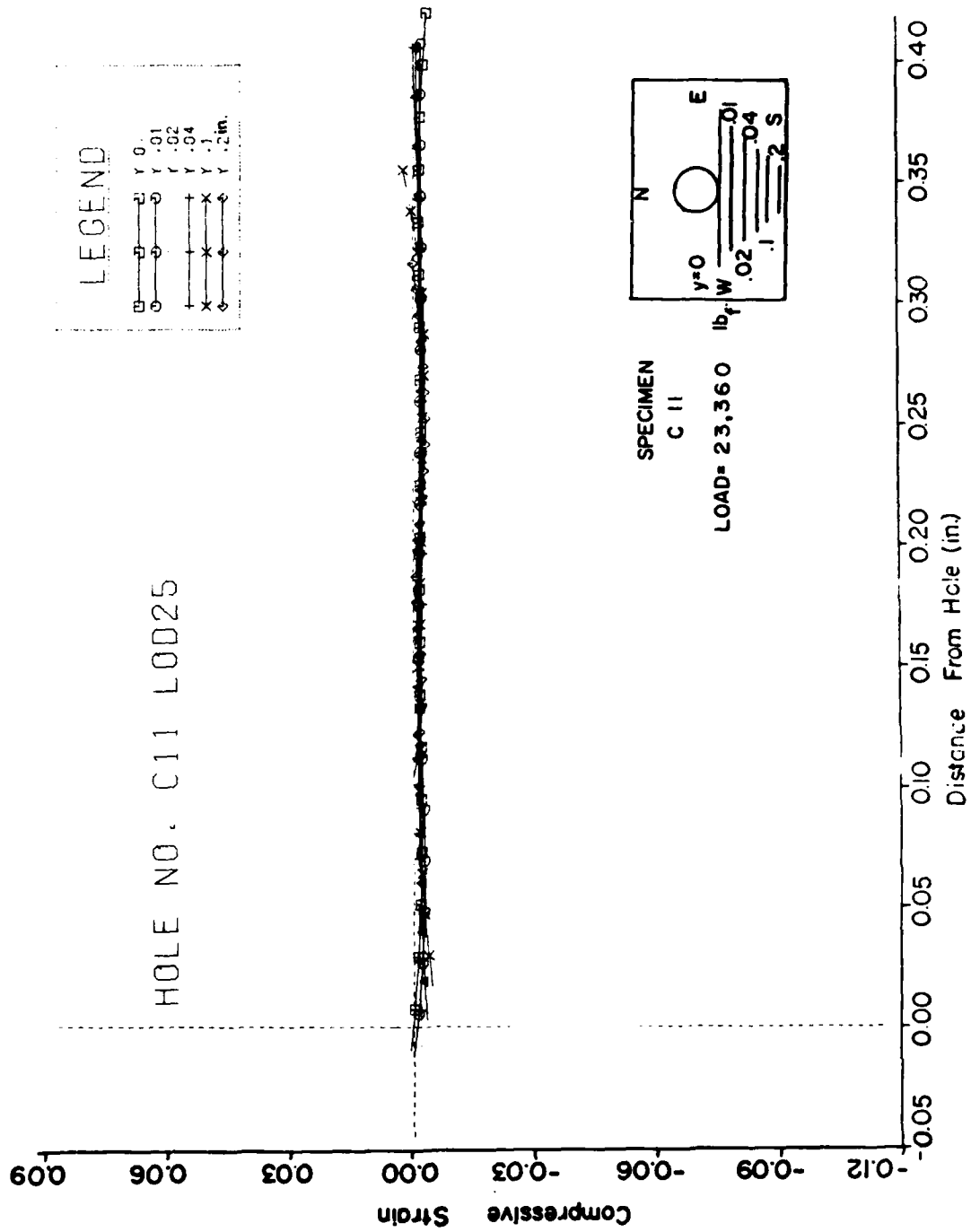


Figure 5.14 Measured Residual Axial Hoop Strain Distributions Along Several Axes Near a Non-Coldworked Hole (Load 23,360 lb<sub>f</sub>).

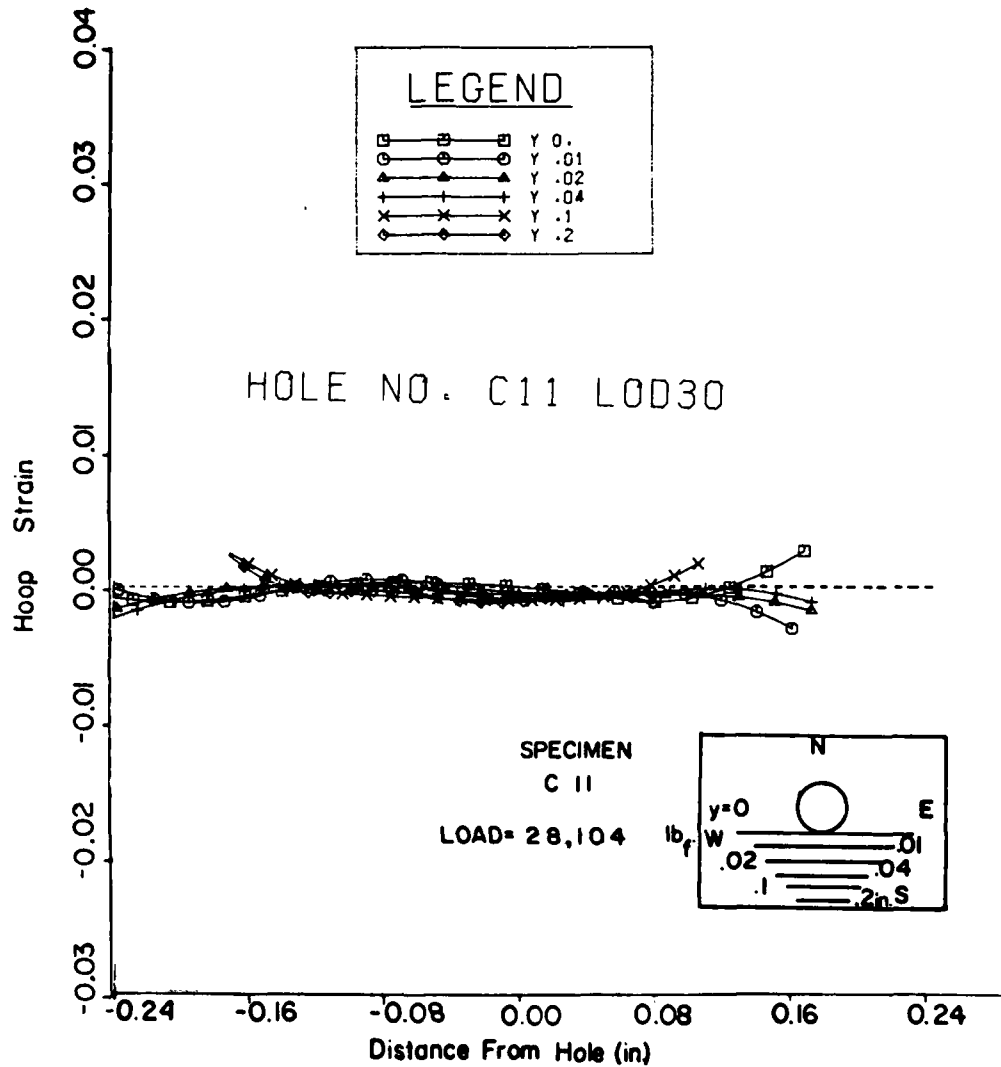


Figure 5.15 Measured Residual Axial Hoop Strain Distributions Along Several Axes at Different Radial Distances for 6.5 mils Radial Interference (Load 28,104 lb<sub>f</sub>).

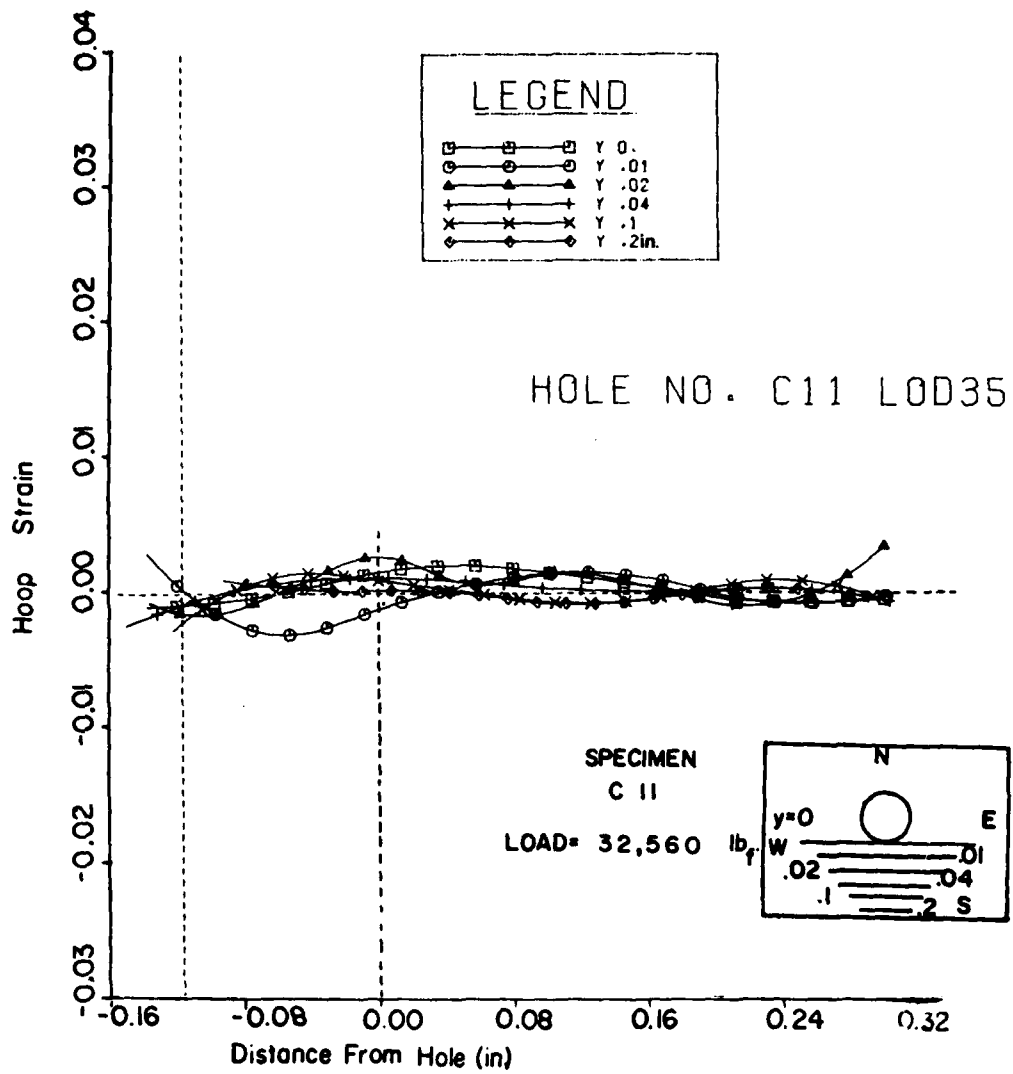


Figure 5.16 Measured Residual Axial Hoop Strain Distributions Along Several Axes Near a Non-Coldworked Hole (Load 32,560 lb<sub>f</sub>).

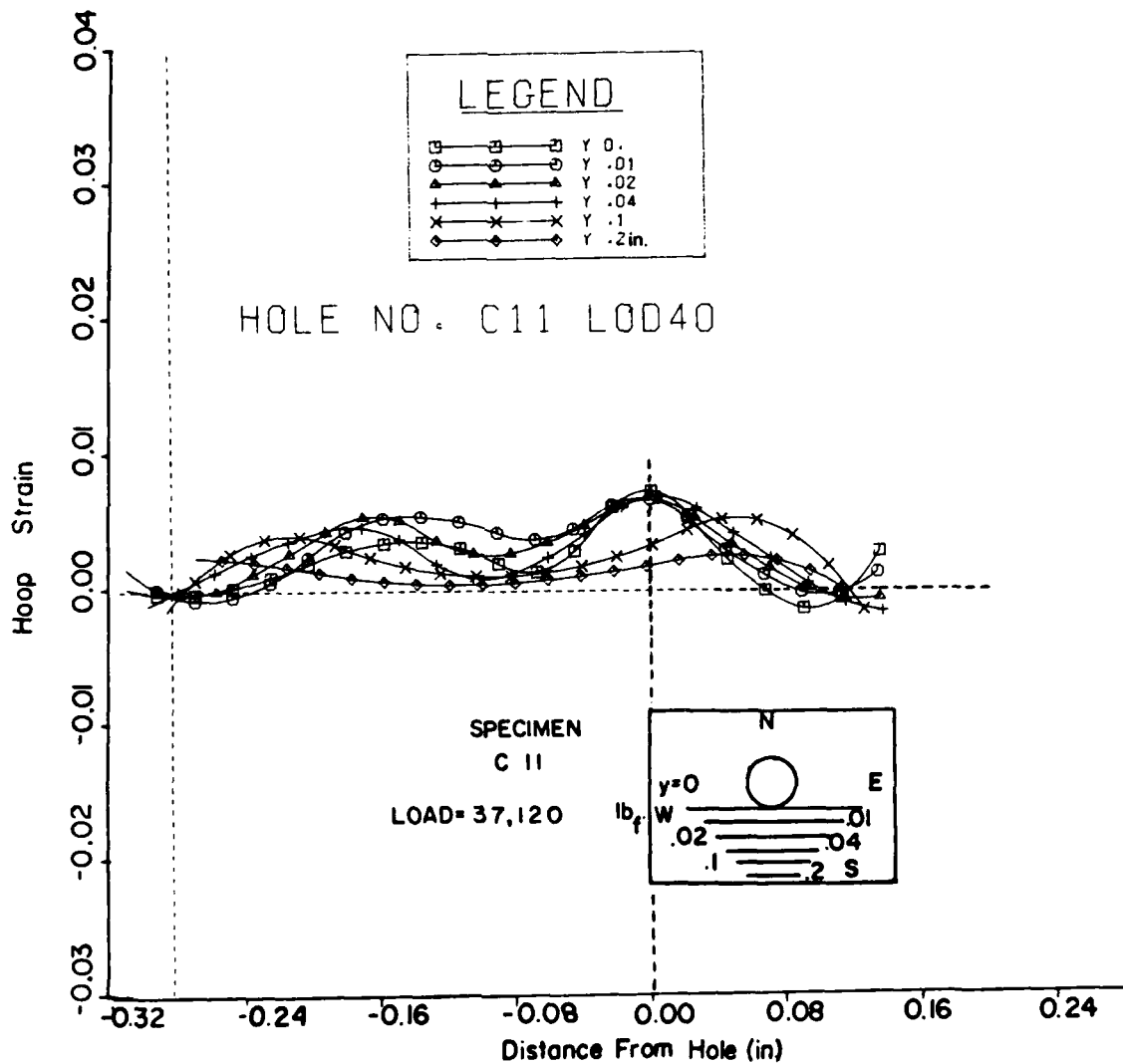


Figure 5.17 Measured Residual Axial Hoop Strain Distribution Along Several Axes Near a Non-Coldworked Hole (Load 37,120 lb<sub>f</sub>).

the hole centerline at various locations,  $y$ , for specimens C9, C10 and C11.

The axial hoop strain evaluation for specimens C9, C10 and C11 were performed along the axes labeled  $y=0.00$ ,  $y = 0.01$  in. (0.254 mm),  $y = 0.02$  in. (0.508 mm),  $y = 0.04$  in. (1.016 mm), and  $y = 0.1$  in. (2.54 mm), where  $y = 0.00$  was an axis drawn tangent to the fastener hole parallel to the direction of loading, and the rest of the axes were arbitrarily marked off relative to it to facilitate the determination of the strain distribution at different distances from the hole boundary.

The figures indicate that at approximately a radial distance from the point at which the residual hoop strains attain their maximum values, the residual strain passes through zero and then attains a local minimum before vanishing entirely in progressing to the edge of the plate along any one of the  $y$  axes. The region gets wider and wider with higher compressive loads. The residual hoop strain at the hole edge decreases with the applied load until a point of instability is reached, a possible indication being the increasing fluctuation (oscillation) of the strains as the buckling (failure) load is approached. (See Figures 5.12 and 5.17).

The plot of Figure 5.8 for specimen C9 portrays the variation of this residual strain distribution with  $y$ . The slight variation in the magnitude of the strains is due to slight differences in radial interference employed.

The results for specimen C10 are included here to emphasize the unsymmetric nature of the mandrelizing process. Analytical solutions to the basic problem of expanding a hole in a plate assume a rotationally symmetric state of plane plastic strain or stress. Figure 5.8 and Figure 5.9 show a strain component for two sides of the centerline. For the former set of plots the assumption of symmetry is probably satisfactory. But Figure 5.9 indicates that such an assumption is not always valid, and could lead to serious errors in the practical application of this process by the designer.

For a rotationally symmetric process some kind of duplication would be expected in the results; however, these plots show quite a variation in the strain magnitudes and indicate that, for this specimen, there may have been asymmetries in the loading under which the left side of the hole would yield first under high in-plane compressive loads.

#### 5.4.2 Transverse Hoop Strain Distribution

Figures 5.18 through 5.28 which were processed from data measured from grating lines along the loading axis, reveal that transverse hoop strain increases with increasing remote applied loads within an annulus bounded by an approximate radial distance  $x = 0.07$  in. (1.78 mm) and the fastener hole boundary. Further away from the hole the effect of the applied stress is negligible.

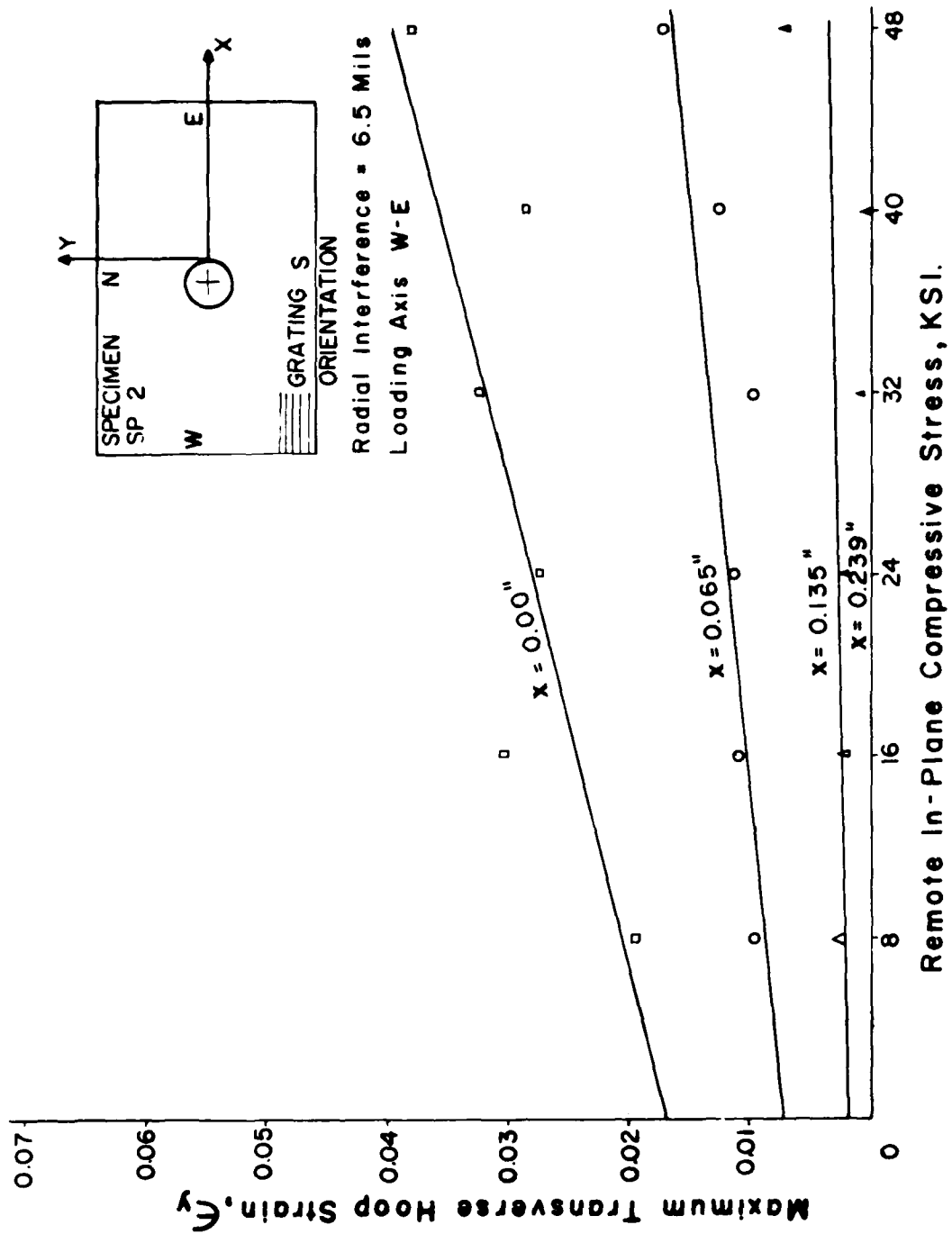


Figure 5.18 Effect of In-Plane Compression on Residual Transverse Maximum Hoop Strain Distributions at a Point on Hole Boundary (Specimen SP 2).

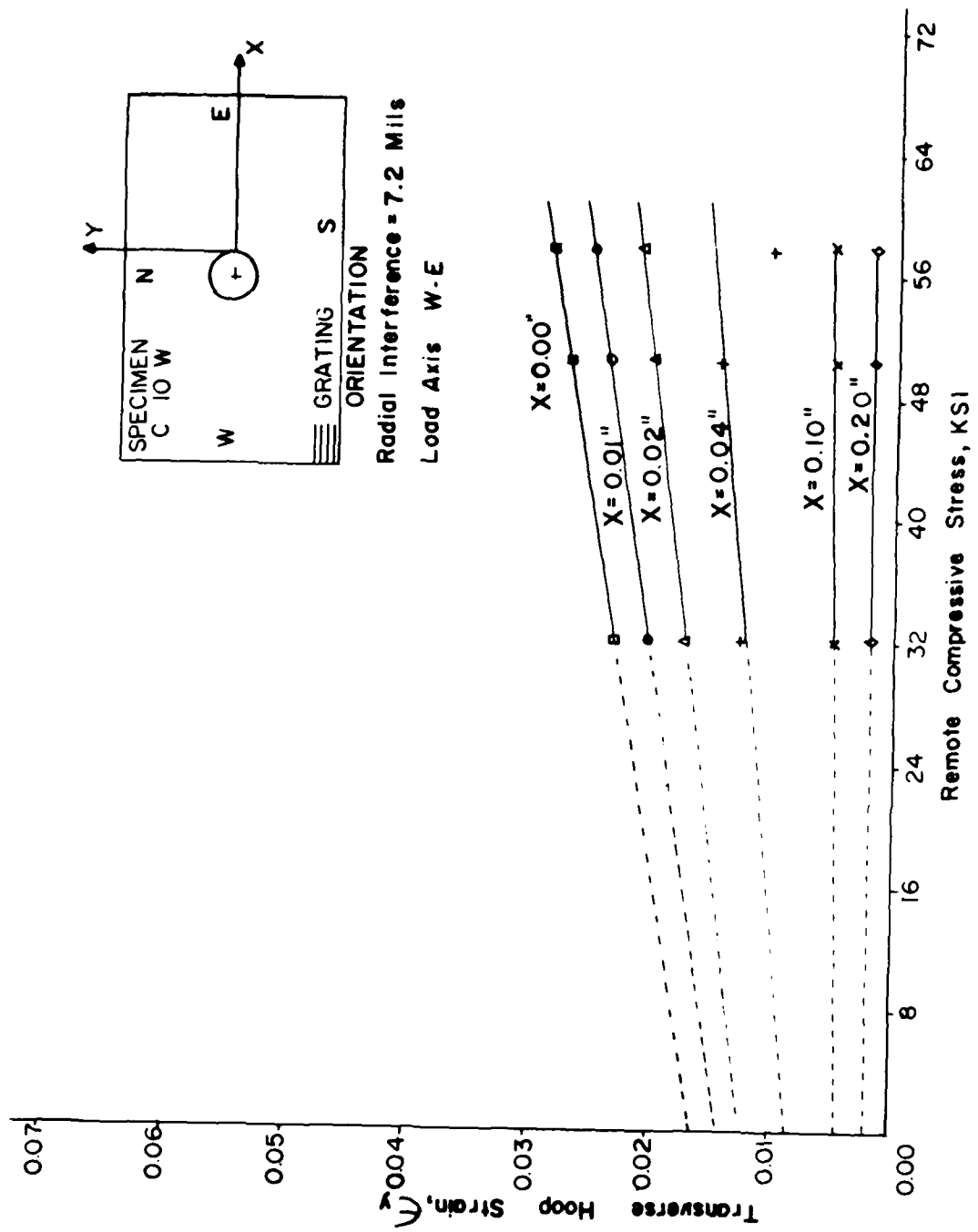


Figure 5.19 Effect of In-Plane Compression on Residual Transverse Maximum Hoop Strain Distributions at a Point on Hole Boundary (Specimen C 10).

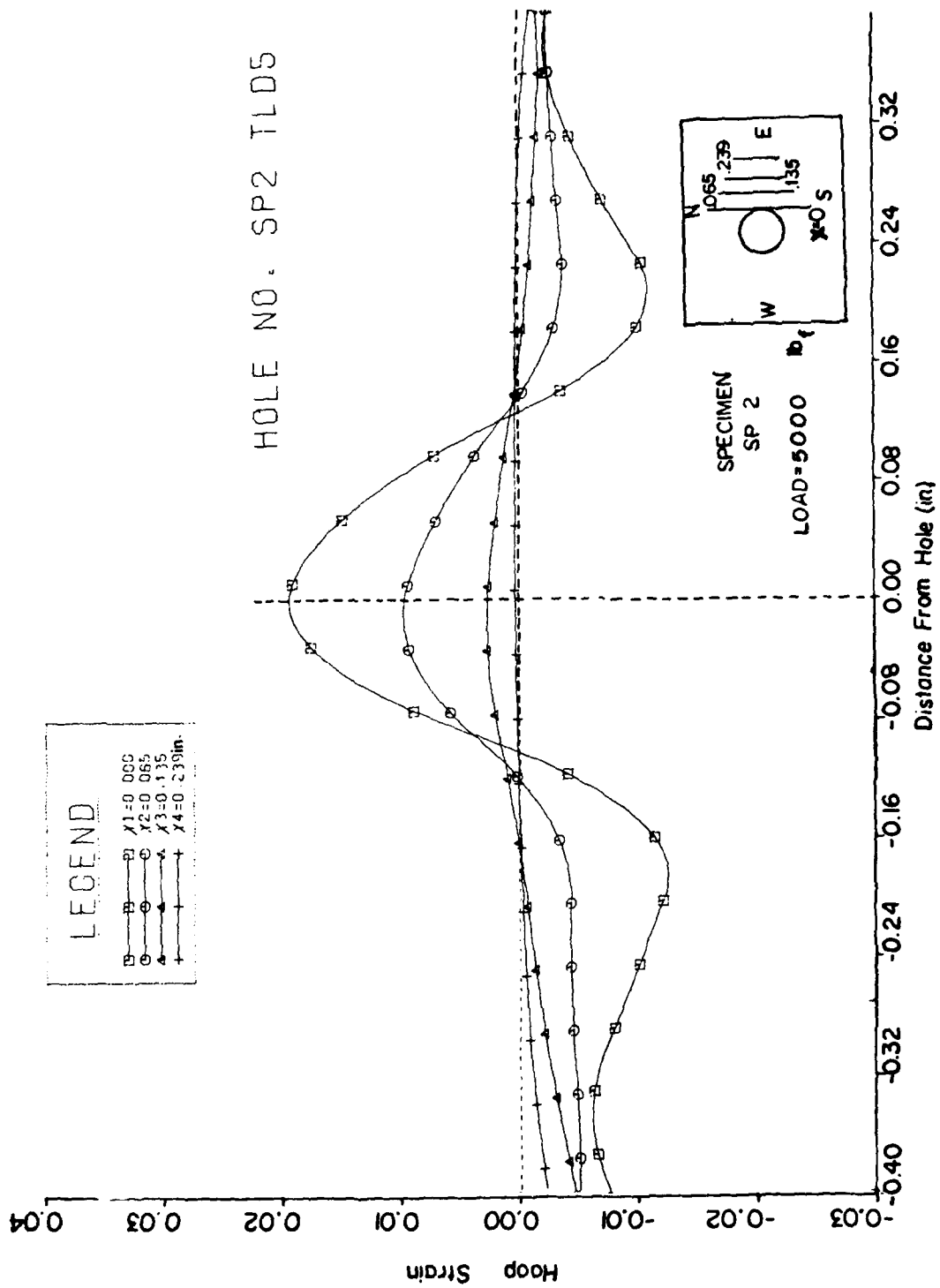


Figure 5.20 Measured Residual Transverse Hoop Strain Distributions Along Several Axes at Different Radial Distances for 6.5 mils Radial Interference (Load 5,000 lb<sub>f</sub>).

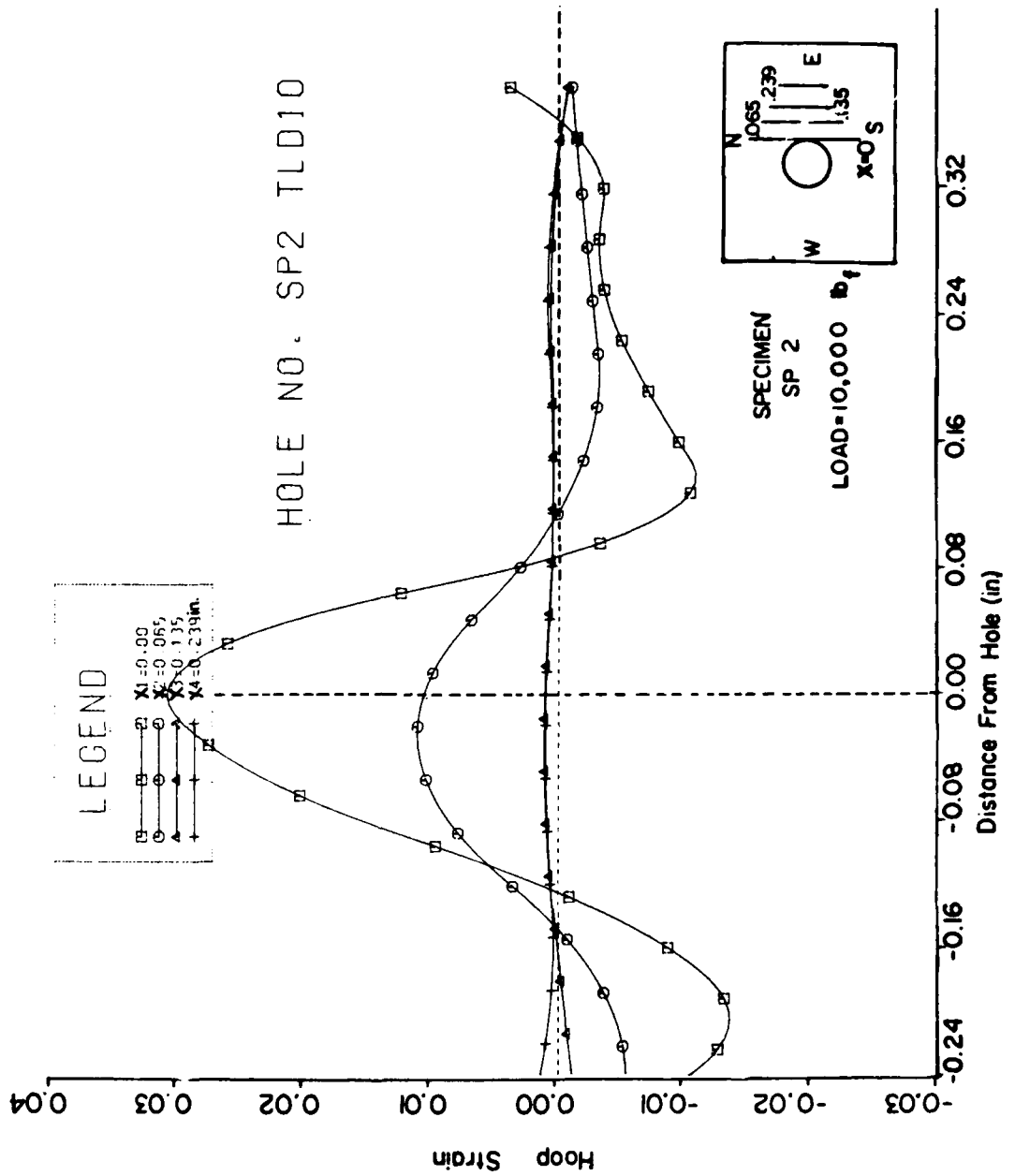


Figure 5.21 Measured Residual Transverse Hoop Strain Distributions Along Several Axes at Different Radial Distances for 6.5 mils Radial Interference (Load 10,000  $lb_f$ ).

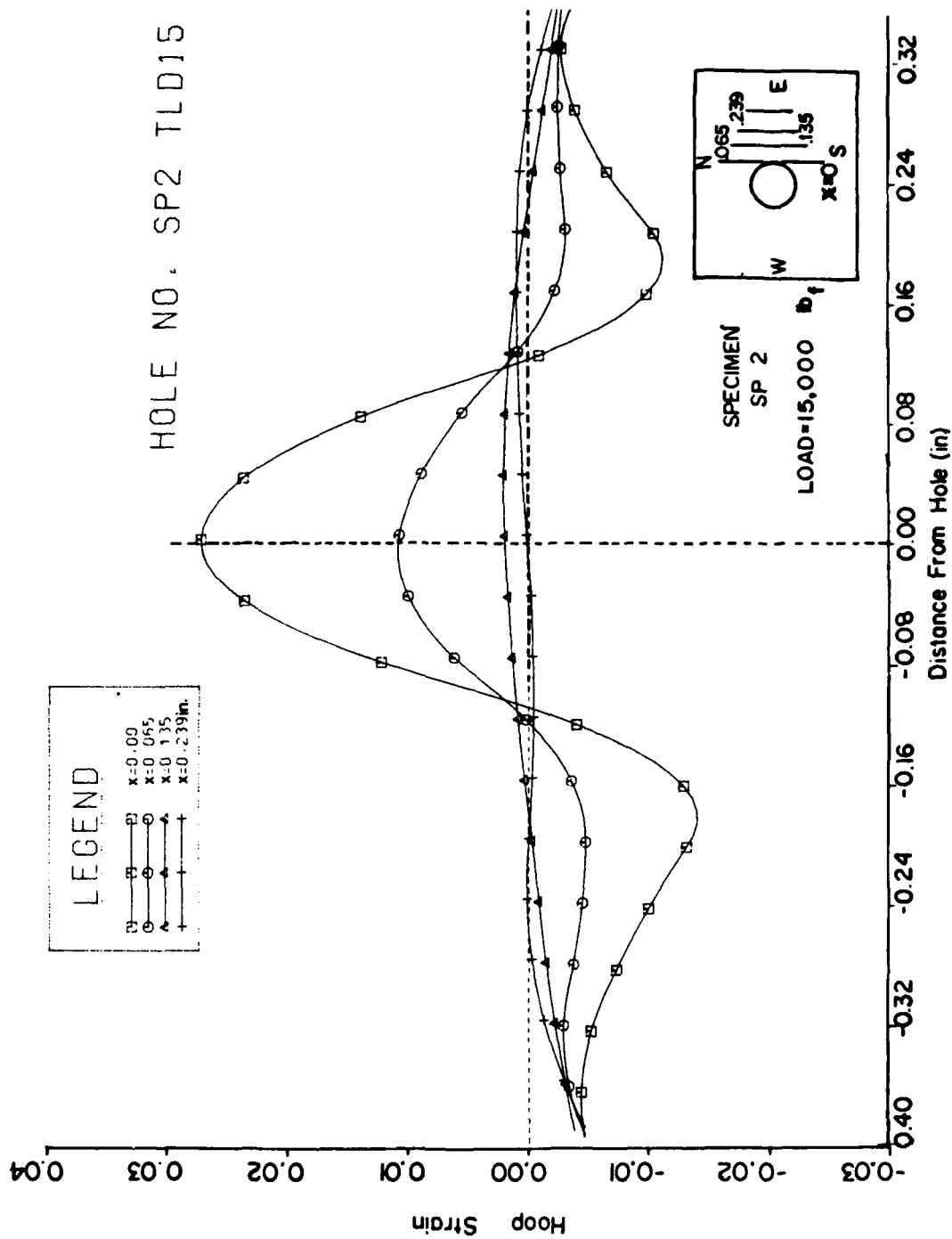


Figure 5.22 Measured Residual Transverse Hoop Strain Distributions Along Several Axes at Different Radial Distances for 6.5 mils Radial Interference (Load 15,000 lb<sub>f</sub>).

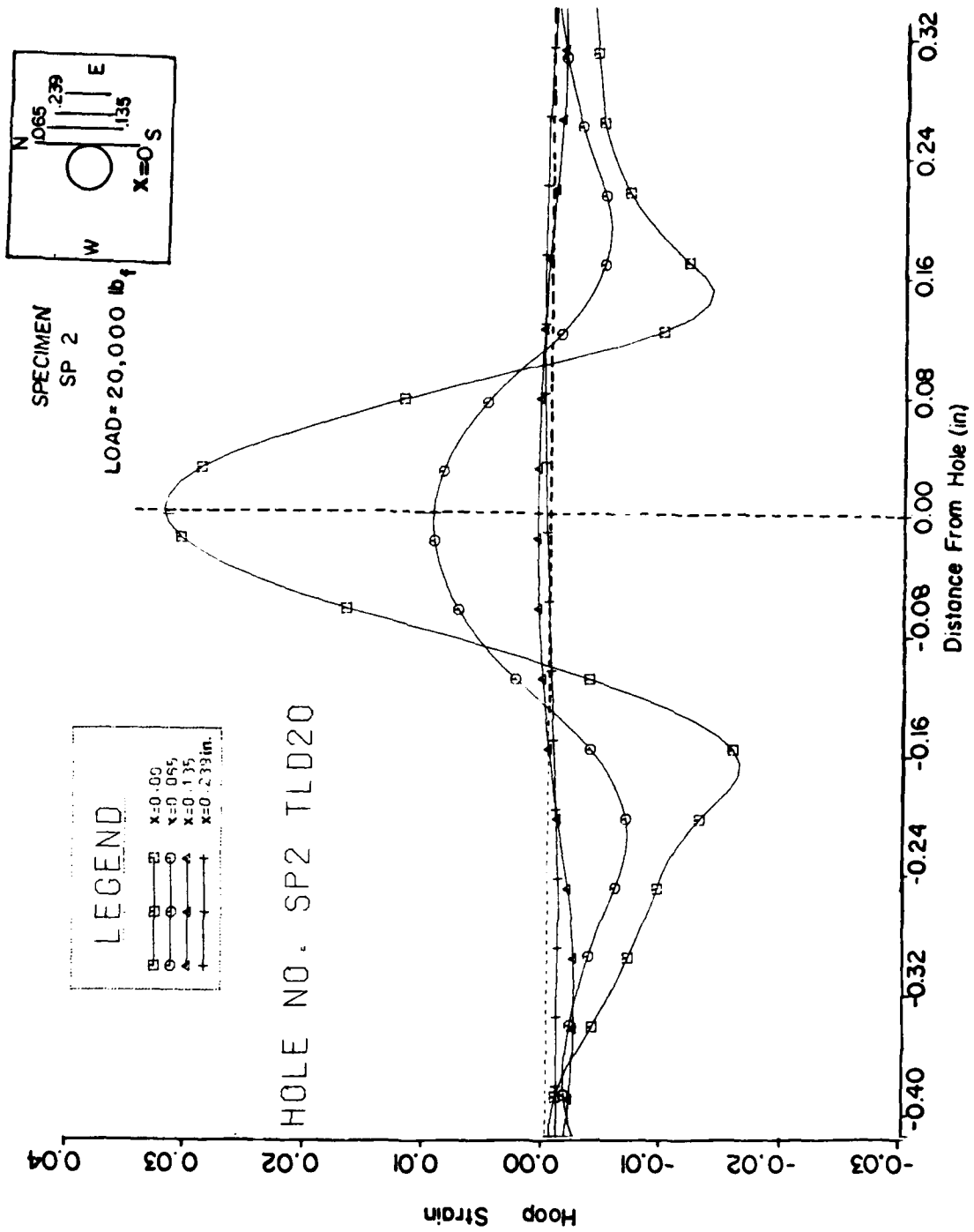


Figure 5.23 Measured Residual Transverse Hoop Strain Distributions Along Several Axes at Different Radial Distances for 6.5 mils Radial Interference (Load 20,000 lb<sub>f</sub>).

HOLE NO: SP2 TLD25K

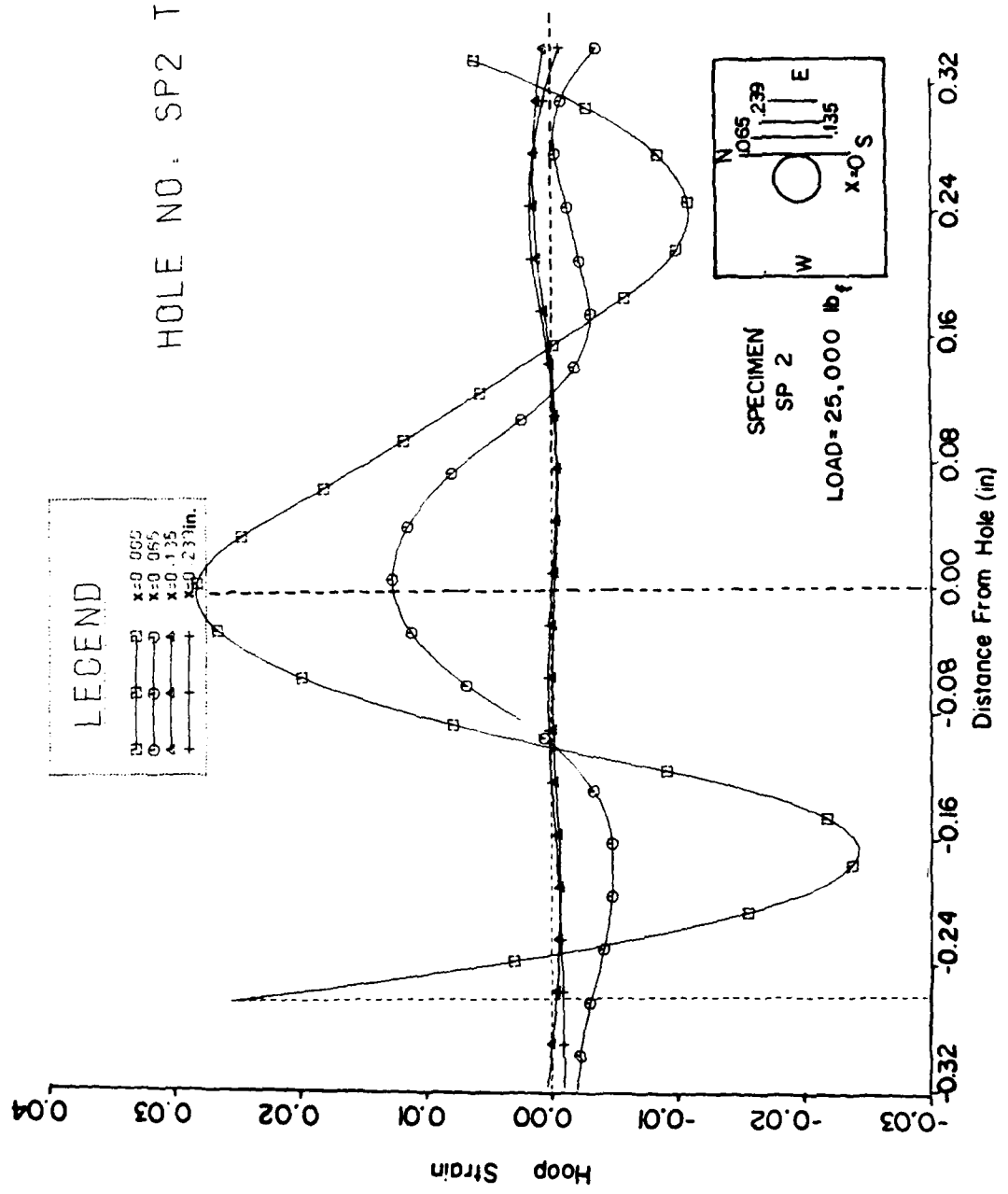


Figure 5.24 Measured Residual Transverse Hoop Strain Distributions Along Several Axes at Different Radial Distances for 6.5 mils Radial Interference (Load 25,000 lb<sub>f</sub>).

HOLE NO. SP2 TLD30

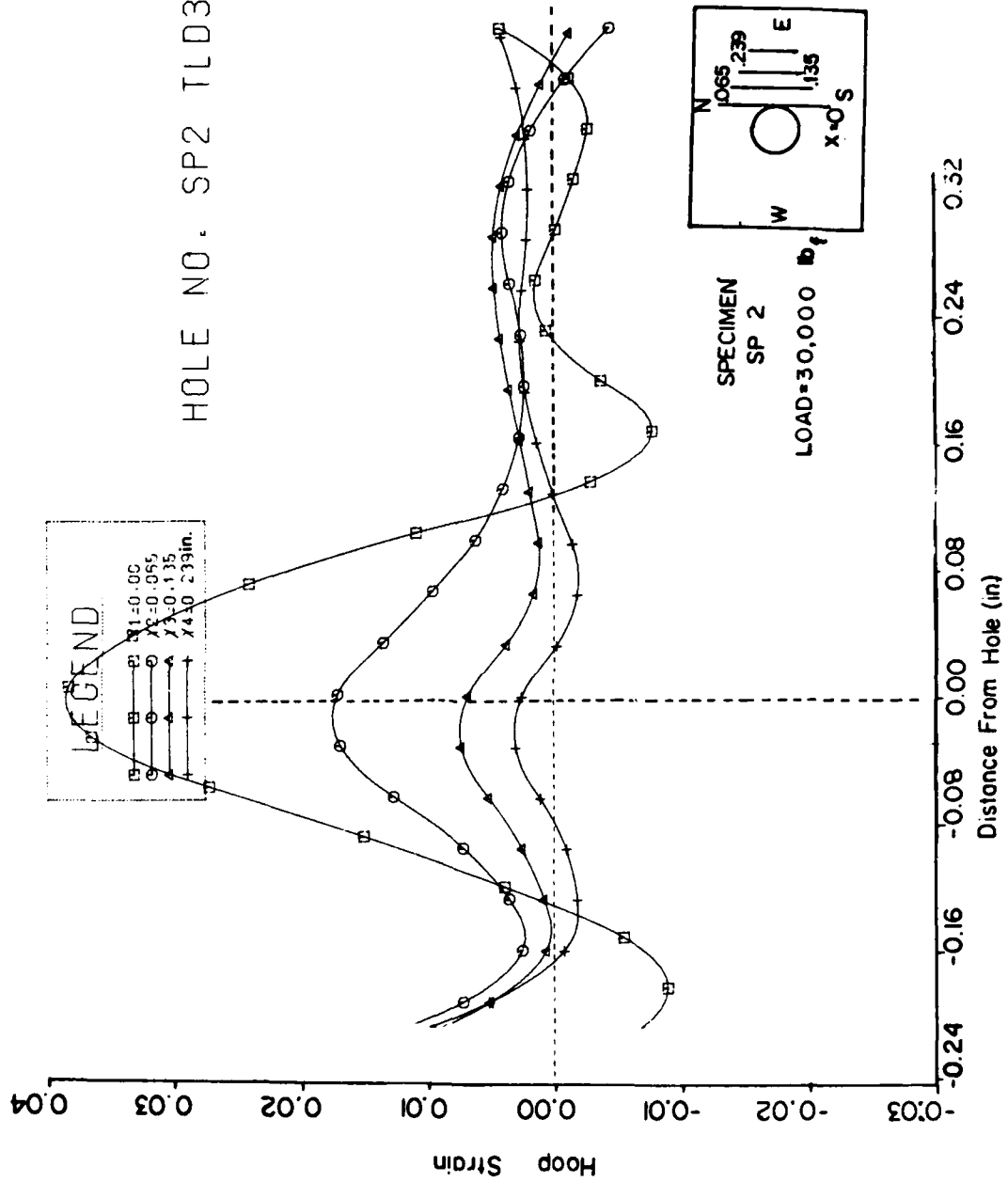


Figure 5.25 Measured Residual Transverse Hoop Strain Distributions Along Several Axes at Different Radial Distances for 6.5 mils Radial Interference (Load 30,000 lb<sub>f</sub>).

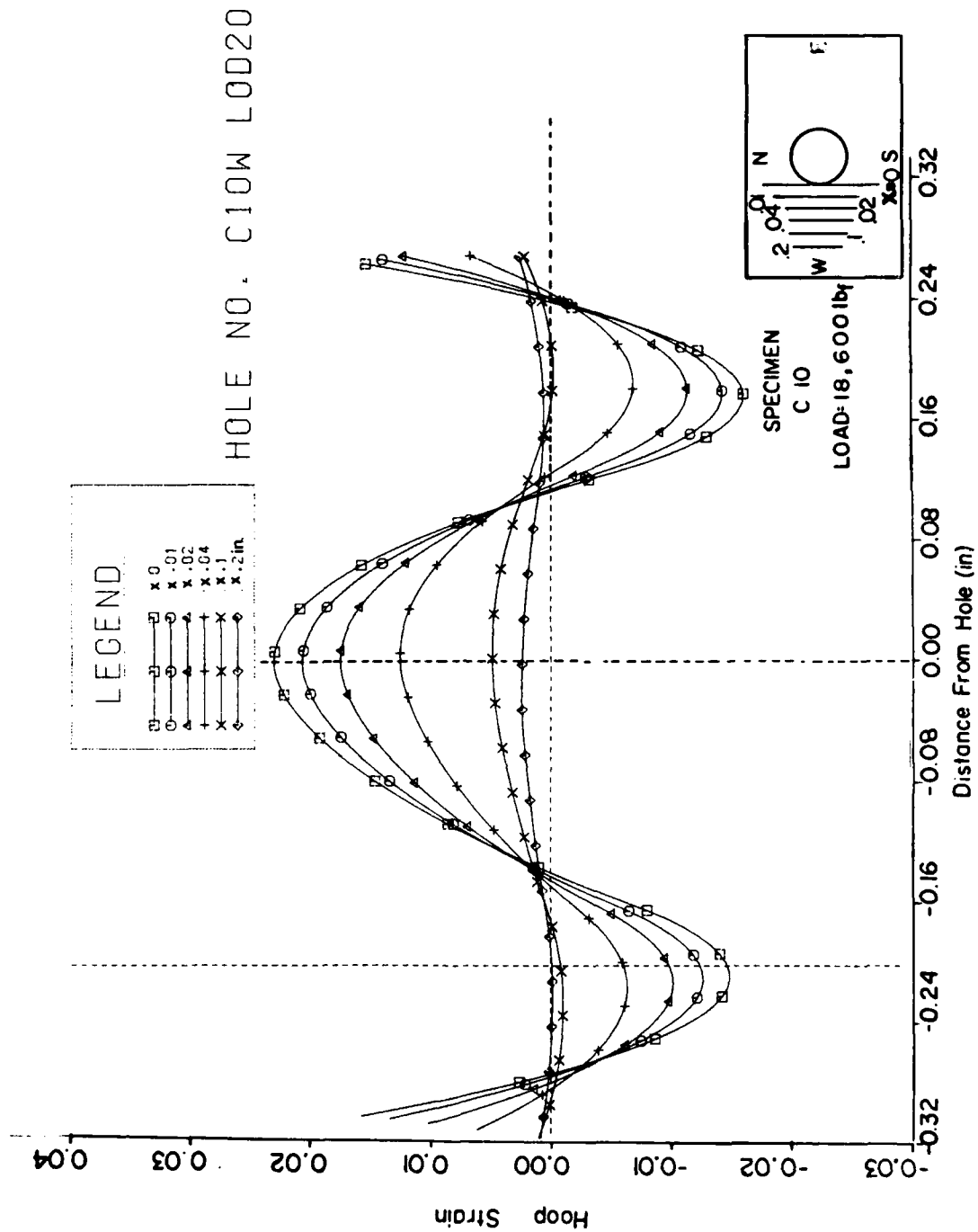


Figure 5.26 Residual Transverse Hoop Strain Distributions Along Several axes for 7.2 mils Radial Interference (Load 18,600 lb<sub>f</sub>).

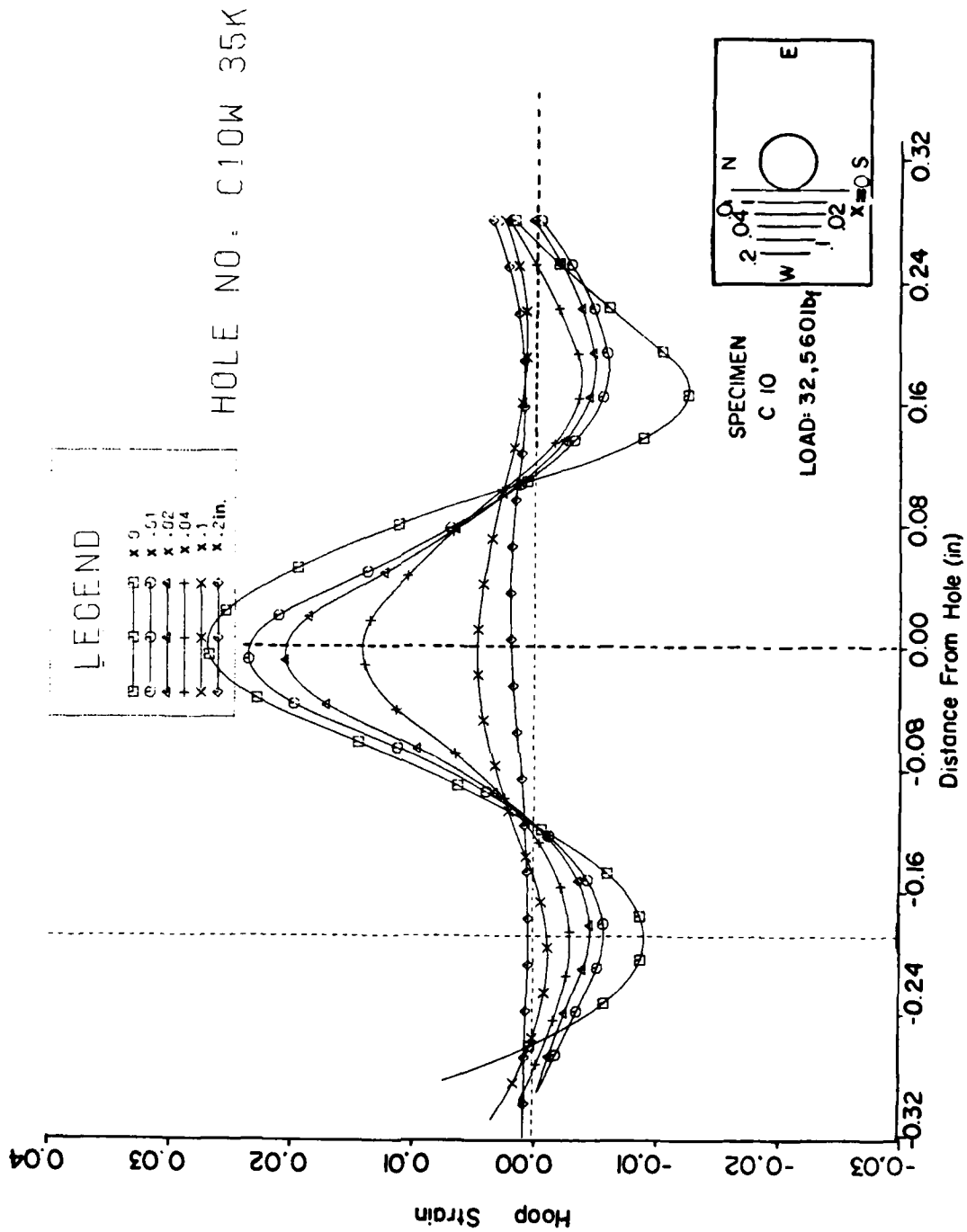


Figure 5.27 Residual Transverse Hoop Strain Distributions Along Several Axes for 7.2 mils Radial Interference (Load 32,560 lb<sub>f</sub>).

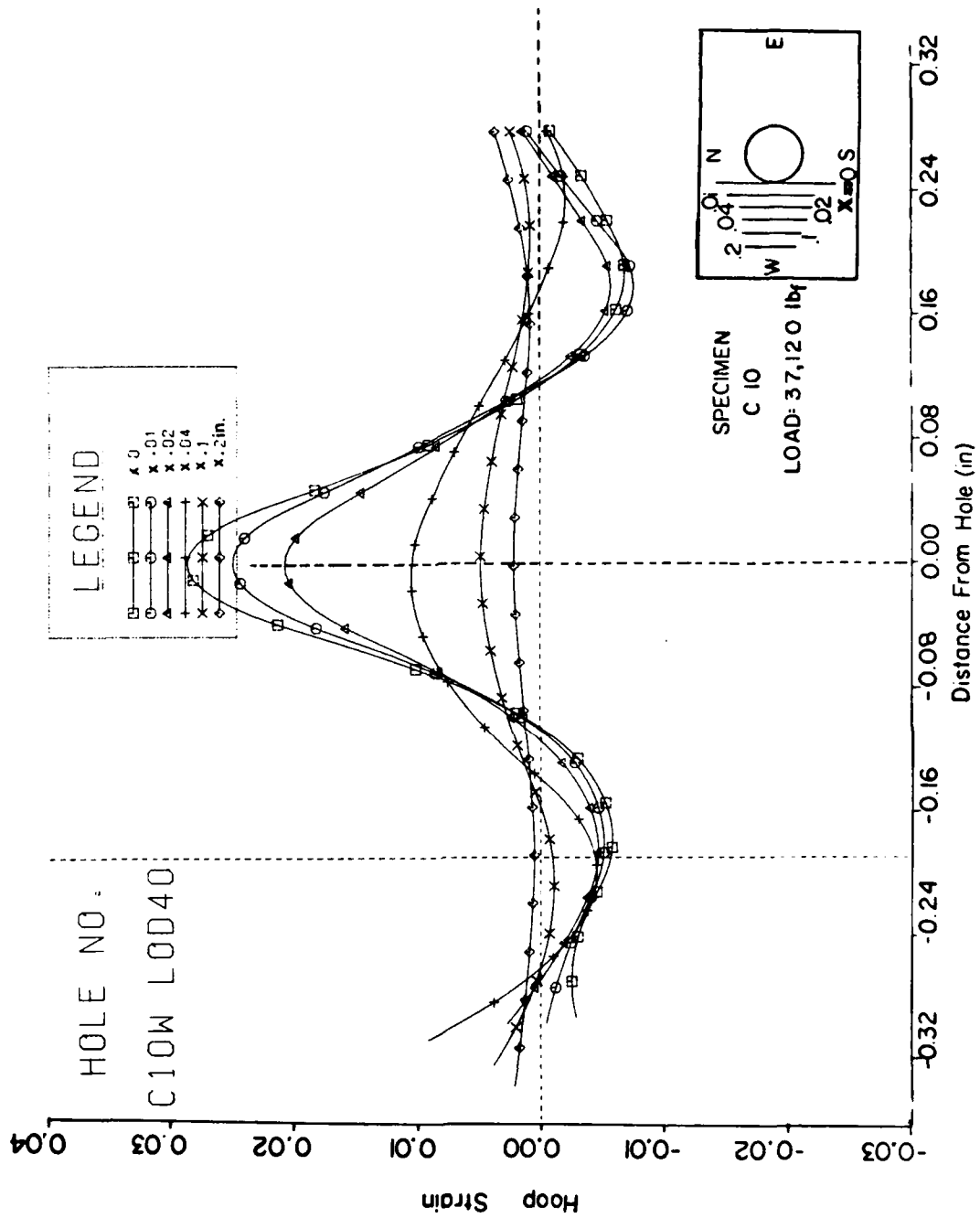


Figure 5.28 Residual Transverse Hoop Strain Distributions Along Several Axes for 7.2 mils Radial Interference (Load 37,120 lb<sub>f</sub>).

Cycling at 24 ksi (165 MPa) does not seem to alter these observations since the transverse hoop strain evaluation for C10 (Figure 5.19) is similar to that of SP2 (Figure 5.18) both in magnitude and rate of increase with the applied remote compressive loads.

For specimen SP2 the detailed hoop strain evaluation was performed along the axes  $X = 0.00$  in,  $X = 0.065$  in. (1.65 mm),  $X = 0.135$  in. (3.43 mm) and  $X = 0.239$  in. (6.07 mm), where the axes are oriented as shown in Figure 5.18. These results are shown in Figures 5.20 through 5.25. Specimen C10 results (Figure 5.19 and Figures 5.26 through 5.28) are in agreement with the trends illustrated via specimen SP2 that the strains increase with load.

The results for specimen SP1 are not reported because they turned out to be unreliable. Data for this specimen was obtained in the initial stages of the investigation before enough experience was gained.

#### 5.4.3 Radial Strain Distribution

Examination of the residual compressive strains reveal that for the case of a fastener hole in an infinite plate (semi-infinite to be exact) the strain distribution assumes an exponential nature see Figures 5.30 through 5.33. The strains attain their maximum value at the edge of the hole and rapidly diminish to zero with distance from the hole edge.

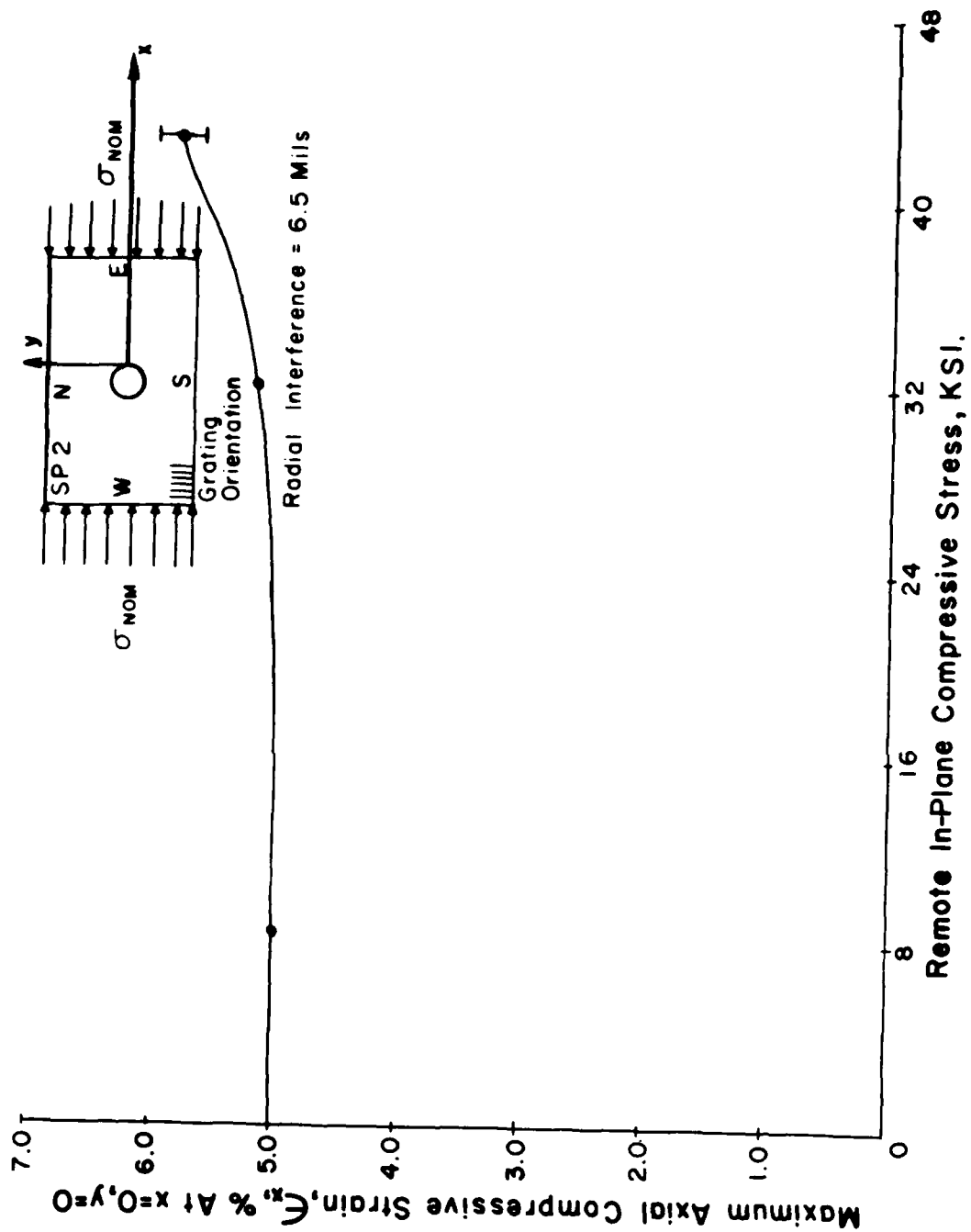


Figure 5.29 Effect of In-Plane Compression on Residual Axial Maximum Compressive Strain Distributions at a Point on Hole Boundary.

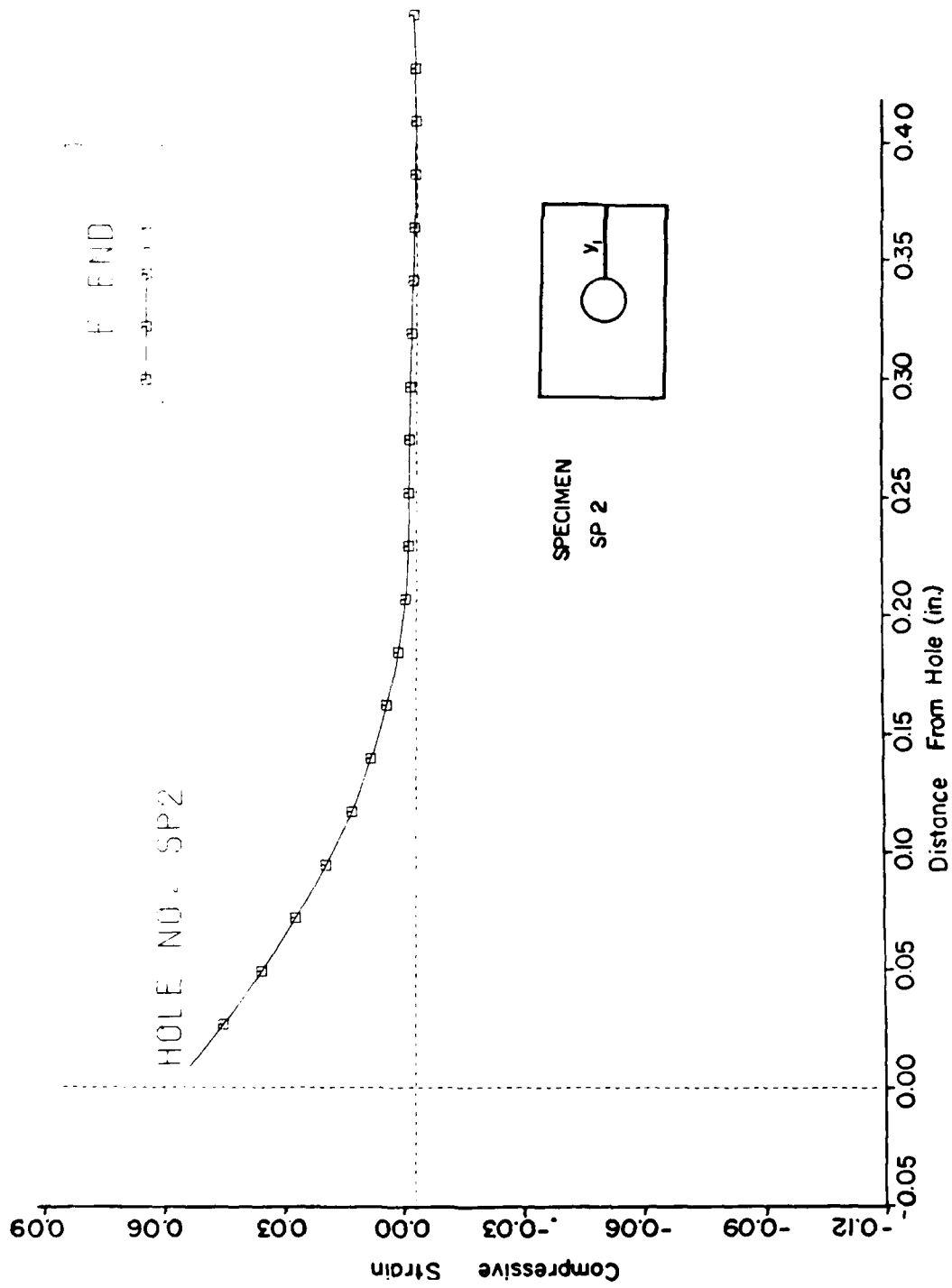


Figure 5.30 Compressive (Radial) Surface Strain Distribution Near a Coldworked Hole for 6.5 mils Radial Interference.

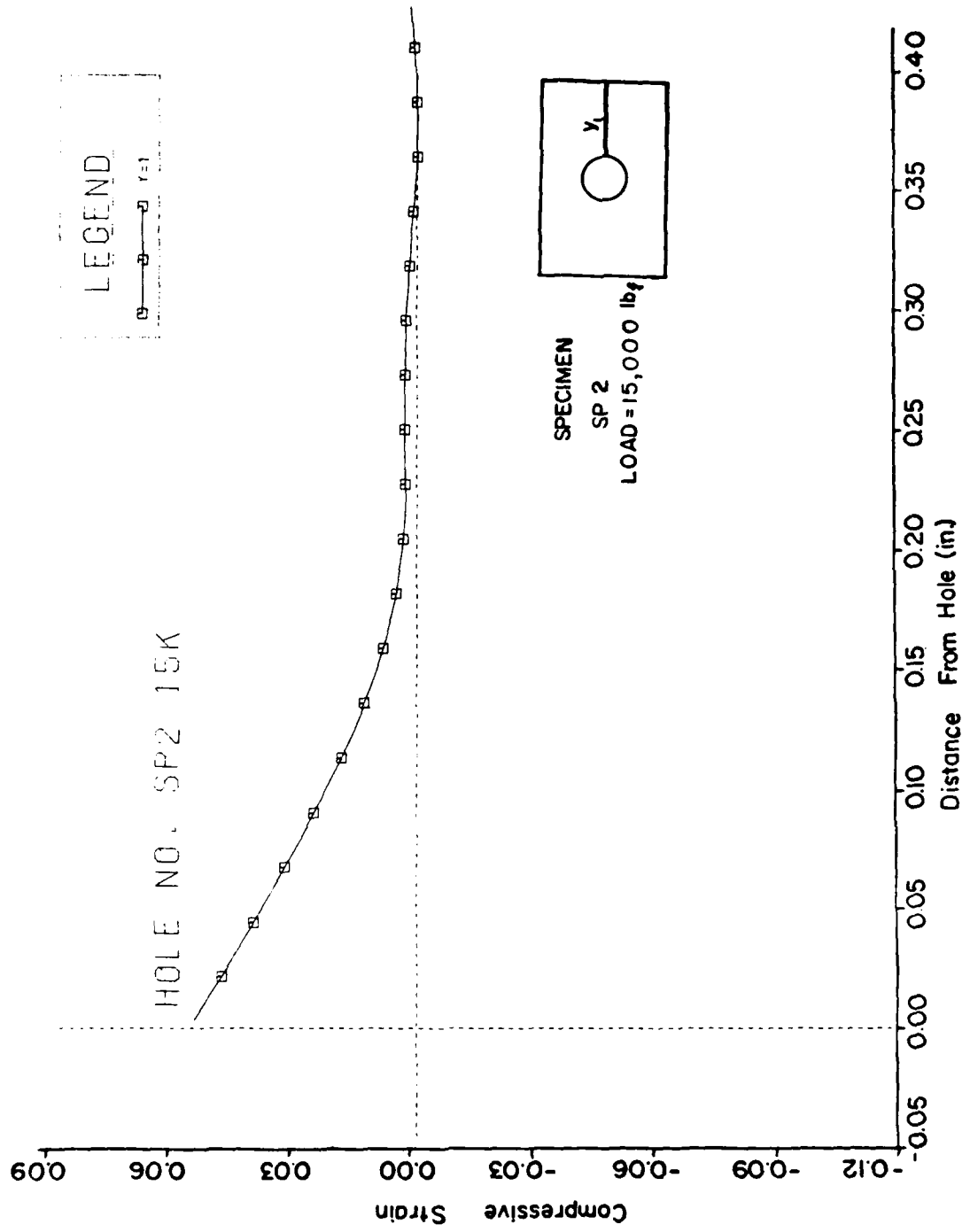


Figure 5.31 Compressive (Radial) Surface Strain Distribution Near a Coldworked Hole for 6.5 mils Radial Interference (Load 15,000 lb<sub>f</sub>).

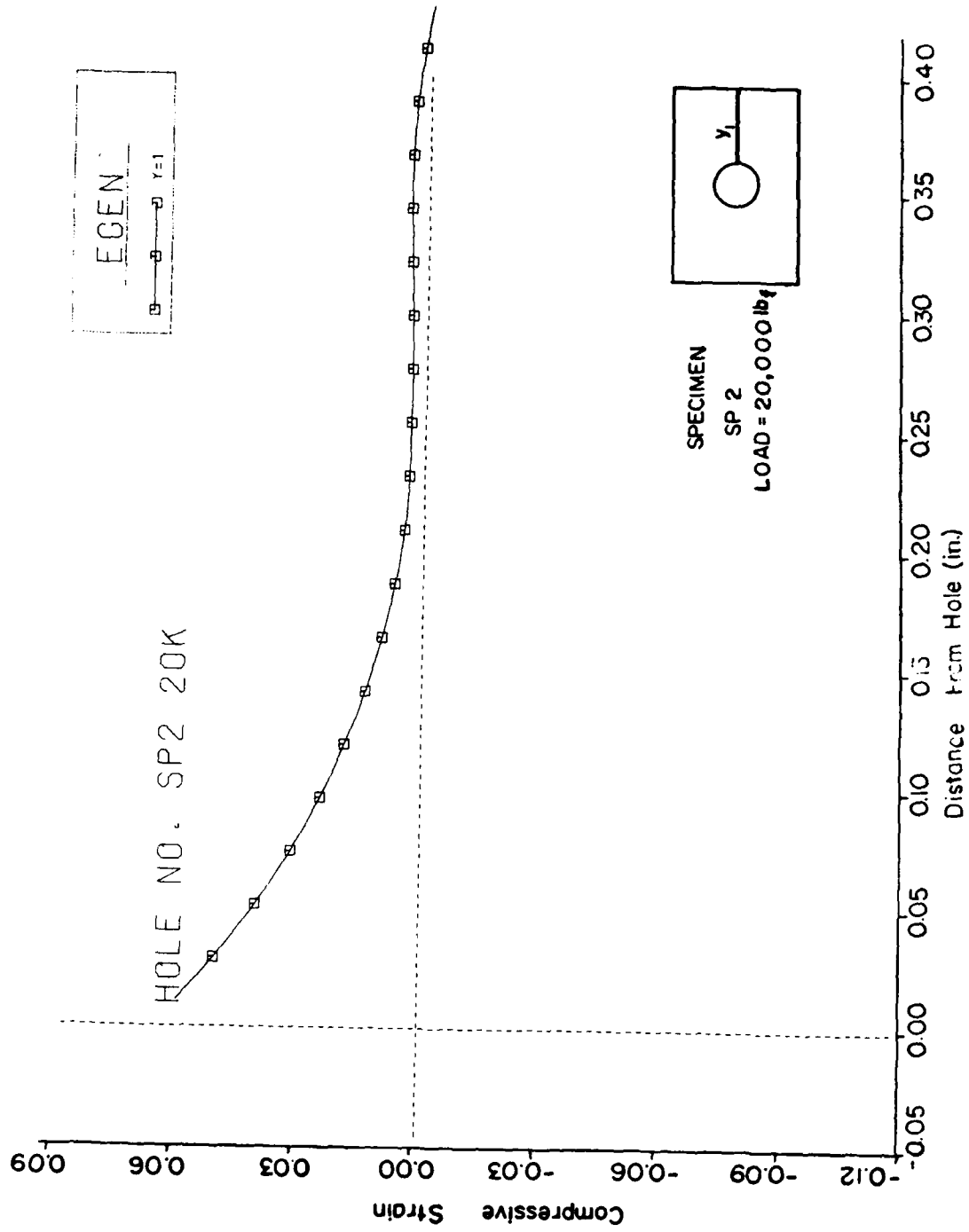


Figure 5.32 Compressive (Radial) Surface Strain Distribution Near a Coldworked Hole for 6.5 mils Radial Interference (Load 20,000 lb<sub>f</sub>).

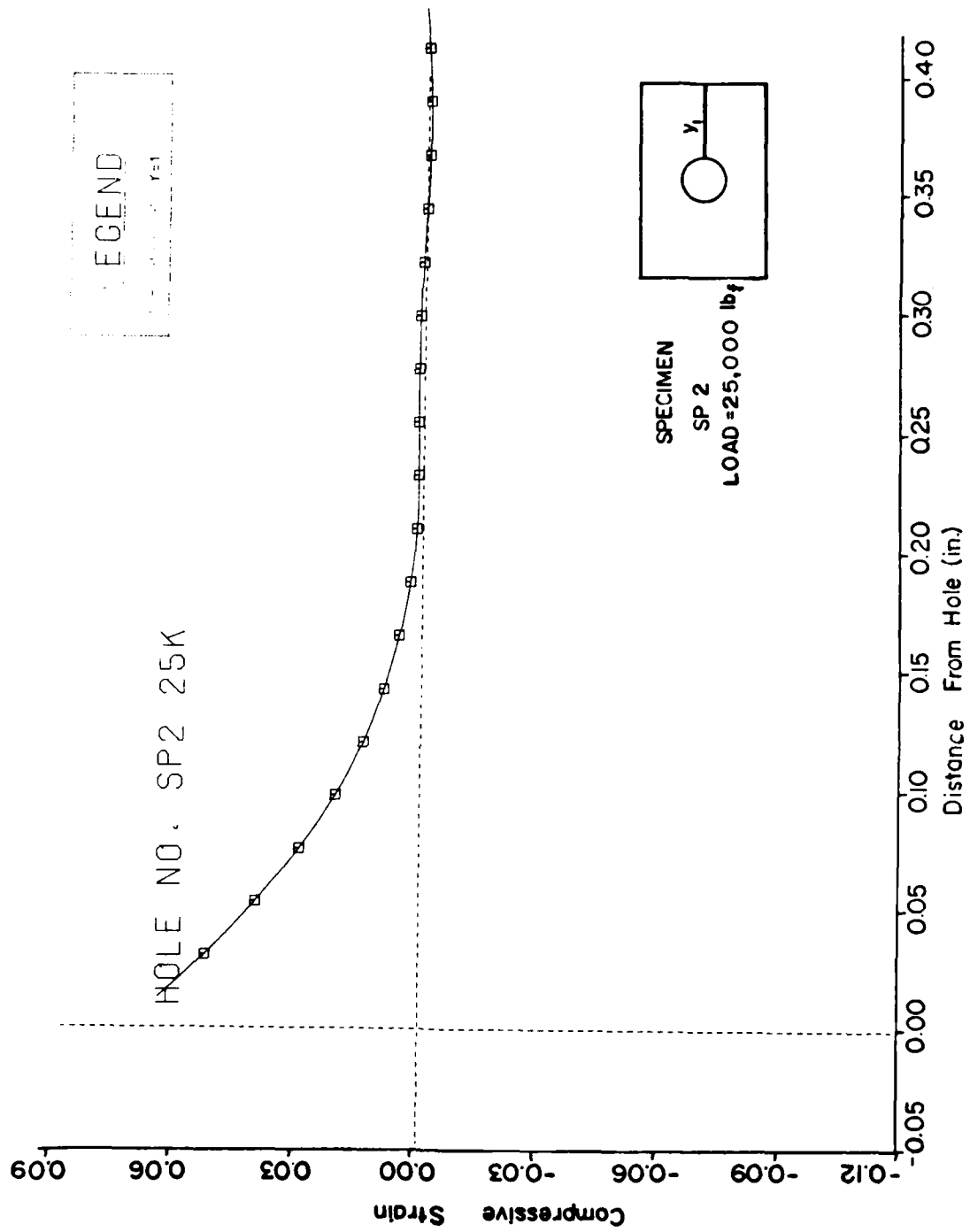


Figure 5.33 Compressive (Radial) Surface Strain Distribution Near a Coldworked Hole for 6.5 mils Radial Interference (Load 25,000 lb<sub>f</sub>).

The effect of the applied loads is to slightly increase this value at the fastener hole edge from around 5.25 percent to a value roughly equal to 6 percent at a maximum attainable load ( $42.4 \text{ lbf} \times 10^3$ ) ( $188.6 \times 10^3 \text{ N}$ ) before specimen failure. Figure 5.29 depicts the subsequent redistribution of the residual radial strains near the coldworked hole for specimen SP2. Low remote load compressive stresses cause no change in the residual strain field.

For higher loads the effects begin to be noticeable only after a remote compressive stress of 24 ksi is reached and then only close to the hole boundary where the strains gradually vary by slightly over one percent. The residual strains, which vary with  $y$ , take on a steady value on reaching an applied nominal stress of around  $24 \times 10^3 \text{ lbf/in}^2$  until specimen failure by buckling and subsequent fracturing of the material.

Figure 5.34 shows a comparison of the results for zero load. The Hsu-Forman and Nadai results are based on a 4 mil (.101 mm) radial expansion whereas the Adler and Dupree finite element result is based on a 6 ml radial expansion. The experimental data is from specimen SP2 with a radial interference of approximately 6 mils (.152 mm).

Total agreement of the different results is not expected due to the assumptions made in the formulations of the

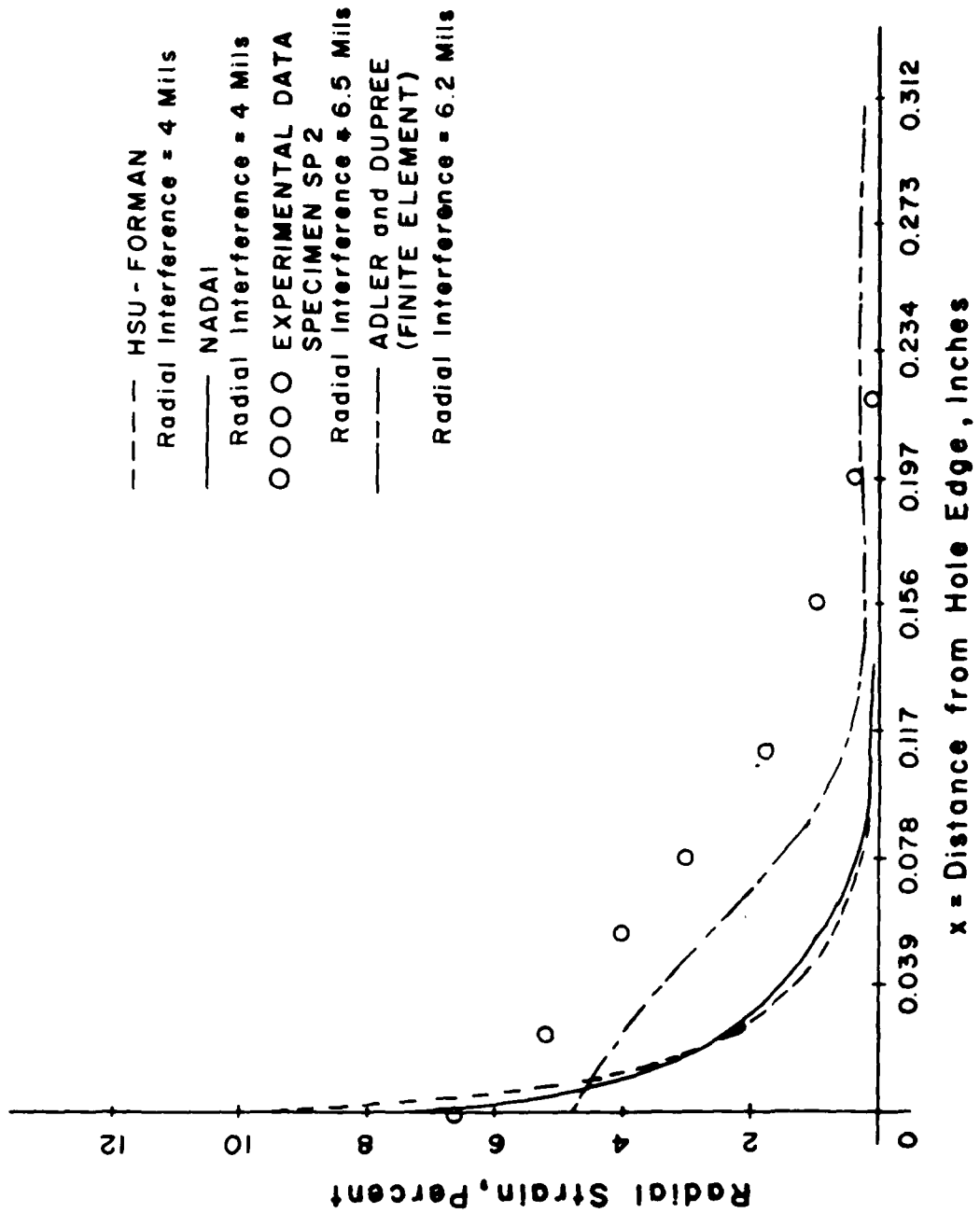


Figure 5.34 Comparison of Experimental Results with Theoretical Predictions of Nadai (41), Hsu and Forman (2), and Adler and Dupree (29).

problems. Nevertheless the essential features of the results are apparent and in qualitative agreement, at least.

## SECTION VI

### HOLE INTERACTION STUDY

#### 6.1 Introduction

In this chapter the interaction between surface strain fields which are created by coldworking two or more fastener holes lying in close proximity to each other is investigated. Needless to say, this situation occurs in almost all fastening situations.

Conventional machine design fastener techniques are based on simple analytical formulae developed from the assumption that there are basically three modes of failure, viz.:

- (1) shearing of rivets,
- (2) bearing failure of the plate or rivet, and
- (3) tensile failure of the plate.

Under such considerations the stiffness of a solid plate not subjected to buckling is expressed by the product  $(gt)$ . Here  $g$  is the shear modulus of the material, and  $t$  is its thickness.

For the case under consideration (a shear web) the effective shear modulus,  $g t_e$ , is given by the empirical formula (4)

$$gt_e = gt \left(1 - \frac{D}{b}\right) \left(1 - \frac{D^3}{h}\right) \quad (6.1)$$

where  $D$  is the diameter of the hole,  $b$  is hole separation distance and  $h$  is the width of the plate.

This and other analytical solutions have only limited applicability, if any, to the new and more sophisticated fastener systems designed to improve joint fatigue life of structural members.

## 6.2 Experimental Procedure

The material and experimental procedures have been described in sections 2.2 and 3.1. The specimen configuration which was illustrated in Figures 3.1.3 is a four hole pattern in a plate dimensioned  $2\frac{1}{2} \times 4\frac{1}{2}$  inches,  $\frac{1}{4}$  of an inch thick, (6.35 x 11.43 x .635 cm). Two such specimens designated SPB and SPC were tested. Both specimens are of the same material and geometry.

In these specimens, the  $(c/d)$  ratio was 1.8, which is below the threshold value of  $(e/d) = 2.0$  commonly employed in the industry. These same specimens, in addition to others, were utilized in the study of plate edge effects on the residual strain fields.

An attempt was made to hold constant most of the crucial independent factors. Among these are the hole separation distance,  $b$ , which was  $1.75 d$ ; the radial interference which was approximately 6 mils; plate thickness which was  $\frac{1}{2}$  in; and the mandrel drawing rate, which was .5 cm/min.

## 6.3 Results and Discussion

### 6.3.1 Radial Strain Distribution

Both hoop strain and compressive residual components of strain were evaluated at various locations around the fastener hole. A comparison can be made with results measured using specimen SPP (a single hole in a plate with roughly its centre located a distance .469 in. (11.93 mm) away from the plate edge), whose  $e/d$  ratio is equal to 1.8. (See Figures 7.4 and 7.5)

Figures 6.1 through 6.5 have been included to show the locations and the moiré fringe pattern obtained on prestressing hole #1 and the overall moiré fringe pattern resulting from coldworking of all the four holes.

The moiré fringe pattern of Figure 6.3 goes with plots illustrated in Figure 6.6 through 6.11. This is a case of specimen SPB after all the fastener holes were coldworked. The departure from symmetry in the pattern was largely a result of the mandrelizing order followed. The coldworking of hole #1 was followed by hole #2. Hole #3 was the last hole in the coldworking process, after hole #4. Data was collected between each of the coldworking stages. Here, only the final strain state of the specimen will be discussed.

As seen from the moiré photograph of Figure 6.3, relatively high residual compressive strains dominate a

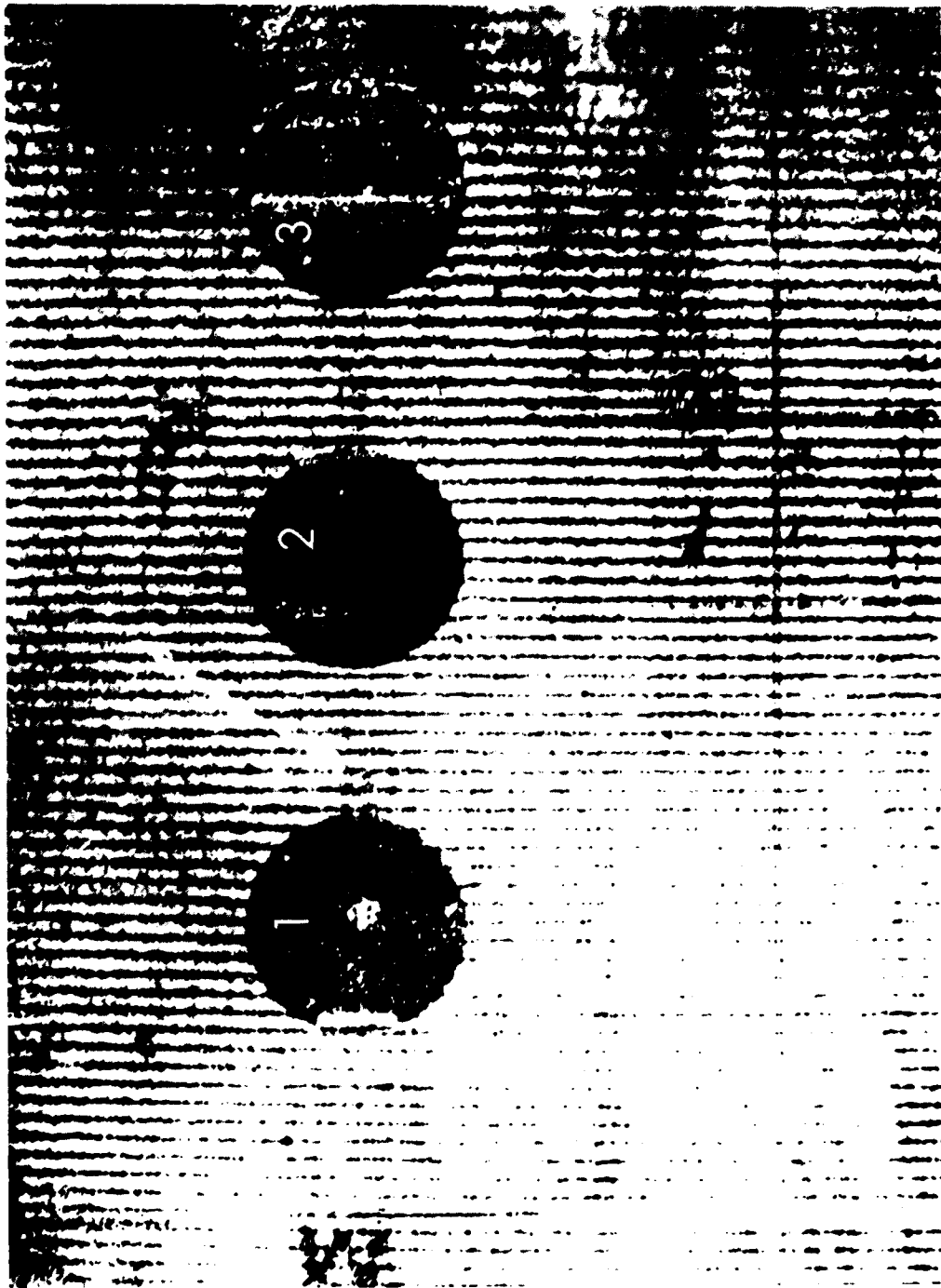


Figure 6.1 Specimen SPB Moiré Fringe Pattern.



Figure 6.2 Moiré Fringe Pattern for Specimen SPB after Coldworking Hole #1.

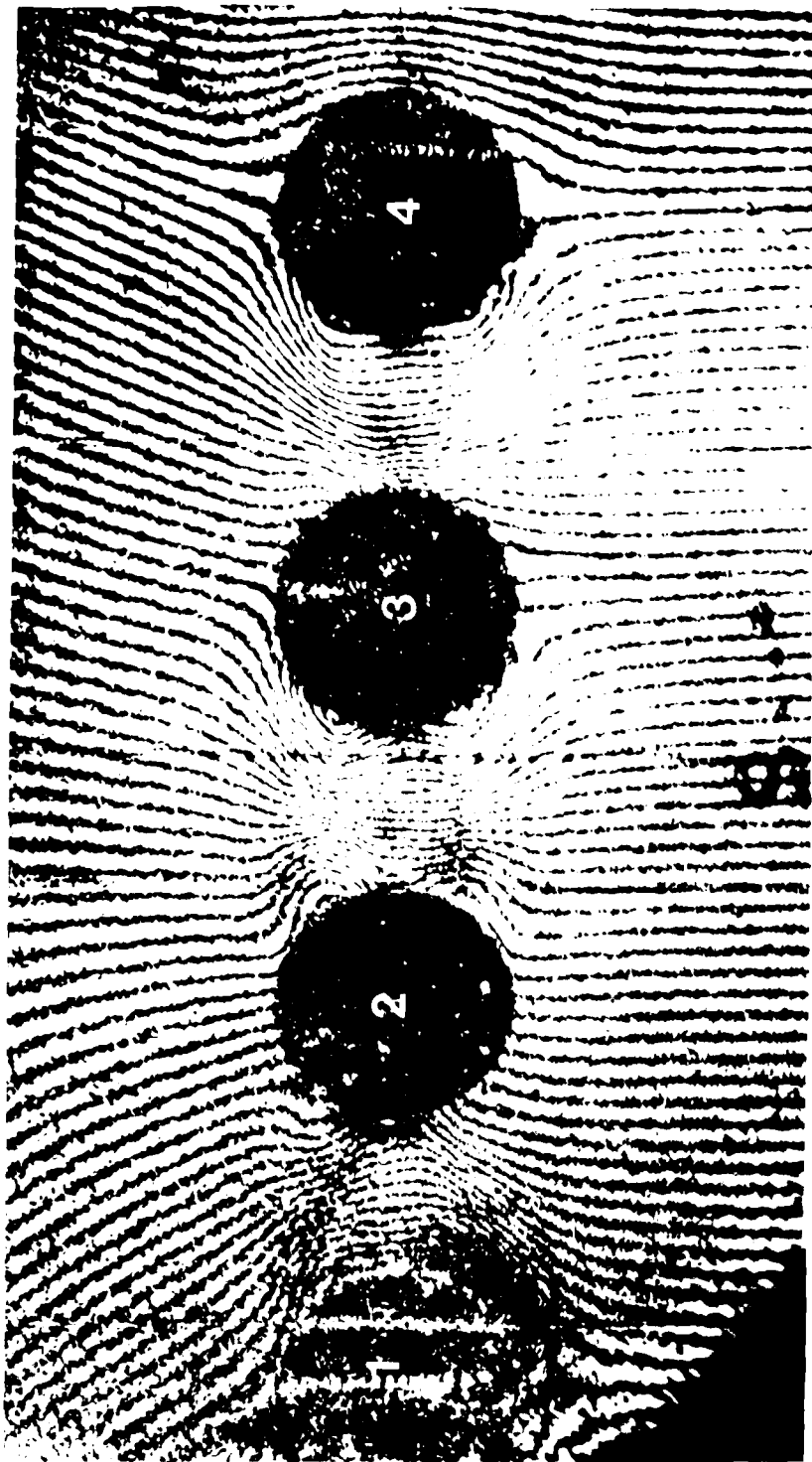


Figure 6.3 Specimen SPB after Coldworking All Holes in Order 1, 2, 4, 3.

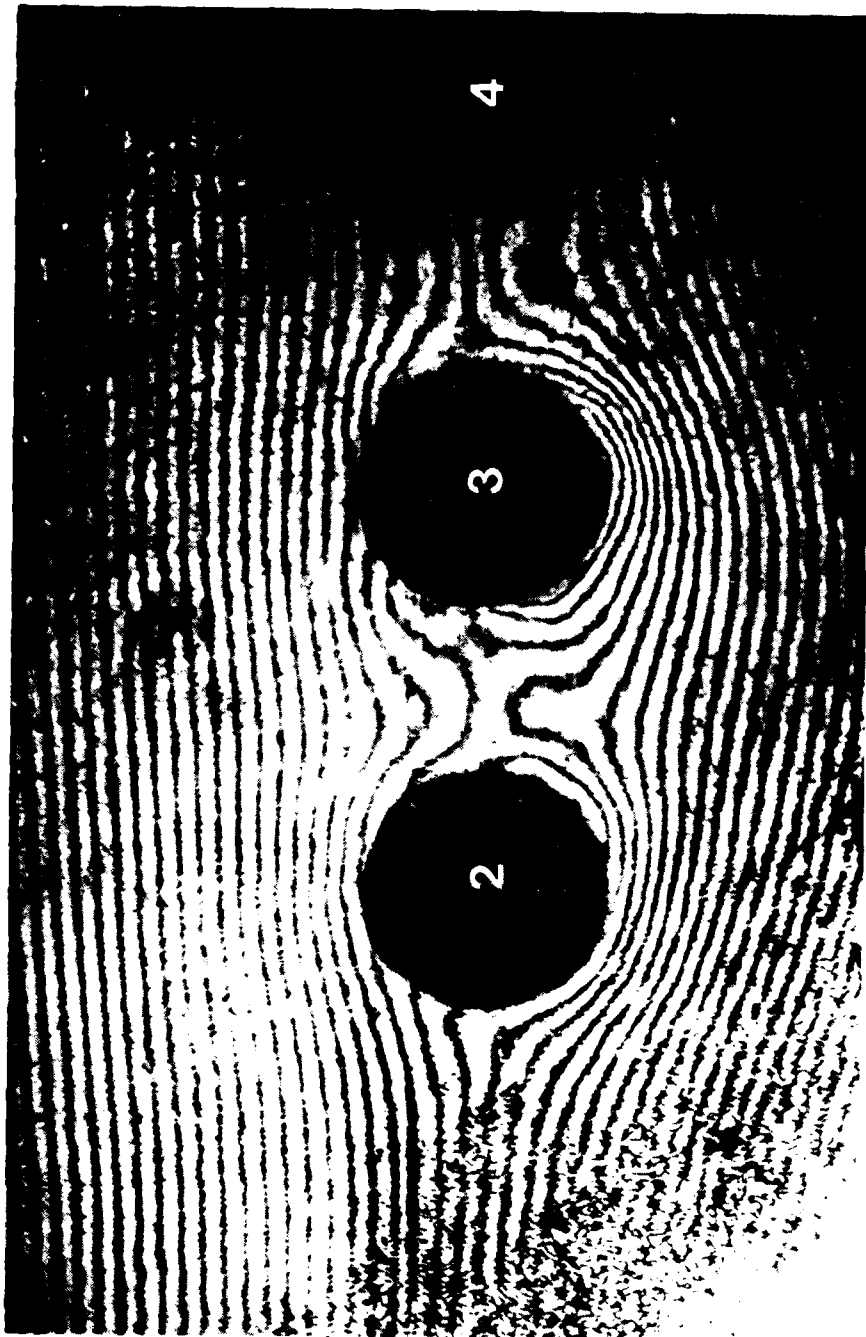


Figure 6.4 Moiré Fringe Pattern of Holes 2-4 in Specimen SPC after Coldworking in Order 1, 2, 4.

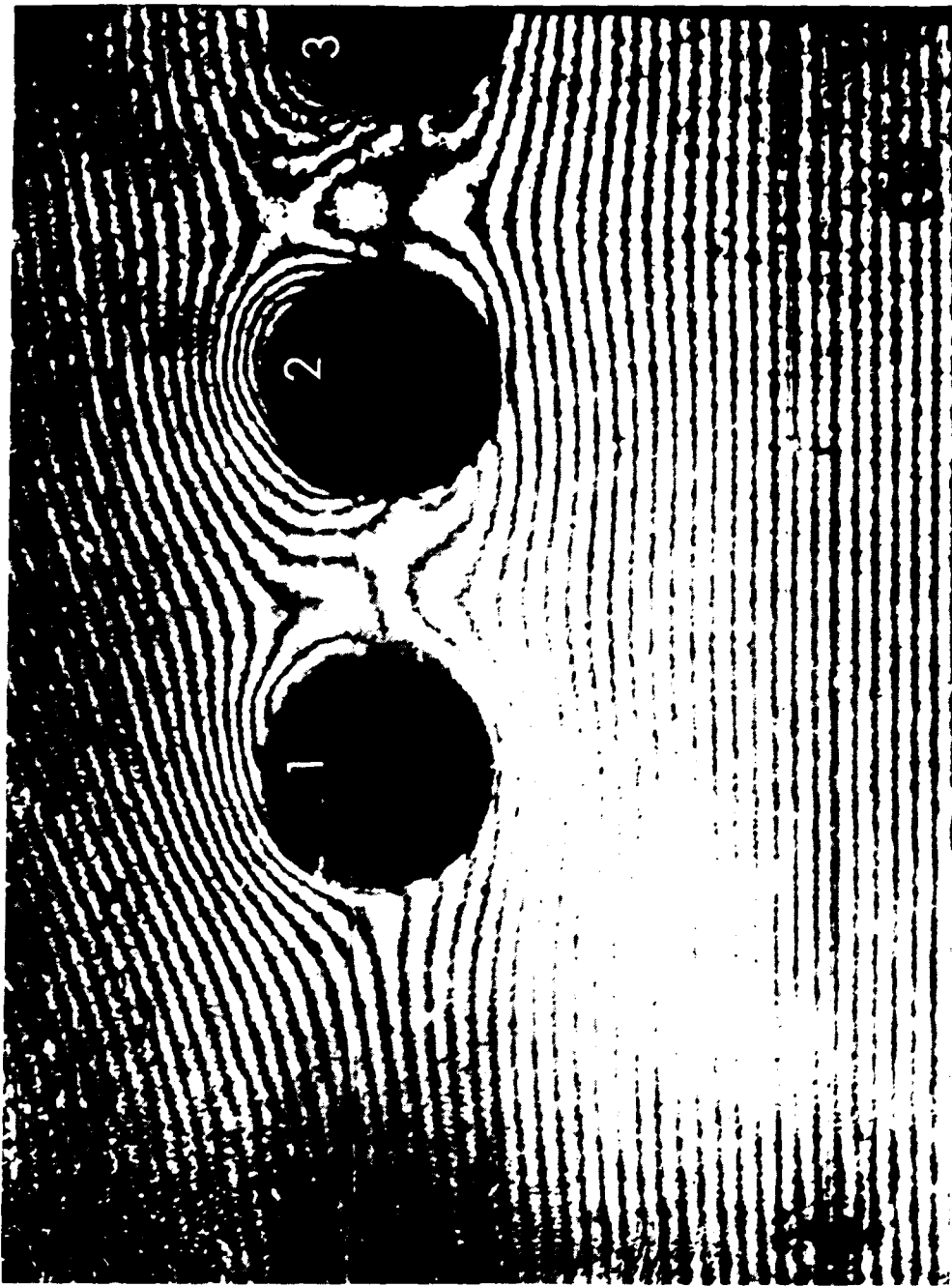


Figure 6.5 Fringe Photograph of Holes 1-3 in Specimen SPC after Coldworking in Order 1, 2, 4, 3.

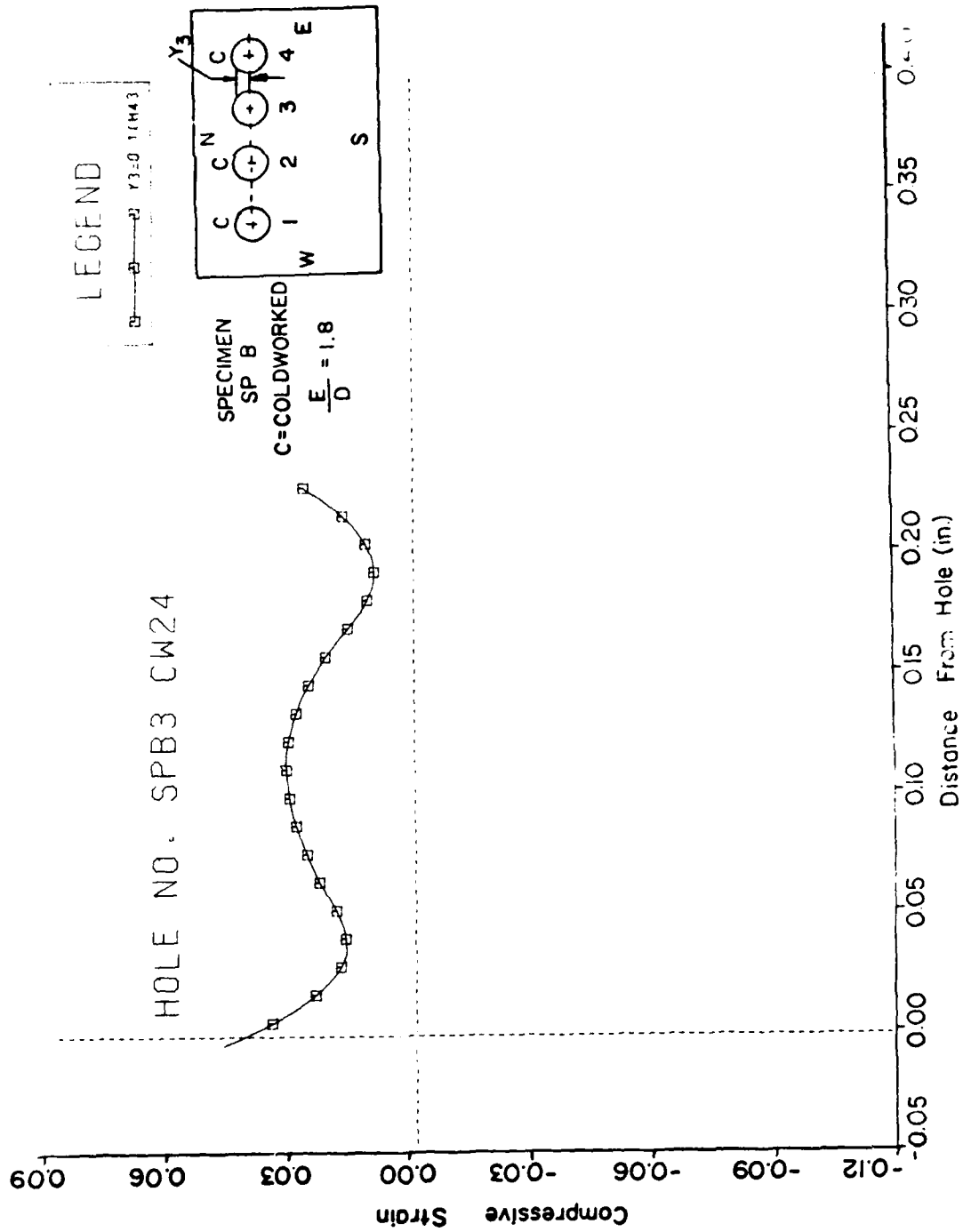


Figure 6.6 Measured Residual Compressive Strain Distribution Along an Axis .1 Inches from the Centerline Between Holes 3 and 4.

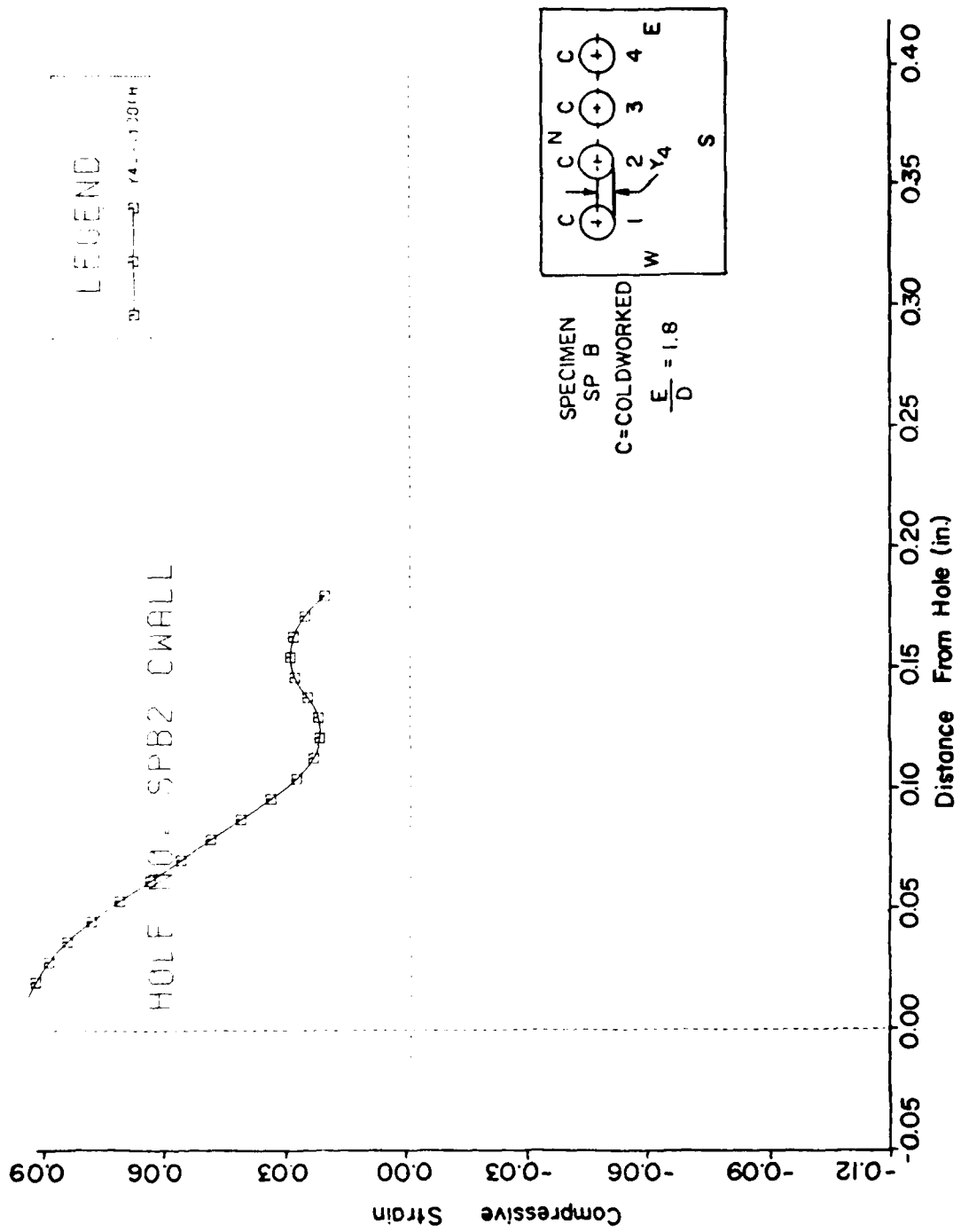


Figure 6.7 Measured Residual Compressive Strain Distributions Along an Axis .13 Inches from the Centerline Between Holes 1 and 2.

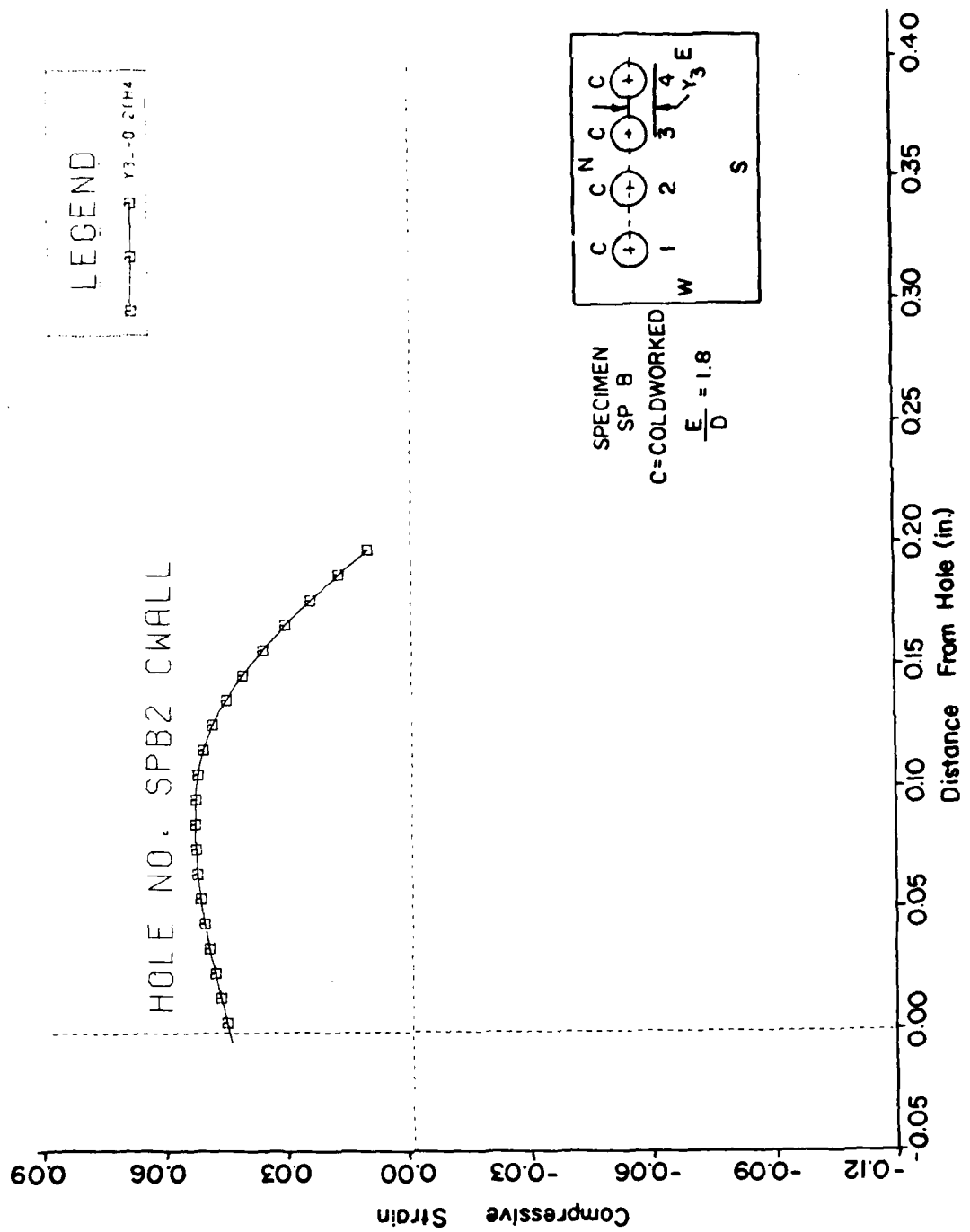


Figure 6.8 Measured Residual Compressive Strain Distribution Along an Axis .2 Inches from the Centerline Between Holes 3 and 4.

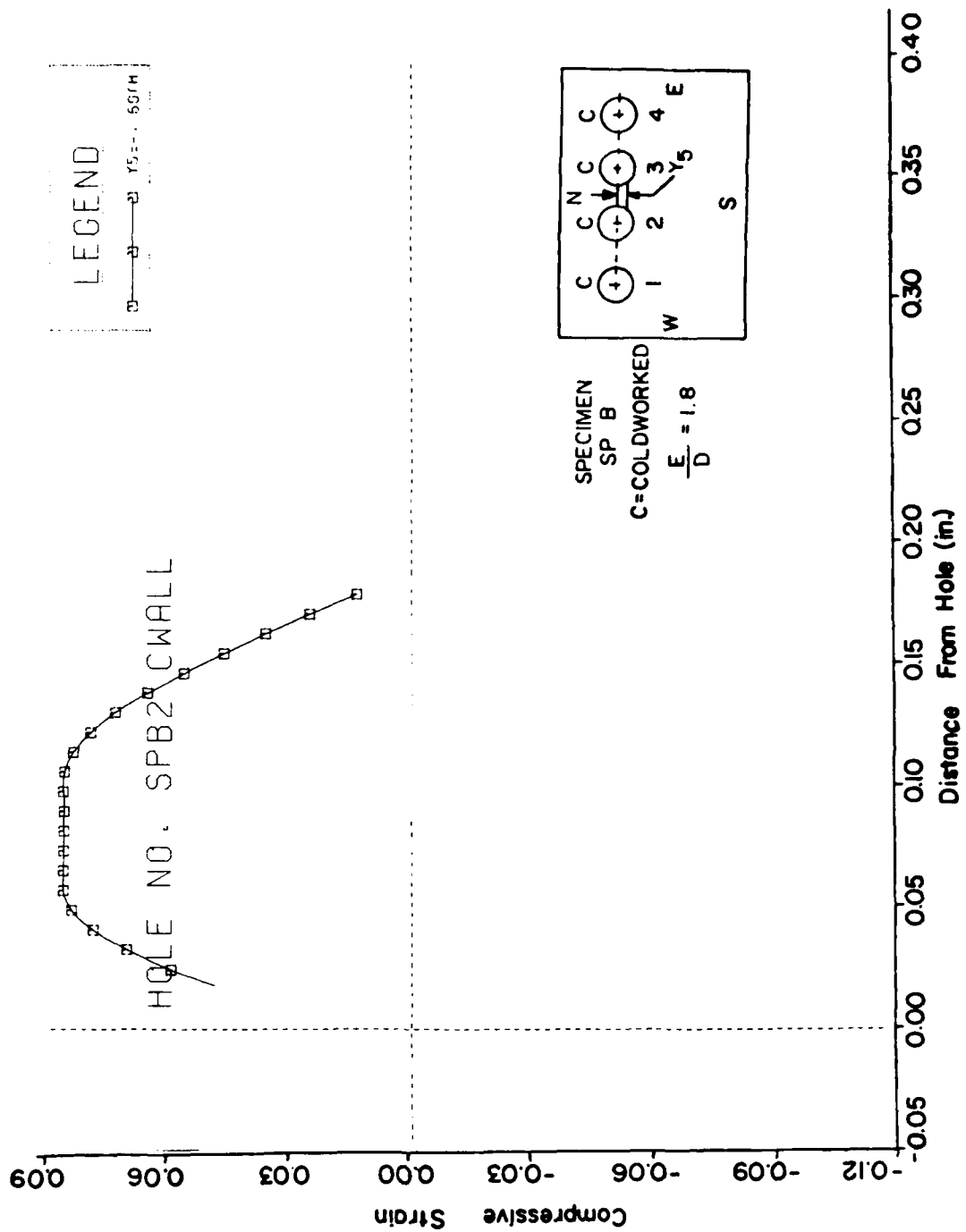


Figure 6.9 Measured Residual Compressive Strain Distributions Along an Axis .06 Inches from the Centerline Between Holes 2 and 3.

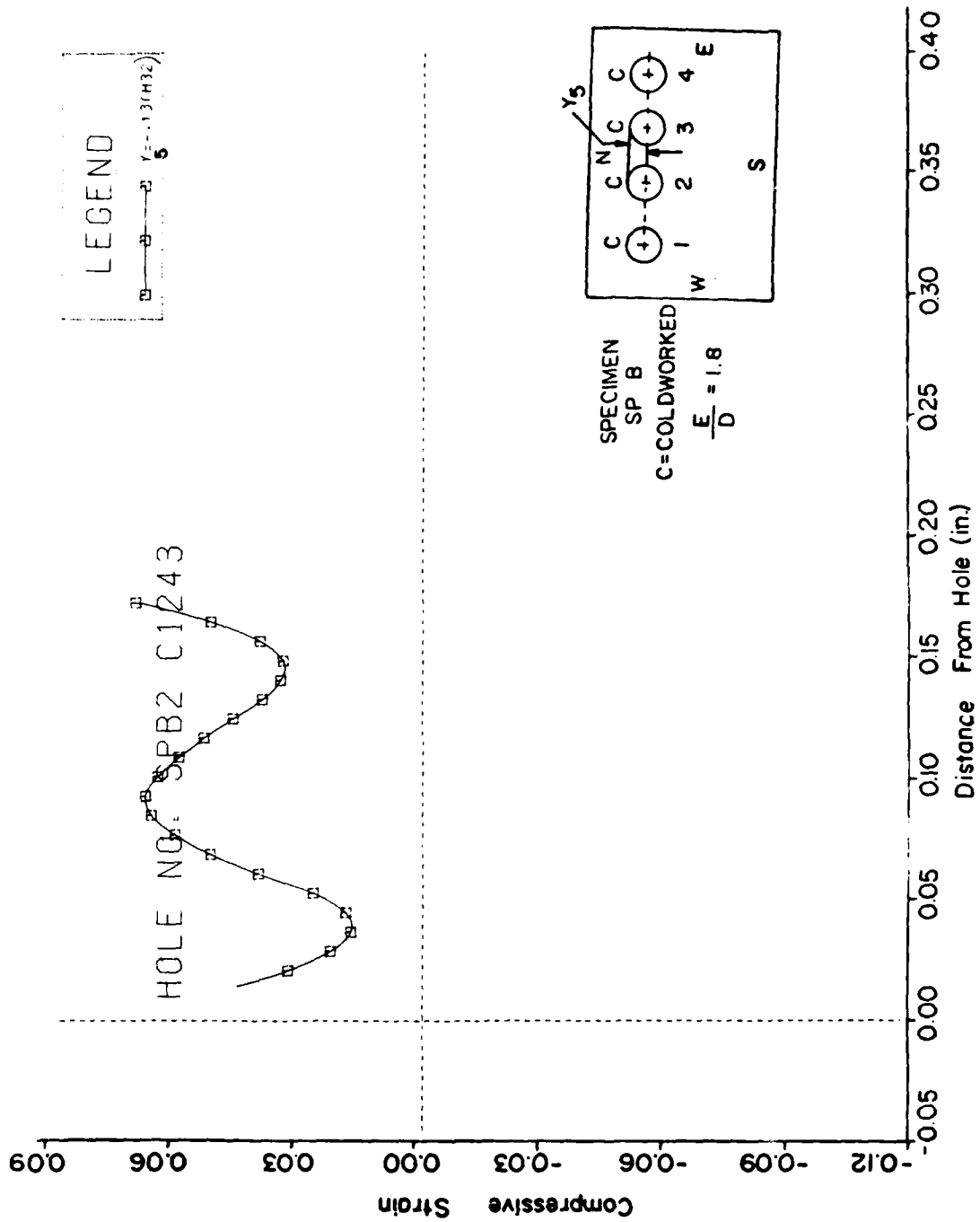


Figure 6.10 Measured Residual Compressive Strain Distributions Along an Axis .13 Inches from the Centerline Between Holes 2 and 3.

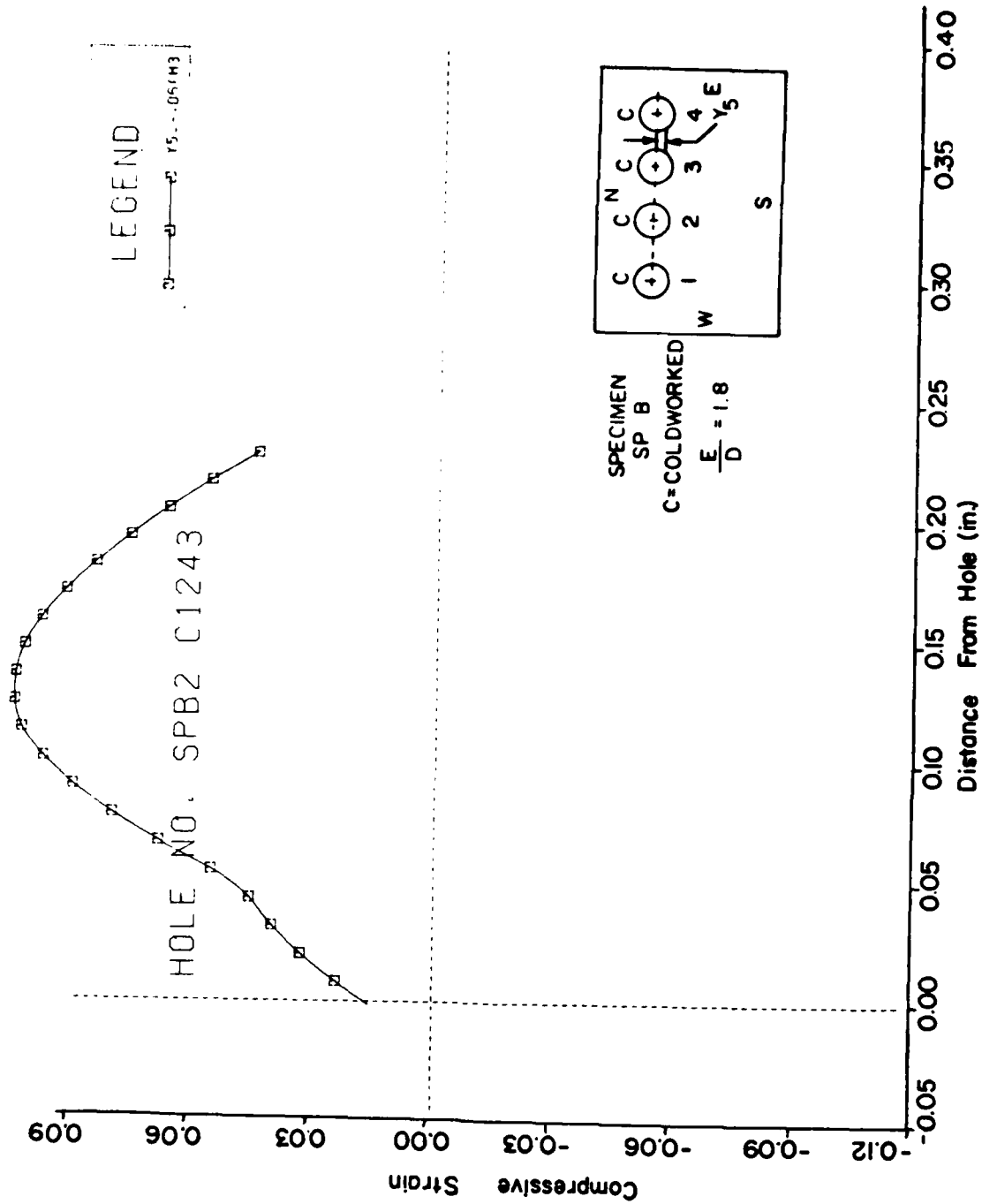


Figure 6.11 Measured Residual Compressive Strain Distributions Along an Axis .06 Inches from the Centerline Between Holes 3 and 4.

diameter-wide band-like region sweeping across all the fastener holes. A datum line was drawn as a tangent to the holes on the northern, (N) side designated as  $y_6 = 0.00$ . The common centerline of the holes is  $y_4$  and axes  $y_3 = .1$  in. (2.54 mm) and  $y_5 = 0.06$  in (1.52 mm) were drawn on either side of this centerline below and above it respectively. The results for this analysis are presented in the plots of Figure 6.6 through Figure 6.11.

In general, the highest residual strain occurs in areas away from the hole edges. These strains approach 8 percent. Figure 6.6 is an exception in that it is a transitional result (Hole # 3 is not yet coldworked) of the compressive strain determined between holes 4 and 3 along  $y_3 = 0.1$  in. from the datum line.

The moiré pattern Figure 6.2 shows that on the side opposite an adjacent hole, the residual compressive strain is higher than on the other. Beginning from the side of hole #1 in this figure the compressive residual strain diminishes to zero and goes negative (hoop strain) as hole #2 is approached. The highest value of the residual compressive strain occurs at an angle of  $45^\circ$  measured from the horizontal centerline. Furthermore, detailed examination reveals that the closeness of the plate edge and the presence of an adjacent hole results in the compressive residual strain departing further from the assumption of rotational symmetry.

The mandrelization process for a hole adjacent to other non-coldworked holes creates a complicated residual strain climate in an area subtended by the above  $45^\circ$  lines on either side of the hole. It is seen in the fringe pattern of Figure 6.2 that the prestressing of hole #1 sends the eastern side of hole #2, two diameters away, into a state of tension. Such was not the case with single-hole specimen SP2 whose residual strain essentially vanished in areas a diameter away from the hole boundary.

### 6.3.2 Hoop Strain Distribution

The measured hoop strain results are presented in Figures 6.12 through 6.18. Figure 6.2 is the fringe photograph which was analyzed to get Figure 6.12. In this plot, axis  $y_1$  and  $y_4$  were drawn above and below the hole centerline and tangent to the hole. The hoop strain evaluated is parallel to the hole centerline along these axes. Axis  $y_6$ , whose detailed analysis will be presented below, was drawn along the edge of the plate. If a tangential axis on the eastern, (E) side of hole #4 in Figure 6.4 called  $y_{10}$  is drawn and axes  $y_{11}$  and  $y_{12}$  are constructed such that they are located one radial distance from each other, and the hoop strains analyzed along them, one would obtain the plot presented in Figure 6.13 after coldworking all but hole #3. Axes  $y_2$  and  $y_3$  were drawn tangent to hole #2 and #4

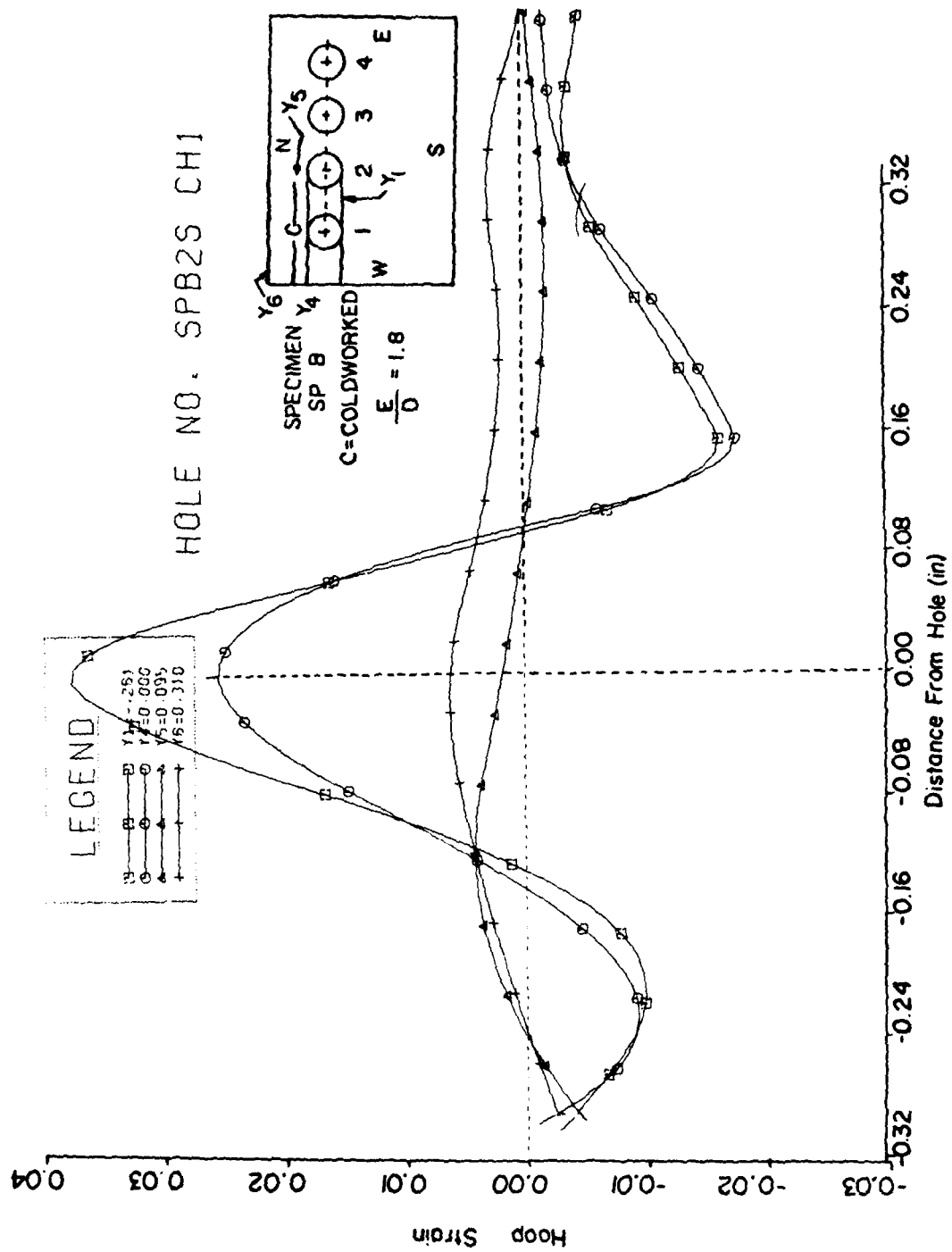


Figure 6.12 Residual Hoop Strain Distribution Along Several Axes after the Coldworking of Hole #1 for 9 mils Radial Interference.

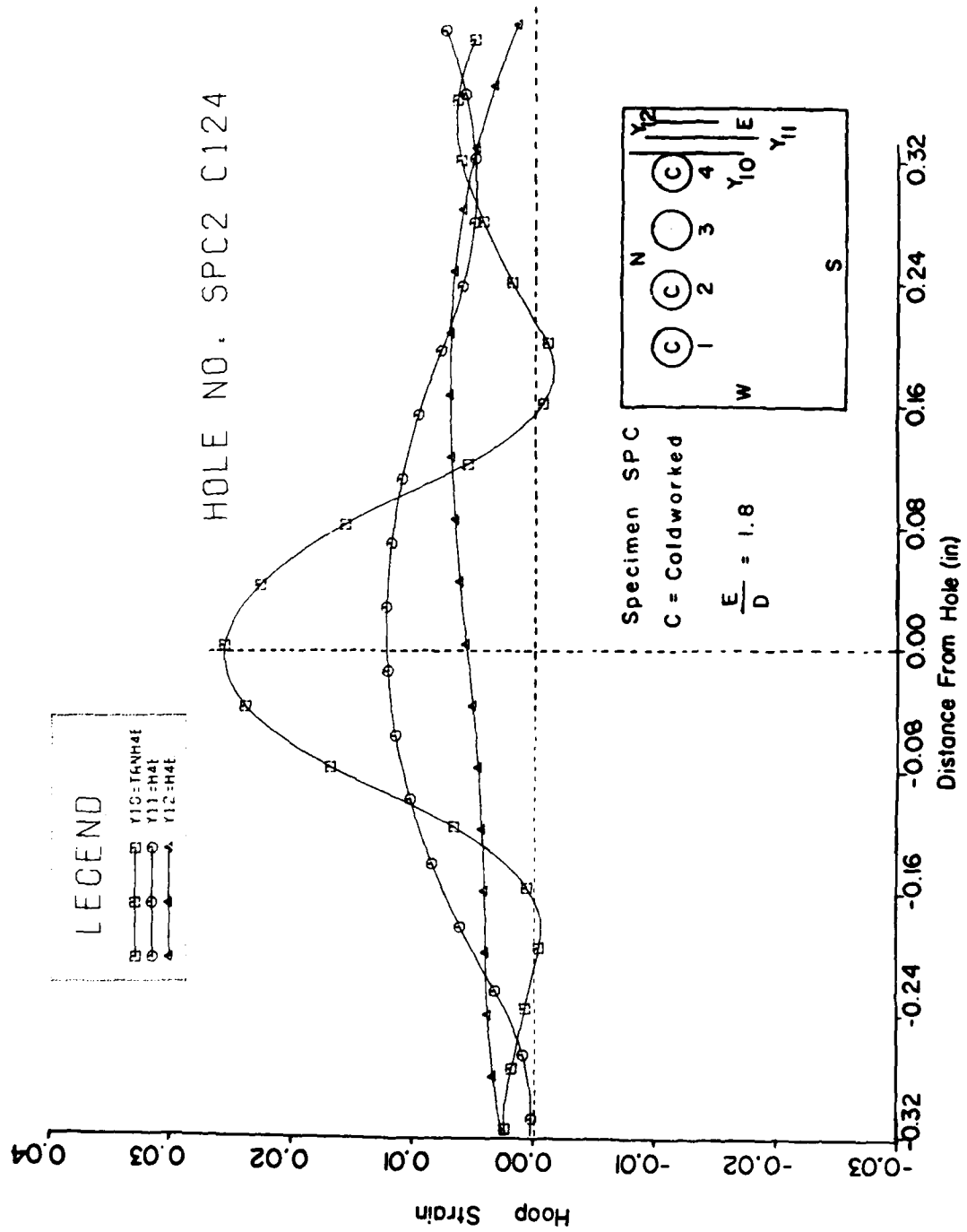


Figure 6.13 Residual Hoop Strain Along Several Axes on the "Eastern" Side of Hole #4 for 6 mils Radial Interference.

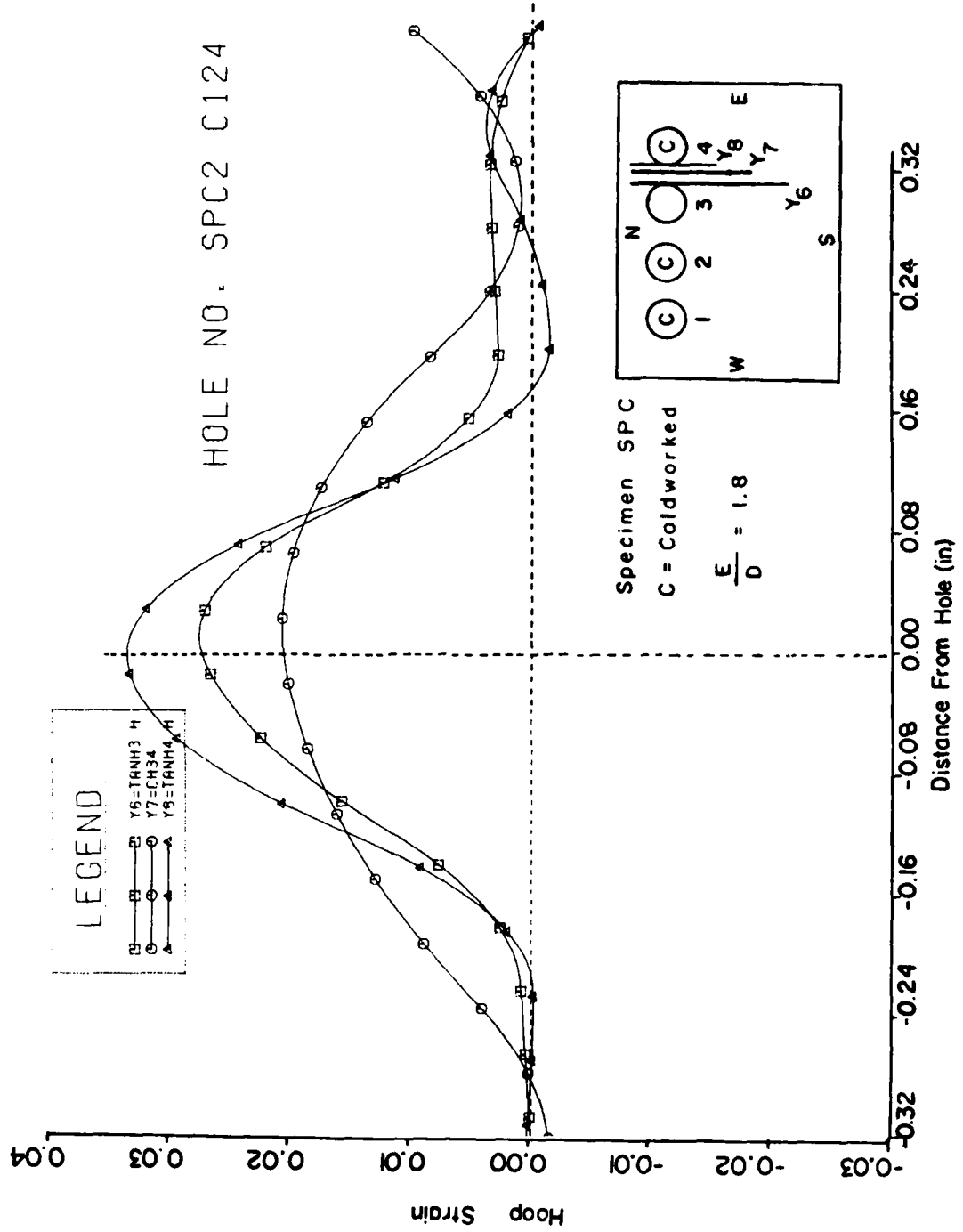


Figure 6.14 Measured Residual Hoop Strain Distributions Along Several Axes Between Holes 3 and 4 for 6 mils Radial Interference.

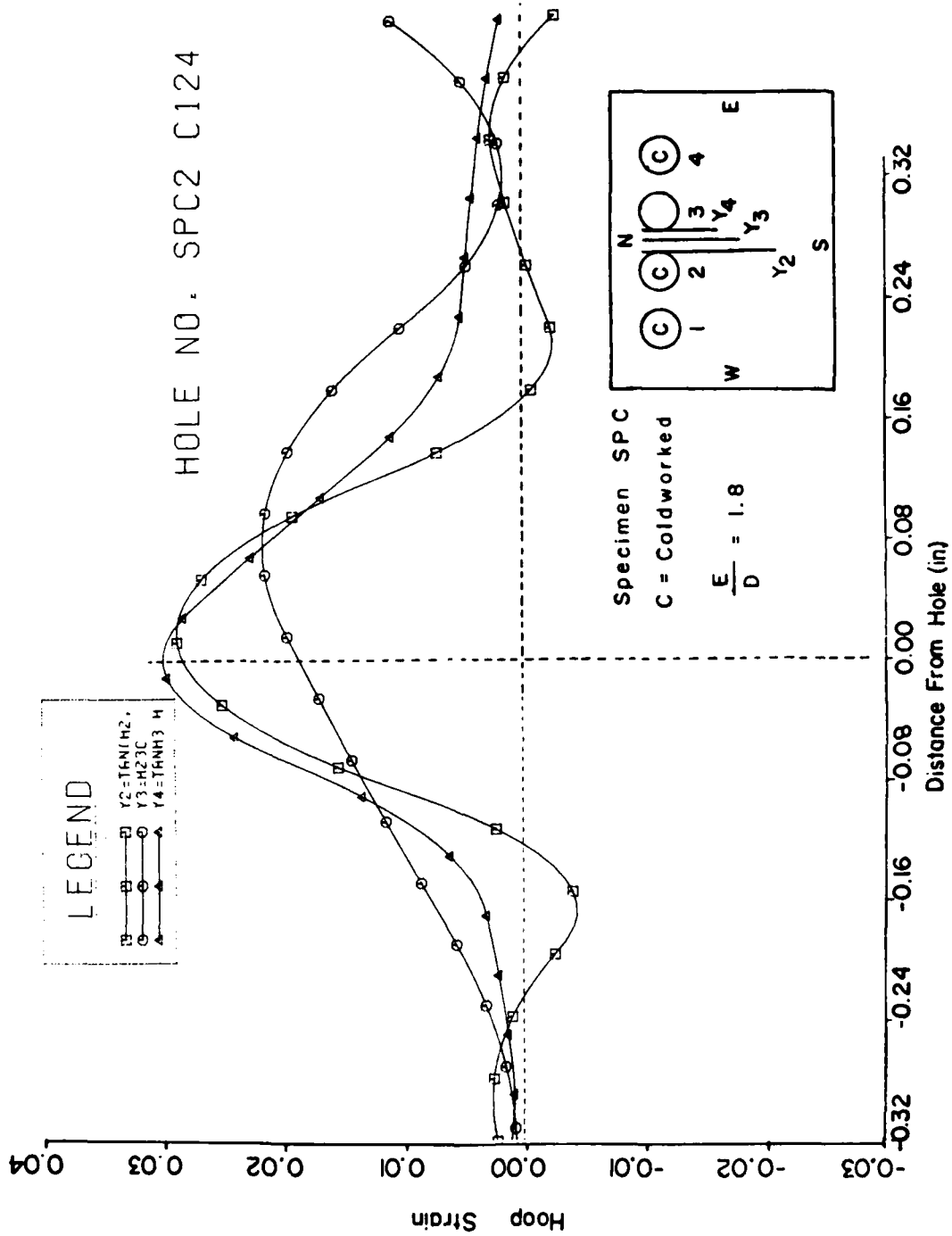


Figure 6.15 Measured Residual Hoop Strain Distributions Along Several Axes Between Holes 2 and 3 for 6 mils Radial Interference.

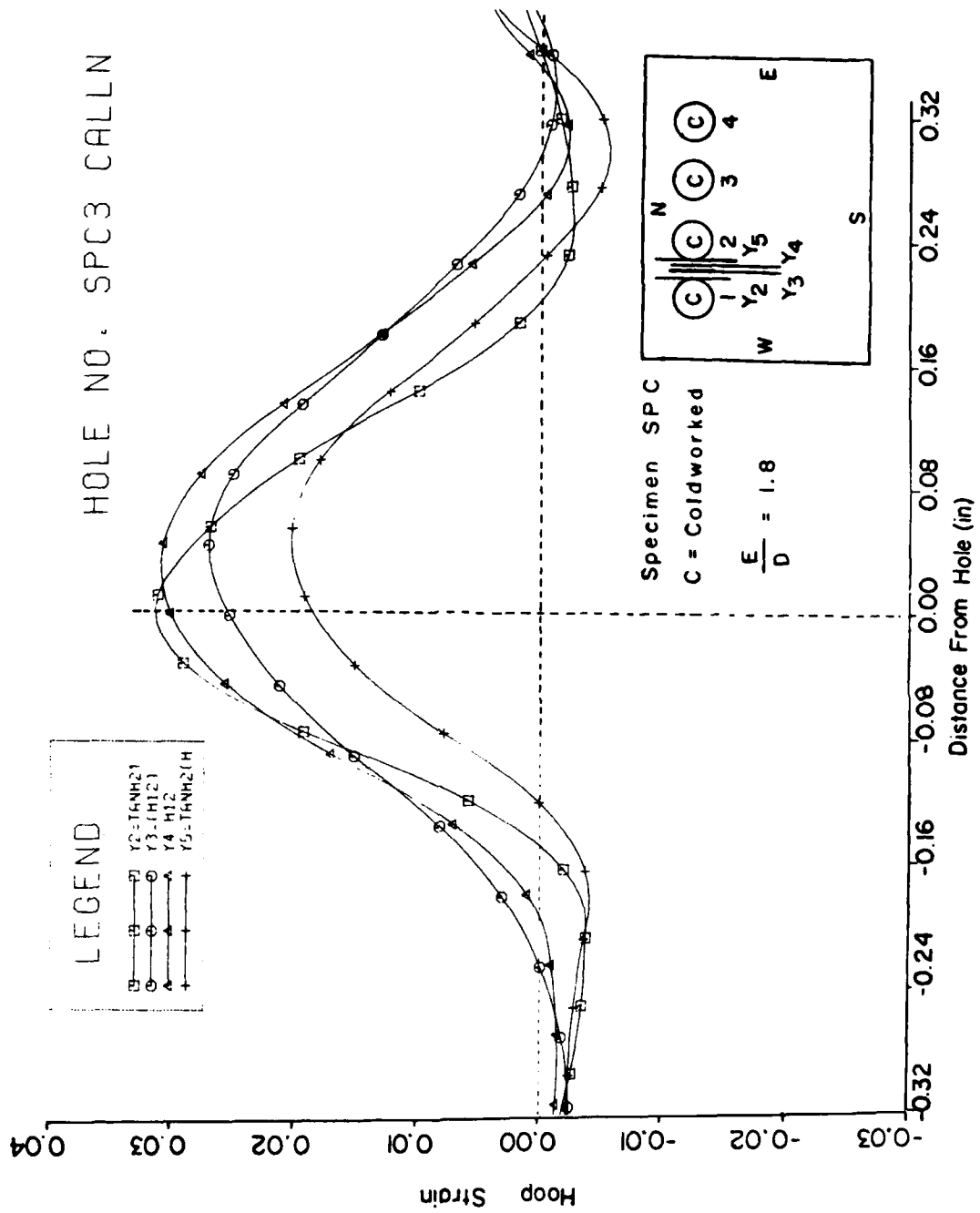


Figure 6.16 Measured Residual Hoop Strain Distributions Along Several Axes Between Holes 1 and 2 for 6 mils Radial Interference.

respectively. Axis  $y_3$  passes through the center of the holes between  $y_2$  and  $y_4$ . The same procedure was followed for the set of axes  $y_6$ ,  $y_7$  and  $y_8$  with  $y_7$  passing through the center of holes 4 and 3. Figure 6.14 and 6.15 are the results of the above two sets respectively.

Examination of these results reveal that the residual hoop strains are highly localized along the hole centerline and approach zero on either side of the holes. It is also apparent that, due to the presence of an adjacent hole, the magnitude of the residual hoop strain increases all around the fastener hole.

The implications of the fanned-out shape of the moiré fringe pattern in the photographs presented in Figures 6.2-6 requires special attention. Chapter 7 is devoted to this topic.

Figure 6.17 presents the final moiré coldworked state photograph and Figure 6.18 presents the results obtained from the photograph.

Hoop strain values of these magnitudes have not been observed before. This behavior can only be attributed to the presence of the other holes.

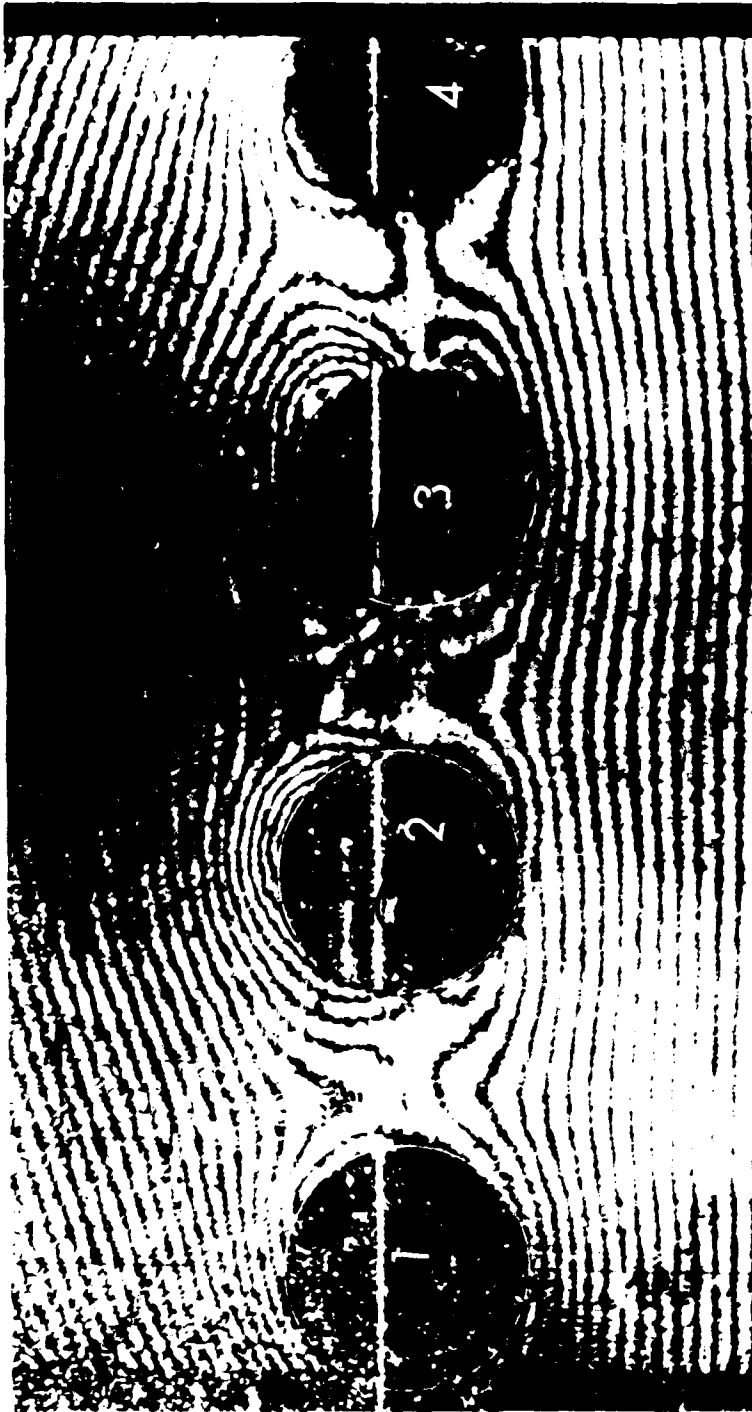


Figure 6.17 Moiré Fringe Photograph of Specimen SPC after Coldworking All Holes (1, 2, 3, 4).

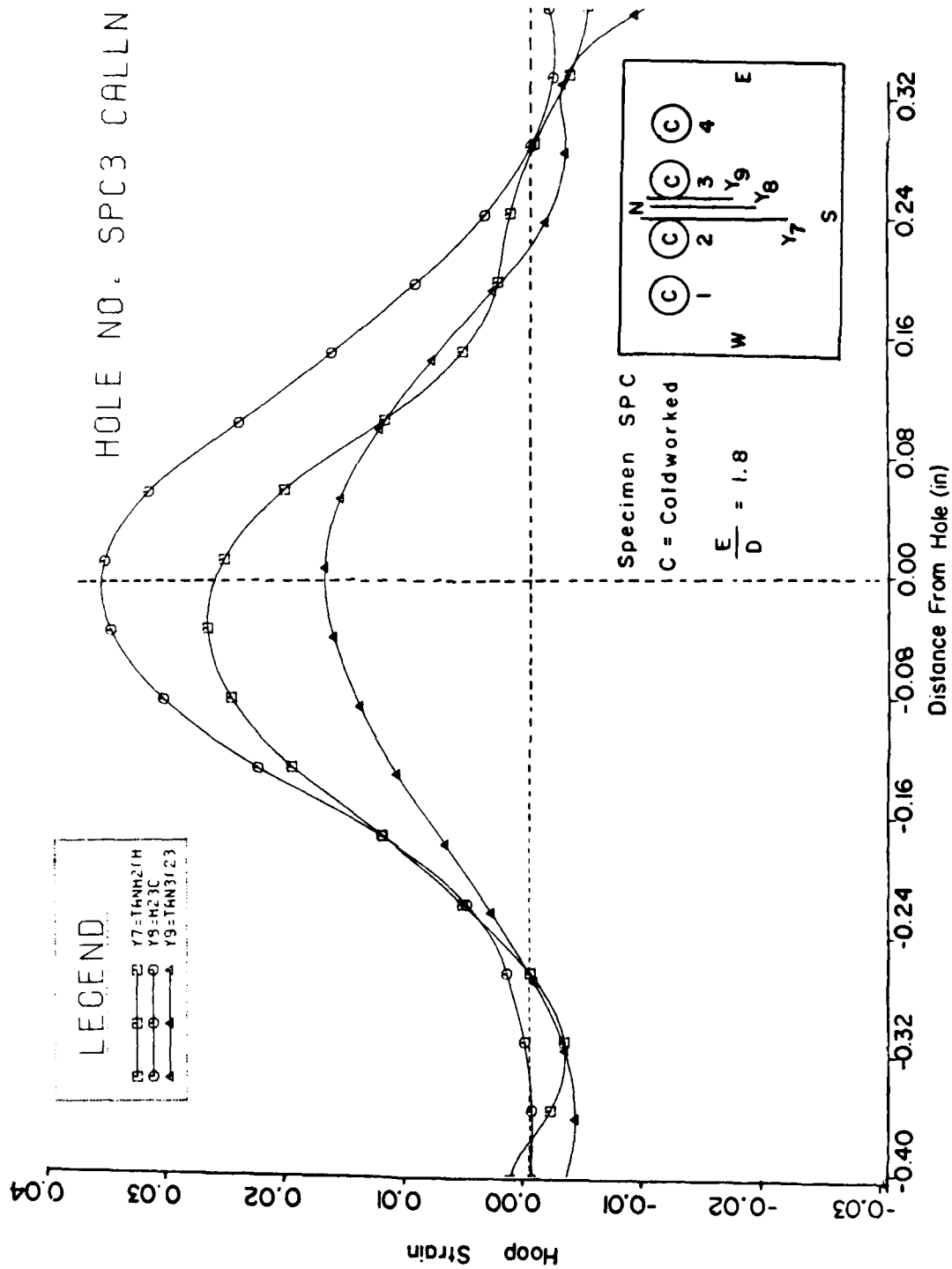


Figure 6.18 Measured Residual Hoop Strain Distributions Along Several Axes Between Holes 2 and 3 for 6 mils Radial Interference.

## SECTION VII

### EDGE EFFECT STUDY

#### 7.1 Overview

The investigation of the effects of a plate edge upon the resulting surface strain field created by the cold-working of the fastener hole is presented in this chapter.

Locating the rivet hole near a straight edge in a plate complicates the matter of evaluating the strain distribution theoretically far beyond the case of a hole in an infinite sheet. For the plane stress problem a transformation of coordinates from rectangular  $(x,y)$  to a bipolar system of coordinates  $\alpha$  and  $\beta$  is almost a necessity so as to render the plane stress biharmonic function say  $\psi$  a linear equation in the latter system.

The bipolar coordinate system is a family of circles through two poles, A, B and the family of circles orthogonal to those of the first family in the  $x,y$  plane. The transformation equations are given by

$$\begin{aligned}
 x &= \frac{a \sin \beta}{\cosh \alpha - \cos \beta} & \alpha &= \frac{i}{2} \log_e \frac{x^2 + (y-ia)^2}{x^2 + (y+ia)^2} \\
 y &= \frac{a \sinh \alpha}{\cosh \alpha - \cos \beta} & \beta &= \frac{1}{2} \log_e \frac{(x+a)^2 + y^2}{(x-a)^2 + y^2} \\
 z &= z & & (7.1)
 \end{aligned}$$

For plane stress  $\sigma_z = 0$  and  $\sigma_x, \sigma_y$  take the form:

$$\sigma_x = \frac{\partial^2 \psi}{\partial y^2}, \quad \sigma_y = \frac{\partial^2 \psi}{\partial x^2} \quad (7.2)$$

where  $\psi$  is the Airy's stress function satisfying the equation:

$$\nabla^4 \psi = 0 \quad (7.3)$$

in which  $\nabla^4 = \nabla^2 \nabla^2$  and  $\nabla^2$  is the laplace's operator which takes the following form in a bipolar system:

$$\nabla^2 = \frac{1}{a^2} (\cosh \beta - \cos \alpha) \left\{ \frac{\partial^2 \psi}{\partial \alpha^2} + \frac{\partial^2 \psi}{\partial \beta^2} \right\} + \frac{\partial^2 \psi}{\partial z^2}$$

Jefferey (33) gives the solution to (7.3) for the relatively simple case of nonplastically stressed hole in a plate subjected to tensile force  $T$  as:

$$\begin{aligned}
\psi = & aT \left\{ \frac{1}{2} \sinh \alpha \left( 1 + 2 \sum_{n=1}^{\infty} e^{-n\alpha} \cosh \alpha \beta \right) \right. \\
& + B_0 \left[ \alpha (\cosh \alpha - \cos \beta) + \sinh \alpha (\cosh \alpha \cos \beta - 1) \right] \\
& + A_1 (\cosh 2\alpha - 1) \cos \beta \\
& + \sum_{n=2}^{\infty} A_n \left[ \cosh (n+1)\alpha - \cosh (n-1)\alpha \right] \\
& + E_n \left[ (n-1) \sinh (n+1)\alpha \right. \\
& \left. - (n+1) \sinh (n-1)\alpha \cos n\beta \right] \left. \right\}
\end{aligned}$$

The constants  $B_0$ ,  $A_1$ ,  $A_n$ ,  $E_n$  are determined by the use of boundary conditions. Because of the nature of the boundary conditions (a row of holes in close proximity to each other near a plate edge) encountered in practice, the use of this analytical solution has not been attempted. It is not known whether the solution could be extended to include nonlinear material behavior.

## 7.2 Material and Experimental Procedures

There are two groups of specimens used in this phase of the investigation. All the specimens were cut from a single plate of 7075-T6 aluminum. Group A had all but one factor constant, and consisted of three specimens SPP, SPT and SPE. Hole diameters were held constant at a nominal value of 0.261 in. (6.63 mm); radial interference for each

one of the specimens during the prestressing operation was maintained constant by a proper selection of sleeve thickness and mandrel combination. The machining of the critical edges nearest the fastener hole was, in-so-far-as possible, made identical, and care was taken to ensure that there were no machining-introduced stress raisers on that edge. Again the mandrel drawing rate was set equal for all specimens at .5 cm/min.

The variable of interest is the edge distance/diameter ratio. The edge distance,  $e$ , is defined as the distance from the hole centerline to the nearest edge of the sheet material. Denoting the hole diameter by " $d$ ", then the ratio ( $e/d$ ) is of practical significance in the design of structural joints (38).

In the design of fatigue-improvement fastener systems an attempt is made to keep the ( $e/d$ ) ratio above a threshold value of 2.0. Values of ( $e/d$ ) greater than 2.0 are known to result in increased fatigue life of the assembly (32). The degree of life increase and the physical reasoning why  $e/d = 2.0$  is a threshold value are not known. The effects on life of using  $e/d$  less than 2.0 have not been explored.

Specimens SPP, SPT and SPE were designed with ( $e/d$ ) ratios of 1.8, 2.0 and 2.25 respectively and specimen SPC of Group B, an in-line multi-hole pattern comprising four holes, was designed with an ( $e/d$ ) ratio of 1.8.

Moiré fringe photographs of specimens SSP and SPT are presented in Figure 7.1, 7.2 and 7.3.

### 7.3 Experimental Results and Discussion

#### 7.3.1 Hoop Strain Distribution

Both residual radial compressive and hoop strains were obtained. The evaluation of hoop strains at the hole boundary along an axis parallel to the plate edge resulted in the plot of Figure 7.4 for specimen SPP with an (e/d) ratio of 1.8. From the graph it is observed that the highest strain occurs at the hole edge (point  $x = 0, y = 0$ ). Like a damped harmonic wave, the residual strains vanish with increasing distance away from the fastener hole. Figure 7.5 displays the detailed analysis of residual hoop strain distribution at various locations,  $y = 0.00, 0.072, 0.181, 0.260$  and  $y = 0.330$  inches (0.00, 1.83, 4.59, 6.60 and 8.38 cm) which is close to the straight edge. Similar detailed results for specimens SPT and SPE whose (e/d) ratios are 2.0 and 2.25 respectively are presented in Figure 7.6 through 7.9. For specimen SPE the hoop strain distribution at the fastener hole is illustrated in Figure 7.8, whereas Figure 7.7 shows the location and magnitude of the minimum residual hoop strain obtained for the same specimen.

Examination of Figure 7.5 and the rest of the results of this section reveal that midway between the hole edge and the straight edge of the plate the strains almost vanish,

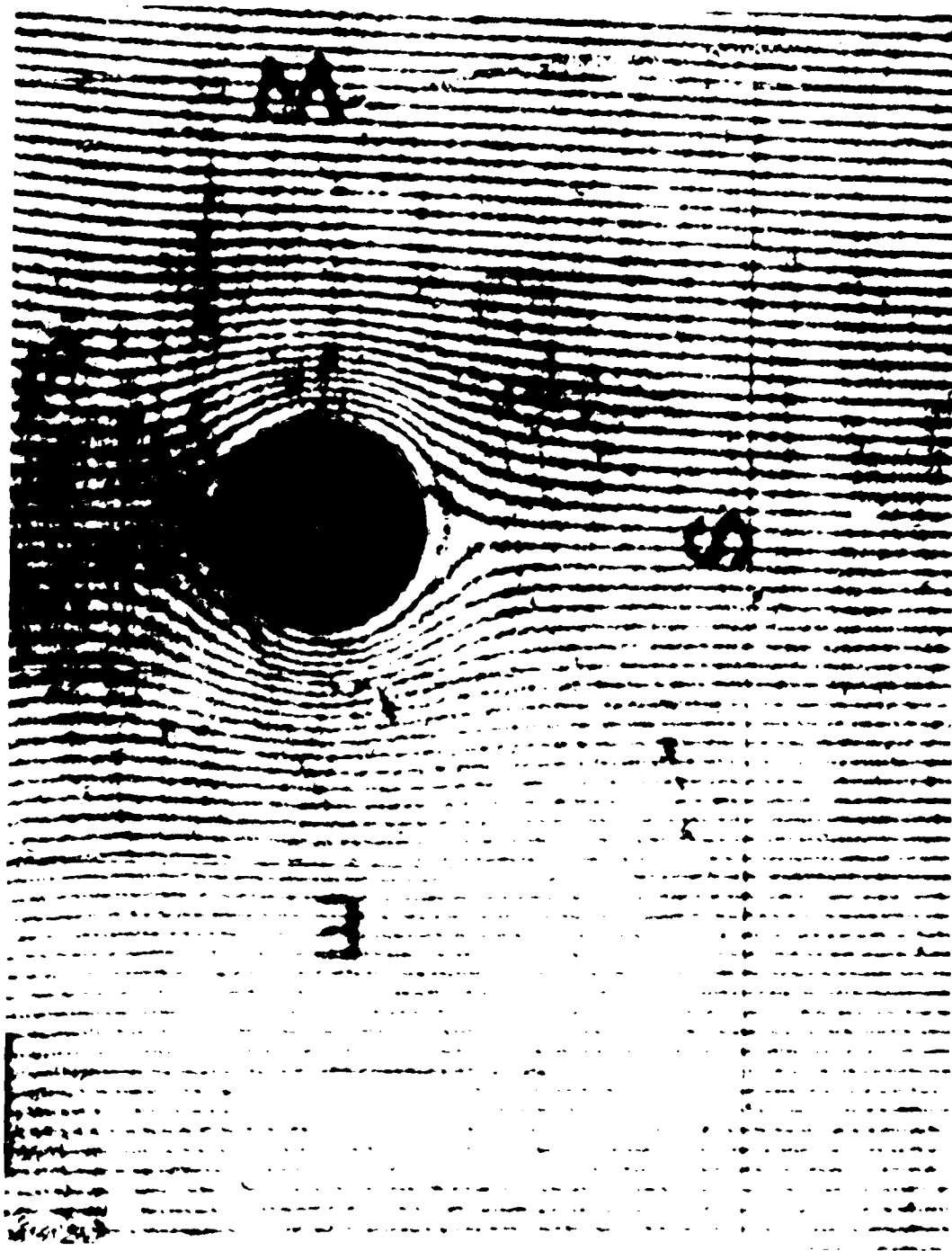


Figure 7.1 SPP after Hole Coldworking; Grating Parallel to Axis N-S.



Figure 7.2 SPT after Hole Coldworking.

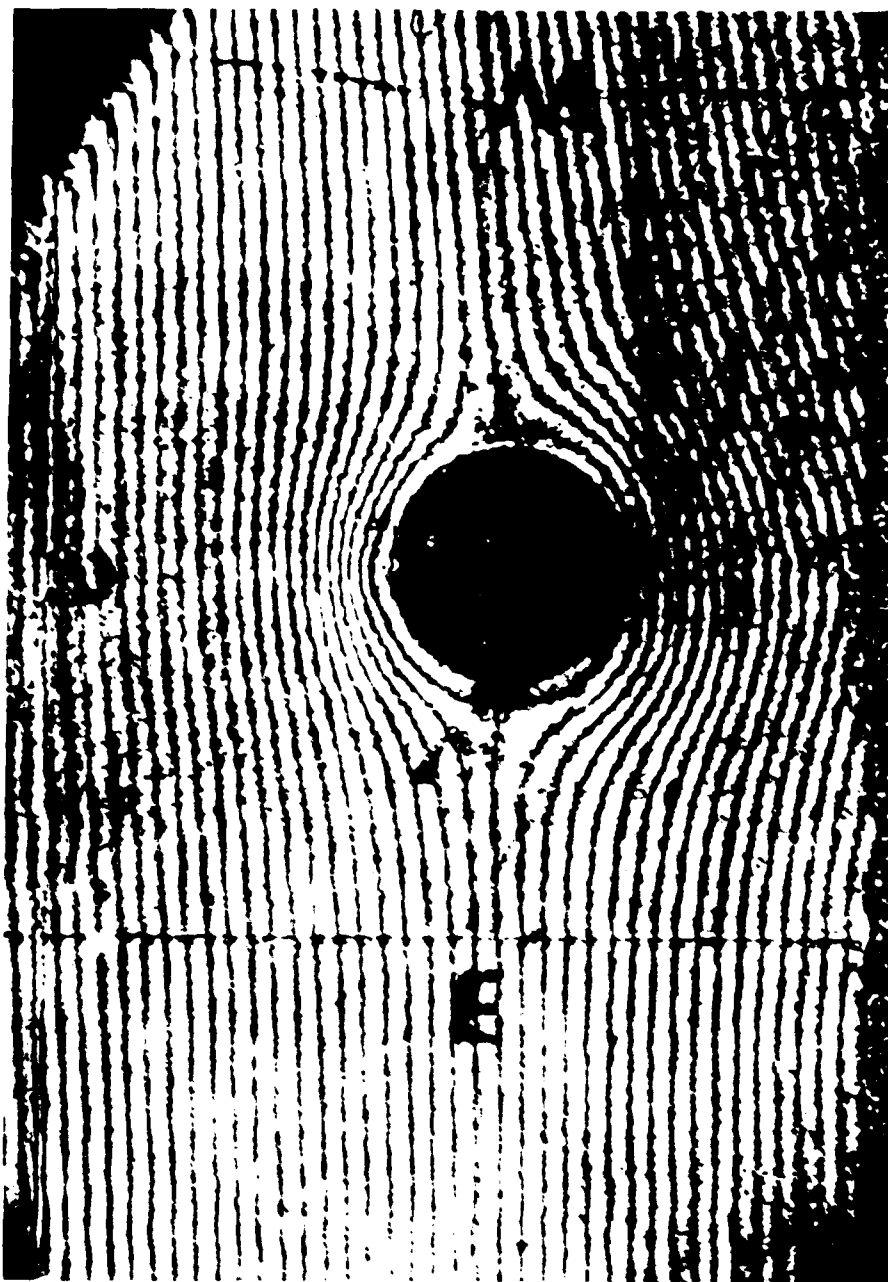


Figure 7.3 SPP Moiré Fringe Photography for Compressive Strain Evaluation Near Plate Edge; Grating Parallel to Axis W-E.

HOLE NO. SP P1 LR

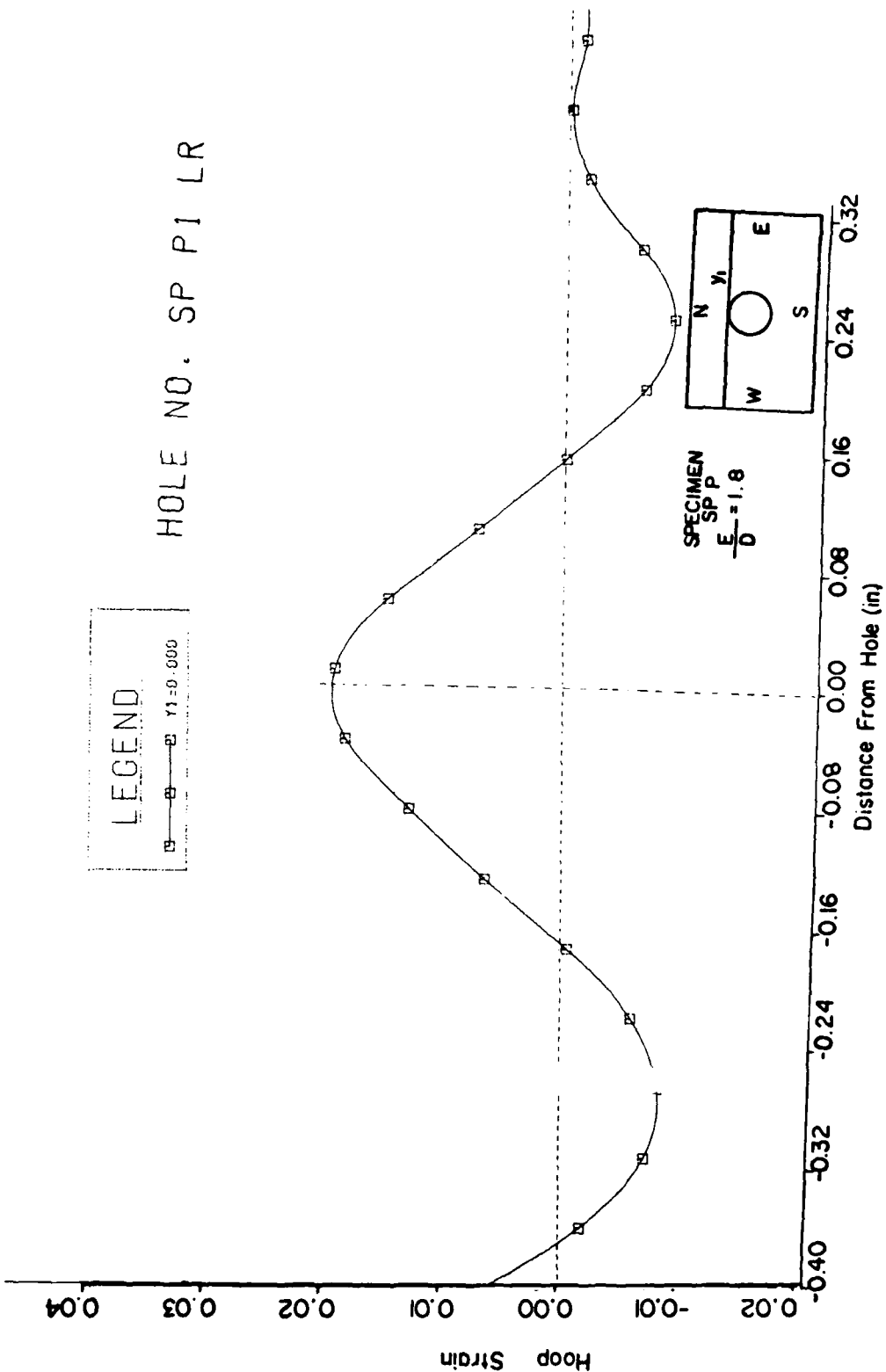


Figure 7.4 Residual Hoop Strain Distribution Along an Axis Tangent to the Hole Boundary for 8.9 mils Radial Interference.

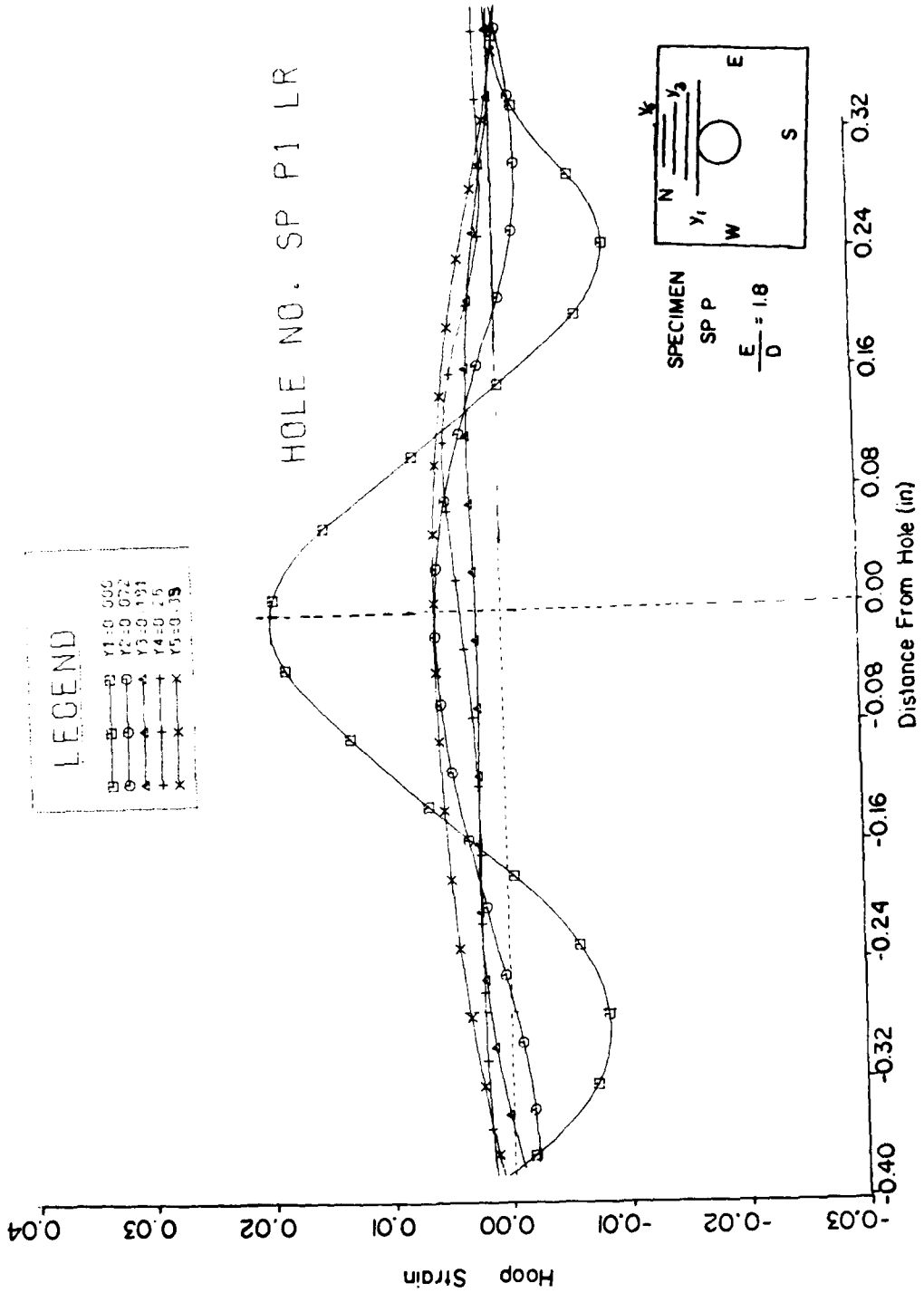


Figure 7.5 Measured Residual Hoop Strain Distributions Along Several Axes Near a Plate Edge at Different Radial Distances for 8.9 mils Interference (Specimen SPP).

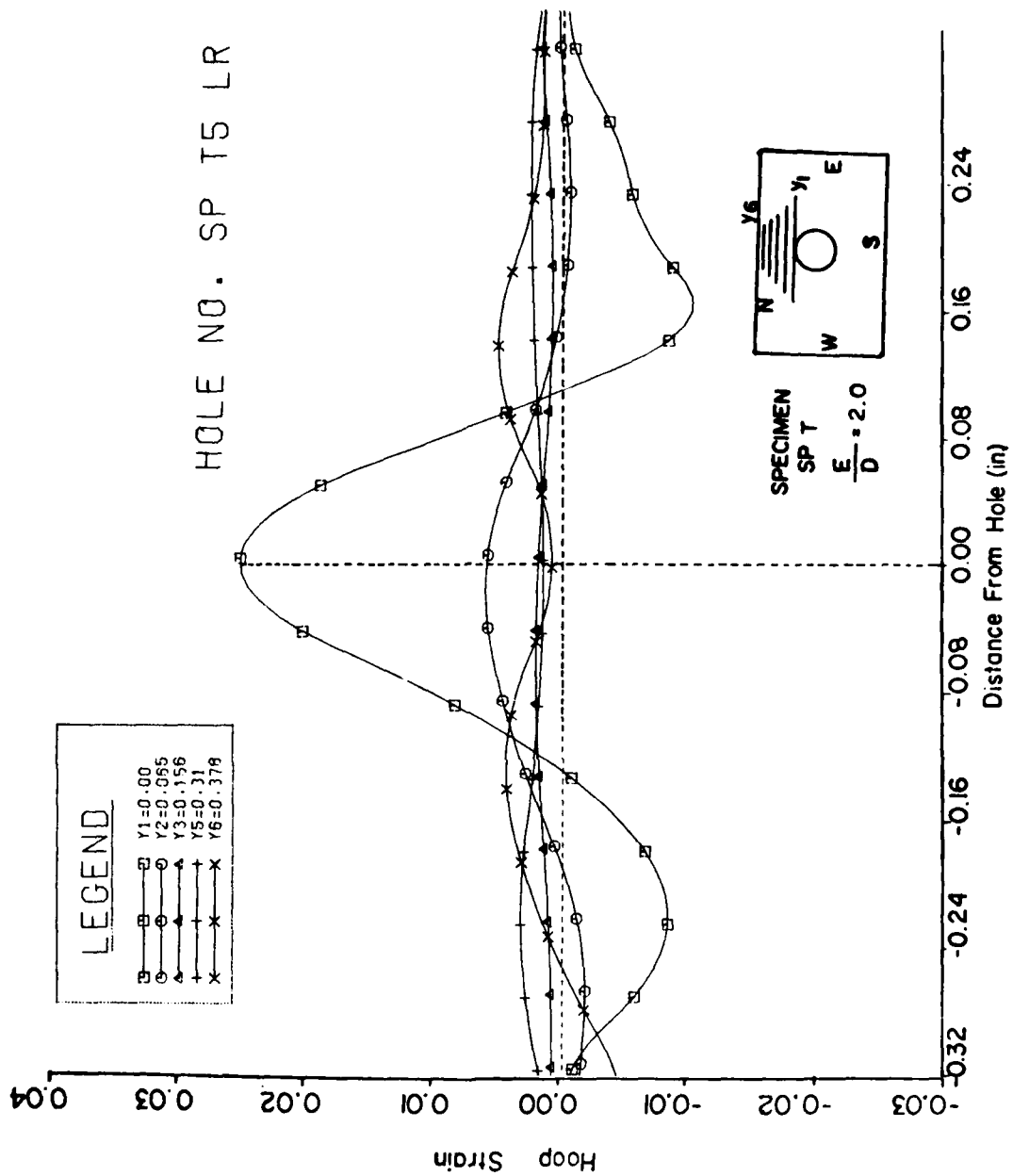


Figure 7.6 Measured Residual Hoop Strain Distributions Along Several Axes Near a Plate Edge at Different Radial Distances for 8.9 mils Interference (Specimen SPT).

HOLE NO. SP E8 LR

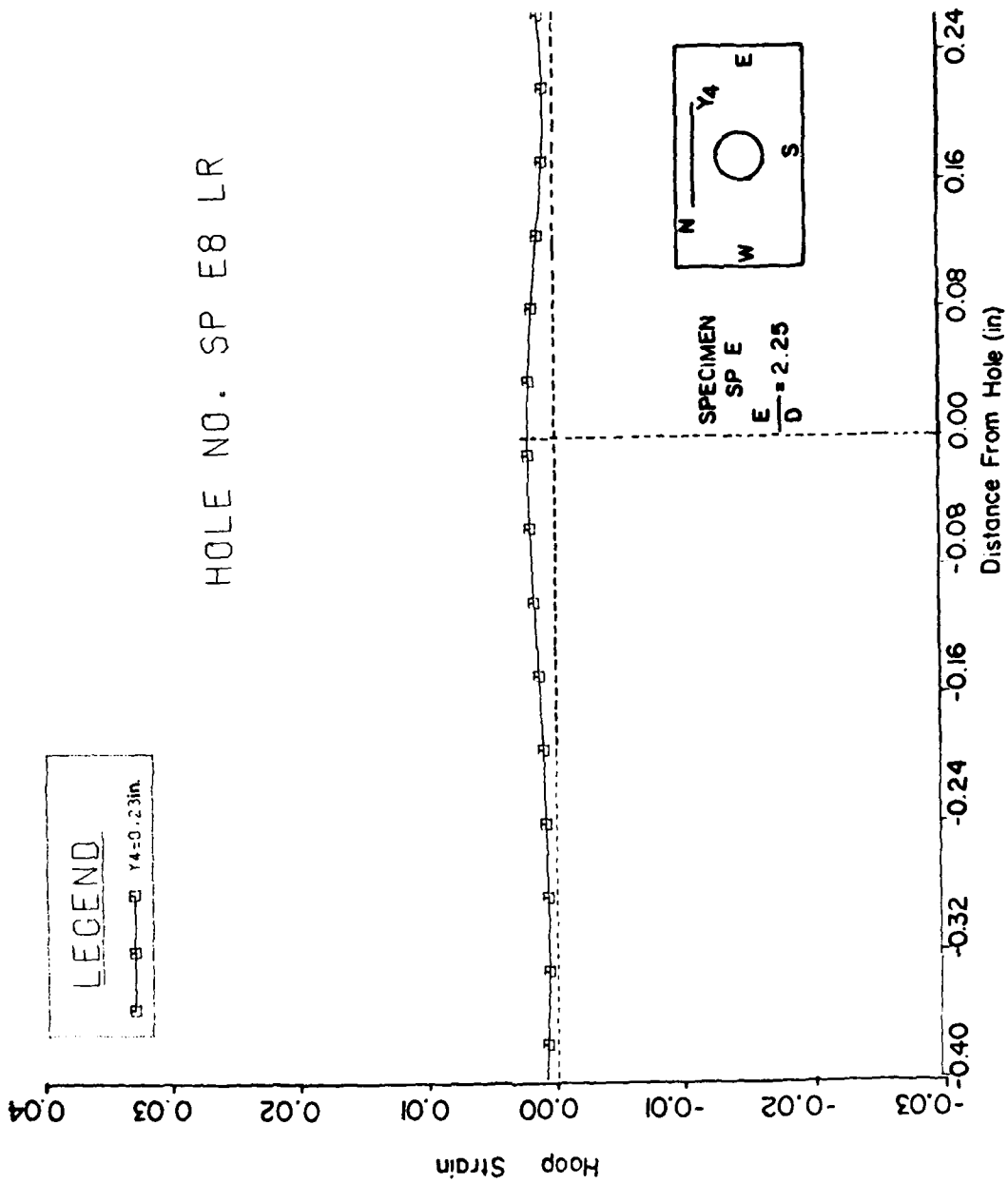


Figure 7.7 Residual Hoop Strain Distribution Along an Axis 0.24 Inches Along a Plate Edge for 8.9 mils Radial Interference.

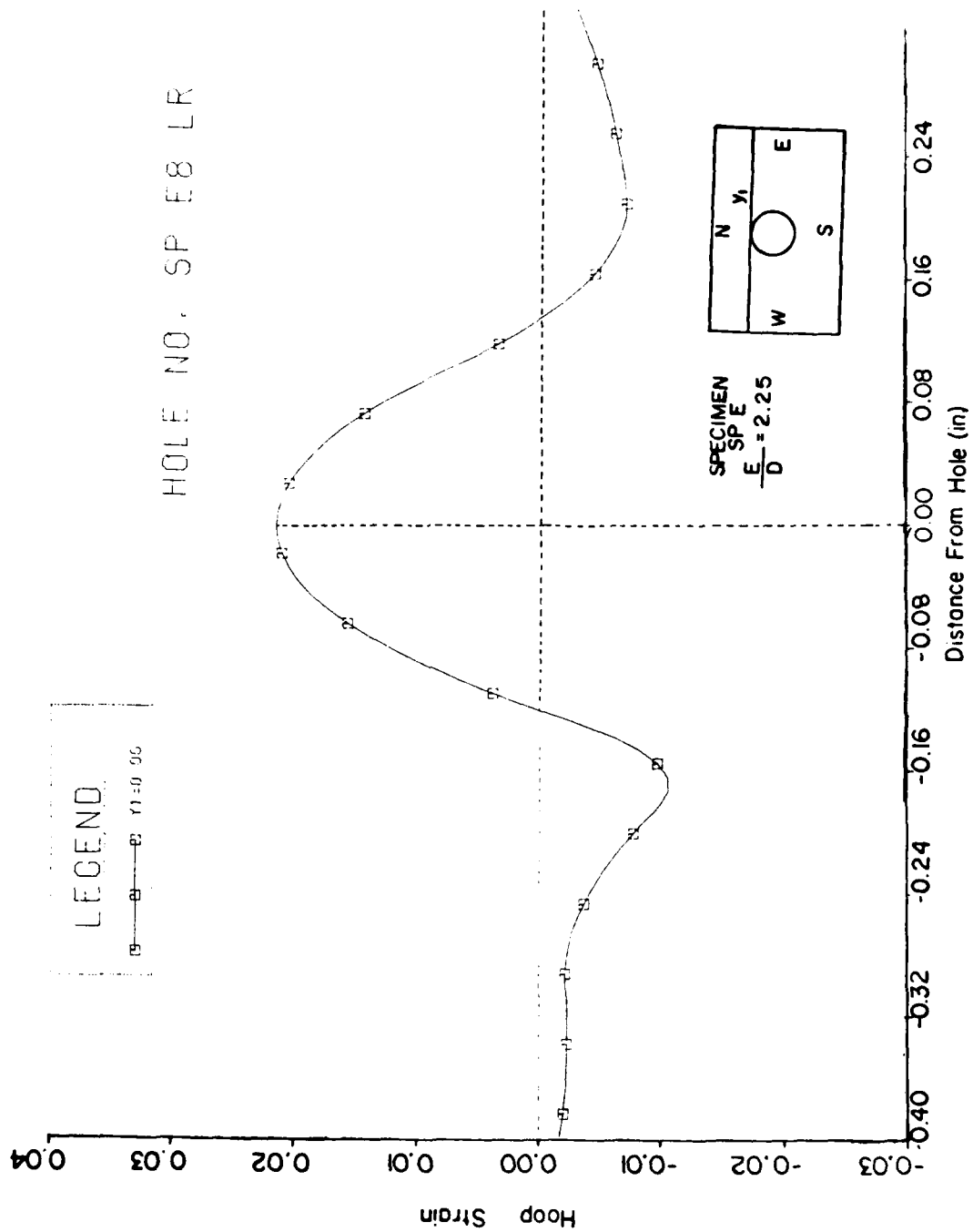


Figure 7.8 Residual Hoop Strain Distribution Along an Axis Tangent to the Hole Boundary for 8.9 mils Radial Interference.

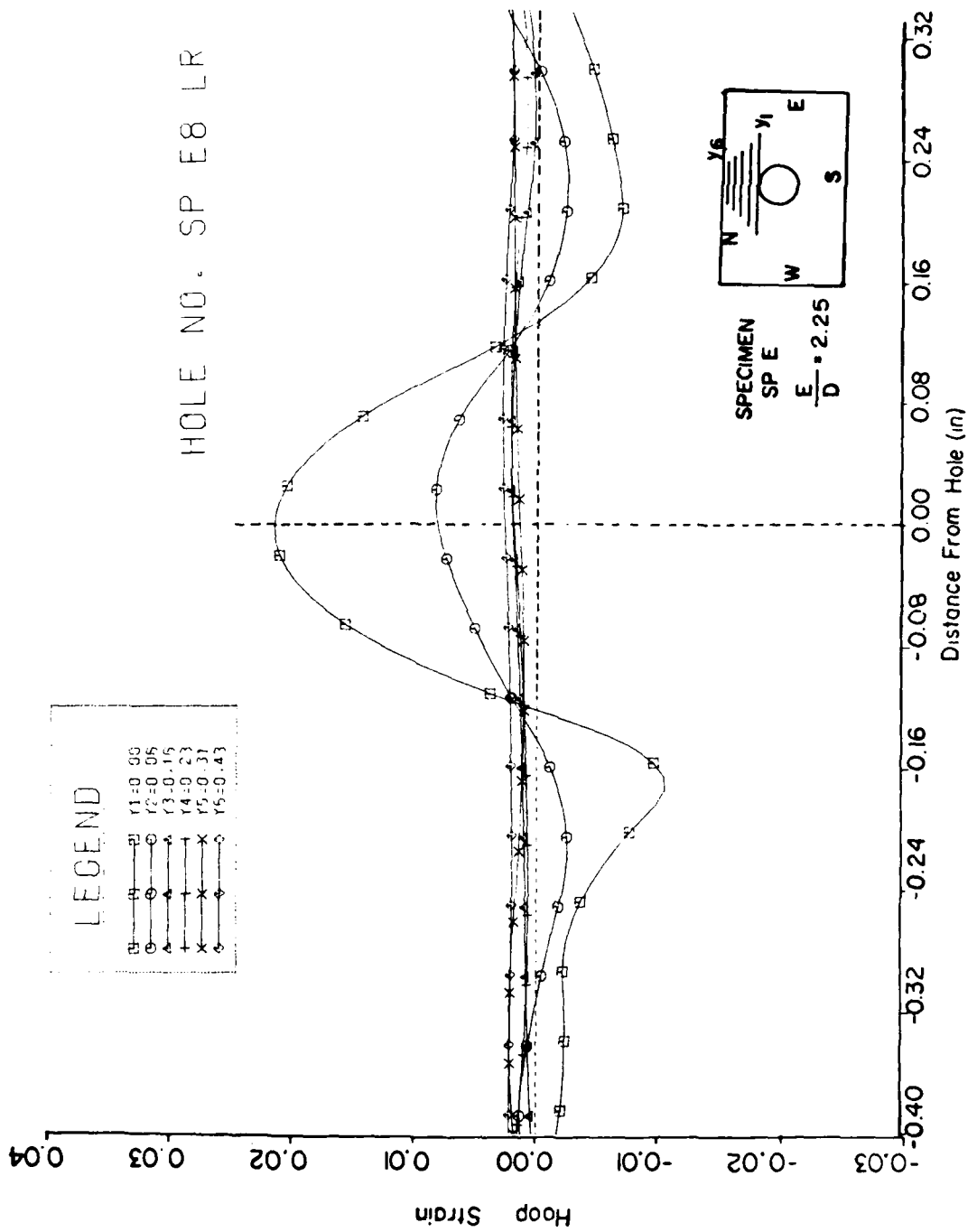


Figure 7.9 Measured Residual Hoop Strain Distributions Along Several Axes Near a Plate Edge at Different Radial Distances for 8.9 mils Interference.

but that they increase again as one approaches the straight edge. Therefore in structural fastener applications there seems to be the possibility that this radial expansion of the hole generates a significant tensile strain climate at the plate edge. This could result in serious problems in stress corrosive environments.

Figure 7.11 is a summary of the results presented in Figures 7.4 through 7.10. Peak residual hoop strain values were plotted as a function of the distance from the fastener hole edge for  $(e/d)$  values of 1.8, 2.0, and 2.25 as shown. Specimen SPP ( $e/d = 1.8$ ) had the highest tensile residual strain at the straight edge, approximately 0.5 percent. Specimen SPT ( $e/d = 2.0$ ), and SPE ( $e/d = 2.25$ ) had lower residual strains of 0.25 percent.

Figure 7.12 is a summary plot of the residual hoop strain distribution along the plate edge for the case of a row of rivet-fastener holes. Mandrelization order of this specimen ( $e/d = 1.8$ ) was holes 1, 2, 4 and #3. It is observed that the strain distribution around hole #3 attains its local minimum which is almost equal in magnitude to a single fastener hole in a semi-infinite plate as shown on the same graph. It can also be seen from the same plot that the strain magnitude increases by a factor of almost 2 when single hole and multi-hole pattern results are compared. The strain distribution, both in magnitude and extent, increases for only one fastener hole coldworked in a

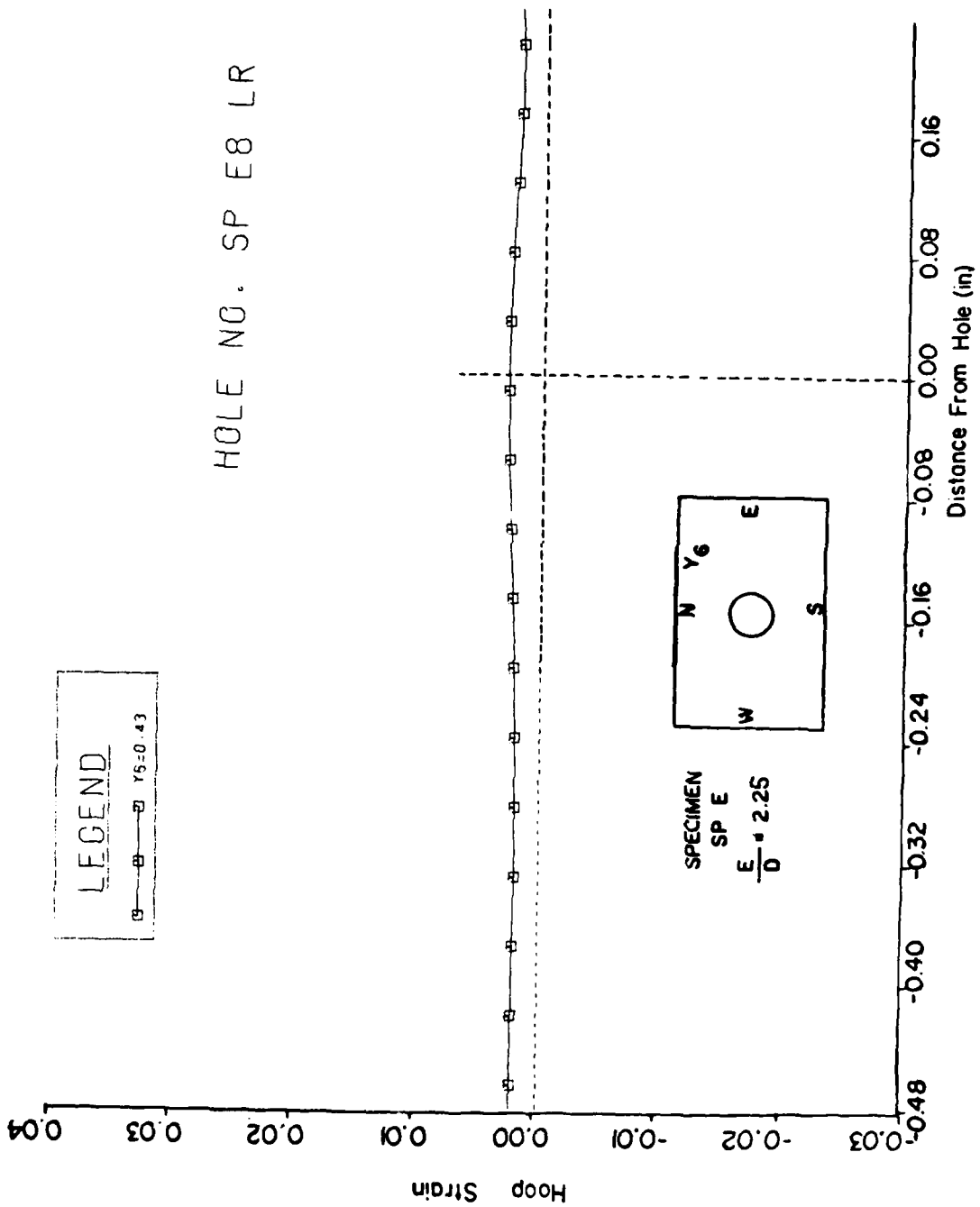


Figure 7.10 Residual Hoop Strain Along Plate Edge for 8.9 mils Radial Interference.

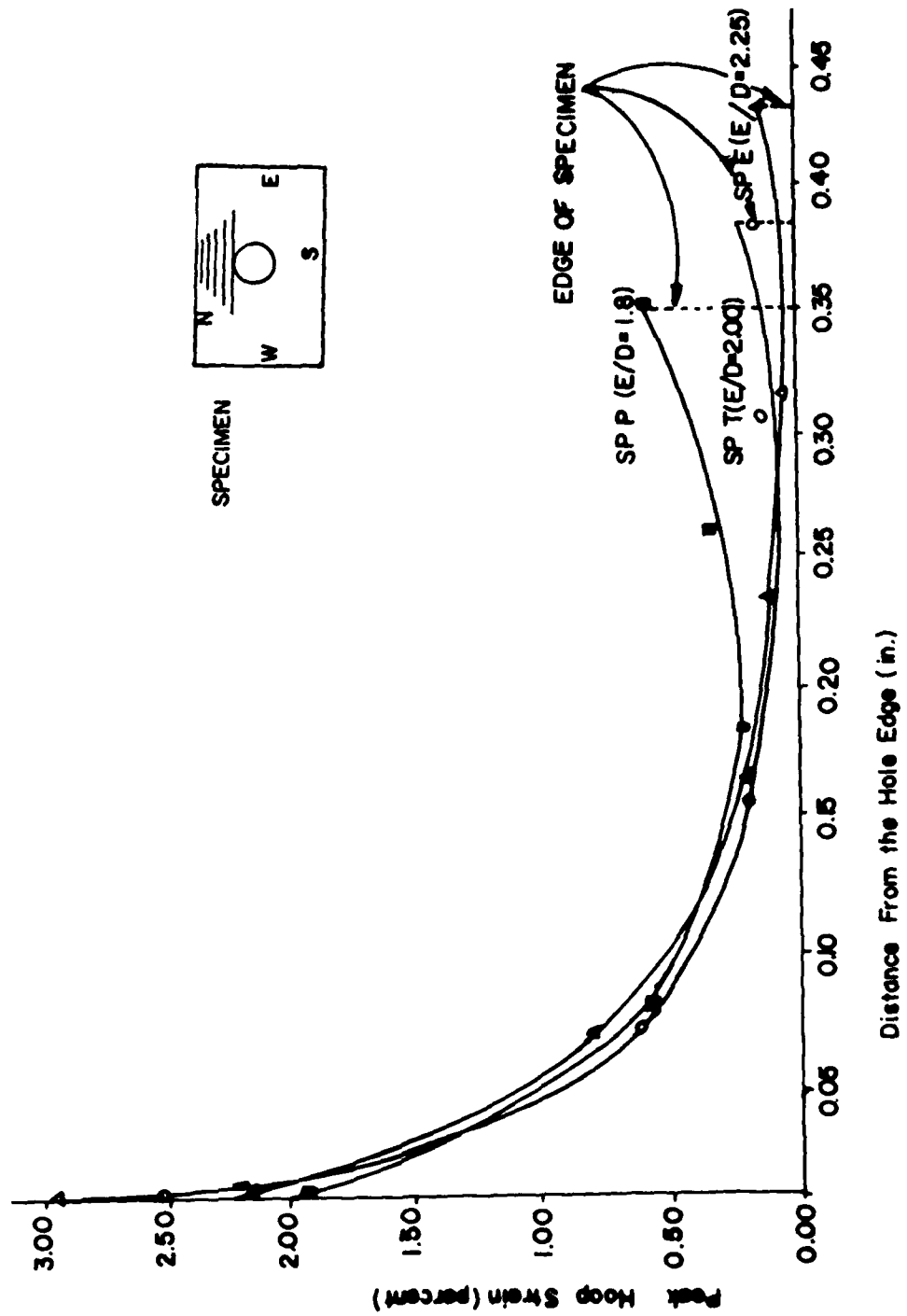


Figure 7.11 Peak Residual Hoop Strain Along Radial Line from Hole Boundary to Plate Edge.

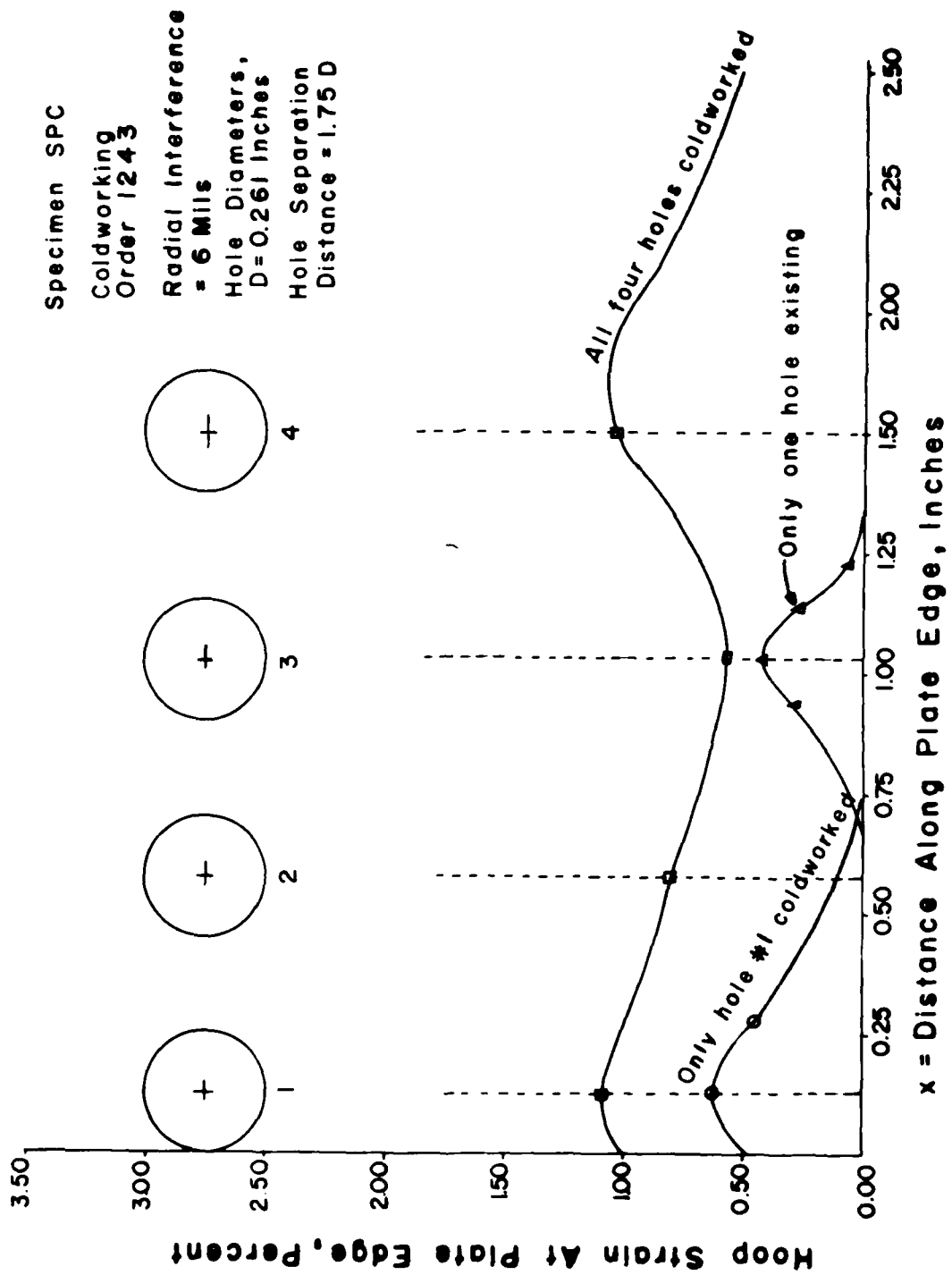


Figure 7.12 Measured Residual Hoop Strain Distributions Along Specimen Edge for Various Coldwork Situations.

row of holes compared with the case of the strain distribution obtained with only one fastener hole existing in a semi-infinite plate.

### 7.3.2 Radial Compressive Strain Distribution

Compressive residual strains are presented in Figure 7.13 through Figure 7.21. Specimen SPE ( $e/d = 2.25$ ) had the highest radial compressive strain (3.5 percent) occurring at the hole boundary, followed by specimens SPT ( $e/d = 2.0$ ) and SPP ( $e/d = 1.8$ ) with 2.5 percent and 2.25 percent respectively. Figure 7.14 presents plots of compressive residual radial strains between a single fastener hole and the straight edge in a semi-infinite plate. For the multi-hole pattern the results are given in Figures 7.15 through 7.21. Figures 7.17 through 7.21 summarize the findings of the multi-hole pattern configuration with regard to residual radial compressive strain distributions as a function of order of fastener hole coldworking. The graphs show a peak residual strain and zero strain values between the fastener hole edge and the straight edge boundary of the plate respectively. (The radial stress should of course go to zero at the edge).

In a multi-hole pattern, the prestressing of a hole markedly affects the strain distribution of adjacent holes. Coldworking of hole #1 resulted in a residual strain value of approximately 2.5 percent. Subsequent coldworking of holes 2, 4, and 3 lowered the strain value to approximately

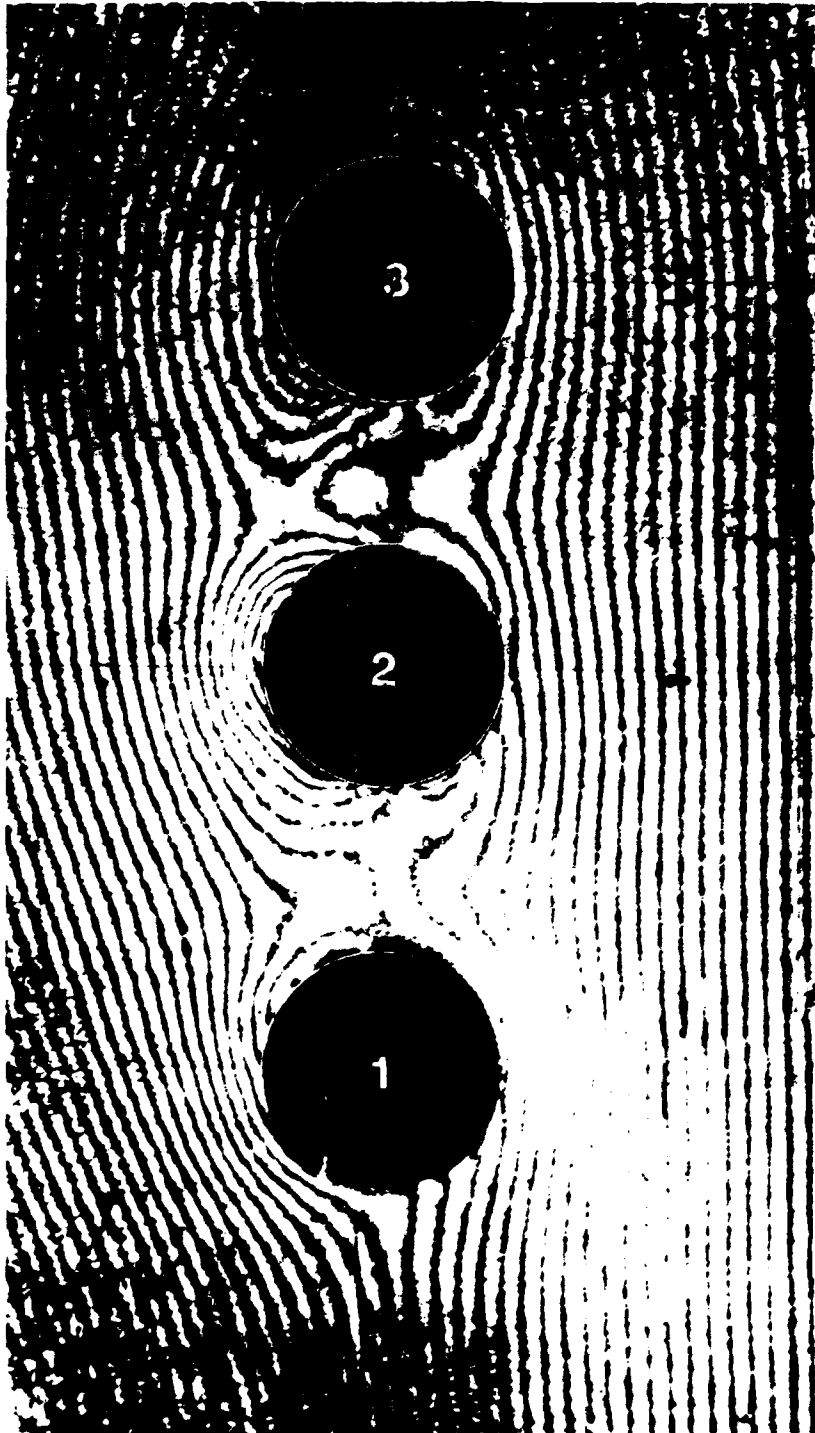


Figure 7.13 Moiré Fringe Photograph used in the Evaluation of Radial Compressive Strains Near a Plate Edge (Specimen SPC).

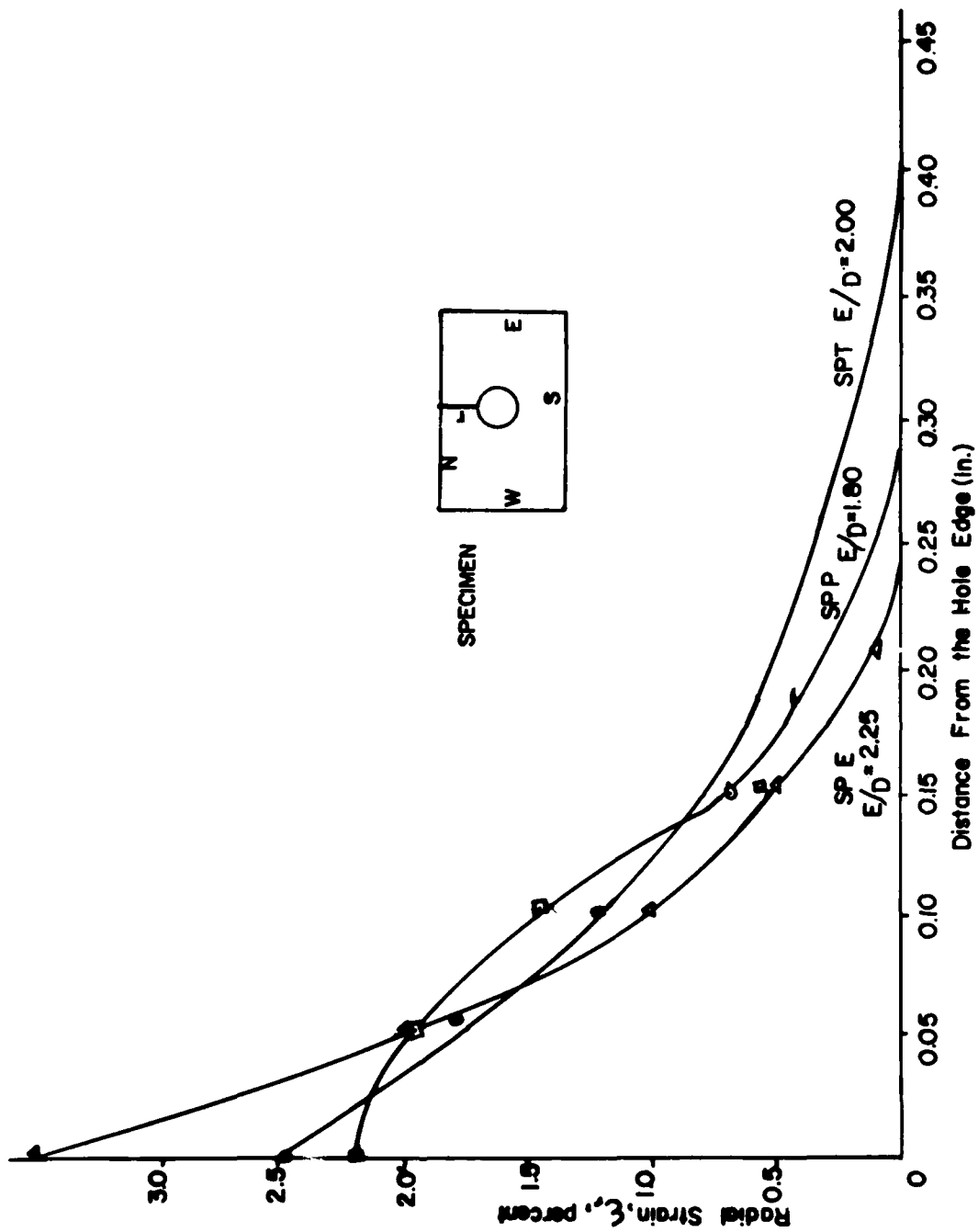


Figure 7.14 Residual Radial Strain from Hole Boundary to Plate Edge.

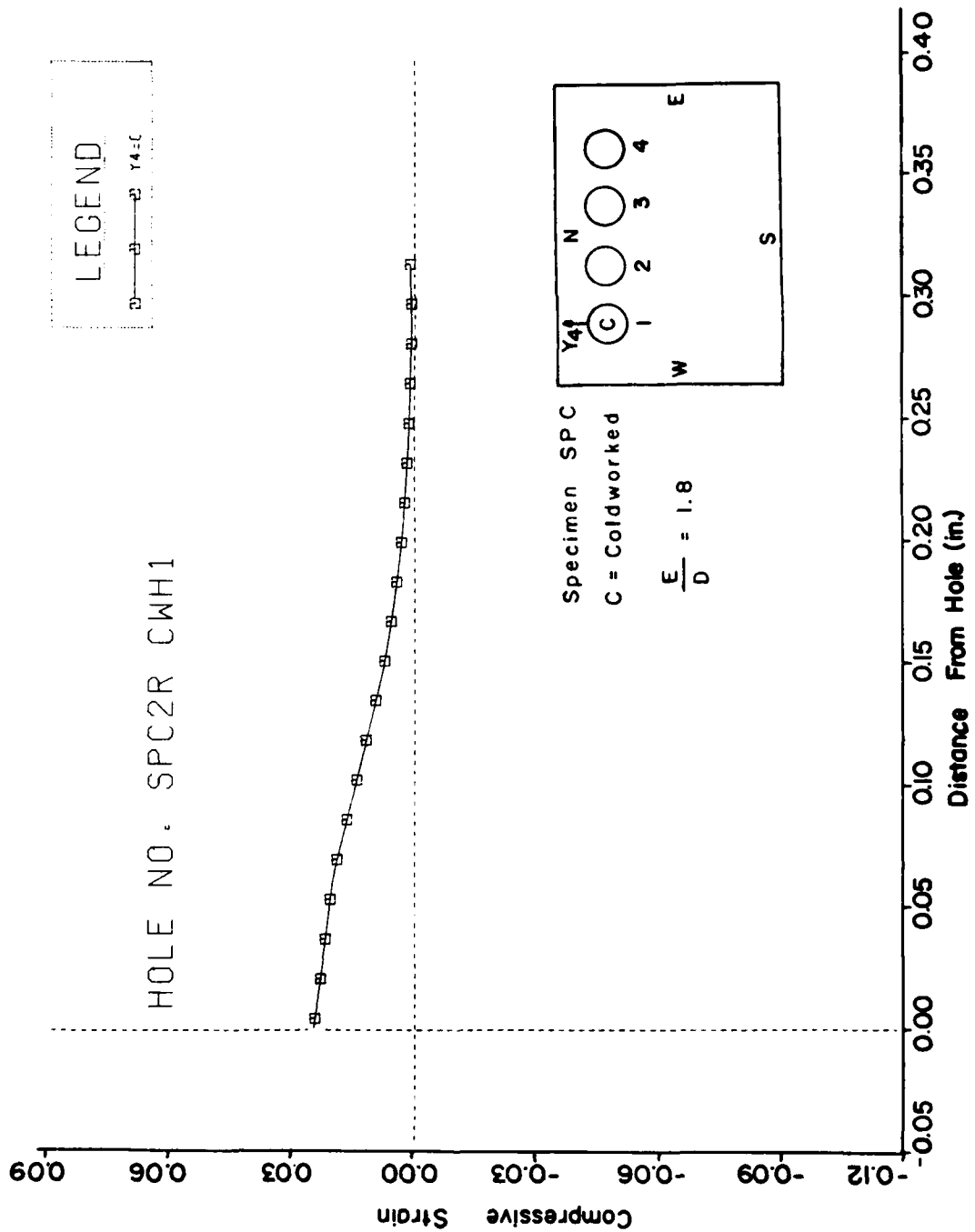


Figure 7.15 Residual Compressive (Radial) Strain Between the Plate Edge and Hole # 1 after Coldworking of Hole #1 Only for 6 mils Radial Interference.

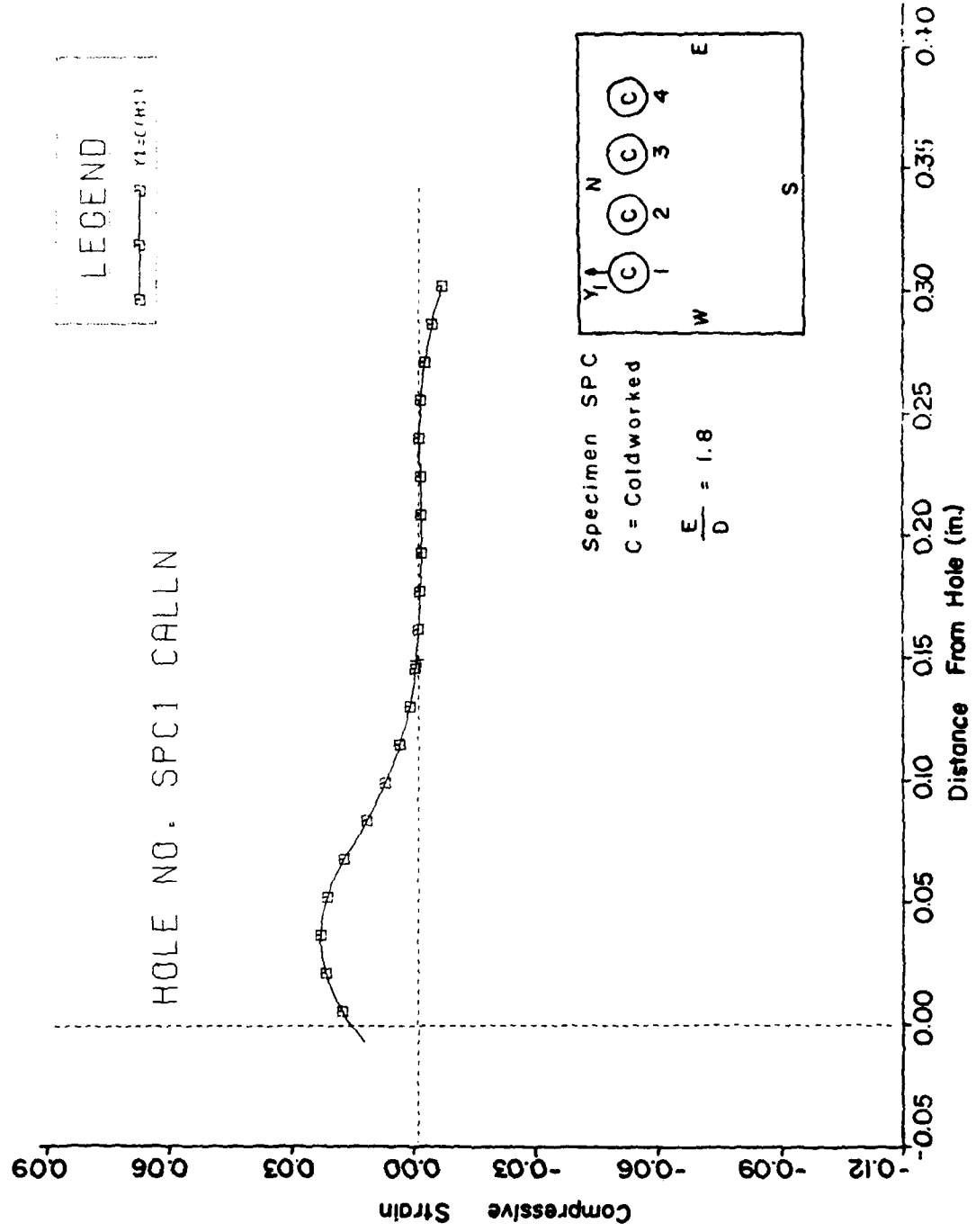


Figure 7.16 Residual Compressive (Radial) Strain Between the Plate Edge and Hole #1 after Coldworking at 6 mils Radial Interference.

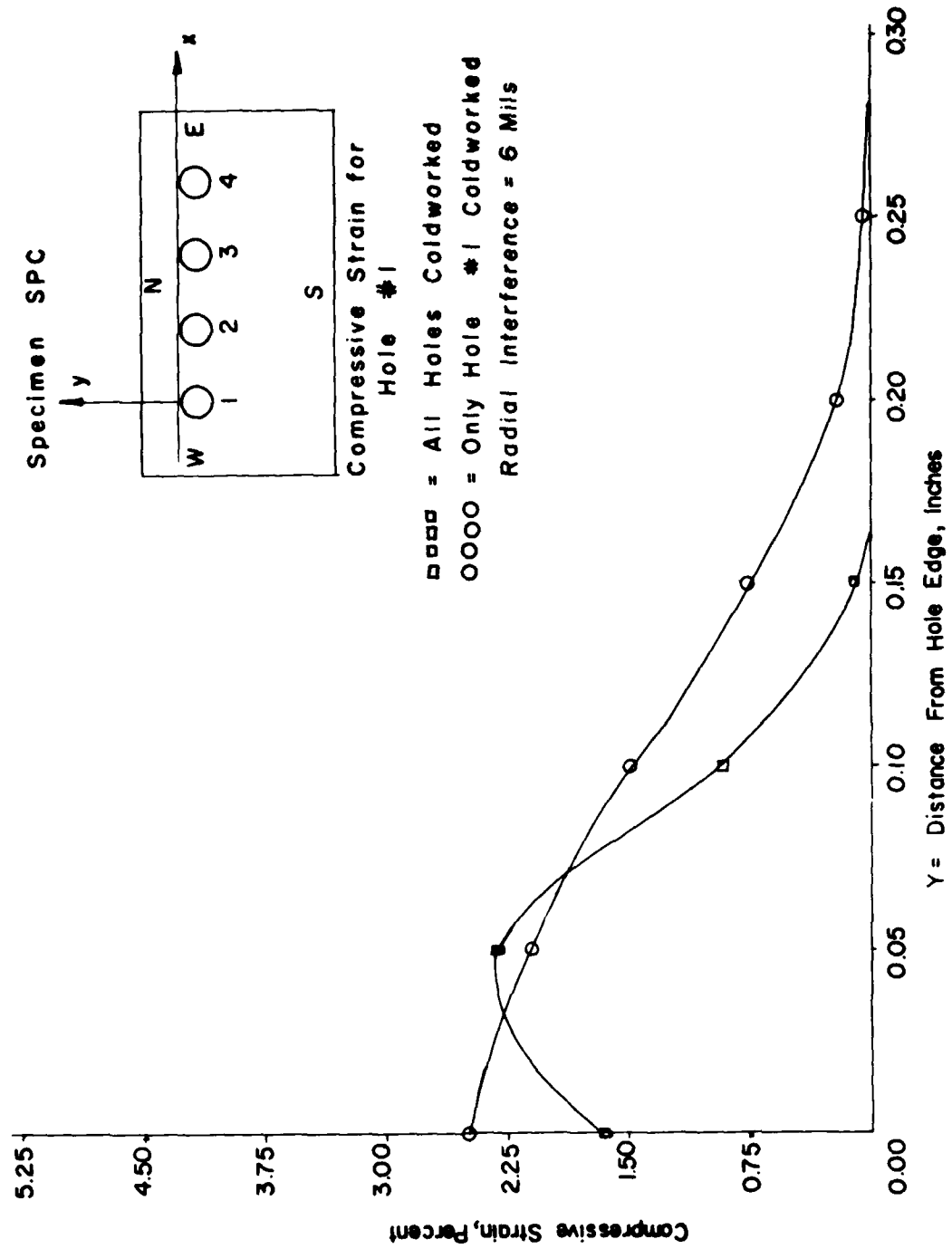


Figure 7.17 Residual Compressive Strain Distributions after Coldworking.

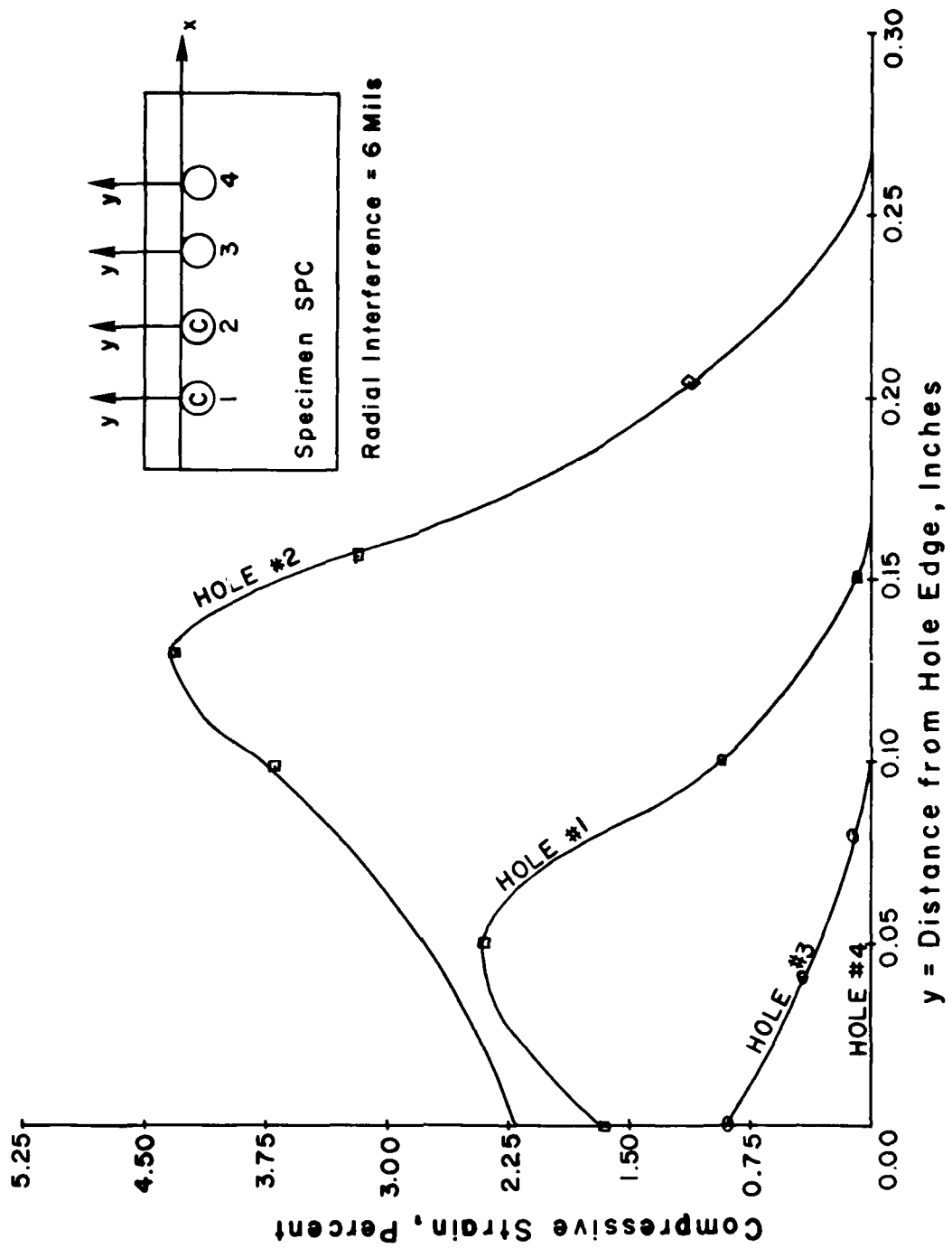


Figure 7.18 Residual Compressive Strain from Hole Boundary to Plate Edge for Multi-Hole Pattern Specimen.

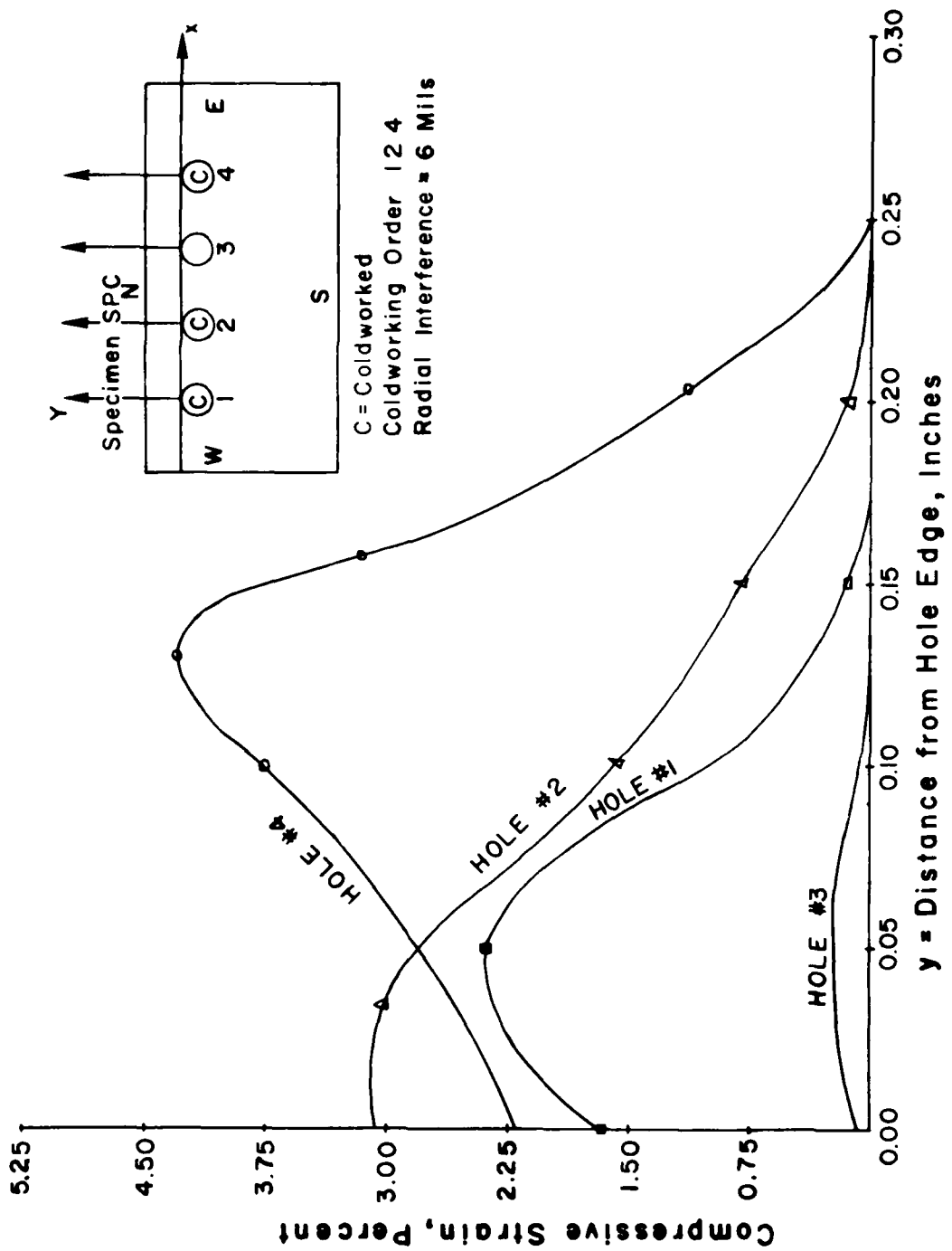


Figure 7.19 Residual Compressive Strain Distributions after Coldworking Holes 1, 2, and 4.

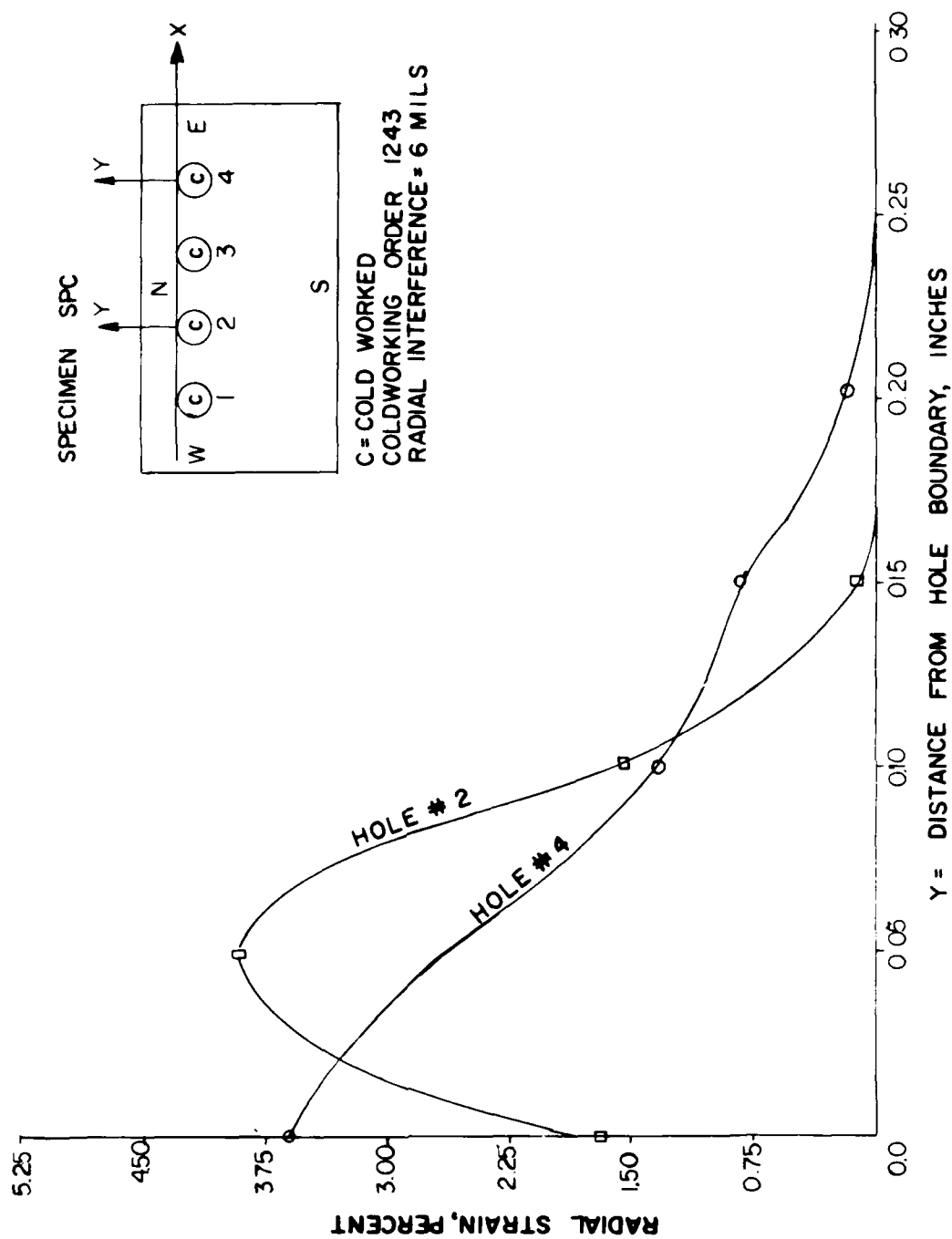


Figure 7.20 Residual Compressive Strain Distributions for Holes 2 and 4 after Coldworking All Holes.

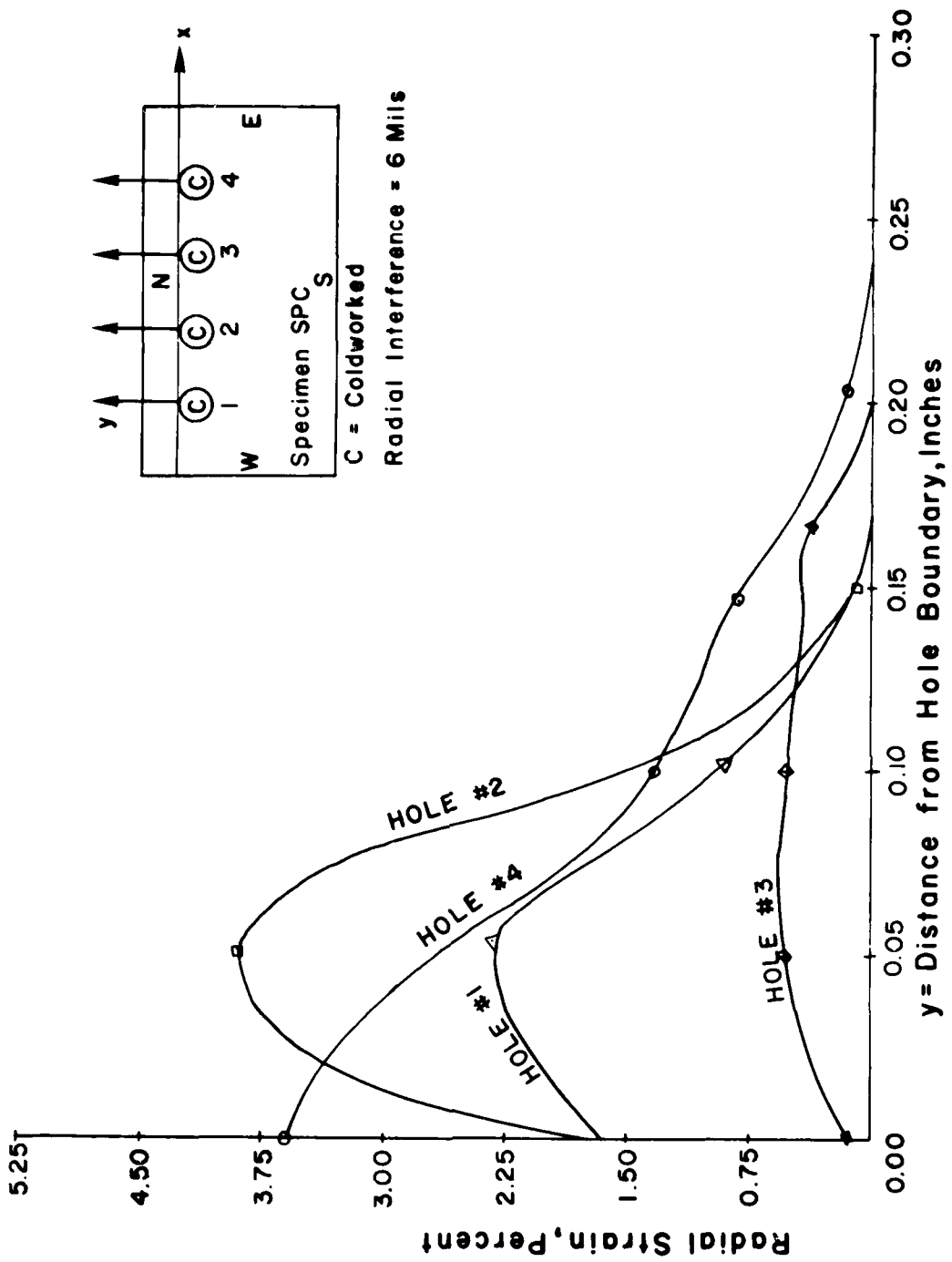


Figure 7.21 Residual Compressive Strain Distributions after Coldworking All Holes.



1.5 percent and reduced the residual compressive area from around 0.25 in. (6.35 mm) to roughly 0.15 in. (3.81 mm) radially away from the fastener hole, thus partially wiping out the beneficial effects of the coldworking operation.

The overall message presented in these figures is that the peak compressive residual strains are shifted away from the most critical and important area, near the fastener hole, to the interior in between the prestressed holes. Also, the subsequent final coldworking of hole #3 seems to be ineffective after the coldworking of the rest of the holes in the row (Figure 7.21).

One possible deduction from the results of a single fastener-hole in a semi-infinite plate might be that with increasing (e/d) ratios the residual compressive strains at the fastener hole boundary increase. The case of mandrelizing a fastener hole in an infinite plate for a given material, specimen configuration, and loading, the strain distribution represents a limiting state. Specimen SP2 with a hole in an infinite plate gave a radial strain value of around 5 percent for a corresponding prestressing radial interference of around 7.5 mils. Nevertheless, for a radial distance greater than 0.05 in. (1.27 mm) the residual strains are approximately of the same magnitude and the values differ by less than 0.5% at any point in this region, Figure 7.14.

In general, it is observed that, for the case of a single fastener hole near a plate edge, regardless of the

(e/d) ratio used, the radial strain starts high at the hole boundary and decreases to zero as the plate edge is approached.

Contrary to this behavior the summary plot of residual hoop strains as a function of the radial distance from the edge of the fastener hole for the same specimens indicate a high value at the hole boundary diminishing to a local minimum, at a distance of approximately 0.168 in. from the hole. A localized higher strain value at the plate edge directly opposite the fastener hole is then attained.

## SECTION IX

### CONCLUSIONS

#### 8.1 Introduction

This investigation has been concerned with the study of:

1. the effects of large in-plane compressive loads on a mandrelized fastener hole,
2. the interaction between the surface strain fields which are created by prestressing two or more fastener holes drilled in close proximity to one another.
3. the effects of a near plate edge on the residual surface strain field, and,
4. ramifications of the existence of a residual strain climate, produced by coldworking a near hole, on the edge of the plate in a corrosive service environment.

The moiré method of strain analysis has proven very useful for the investigation. With this methodology, the measurement of small and large elastic and plastic strains over an extended field was accomplished.

#### 8.2 Experimental Apparatus

Optical spatial filtering proved to be indispensable in separating the u-field and v-field isothetics.

The fringe analysis system minimized data reduction problems. The microprocessor-controlled digitizer was instrumental in obtaining reliable displacement field data. This was an extremely important factor since the data must be differentiated to find the strains. Additionally, mismatch techniques were introduced in the fringe formation process to improve the accuracy of the measured displacement gradients in the x and y directions.

In the optical analyzer, ordinary focusing errors are not significant since for a lens whose aberration characteristics are smaller than the diffraction limit of the lens aperture, about 84 percent of the energy from any point of the specimen and master grating assembly falls in a small region called the Airy disk on the image plane. The rest falls immediately outside it. As long as the area of this Airy disk is smaller than the separation distance between the moire fringes, focusing problems are negligible. This was almost always the case in this investigation.

### 8.3 Summary of Results

The results can be summarized as follows:

1. The axial residual hoop strains decrease with increasing remote in-plane compressive applied stress, especially in areas close to the fastener hole.

2. The effect of cycling is a decrease in the residual hoop strain around the hole except in areas where flaws exist at the fastener hole boundary.

3. The transverse residual hoop strain increases with increasing overload applied stress in areas within 0.135 in. of a (0.261 in. diameter) hole boundary.

4. Remote in-plane compressive loads smaller than buckling loads and cycling of loads have no effect on a non-coldworked fastener hole.

5. The residual strain climate around a coldworked hole is not symmetric. The assumption of uniform radial loading in the analytical theories is not entirely an accurate model.

6. The residual radial compressive strain remains essentially constant with remote compressive load application.

7. The residual radial compressive strain distribution assumes an exponential nature. The strains attain their maximum value at the edge of the hole and rapidly diminish to zero with distance from the hole edge.

8. For the specimens subject to large in-plane compressive overload, the results for the initial stages (after coldworking only) agree quite well with those obtained by previous investigators, notably W. Adler and D. Dupree (29), and by Cloud (24). The discrepancies probably result from experimental factors such as levels of coldworking.

9. The observed results for specimen C10, Figure 5.8, seem to be quite in agreement with the theory that under loading that produces cyclic plastic strains, the residual stresses, which are nothing more than unevenly distributed mean stresses, tend to become smaller with cycling. This behavior is commonly called cycle-dependent stress relaxation.

10. However, the results presented in Figure 5.6 for specimen C10 indicate that, in the presence of residual stresses, the material is experiencing cyclic creep on being cycled. This phenomena does indeed occur under tensile mean (residual) stresses. The moiré fringe photographs suggest that there existed a flaw, a microscopic crack, at the fastener hole boundary of this specimen. In those small but critical neighborhoods near a crack, the presence of even moderate residual tensile stresses could be detrimental, and a runaway crack condition is possible especially under a load control test as in this particular case. Nevertheless, there is one strong message that is clear in the results of the compressive overload study: a machine part may be properly mandrelized to introduce beneficial compressive residual stresses and the service loads in the member kept small enough so that the residual stresses are stable for a good part of the machine's life. But should large overloads be encouraged, the benefit of the original compressive residuals would be lost.

11. Two hole diameters is approximately a minimum hole separation distance, for a radial interference of 6 mils, below which the effect of coldworking a row of fastener holes diminishes the residual compressive strain field around the fastener holes, thus nullifying the advantages of the coldworking process.

12. The coldworking of a single fastener hole or a row of holes near an edge of a plate results in an undesirable tensile strain climate on the plate edge. (See also conclusion no. 16.)

13. The results also indicate that the level of radial interference for a multi-hole prestressing operation needs to be given some consideration. Maximum fatigue life presumably would be obtained if the resultant stresses were evenly distributed across the member at maximum load. But, experiments indicated that (test specimens SPB and SPC - a multi-hole pattern), if the level of coldworking was kept constant from hole to hole, the beneficial overstressing effects originally sought tended to be nullified. In general, the compressive residual strains were higher away from the hole boundary. This is in contrast to what is observed with a coldworked single hole in a plate. A partial explanation is that the hole edge (side) adjacent to the one being prestressed goes into a state of tension, and this state of strain must first be overcome before establishing the permanent strain that is to be imposed.

14. Nullification of the pre-stress would not be a serious flaw if there were not the possibility of premature structural failure in service due to high levels of cold-working. Plastic flow occurs when the difference between the circumferential and radial stresses equals the yield strength. Since these stresses have opposite signs, the difference can become very large without the appearance of detrimental tangential stresses large enough to cause failure.

15. Examination of the specimen photographs and the data photographic plates in an optical analyser revealed that the hole experiences some sort of "rigid body motion" perhaps more so than the actual deformation imposed by the mandrel in the direction perpendicular and towards the straight edge boundary of the plate. This effect is more pronounced in specimens with  $(e/d)$  ratios smaller than the threshold value of  $e/d = 2.0$ .

16. For a single fastener hole in a plate, residual hoop strains attain a high value at the hole boundary diminishing to a local minimum at a distance of approximately 0.168 in. from the hole. A localized higher strain value exists at the plate edge directly opposite the fastener hole. ( $\epsilon = .0025$  for  $e/d = 2$ , for example.)

17. In a row of rivet holes, the peak compressive radial residual strains are shifted away from the most critical and important area near the fastener hole to the interior between the pre-stressed holes.

18. Experimental projects of this nature have their own shortcomings. Nevertheless, in spite of the limitations on the results presented in this study, drastic assumptions commonly made in analytical work about the materials constitutive behavior and magnitudes of the strains were not made here. Possible asymmetries found in real fastener joints which present formidable difficulties in formulation were pointed out.

#### 8.4 Future Research

Future fastener research should be directed towards the determination of the effects of the factors that were not considered in this investigation, namely different levels of coldworking on the multi-hole pattern in order to arrive at an optimum coldworking level as a function of  $(e/d)$  ratio.

An extremely important step is to measure residual stresses and to correlate them with the residual strains determined in this study.

Other pertinent variables should include plate thickness, hole straightness and ovality, sheet material, and hole separation distance. These variables and others undoubtedly play a significant role in the redistribution of the resulting residual strains and therefore on the fatigue life of the structure after the coldworking operation.

## REFERENCES

1. Mangasarian, O.L., "Stresses in the Plastic Range Around a Normally Loaded Circular Hole in an Infinite Sheet" (J. Appl. Mech., Vol. 27, 1960), pp. 65-73.
2. Forman, R.G. and Y.C. Hsu, "Elastic-Plastic Analysis of an Infinite Sheet Having a Circular Hole Under Pressure" (J. Appl. Mech., Vol. 42, 1975), pp. 347-352.
3. Sachs, G., and J.D. Lubahn, "The Strength of Cylindrical Dies" (J. Appl. Mech., Vol. 10, 1943), pp. A147-A155.
4. Kuhn, P., Stresses in Aircraft and Shell Structures (McGraw-Hill, New York, 1956).
5. Calcote, L.R., and C.E. Bowman, "Experimental Determination of the Elastic-Plastic Boundary" (Exp. Mech., Vol. 5, Aug. 1965), pp. 262-266.
6. Opper, G.U., and P.W. Hill, "Strain Measurements at the Root of Cracks and Notches" (Exp. Mech., Vol. 4, No. 7, July 1964), pp. 206-211.
7. Regalbuto, J.A., and O.E. Wheeler, "Stress Distributions from Interference Fits and Uniaxial Tension" (Exp. Mech., Vol. 10, No. 7, July 1970), pp. 274-280.
8. Kasgard, P.V., E.E. Day, and A.S. Kobayashi, "Exploratory Study on Optimum Coining for Improvement of Fatigue Life" (Exp. Mech., Vol. 4, 1964), pp. 297-305.
9. Dechaene, R., and A. Vinkier, "Use of the Moiré Effect to Measure Plastic Strains" (J. of Basic Eng., Vol. 82, Series D, June 1960), pp. 426-434.
10. Morse, S., A.J. Durelli, and C.A. Sciammarella, "Geometry of Moiré Fringes in Strain Analysis" (J. of Eng. Mech. Div., Proceedings of the American Society of Civil Engineers, Vol. 86, No. EM4, Aug. 1960), pp. 105-117.

11. Schiapparella, C.A., and A.J. Dureli, "Moiré Fringes as a Means of Analyzing Strains" (J. of Eng. Mech. Div., Vol. 87, No. EMI, Feb. 1961), pp. 55-74.
12. Theocaris, P.S., "Isopachic Patterns by the Moiré Method" (Exp. Mech., Vol. 4, June 1964), pp. 153-159.
13. Weller, R., and B.M. Shepard, "Displacement Measurement by Mechanical Interferometry" (Exp. Stress Analysis, Vol. 6, No. 1, 1948), pp. 35-38.
14. Chiang, F., "Production of High-density Moiré Grids-- Discussion" (Exp. Mech., Vol. 9, June 1969), pp. 286-288.
15. Post, D., "The Moiré Grid-analyzer Method for Strain Analysis" (Exp. Mech., Vol. 5, Nov. 1965), pp. 368-377.
16. Post, D., "New Optical Methods of Moiré Fringe Multiplication" (Exp. Mech., Vol. 8, Feb. 1968), pp. 63-68.
17. Post, D., "Sharpening and Multiplication of Moiré Fringes" (Exp. Mech., Vol. 7, April 1967), pp. 154-
18. Luxmoore, A., and R. Herman, "An Investigation of Photoresists for Use in Optical Strain Analysis" (J. of Strain Analysis, Vol. 5, No. 3, 1970) pp. 162-168.
19. Zandman, F., "The Transfer-grid Method, a Practical Moire Stress-analysis Tool" (Exp. Mech., Vol. 7, July 1967), pp. 19A-22A.
20. Sciammarella, C., "Moiré-fringe Multiplication by Means of Filtering and a Wavefront Reconstruction Process" (Exp. Mech., Vol. 9, April 1969), pp. 179-185.
21. Little, R.W., Elasticity (Englewood Cliffs, N.J., Prentice-Hall, Inc., 1973).
22. Sokolnikoff, I.S., Mathematical Theory of Elasticity, Second Edition (McGraw-Hill, New York, 1956).
23. Nadai, A., Theory of Flow and Fracture of Solids, Second Edition, Volume 1 (McGraw-Hill, New York, 1950).
24. Cloud, G., "Residual Surface Strain Distribution Near Holes Coldworked to Various Degrees" (AFML-TR-78-153, Air Force Materials Laboratory, Wright-Patterson AFB, Ohio, Nov. 1978).

25. Cloud, G., "Simple Optical Processing of Moiré Grating Photographs" (Exp. Mech., to be published Aug. 1980).
26. Thompson, B.J., "Coherent Optical Processing--A Tutorial Review, 1972" reproduced from "Optical Transforms" (Ed. H.S. Lipson), Chapter 8, "Optical Data Processing" 1970, p.267.
27. Chichener, N.A., A.J. Durelli and J.A. Clark, "Developments in the Optical Spatial Filtering of Superimposed Crossed Gratings" (Exp. Mech., Vol. 12, July 1972), pp. 496-501.
28. Chiang, F., "Techniques of Optical Spatial Filtering Applied to the Processing of Moire-Fringe Patterns" (Exp. Mech., Vol. 9, Nov. 1969), pp. 523-526.
29. Adler, W.F., and D.M. Dupree, "Stress Analysis of Cold-worked Fastener Holes" (AFML-TR-74-44, Air Force Materials Laboratory, Wright-Patterson AFB, Ohio, July, 1974).
30. Ford, S.C., B.N. Leis, D.A. Utah, W. Griffith, S.G. Sampath and P.N. Mincer, "Interference-Fit Fastener Investigation" (AFFDL-TR-93, Air Force Flight Dynamics Laboratory, Wright-Patterson AFB, Ohio, Sept. 1975).
31. Cathy, W.H. and A.F. Grandt, Jr., "Fracture Mechanics Consideration of Residual Stresses Introduced by Coldworking Fastener Holes" (preliminary Draft Report).
32. Moore, T.K., "The Influence of Hole Processing and Joint Variables on the Fatigue Life of Shear Joints" (Technical Report AFML-TR-77-167, Vol. 1, Air Force Materials Laboratory, Wright-Patterson AFB, Ohio, Feb. 1978).
33. Jeffery, G.B., "Plane Stress and Plane Strain in Bipolar Co-ordinates" (Transactions of the Royal Society, 221, London, 1921), p. 265.
34. Parks, V.J., "The Moiré Grid-analyzer Method for Strain Analysis--A Discussion" (Exp. Mech., Vol. 6, May 1966), pp. 287-288.
35. Juvinall, R.C., Engineering Considerations of Stress, Strain and Strength (McGraw-Hill, New York, 1967).
36. Sandor, B.I., Fundamentals of Cyclic Stress and Strain (The University of Wisconsin Press, Madison, 1972)

37. Holister, G.S., and A.R. Luxmoore, "The Productions of High Density Moire Grids" (Exp. Mech., Vol. 8, May 1968), p. 210.
38. Timoshenko, S.P. and J.N. Goodier, Theory of Elasticity, Third Edition (McGraw-Hill, New York, 1970).
39. Dalley, J.W., and W.F. Riley, Experimental Stress Analysis, Second Edition (McGraw-Hill, New York, 1978).
40. Chandawanich, N., and W.N. Sharpe, Jr., "An Experimental Study of Crack Initiation and Stress Intensity Factor Around Coldworked Holes" (Proc. 1978 SESA Spring Meeting, Wichita, Kansas, May 1978).
41. Nadai, A., "Theory of the Expanding of Boiler and Condenser Tube Joints Through Rolling" (Transactions, American Society of Mechanical Engineers, Vol. 65, Nov. 1943), pp. 865-880.
42. Taylor, G.I., "The Formation and Enlargement of a Circular Hole in a Thin Plastic Sheet" (J. of Appl. Mech. and Appl. Math, Series 7:1, 1948), pp. 103-124.
43. Swainger, K.H., "Compatibility of Stress and Strain in Yielded Metals" (Phil. Mag., Series 7:36, p.443).
44. Sharpe, W.N., Jr., "Measurement of Residual Strains Around Coldworked Fastener Holes" (AFOSR-TR-77-0020, Air Force Office of Scientific Research, Bolling AFB, Washington, 1976).
45. Gibson, H.S., Jr., C.G. Trevillion, L. Faulkner, "Thick Section Aluminum Hole Coldworking," (AFML-TR-78-74,) Air Force Materials Laboratory, Wright-Patterson AFB, Ohio, May, 1978.
46. Carter, A.E. and S. Hanagud, "Stress in the Plastic Range Around a Normally Loaded Circular Hole in an Infinite Sheet," (J. Appl. Mech. 42:2, 347-352, 1975).

## APPENDIX A

### Computer Program and Subroutines

```

PROGRAM HOOP (INPUT, OUTPUT = 65)

C
C
COMMON/INTP/TINT (101,2)
COMMON/DIFY/YDIF (101), DY (100)
COMMON/PLOTTER/XRAY (900), YRAY (900), INUM
COMMON X (80,2), Y (80,2), NPTS (2), XPL (101), XL,
      XH,YL, YH, XMIN, XMAX
REAL M
LOGICAL FIN

C
FIN=. FALSE.
IC = 0
INUM = 0

C
C -----ENTER RUN DATA
C
      READ 1, ISET
      FORMAT (A10)
100    CALL READIN (P,M,C,XO,IPR,FIN)
      IF (FIN) GO TO 500
      XO=.2

C
C -----DETERMINE X-RANGE FOR INTERPOLATION & DELTA VALUE
C
      CALL RANGE (DEL)

C
C -----COMPUTE INTERPOLATED SMOOTH CURVES THRU DATA AND
      BASE SETS
C
      CALL INTERP (DEL)

C
C -----CORRECT ABSCISSA ARRAY
C
      CALL CORRECT (XO)

C
C -----COMPUTE CURVE DIFFERENCES & DERIVATIVES
C
      PMC=P*M*C
      CALL DIFF (PMC,DEL)

C
      IC=IC+1
      GO TO 100
500    CALL PLOTH (IC,ISET)
      STOP
      END

```

```

SUBROUTINE READIN (F,M,C,XO,IPR,FIN)
COMMON /STNAM/ ISTNM(9),IST
COMMON X(80,2),Y(RC,2),NPTS(2),XPL(101),XL,XH,YL,YH,XMIN,XMAX
REAL M
LOGICAL FIN
DATA IST/Q/

C-----INPUT RUN CONSTANTS
C
C
1  IST=IST+1
   READ 1,ISTNM(IST)
   FORMAT(A10)
   IF (EOF(5LINPUT)).NE.C) GO TO 50
   READ *F,M,C,XO,IPR
   IF (P.LT.10) .OR. M.GT.100000.) GO TO 999
   IF (M.LT.C) .OR. M.GT.5.) GO TO 999
   IF (C.LT.C) .OR. C.GT.1.) GO TO 999
   IF (XO.LT.0) .OR. XO.GT.1.) GO TO 999

C-----INPUT DATA VALUES
C
C
2  READ *NPTS(1),Y(1,1)
   IF (NPTS(1).LE.0) GO TO 999
   IF (ABS(Y(1,1)).GT.3) GO TO 999
   N=NPTS(1)
   READ * (X(J,1),J=1,N)
   DO 3 I=1,N
     PRINT 9001,X(I,1)
   CONTINUE
   XLAST=25
   DO 5 I=1,N
     IF (X(I,1).GT.1) .OR. X(I,1).LT.XLAST) GO TO 999
   XLAST=X(I,1)
   CONTINUE

C-----COMPUTE REMAINING DATA Y-VALUES
C
C
3  DO 10 I=2,N
   Y(I,1)=Y(I-1,1)+1.C
   CONTINUE

C-----INPUT BASELINE VALUES
C
C

```



```

2C XMIN=X(1,2)
C XL=X(1,1)
4C IF(X(N1,1).GE.X(N2,2)) GO TO 6C
C XMAX=X(N1,1)
C XH=X(N2,2)
C GO TO 8C
6C XMAX=X(N2,2)
C XH=X(N1,1)
8C DEL=(X*AX-XMIN)/100.0
C YL=Y(1,2)
C IF(Y(1,1).LT.Y(1,2)) YL=Y(1,1)
C YH=Y(N2,2)
C IF(Y(N1,1).GT.Y(N2,2)) YH=Y(N1,1)
C RETURN
C END
C SUBROUTINE INTERP(DEL)
C COMMON /INTP/ YINT(101,2)
C COMMON X(80,2),Y(80,2),NPTS(2),XPL(101),XL,XH,YL,YH,XMIN,XMAX
C DIMENSION W(80),RD(80),XN(80),FN(80),GN(80),DN(80),THETA(80),
C +W(1200)
C DIMENSION XD(80),YD(80)
C DATA WD/80*1.0/
C DATA RD/80*0.0/
C DATA XN/80*0.0/
C DATA FN/80*0.0/
C DATA GN/80*0.0/
C DATA DN/80*0.0/
C DATA THETA/80*0.0/
C DATA W/1200*0.0/
C
C DO 10 I=1,101
C XPL(I)=XMIN+DEL*(I-1)
C CONTINUE
C
C DO 40 I=1,2
C DO 15 J=1,80
C XD(J)=X(J,I)
C YD(J)=Y(J,I)

```



```

IF(X.LT.XN(1)) GO TO 100
IF(X.GT.XN(N)) GO TO 110
DO 8 K=1,N
IF(X.NE.XN(K)) GO TO 8
KK=K
GO TO 120
CONTINUE
DO 10 K=2,N
IF(X.GT.XN(K)) GO TO 10
JK=K
GO TO 20
CONTINUE
HH=XN(JK)-XN(JK-1)
HH3=HH**3
T1=HH*GN(JK-1)+FN(JK-1)-FN(JK)
T2=HH*GN(JK)+FN(JK-1)-FN(JK)
T3=XN(JK)-X
T4=X-XN(JK-1)
IF(ITYPE.EQ.2) GO TO 201
SPLIN2=(T3*FN(JK-1)+T4*FN(JK))/HH+T3*T4*(T3*T1-T4*T2)/HH3
RETURN
SPLIN2=(FN(JK)-FN(JK-1))/HH-T3*T4*(HH-T3*T4*(GN(JK-1)+6N(JK))+2.*(FN(JK-1)-FN(JK)))/HH3+(XN(JK-1)+XN(JK)-2.*X)*(T3*T1-T4*T2)/HH3
RETURN
JK=2
GO TO 20
JK=N
GO TO 20
IF(ITYPE.EQ.2) GO TO 301
SPLIN2=FN(KK)
RETURN
SPLIN2=6N(KK)
RETURN
END
SUBROUTINE SPLIN3(M,N,XD,YD,WD,PD,XN,FN,GN,DN,THETA,h,IPRINT)
DIMENSION W(1200),XD(80),YD(80),WD(80),RD(80),XN(80),FN(80),GN(80),DN(80)
+ ,DN(80),S(7),THEFA(80)
TRANSFER KNOTS TO *, AND INSERT EXTRA KNOTS AT ENDS OF RANGE
XN(N)=AMAX1(XN(N),XD(M))
DO 1 I=1,N
1 W(I+3)=X(I)

```

```

DO 2 J=1,3
K=4-J
W(K)=W(K+1)+W(K+1)-W(K+2)
K=J+N
2 W(K+3)=W(K+2)+W(K+2)-W(K+1)
C SET UP THE LEAST SQUARES EQUATIONS IN W
C
J=1
J=2
K=N+13
AA=1.0/((W(3)-W(4))*(W(3)-W(5))*(W(3)-W(6))*(W(3)-W(7)))
D=1.0/((W(5)-W(1))*(W(5)-W(2))*(W(5)-W(3))*(W(5)-W(4)))
3 A=AA
AA=1.0/((W(J+2)-W(J+3))*(W(J+2)-W(J+4))*(W(J+2)-W(J+5))*
1 (W(J+2)-W(J+6)))
R=AA*(W(J+2)-W(J+1))
DD=D
D=1.0/((W(J+4)-W(J))*(W(J+4)-W(J+1))*(W(J+4)-W(J+2))*
1 (W(J+4)-W(J+3)))
C=DD*(W(J+3)-W(J-1))/(W(J+3)-W(J+4))
FN(J-1)=K-7
IF(J-2) 4,4,5
4 W(K-6)=-D
W(K-5)=-C-D
W(K-4)=A+B
W(K-3)=AA
W(K-2)=C
IF(I-M) 6,6,7
6 W(K-1)=1.
W(K)=0
7 C TO 8
5 W(K-4)=-AW*(W(K-4)+C+D)
W(K-3)=AV*B
W(K-2)=AV*AA
8 K=K+7
9 IF(I-M) 9,9,12
9 IF(W(J+3)-XD(I)) 11,10,11
10 W(K-6)=DD*WD(I)*(W(J+3)-XD(I))*3
W(K-5)=WD(I)*(C*(W(J+3)-XD(I))*3+D*(W(J+4)-XD(I))*3)
W(K-4)=WD(I)*(A*(XD(I)-W(J+1))*3+B*(XD(I)-W(J+2))*3)
W(K-3)=WD(I)*AA*(XD(I)-W(J+2))*3
W(K-2)=WD(I)*YD(I)
W(K-1)=C.

```

```

W(K)=0.
I=I+1
GO TO 8 11,4,4
12 IF(J-N) 11,4,4
11 J=J+1
AW=6.*THETA(J-1)
W(K-6)=AW*DD
W(K-5)=AW*C
W(K-4)=A+B
GO TO 3
7 W(K-1)=C.
W(K)=1.
FN(J)=K
APPLY HOUSEHOLDER ORTHOGONAL TRANSFORMATIONS TO OBTAIN AN UPPER
TRIANGULAR LEAST SQUARES MATRIX
KUMAX=K
I=1
IPR=N-1
NPINIT=7
13 I=I+1 IPR+7
NP=NPINIT
J=I+NP
KL=MAX0(IPR+8,IFIX(FN(J-8)+1.5))
KU=IFIX(FN(J-7)+0.5)
IF(NP-3) 14,14,15
14 W(IPR+1)=0.
W(IPR+2)=0.
W(IPR+3)=0.
W(IPR+4)=0.
15 IF(KU-KL) 25,25,17
17 NPINIT=MAX0(3,NPINIT-1)
GO TO 18
16 NP=NP+1
J=IPR+NP
W(J)=W(J-1)
W(J-1)=W(J-2)
W(J-2)=W(J-3)
W(J-3)=0.
KL=KU+1
J=I+NP
KU=IFIX(FN(J-7)+0.5)

```

C  
C  
C  
C

```

18 DO 19 J=1, NP
   JP=IPR+J
   S(J)=W(IPR+1)*W(JP)
19 KPIV=0
   PIVMAX=ABS(W(IPR+1))
   DO 20 K=KL, KU, 7
   DO 21 J=1, NP
     J=K+J
21 S(J)=S(J)+W(JJ-1)*W(K)
   IF(PIVMAX-ABS(W(K))) 70, 20, 20
70 PIVMAX=ABS(W(K))
   KPIV=K
20 CONTINUE
   IF(KPIV) 71, 71, 72
72 DO 73 J=1, NP
   JJ=IPR+J
   A=W(JJ)
   W(KPIV)=W(KPIV)
   KPIV=KPIV+1
73 CONTINUE
74 AA=SIGN(SQRT(S(1)), W(IPR+1))
   B=W(IPR+1)+AA
   A=1/C/(AA*B)
   DO 22 J=2, NP
     JP=IPR+J
     S(J)=A*(S(J)+AA*W(JF))
     W(JP)=W(JP)-B*S(J)
22 DO 23 K=KL, KU, 7
   A=W(K)
   DO 24 J=2, NP
     J=K+J
     W(JJ-2)=W(JJ-1)-A*S(J)
24 CONTINUE
25 CONTINUE
   IF(KU-KUMAX) 25, 26, 26
27 IF(NP-7) 16, 27, 27
   GM(I)=SQRT(W(IPR+1)**2+W(KU+1)**2)
27 A=W(IPR+1)/GN(I)
   B=W(KU+5)/GN(I)
   C=W(KU+5)
   DO 28 J=1, 3
     JP=IPR+J

```

```

JJ=KU+J
W(JP)=A*W(JP+1)+B*W(JJ+1)
W(JJ)=A*W(JJ+1)-B*W(JP+1)
W(JJ+4)=-B*W(JP+4)
28 W(JPR+4)=A*W(JP+4)
W(KU+4)=B*C
50 TO 13
26 IF(NP-4) 29,29,13
C
C
BACK-SUBSTITUTION TO OBTAIN MULTIPLIERS OF FUNDAMENTAL SPLINES
29 K=KUMAX
DO 30 J=1,4
K=K-1
JJ=IPR+J
DO 31 I=1,3
KK=K+I
JK=JJ+I
W(KK)=W(JK)
L=IPR+1
LK=KK
32 IF(L-JJ) 33,34,34
33 L=L+1
LK=LK+1
W(KK)=W(KK)-W(LK)*W(L)
50 TO 32
34 W(KK)=W(KK)/W(IPR+1)
31 CONTINUE
30 CONTINUE
L=N
35 IF(IPR-N) 36,36,37
37 K=K-3
L=L-1
DO 38 I=1,3
KK=K+I
JJ=IPR+I
38 W(KK)=(W(JJ+4)-W(IPR+1)*W(KK+3)-W(IPR+2)*W(KK+6)-W(IPR+3)*W(KK+9)
-W(IPR+4)*W(KK+12))/GN(L)
IPR=IPR-7
50 TO 35
36 KRES=K
C

```



```

B=(S(1)*S(5)-S(2)*S(4))/DET
K=KSDATA
DC 45 I=1,M
K=K+3
45 RD(I)=RD(I)-A*W(K-1)-B*W(K)
KL=KRES+1
DO 46 K=KL,KUMAX,3
46 W(K)=W(K)+A*W(K+1)+B*W(K+2)
C
C
C COMPUTE ELEMENTS OF FN,GN AND DN
K=KRES
AA=1.0/((W(2)-W(3))*(W(2)-W(4))*(W(2)-W(5))*(W(2)-W(6)))
DN(1)=0.
DO 47 J=1,N
A=AA*W(K+4)*(XN(J)-W(J+1))*2
1 AA=1.0/((W(J+2)-W(J+3))*(W(J+2)-W(J+4))*(W(J+2)-W(J+5))*
(W(J+2)-W(J+6)))
1 B=AA*(W(K+7)+W(K+4))*(W(J+2)-W(J+6))/(W(J+2)-W(J+1))*
(XN(J)-W(J+2))*2
1 DD=W(K+1)*(W(J+4)-XN(J))/(W(J+4)-W(J+1))*(W(J+4)-W(J+1))*
(W(J+4)-W(J+2))
FN(J)=A*(XN(J)-W(J+1))+B*(XN(J)-W(J+2))+DD*(W(J+4)-XN(J))
GN(J)=3.0*(A+B-DD)
IF(J-1) 48,48,49
40 DN(J)=6.0*(GN(J-1)+GN(J)+2.0*(FN(J-1)-FN(J))/(XN(J)-XN(J-1)))/
1(XN(J)-XN(J-1))*2
DN(J-1)=DN(J)-DN(J-1)
48 K=K+3
47 CONTINUE
C
C
C PROVIDE PRINT IF REQUESTED
IF(IPRINT) 50,50,51
50 RETURN
C
51 PRINT 52
52 FORMAT(1H1,35X,*SPLINE APPROXIMATION OBTAINED BY SPLIN3+//4X,1HI,
19X,SHXN(I),18X,5HFN(I),13X,16H3RD DERIV CHANGE,11X,
2RHFHETA(I)//)
I=1
54 PRINT 63,I,XN(I),FN(I),GN(I)
I=I+1
IF(I-N) 55,56,56

```

```

55 PRINT 63,I,XM(I),FN(I),GN(I),DN(I),THETA(I)
56 GO TO 54
57 PRINT 63,I,XN(I),FN(I),GN(I)
58 PRINT 63,I,XN(I),FN(I),GN(I)
59 FORMAT(//4X,1HI,9X,5HXD(I),18X,5HYD(I),18X,5HWD(I),19X,3HFIT,
118X,8HRESIDUAL//)
J=>
DO 58 I=1,M
59 IF(XD(I)-XN(J)) 6C,60,61
60 PRINT 63,I,XD(I),YD(I),WD(I),YDRD ,RD(I)
61 FORMAT(5X)
62 J=J+1
63 YDRD = YD(I)-RD(I)
64 PRINT 63,I,XD(I),YD(I),WD(I),YDRD ,RD(I)
65 FORMAT(15,5E23.14)
66 CONTINUE
67 GO TO 59
68 END
SUBROUTINE DIFF(PMC,DEL)
COMMON /INTP/ YINT(101,2)
COMMON /PLOTTER/ XRAY(900) YRAY(900),INUM
COMMON /DIFF/ YDIF(101),DY(100)
COMMON X(80,2),Y(80,2),MPTS(2),XPL(101),DUM6(6)
C ----COMPUTE DIFFERENCES AND DIVIDE BY PMC
C
DE 20 K=1,101
YDIF(K)=(YINT(K,1)-YINT(K,2))/PMC
CONTINUE
C ----COMPUTE DERIVATIVES
C
DO 40 K=2,101
DY(K-1)=(YDIF(K)-YDIF(K-1))/DEL
INUM=INUM+1
XRAY(INUM)=XPL(K)
YRAY(INUM)=DY(K-1)
CONTINUE
RETURN
END
SUBROUTINE PLOTR(IC,ISET)
COMMON /STNAM/ ISTNAM(0) IST
COMMON /PLOTTER/ X(900),Y(900),II

```

```

1 DIMENSION IBUF(257), XRAY(102), YRAY(102)
C DIMENSION XLEG(5), YLEG(5)
C NC=IC*100
C DO 1 I=1,NC
C CONTINUE
C ----INIT PLOTTING PARAMETERS
C CALL PLOTS(IRUF,257,0)
C XRAY(101)=-0.05
C XRAY(102)=0.05
C YRAY(101)=-0.01
C YRAY(102)=0.01
C ----PRINT AXES AND TITLES
C CALL AXIS(0,0,"DISTANCE FROM HOLE (IN.)",-24,9.0,0.0,
C +XRAY(101),XRAY(102))
C CALL AXIS(0,0,"COMPRESSIVE STRAIN",18,7.0,90.0,
C +YRAY(101),YRAY(102))
C CALL DASHLN(C,1,0.9,1,0.042,C42)
C CALL DASHLN(C,1,0.9,1,0.042,C42)
C CALL SYMBOL(1,2,6,C,2,"HOLE,NC",C,9)
C CALL SYMBOL(3,0,6,C,2,"ISET,0",10)
C ----LEGEND INITIALIZE
C CALL SYMROL(7,2,6,6,0,2,"LEGEND",0,6)
C CALL DASHLN(7,2,6,6,8,4,6,56,C14,C014)
C HD=6.45
C XLEG(1)=7.0
C XLEG(2)=7.45
C XLEG(3)=7.9
C XLEG(4)=0.0
C XLEG(5)=1.0
C YLEG(4)=0.0
C YLEG(5)=1.0
C ----PRINT PLCT LINES
C DO 30 I=1,IC
C K=I-1
C N=100+K
C DO 20 J=1,100
C XRAY(J)=X(J+N)
C YRAY(J)=Y(J+N)

```



```

CC CC
DN = AN ARRAY CONTAINING THE VALUES OF THE 3RD DERIVATIVE
ESTIMATE OF THE SPLINE ACROSS THE KNOTS (ROUGH
ESTIMATE OF THE ERROR IN THE FIT) (OUTPUT)
THETA = WORKING ARRAY (MUST BE DIMENSIONED ATLEAST 7*M+8*N+6)
W = WORKING ARRAY (MUST BE DIMENSIONED ATLEAST 7*M+8*N+6)
IPRINT = 1 PRINT RESULTS AFTER EACH ITERATION
        0 NO PRINT RESULTS FOR BEST FIT ONLY
        -1 FIT OPTION
IFIT = 0 PROGRAM WILL AUTOMATICALLY SELECT KNOT POSITIONS
        1 CALCULATE THE SPLINE WITH THE INPUT SET OF KNOT
        POSITIONS **CAUTION N MUST BE .GE. 5 AND XN(1)=XD(1),
        XN(N)=XD(M) FOR CORRECT RESULTS.

```

THE NORMAL MODE OF OPERATION IS TO ALLOW THE PROGRAM TO  
AUTOMATICALLY SELECT THE OPTIMAL KNOT POSITIONS BASED ON  
STATISTICAL ERROR TESTS. IN THIS MODE OF OPERATION IT IS DIFFICULT  
TO PREDICT THE REQUIRED DIMENSION FOR THE ARRAYS XN, FN, GN, DN,  
THETA AND W. THE PROGRAM WILL NEVER MAKE N GT M OR A SAFE  
DIMENSIONALITY FOR THESE ARRAYS WOULD MAKE M SPLIN3  
TO CALCULATE THE LEAST SQUARES SPLINE APPROXIMATION.

```

* * * * *
1 DIMENSION XD(80), YD(80), WD(80), RD(80), XM(80), FN(80), GN(80), DN(80),
  THETA(80), W(1200)
OMIT DATA WITH ZERO WEIGHTS
MM=1
J=1
DO 1 I=2,M
  IF(WD(I)) 3,2,3
  IF(I-M) 4,3,3
2  W(J)=XD(I)
  W(J+1)=YD(I)
  W(J+2)=FLOAT(I)
  J=J+3
3  MM=MM+1

```

```

XD(MM)=XD(I)
YD(MM)=YD(I)
WD(MM)=WD(I)
1 CONTINUE
J=1
K=MM
7 IF(K-M) 5,6,6
5 K=K+1
XD(K)=W(J)
YD(K)=W(J+1)
WD(K)=W(J+2)
J=J+2
GO TO 7
C
C INITIALIZATION OF ITERATIONS
6 IF(IFIT.EQ.1) GO TO 11
JA=1
IF(WD(1)) 9,8,9
8 JA=2
9 N=
XN(1)=XD(1)
XN(5)=XD(MM)
XN(3)=0.5*(XN(1)+XN(5))
XN(2)=0.5*(XN(1)+XN(3))
XN(4)=0.5*(XN(3)+XN(5))
110 IW=7*MM+R*N+6
DO 10 I=1,N
J=IW+I
W(J)=XN(I)
IP=-IPRINT
C
C CALCULATE THE HISTOGRAMS FOR NEW SCALE FACTORS
11 J=0
K=1
SA=0
12 SA=SA+WD(K)**2
K=K+1
IF(XD(K)-XD(1)) 12,12,13
13 SA=(SA+0.5*WD(K)**2)/(XD(K)-XD(1))
14 J=J+1
16 IF(XD(K)-XN(J+1)) 15,15,16
GN TO 14
15 SA=SA*(XN(J+1)-XN(J))

```

```

15 GN(J)=SA*(XD(K)-XN(J))+0.5*WD(K)**2
17 K=K+1
18 IF(K-MM) 18,18,10
19 IF(XD(K)-XN(J+1)) 20,20,21
20 GN(J)=GN(J)+WD(K)**2
21 SA=0.5*(WD(K-1)**2+WD(K)**2)/(XD(K)-XD(K-1))
22 GN(J)=GN(J)+0.5*WD(K-1)**2+SA*(XN(J+1)-XD(K-1))
23 GN(J-1)=0.00025216*GN(1)*(W(K)-W(K-1))**8/(XN(2)-XN(1))
24 IF(XN(J)-W(K)) 23,23,24
25 K=K+1
26 GN(J-2)=ALOF(GN(J-2)+GN(J-1))
27 NN=N-2
28 HS=1.386294
29 DO 97 J=2,NN
30 GN(J)=AMIN1(GN(J),GN(J-1))+HS)
31 J=NN-1
32 GN(J)=AMIN1(GN(J),GN(J+1))+HS)
33 IF(J) 99,99,98
34 DO 25 J=3,N
35 THETA(J-1)=SQRT(EXP(GN(J-2)))/(XN(J)-XN(J-2)))
36 CALL SPLIN3(MM,N,XD,YD,WD,RD,XN,FN,GN,DM,THETA,W,IP)
37 IF(IFIT.EQ.1) 60,60,41
38 APPLY STATISTICAL TEST FOR EXTRA KNOTS
39 J=IW+1
40 JJ=C
41 K=JA
42 TMAY=0
43 IIS=1
44 ICE=-1
45 SW=C.

```

```

SR=0
RP=0
J=J+1
JJ=JJ+1
W(W(J))-XD(K) 28,29,30
27 KC=KC+1
30 SW=SW+RD(K)**2
SR=SR+RP*RD(K)
RP=RD(K)
K=K+1
GO TO 27
IF(WD(K)) 31,28,31
29 KC=KC+1
31 SW=SW+RD(K)**2
SR=SR+RP*RD(K)
IF(SR) 32,32,33
32 SW=(SW/SR)**2
33 RP=SQRT(SR/FLOAT(KC)) 32,32,34
34 IF (FLOAT(KC)=SW) 36 TO 37
IF (IIS.EQ.3) 60 TO 37
IF (IIS.EQ.2) 60 TO 36
RP=RP
IIS=IIS-1
IF (FLOAT(KC)=2.*SW) 38,38,39
W(JJ-1)=PRP
37 TMAX=AMAX1(TMAX,PRP)
39 IIS=2
36 W(JJ)=RP
TMAX=AMAX1(TMAX,RP)
GO TO 38
32 IIS=1
38 IF(W(J)-XN(N)) 26,40,40
C TEST WHETHER ANCTHER ITERATION IS REQUIRED
C
C 40 IF(TMAX) 41,41,42
C
C CALCULATE NEW TREND ARRAY, INCLUDING LARGER TRENDS ONLY
C
C 42 IMAX=C.5*TMAX
I=0
J=1
JW=1

```

```

K=IW+1
THETA(JW)=W(K)
43 I=I+1
K=K+1
IF(W(I)-TMAX) 44,44,45
44 JW=JW+1
THETA(JW)=W(K)
46 FN(J)=0.
J=J+1
IF(W(K)-XN(J)) 47,47,46
45 JW=JW+2
THETA(JW-1)=0.5*(W(K-1)+W(K))
THETA(JW)=W(K)
IF(XN(J+1)-THETA(JW-1)) 46,46,48
48 FN(J)=1.
J=J+1
47 IF(J=N) 43,40,49
C
C
C
MAKE KNPT SPACINGS BE USED FOUR TIMES
49 IK=1
KL=1
FN(2)=AMAX1(FN(1),FN(2))
50 K=KL+3
51 IF(FN(K)) 52,52,53
52 K=K-1
IF(K-KL) 54,54,51
53 K=K-1
FN(K)=1.
IF(K-KL) 54,54,53
54 K=K+1
IF(K=N) 55,56,56
55 IF(XN(K+1)-XN(K)-1.5*(XN(K)-XN(K-1))) 54,54,56
56 KU=K
FN(K-2)=AMAX1(FN(K-2),FN(K-1))
57 KU=K
58 K=K-1
IF(K-KL) 59,59,60
60 IF(XN(K)-XN(K-1)-1.5*(XN(K+1)-XN(K))) 58,58,61
61 FN(K+1)=AMAX1(FN(K),FN(K+1))
62 K=K
K7=4
IF(FN(K)) 62,62,63
63 K=K+1

```

```

64 IF(K-KK1) 64,65,65
66 IF(FN(K)) 66,66,63
62 KZ=K+1
67 IF(K-KKU) 67,65,65
68 IF(FN(K)) 62,62,68
69 IF(KZ-3) 69,69,70
71 J=J+1
70 IF(J-K) 71,63,63
72 IF(K+1-KKU) 72,65,65
73 FN(K)=1
74 IF(KL-KKL) 73,74,74
75 FN(KKL-2)=AMAX1(FN(KKL-2),FN(KKL+1))
76 FN(KKL-1)=AMAX1(FN(KKL-1),FN(KKL+3))
77 K=K+1
78 IF(FN(K)) 76,76,77
79 IF(K-KKL) 78,79,79
80 IF(K)=1
81 IF(K-KKL) 77,79,79
82 IF(K-EG) 80,80,57
83 IF(K-EP) 80,80,80
84 IF(KU-N) 81,82,82
85 KL=KL+1
86 FN(KL)=AMAX1(FN(KL+1),FN(KL-2))
87 FN(KL)=AMAX1(FN(KL),FN(KL-4))
88 TO 50
89 TK=2
90 KKL=N
91 TO 75

```

C C C  
INSERT EXTRA KNCTS FOR NEW APPROXIMATION

```

80 DO 83 J=1,N
83 GN(J)=XN(J)
NN=1
DO 84 J=2,N
IF(FN(J-1)) 85,85,86

```

```

86 NN=NN+1
87 XN(NN)=0.5*(GN(J-1)+6N(J))
88 NN=NN+1
89 XN(NN)=GN(J)
90 CONTINUE
91 N=NN
92 IW=7*MM+R*N+6
93 DO 87 J=1,JW
94 I=IW+J
95 W(I)=THETA(J)
96 GO TO 11
97
98 RESTORE DATA WITH ZERO WEIGHTS
99
100 IF(MM-M) 88,89,89
101 IF(IPRINT) 90,90,91
102 J=.2
103 K=MM
104 J=J+3
105 K=K+1
106 W(J)=XD(K)
107 W(J+1)=YD(K)
108 W(J+2)=WD(K)
109 IF(K-M) 92,93,93
110 I=INT(W(J+2)+0.1)
111 IF(K-I) 95,95,96
112 XD(K)=XD(MM)
113 YD(K)=YD(MM)
114 WD(K)=WD(MM)
115 K=K-1
116 MM=MM-1
117 GO TO 94
118 XD(K)=W(J)
119 YD(K)=W(J+1)
120 WD(K)=0.
121 K=K-1
122 J=J-3
123 IF(J) 91,91,93
124 CALL SPLIN3(M,N,XD,YD,WD,RD,XN,EN,GN,DN,THETA,W,IABS(IPPINT))
125 RETURN
126
127 SUBROUTINE WRITOUT(IC,DEL)
128 COMMON /INIP/ YINT(101,?)
129 COMMON /DIFY/ YDIF(101),DY(100)
130

```

```

COMMON X(80,2),Y(80,2),NPTS(2),XPL(101),XL,XH,YL,YH,XMIN,XMAX
C
C
100 IC
105 XMIN,XMAX,DEL
110 XPL(1),YINT(1,1),YINT(1,2),YDIF(1)
D N 50 K=2,101
115 XPL(K),YINT(K,1),YINT(K,2),YDIF(K),DY(K-1)
CONTINUE
C
120 PRINT 120
FORMAT(1H1, // 5X,"OUTPUT -- MOIRE DATA ANALYSIS -- SET #",I2, //)
FORMAT(5X,"COMPUTED VALUES USED --", //10X,"XMIN = ",E17.9//10X,
+"XMAX = ",E17.9//7X,"DELTA X = ",E17.9//)
FORMAT(4X,"DISTANCE FROM HOLE",10X,"Y1",19X,"Y2",15X,
+"DISPLACEMENT",12X,"STRAIN",/)
FORMAT(4X,5(E16.9,5X))
FORMAT(1H1)
RETURN
END
SUBROUTINE PLOTM(IP,ISET)
COMMON /INTP/ YINT(101,2)
COMMON /DIFY/ YDIF(101),DY(100)
COMMON X(80,2),Y(80,2),NPTS(2),XPL(101),XL,XH,YL,YH,XMIN,XMAX
DIMENSION IBUF(257),HOLDX(103),HOLDY(103)
C
C ----INITIALIZE PLOT PARAMETERS
CALL PLOTS(IBUF,257,0)
C
C ----DETERMINE PLOT TYPE
IF(IP-2) 100,200,300
C
C ----BASIC PLOT
CALL AXIS(0,0,0,"X",-18.0,0.0,0.0,0.05)
CALL AXIS(0,0,0,"F",12.8,0.0,0.0,0.0,4.0)
D N 110 I=1,N
HOLDY(I)=X(I,1)
HOLDX(I)=Y(I,1)

```

```

110 CONTINUE
    HOLDX(N+1)=0.0
    HOLDX(N+2)=0.05
    HOLDY(N+1)=0.0
    HOLDY(N+2)=4.0
    CALL LINE(HOLDX,HOLDY,N,1,5,1)
    N=NPTS(2)
    DO 120 I=1,N
    HOLDX(I)=X(I,2)
    HOLDY(I)=Y(I,2)
    CONTINUE
    HOLDX(N+1)=0.0
    HOLDX(N+2)=0.05
    HOLDY(N+1)=0.0
    HOLDY(N+2)=4.0
    CALL LINE(HOLDX,HOLDY,N,1,5,2)
    GO TO 500

C -----DIFFERENCE PLOT
200 CALL AXIS(0,0,0,"DISTANCE FROM HOLE (IN.)",-24,9,0,-.05,.05)
    CALL AXIS(0,0,0,"DISPLACEMENT",12,7,.90,-.001,-.001)
    DO 210 I=1,161
    HOLDX(I)=XPL(I)
    HOLDY(I)=YDIF(I)
    CONTINUE
    HOLDX(102)=-0.05
    HOLDX(103)=-0.05
    HOLDY(102)=-0.001
    HOLDY(103)=-0.001
    CALL LINE(HOLDX,HOLDY,101,1,0,0)
    CALL DASHLN(0,1,9,1,042,042)
    CALL DASHLN(1,0,1,7,042,042)
    GO TO 500

C -----STRAIN PLOT
300 CALL AXIS(0,0,0,"DISTANCE FROM HOLE (IN.)",-24,9,0,-.05,.05)
    CALL AXIS(0,0,0,"COMPRESSIVE STRAIN",18,7,.90,-.01,-.01)
    DO 310 I=1,160
    HOLDX(I)=XPL(I+1)
    HOLDY(I)=DY(I)
    CONTINUE
    HOLDX(101)=-0.05

```



```

XLEG(1)=7.0
XLEG(2)=7.45
XLEG(3)=7.9
XLEG(4)=0.0
YLEG(5)=1.0
YLEG(6)=0.0
YLEG(7)=1.0

C ----PRINT PLOT LINES
C
D 30 I=1,IC
K=I-1
N=100*K
DO 20 J=1,100
XRAY(J)=X(J+N)
YRAY(J)=Y(J+N)
CONTINUE
CALL LINE(XRAY,YRAY,100,1,5,K)
PRINT LEGEND
HTD=HTD-C.14
YLEG(1)=HTD
YLEG(2)=HTD
YLEG(3)=HTD
CALL LINE(XLEG,YLEG,3,1,1,K)
CALL SYMBOL(8.1,HTD-.642,6.084,ISTNAM(I),0.,10)
CONTINUE
COMPLETE LEGEND
HTD=HTD-C.14
CALL DASHLN(6.8,7-C,6.8,HTD,.014,.014)
CALL DASHLN(6.8,HTD,9.0,HTD,.014,.014)
CALL DASHLN(9.0,HTD,9.0,HTD,.014,.014)
CALL DASHLN(9.0,7-C,6.8,7-C,.014,.014)

C ----EXIT PLOT ROUTINE
C
CALL PLOT(12.0,0.0,999)
RETURN
END
SUBROUTINE TPLPTR(IC,ISET)
COMMON /SINAM/ ISTNAM(9) IST
COMMON /PLOTTER/ X(900) Y(900) II
DIMENSION IBUF(257),XRAY(102),YRAY(102)
NC=IC*1-C

```

```

1 DO 1 I=1,NC
C CONTINUE
C -----INIT PLOTTING PARAMETERS
C CALL PLOTS(IBUF,257,0)
C XRAY(101)=-0.05
C XRAY(102)=0.05
C YRAY(101)=-0.1
C YRAY(102)=0.025
C -----PRINT AXES AND TITLES
C CALL AXIS(0,0,"DISTANCE FROM HOLE (IN.)",-24,9.0,0.0,
C +XRAY(101),XRAY(102))
C CALL AXIS(0,0,"COMPRESSIVE STRAIN",18,7.0,90.0,
C +YRAY(101),YRAY(102))
C CALL DASHLN(0,4,9,4,0.042,.C42)
C CALL DASHLN(1,5,0,1,1,0.042,.C42)
C CALL SYMBOL(1,5,6,0,2,"HOLE NC",C,0)
C CALL SYMBOL(3,0,6,0,2,ISET,0,10)
C -----LEGEND INITIALIZATION
C CALL SYMBOL(7,2,6,6,0,2,"LEGEND",0,6)
C CALL DASHLN(7,2,6,6,8,4,6.56,.C14,.014)
C HTD=6.45
C XLEG(1)=7.0
C XLEG(2)=7.45
C XLEG(3)=7.9
C XLEG(4)=0.0
C XLEG(5)=1.0
C YLEG(4)=0.0
C YLEG(5)=1.0
C -----PRINT PLOT LINES
C DO 30 I=1,IC
C K=I-1
C N=100*K
C DO 20 J=1,100
C XRAY(J)=X(J+N)
C YRAY(J)=Y(J+N)
C CONTINUE
C CALL LINE(XRAY,YRAY,100,1,5,K)
C -----PRINT LEGEND

```

```

HTD=HTD-C.14
YLEG(1)=HTD
YLEG(2)=HTD
YLEG(3)=HTD
CALL LINE(XLEG,YLEG,3,1,1,K)
CALL SYMBOL(8.1,HTD,.042,0.084,ISTNAM(I),0.,10)
3C ----COMPLETE LEGEND
C ----HTD=HTD-C.14
CALL DASHLN(6.8,7.0,6.8,HTD,.C14,.014)
CALL DASHLN(6.8,HTD,9.0,HTD,.014,.014)
CALL DASHLN(9.0,HTD,9.0,7.0,.014,.014)
CALL DASHLN(9.0,7.0,6.8,7.0,.014,.014)
C ----EXIT PLOT ROUTINE
C
CALL PLOT(12.0,C.0,599)
RETURN
END
SUBROUTINE TPLOTM(IP,ISET)
COMMON /INTP/ YINT(101,2)
COMMON /DIFY/ YDIF(101),DY(100)
COMMON X(80,2),Y(80,2),NPTS(2),XPL(101),XL,XH,YL,YH,XMIN,XMAX
DIMENSION IBUF(257),HOLDX(103),HOLDY(103)
C ----INITIALIZE PLOT PARAMETERS
C
CALL PLOTS(IBUF,257,0)
C ----DETERMINE PLOT TYPE
C
IF(IP-2) 100,200,300
C ----BASIC PLOT
C
100 CALL AXIS(0.,0.,"X",-1.8,0.0,0.,C.0,0.05)
CALL AXIS(0.,0.,"FRINGE ORDER",12,6.0,0.0,0.0,4.0)
N=NPTS(1)
DO 110 I=1,N
HOLDX(I)=X(I,1)
HOLDY(I)=Y(I,1)
CONTINUE
HOLDX(N+1)=0.0
HOLDX(N+2)=0.05
110

```

```

HOLDY(N+1)=0.0
HOLDY(N+2)=4.0
CALL LINE(HOLDX,HOLDY,N,1,5,1)
N=NPTS(2)
DO 120 I=1,N
HOLDX(I)=X(I,2)
HOLDY(I)=Y(I,2)
CONTINUE
HOLDX(N+1)=0.0
HOLDX(N+2)=0.05
HOLDY(N+1)=0.0
HOLDY(N+2)=4.0
CALL LINE(HOLDX,HOLDY,N,1,5,2)
GO TO 500

C ----DIFFERENCE PLOT
C
200 CALL AXIS(0,0,"DISTANCE FROM HOLE (IN.)",-24,9,0,-.05,.05)
DO 210 I=1,161
HOLDX(I)=XPL(I)
HOLDY(I)=YDIF(I)
CONTINUE
HOLDX(102)=-0.05
HOLDY(102)=0.05
HOLDY(103)=0.001
CALL LINE(HOLDX,HOLDY,101,1,0,C)
CALL DASHLN(0,1,9,1,1,0,042,C42)
GO TO 500

C ----STRAIN PLOT
C
300 CALL AXIS(0,0,"DISTANCE FROM HOLE (IN.)",-24,9,0,-.05,.05)
DO 310 I=1,160
HOLDX(I)=XPL(I+1)
HOLDY(I)=DY(I)
CONTINUE
HOLDX(101)=-0.05
HOLDY(102)=0.05
HOLDY(101)=0.1
HOLDY(102)=0.025

```



